UNIVERSITY OF CRETE

DEPARTMENT OF PHYSICS

PhD THESIS

Measuring star-formation rates in galaxies and their correlation with X-ray emission

Konstantinos Kouroumpatzakis

Advisor: *Prof.* Andreas Zezas - University of Crete

This page intentionally left blank

University of Crete
Department of Physics

PhD THESIS

Doctor of Philosophy
in
ASTROPHYSICS

Defended by
Konstantinos Kouroumpatzakis

Measuring star-formation rates in galaxies and their correlation with X-ray emission

Committee

Professor	Andreas Zezas	University of Crete
Professor	Vasileios Charmandaris	University of Crete
Professor	Iosif Papadakis	University of Crete
Assistant Professor	Vassiliki Pavlidou	University of Crete
Research Director	Pablo Reig	Institute of Astrophysics/FORTH
Associate Researcher	Tanio Diaz Santos	Institute of Astrophysics/FORTH
Research Director	Manolis Xylouris	IAASARS/NOA

Date of the defence:
22/12/2020

This page intentionally left blank

Abstract

We present a study of different star-formation rate (SFR) indicators, focusing on Hα emission, and its comparison with other traditional and emerging (X-ray luminosity) SFR tracers. We present Hα photometry for the Star-Formation Reference Survey (SFRS), a representative sample of star-forming galaxies in the local Universe. Based on this data and the multiwavelength coverage of the SFRS, we provide calibrations of Hα-based SFRs with UV, FIR, and radio (1.4 GHz) indicators. We explore the effect of extinction correction based on the Balmer decrement, infrared excess (IRX), and fits of spectral energy distributions (SEDs), as well as, corrections for the contribution of the [N II] lines emission.

We find excellent agreement between the FIR + FUV hybrid indicator and the Hα-based SFR, as well as with the 24μm + Hα indicator. We also find good agreement between the 1.4 GHz continuum emission and the Hα SFRs. The comparison between the SFRs derived through SED fits, and the FIR + FUV hybrid indicator, show an excellent agreement for SFR $\gtrsim 1$ M$_\odot$ yr^{-1}, and increased scatter for lower SFR, attributed to stochastic effects and sensitivity on extinction and stellar population age variations.

The extinction based on the Balmer decrement is found to be on average about two times larger than the ones based on the IRX, or the SED fits. This difference is attributed to the fact that the Balmer emission probes younger stellar populations, in comparison to the FIR and FUV emission, making it more sensitive to the attenuation caused by dust in birth clouds. We find a correlation between extinction and metallicity, and we provide a functional description of this correlation for the IRX and Balmer-decrement extinction indicators. We show that galaxies deviating from this relation are mainly dwarf, highly star-forming galaxies, where a larger part of the overall attenuation is attributed to the dust in the birth clouds rather than the general ISM.

For a subset of the SFRS sample with good quality *Chandra* data, we explore the connection between SFR and X-ray luminosity (L_X) originating from high-mass X-ray binaries (HMXBs). By performing this analysis in sub-galactic scales, we study this relation in a range over ~ 7 dex in SFR and ~ 8 dex in specific SFR (sSFR). There

is good agreement with established L_X–SFR relations down to SFR $\simeq 10^{-3}\,\mathrm{M_\odot\,yr^{-1}}$, below which an excess in X-ray luminosity emerges. This excess likely arises from low-mass X-ray binaries. The intrinsic scatter of the L_X–SFR relation is constant, and not correlated with SFR. We find that different star formation indicators scale with L_X in different ways, and we attribute the differences to the effect of star formation history. The SFR derived from Hα shows the tightest correlation with X-ray luminosity because Hα emission probes stellar populations with ages similar to HMXB formation timescales, but the Hα-based SFR is reliable only for sSFR $> 10^{-12}\,\mathrm{M_\odot\,yr^{-1}/M_\odot}$, below which the contribution from older stellar populations (and low-mass X-ray binaries) cannot be neglected.

In order to explore the effect of metallicity on the X-ray luminosity - SFR relation, we present a systematic study of the metallicity variations within the collisional ring galaxy NGC 922, based on long-slit spectroscopic, X-ray, and IR observations. We find a metallicity difference between star-forming regions in the bulge and the ring, with metallicities ranging from almost solar to significantly sub-solar ($[12 + \log(\mathrm{O/H})] \sim 8.2$). We detect He I emission in the bulge and the ring star-forming regions indicating ionization from massive stars associated with recent ($< 10\,\mathrm{Myr}$) star-formation, in agreement with the presence of very young star-clusters in all studied regions. We find an anti-correlation between the X-ray luminosity and metallicity of the sub-galactic regions of NGC 922. The different regions have similar stellar population ages leaving metallicity as the main driver of the anti-correlation. The dependence of the X-ray emission of the different regions in NGC 922 on metallicity, is in agreement with similar studies of the integrated X-ray output of galaxies and predictions from X-ray binary population models.

Περίληψη

Παρουσιάζουμε μια εκτεταμένη μελέτη δεικτών ρυθμού αστρογένεσης (ΡΑ) γαλαξιών και αστρικών πληθυσμών (ΑΠ), εστιάζοντας στην γραμμή εκπομπής υδρογόνου α (Ηα λ6563 Å) και την σύγκριση του με άλλους συνήθεις αλλά και νέους δείκτες ΡΑ. Παρουσιάζουμε φωτομετρία στην φασματική γραμμή Ηα για το αντιπροσωπευτικό δείγμα γαλαξιών *Star Formation Reference Survey* (SFRS) του τοπικού Σύμπαντος. Βασισμένοι στα δεδομένα αυτά και την μεγάλου εύρους φασματική κάλυψη του SFRS, παρουσιάζουμε βαθμονομήσεις ΡΑ βασισμένων σε εκπομπή Ηα, υπεριώδους (ΥΙ), μακρινού υπερύθρου (ΜΥΡ), και ραδιοκυμάτων (1.4 GHz). Διερευνούμε το αποτέλεσμα της διόρθωσης της απόσβεσης μέσω της μείωσης Balmer, της περίσσειας υπερύθρου (IR excess), και φασματικών κατανομών ενέργειας (spectral energy distributions, SED). Επίσης διερευνούμε το αποτέλεσμα της συνεισφοράς της εκπομπής των γραμμών του αζώτου ([N II], λλ6548, 6583 Å) στις μετρήσεις της λαμπρότητας της γραμμής Ηα μέσω επεικόνησης με φίλτρα μικρού φασματικού εύρους.

Βρίσκουμε πολύ καλή συμφωνία των ΡΑ υπολογισμένων μέσω του Ηα, και υβριδικών δεικτών που βασίζονται στο συνδυασμό ΜΥΡ + ΥΙ και του Ηα, όπως επίσης και του συνδυασμού 24 μm + Ηα. Βρίσκουμε επίσης πολύ καλή συμφωνία και με τους ΡΑ υπολογισμένους από SED αν και αυτή η σχέση έχει μεγάλη διασπορά σε μικρές τιμες ΡΑ. Η μεσοατρική απόσβεση του φωτός (A_V) μετρημένη μέσω της μείωσης Balmer είναι περίπου δυο φορές μεγαλύτερη σε σχέση με την απόσβεση που εκτιμάται μέσω της περίσσειας υπερύθρου, και των SED (που μεταξύ τους είναι παρόμοιες). Αυτή η διαφορά οφείλεται στο γεγονός ότι οι γραμμές Balmer σχετίζονται με νεότερους αστρικούς πληθυσμούς, και επομένως φέρουν μεγαλύτερη απορρόφηση λόγω του ότι πολλά από αυτά τα πολύ νεαρά αστέρια εξακολουθούν να καλύπτονται απο τα μητρικά νέφη αστρογένεσης. Επίσης ποσοτικοποιούμε την συσχέτιση μεταξύ απόσβεσης και μεταλλικότητας των γαλαξιών. Παρατηρούμε πως οι γαλαξίες που τείνουν να διαφέρουν από την γενικότερη σχέση είναι μικρότεροι γαλαξίες με υψηλό ειδικό ΡΑ (εΡΑ, sSFR).

Για ένα δείγμα του SFRS με καλής ποιότητας δεδομένα ακτίνων X (Chandra) διερευνούμε την συσχέτιση μεταξύ της φωτεινότητας ακτίνων X (ΦX) απο υψηλής μάζας δυαδικά

συστήματα αστέρων ακτίνων X (HMXBs) και PA. Μελετώντας αυτό το φαινόμενο σε υπό-γαλαξιακές κλίμακες έως και 1×1 kpc^2 μελετούμε αυτή την συσχέτιση σε ένα εύρος $\sim$7 και $\sim$8 τάξεων μεγέθους σε PA και εPA αντίστοιχα. Βρίσκουμε συμφωνία με υπάρχουσες μελέτες ΦX-PA για PA μέχρι $\simeq 10^{-3}\,\mathrm{M_\odot\,yr^{-1}}$και περίσσεια εκπομπή ακτίνων X για ΑΠ με μικρότερους PA. Η περίσσεια αυτή πιθανότατα προκαλείται από ένα πληθυσμό δυαδικών συστημάτων αστέρων χαμηλής μάζας ακτίνων X (LMXBs). Η εγγενής διασπορά της συσχέτισης ΦX-PA είναι σταθερή και δεν εξαρτάται από την τιμή του PA. Βρίσκουμε πως οι διαφορετικοί δείκτες PA έχουν διαφορετική σχέση αναλογίας με την ΦX, ένα φαινόμενο που αποδίδουμε στην επίδραση που έχουν οι διάφορες ιστορίες αστρογένεσης στους διάφορους γαλαξίες. Οι PA μέσω Hα έχουν την καλύτερη συσχέτιση με ΦX καθώς η εκπομπή Hα προέρχεται απο ΑΠ με ηλικίες παραπλήσιες με τα HMXBs. Βρίσκουμε πως οι μετρήσεις PA μέσω Hα είναι αξιόπιστες για εPA $> 10^{-12}\,\mathrm{M_\odot\,yr^{-1}/M_\odot}$. Για περιοχές με μικρότερες τιμές εPA η συνεισφορά των παλαιών ΑΠ δεν μπορεί να θεωρηθεί αμελητέα.

Προκειμένου να μελετήσουμε την επίδραση της μεταλλικότητας στην συσχέτιση ΦX-PA παρουσιάζουμε μια συστηματική μελέτη των διαφοροποιήσεων της μεταλλικότητας και της ΦX εντός του δακτυλιοειδή γαλαξία NGC 922. Βρίσκουμε πως ο δακτύλιος του NGC 922 έχει πολύ χαμηλότερη μεταλλικότητα ($[12 + \log(\mathrm{O/H})] \sim 8.2$) σε σύγκριση με τον πυρήνα. Παρατηρούμε γραμμές εκπομπής He I που σχετίζονται με νέους αστρικούς πληθυσμούς στις υπό-γαλαξιακές περιοχές του δακτυλίου αλλά και του πυρήνα. Αυτό το αποτέλεσμα είναι σε συμφωνία με την παρουσία νεαρών αστρικών σμηνών σε όλες τις υπό-μελέτη περιοχές. Βρίσκουμε πως υπάρχει μια αντι-συσχέτιση μεταξύ της ΦX και της μεταλικότητας στον γαλαξία NGC 922. Οι διάφορες υπο-γαλαξιακές περιοχές έχουν ΑΠ παραπλήσιας ηλικίας και έτσι η διαφορετική μεταλλικότητα των περιοχών αυτών είναι ο κύριος λόγος για αυτήν την αντι-συσχέτιση. Η αντι-συσχέτιση της ΦX με την μεταλλικότητα των διαφορετικών περιοχών του NGC 922 είναι σε συμφωνία με παρόμοιες μελέτες που συμπεριλάβαιναν την εκπομπή ολόκληρων γαλαξιών, αλλά και με μοντέλα προσομοίωσης την εξέλιξη δυαδικών συστημάτων εκπομπής ακτίνων X.

To my beloved father who i will always miss.

To my beloved mother, brother, and Rea, who's love and support to me is boundless.

This page intentionally left blank

Declaration

I hereby declare that the work in this thesis is that of the candidate alone, except where indicated below.

Chapter 2: is a paper in preparation, co-authored by *Zezas A.; Maragkoudakis A.; Bonfini P.; Willner S. P.; Ashby M. L. N.*

Chapter 3: is published in the Monthly Notices of the Royal Astronomical Society as: *Kouroumpatzakis, K.; Zezas, A.; Sell, P.; Kovlakas, K.; Bonfini, P.; Willner, S. P.; Ashby, M. L. N.; Maragkoudakis, A.; Jarrett, T. H., 2020, MNRAS, 494, 5967-5984.*

Chapter 4: is published in the Monthly Notices of the Royal Astronomical Society as: *Kouroumpatzakis, K.; Zezas, A.; Wolter, A.; Fruscione, A.; Anastasopoulou, K.; Prestwich, A., 2021, MNRAS, 500, 962-975.*

This page intentionally left blank

Preface and Acknowledgments

This work would have not be possible without the help of numerous people.

First, I would like to express my deep gratitude to professor Andreas Zezas. He was always there to offer support, and share his wisdom. His advise, and guidance was of great importance in realising this thesis, and shaping me as an astrophysicist.

I would like to thank my *Skinakas family*, the personnel of Skinakas observatory: Anna Steiakaki, Tasos Kougentakis, Yiorgos Paterakis, Dr. Makis Palaiologou, and Vagelis Pantoulas who selflessly offered their help and companionship, from the first moment of my arrival in Heraklion.

I would like to thank Dr. Konstantinos Kovlakas, Dr. Paolo Bonfini, Dr. Konstantina Anastasopoulou, Dr. Paul Sell, Dr. Jeff Andrews, Dr. Dmitry Blinov, Dr. Yiannis Liodakis, Nikos Mandarakas, Dr. Steven Willner, Dr. Alexandros Maragkoudakis, Dr. Mathew Ashby, Dr. Pablo Reig, and Dr. Anna Wolter, for our valuable collaborations where they gave me the chance to expand my knowledge in various ways.

I deeply thank, Dr. Ioanna Leonidaki, Maria Kopsacheili, Johny Kypriotakis, Dr. Grigoris Maravelias, and Elias Kyritsis for the numerous nights we spent together at the Skinakas observatory. Their companionship made the long observing nights far better, while our interaction was also very educational.

I would like to thank professor Vassilis Charmandaris, Dr. Tanio Diaz Santos, Dr. Steven Williams, Yiorgos Korkidis, Dr. Carolina Casadio, Rafail Skalidis, Dr. Eva Ntormousi, and Dr. Fabio del Sordo for our extended discussions, and valuable suggestions which helped me get a better understanding in a variety of subjects of astrophysics.

I am thankful to all the people of the astrophysics group in the University of Crete, and the Institute of Astrophysics of FORTH, who make this institute a wonderful place to live, work, learn, and conduct research.

Finally, I would also like to thank my good friend Dr. Theodore Koutmeridis, who believed in me since our teenage years.

This page intentionally left blank

Contents

This page intentionally left blank

List of Tables

List of Figures

Abbreviations

Term	Explanation
SFR	Star-formation rate
sSFR	Specific star-formation rate
AGN	Active galactic nuclei
UV	Ultra-violet
IR	Infrared
FIR	Far infrared
TIR	Total infrared
XRB	X-ray binary
ULX	Ultraluminous X-ray source
LMXB	Low-mass X-ray binary
HMXB	High-mass X-ray binary
LF	Luminosity function
XLF	X-ray luminosity function
BH	Black hole
NS	Neutron star
RiG	Ring galaxy

This page intentionally left blank

1

Introduction

Star formation is an inevitable outcome of the physical laws of the Universe. Under the effect of self-gravity, gas collapses and forms new stars. This process, that has been going on since the very early stages of the Universe (first galaxies appear at redshift z $\simeq$ 30; e.g. Barkana & Loeb 2001), has transformed the Cosmos from a soup of hydrogen (and helium) to the diversity of elements, structures, and phenomena we observe today. Star-formation is also the basis of galaxy formation and evolution, therefore, a fundamental characteristic of galaxies. The level of the star-formation taking place in a galaxy, or a large stellar population (SP), is measured by the *star-formation rate (SFR)*. The SFR measures the amount of newly born stars in a fraction of time, usually measured in solar-masses per year ($M_\odot\,yr^{-1}$ or $\dot{M}_\star$).

Given the importance of star formation in the evolution of galaxies (by building their stellar content and driving their chemical evolution) the measurement of star-formation at our local Universe (e.g. Kennicutt & Evans 2012), as well as over its cosmological history (e.g. Madau & Dickinson 2014) has been a fundamental aspect of extragalactic Astrophysics.

Collectively, the effect of the star formation that took place in the past of a galaxy, has built its present-day stellar mass ($M_\star$). Many studies have shown that there is a tight correlation between the SFR and stellar mass of a galaxy: the so-called *main*

sequence of galaxies (Figure 1.1; e.g. Noeske *et al.* 2007; Elbaz *et al.* 2007; Draine & Li 2007). This correlation indicates that the more massive a galaxy is, the more stars it has the ability to generate.

The ratio of SFR over the stellar mass of a galaxy defines its specific SFR (sSFR). It can be interpreted as the timescale required to build its present-day stellar mass assuming the current SFR. In practice, it is a measure of the intensity of star-forming activity. Galaxies with high sSFR ($\gtrsim 10^{-9}$ $M_\odot\,yr^{-1}/M_\odot$) are considered as being dominated by their star-forming activity. In addition, the mechanical energy released by stellar winds (e.g. Puls *et al.* 1996; Toalá & Arthur 2011) and supernova explosions (e.g. Mac Low *et al.* 2005; Kiewe *et al.* 2012; Walch & Naab 2015) together with active galactic nuclei (AGN; e.g. Magorrian *et al.* 1998; Ferrarese & Merritt 2000; Gebhardt *et al.* 2000; Kormendy & Ho 2013), plays a very important role in regulating star-formation, and galaxy evolution. This feedback process is inextricably linked with the star-forming activity and its evolution.

Similarly, a galaxy's SFR is connected with phenomena related with the life and death of these massive stars, like the X-ray emission from high-mass X-ray binaries (HMXBs; e.g. Mineo *et al.* 2014), or ultra-luminous X-ray sources (ULXs; e.g. Kovlakas *et al.* 2020). HMXBs, are binary systems composed from a massive star of spectral type O and B, and a stellar remnant (usually a black hole, or a neutron star). ULXs are very luminous X-ray sources with luminosities in excess of 10^{39}erg s^{-1}, exceeding the Eddington limit of typical stellar black holes.

The epoch of multi-messenger astrophysics has recently began, and the ground breaking observations of gravitational waves (GWs) from merging compact objects have changed our view of the Universe. The efforts on efficiently identifying the origin of the sources, and their electromagnetic (EM) counterparts, is of high importance in order to understand their nature. The SFR and star-formation history (SFH) of a galaxy is strongly correlated with the production of these stellar remnants, because only the most massive stars result in black holes or neutron stars when they end their lives. Therefore, being able to accurately measure a galaxy's SFR is quite important in order to be able to accurately pinpoint the hosts of these sources (e.g. Artale *et al.* 2019, Kovlakas et al 2021, submitted), but also in order to understand how they are formed.

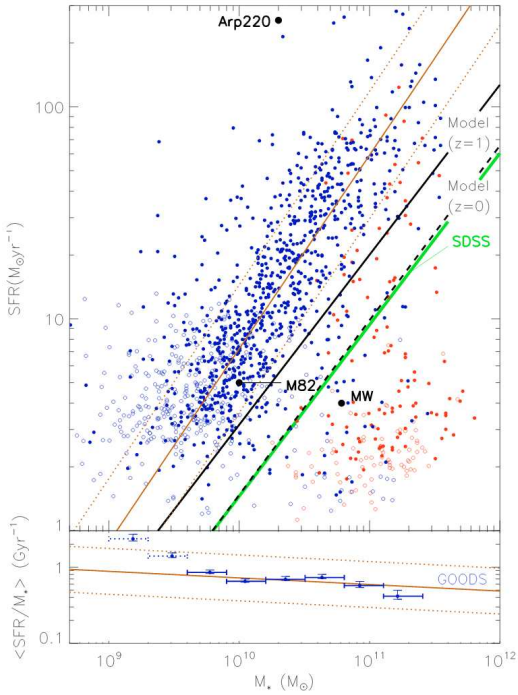

Figure 1.1: SFR (top plot) and sSFR (bottom plot) as a function of stellar mass for galaxies of the GOODS sample (Dickinson *et al.* 2003). Blue and red colours represent galaxies separated by their (U-B) colours. Adopted from Elbaz *et al.* (2007)

1.1 Measuring star-formation rates

Given the importance of star-formation in the evolution of galaxies, several direct or indirect methods have been developed in order to measure it. The SFR is typically calculated by measuring, either directly or indirectly, the populations of massive stars residing in a stellar population. These stars are relatively very short-lived, with O stars having lifespans $t_{\rm end} \lesssim 8$ Myr (e.g. Weidner & Vink 2010). Assuming an initial mass function (IMF; e.g. Salpeter 1955; Miller & Scalo 1979; Kroupa 2001; Chabrier 2003) this measurement can give an estimation for all the recently born stars of any mass. Thus, to have a robust SFR measurement the stellar population under study must have large enough size in order to be a good representation of the IMF (Kennicutt & Evans 2012, and references therein).

While the most direct way of measuring the populations of massive stars is counting stars using resolved stellar populations, this is only possible in our nearest galaxies. In order to overcome this limitation indirect methods based on the integrated emission in different wavelengths have been developed. These methods, covering the full range of the EM spectrum from the X-rays to radio, probe photospheric emission from the stars

(e.g. UV, optical), reprocessed emission by gas (e.g. atomic emission lines) or dust (e.g. mid and far-IR; e.g. Moustakas & Kennicutt 2006; Calzetti *et al.* 2007; Kennicutt *et al.* 2008, 2009; Rieke *et al.* 2009; Hao *et al.* 2011; Boquien *et al.* 2010; Calzetti *et al.* 2010; Murphy *et al.* 2011; Davies *et al.* 2017; Mahajan *et al.* 2019). These studies, among many others, have placed the foundations for measuring SFR.

However, it has been shown that measuring SFRs is a task subject to systematic effects depending on the available data and the SFR indicator used. For example, because older stellar populations can also contribute in some of the bands that are used to trace these massive stars (e.g. UV from post-AGB stars; van Winckel 2003), the SFRs can be significantly biased in stellar populations with a strong older component, i.e. specific SFR (SFR in a unit of stellar mass; sSFR) sSFR $\lesssim 10^{-12}$ ($\mathrm{M_\odot\,yr^{-1}/M_\odot}$) (Section 3.5.1, Figure 3.10).

1.1.1 Star-formation rates based on Hα emission

The atomic hydrogen gas residing in the ISM can be ionized by the UV emission produced by massive stars. The electrons from the ionized hydrogen gas (H II) that recombine with the nuclei, cascade the hydrogen-atom energy levels while emitting radiation. They produce the well known *Lyman* ($n' = 1$), *Balmer* ($n' = 2$), *Paschen* ($n' = 3$), *Bracket* ($n' = 4$), e.t.c. spectral lines. When a hydrogen atom recombines, the electron may initially reside to any energy level. Out of the Balmer transitions about half the time the electrons will cascade from the $n' = 3$ to $n' = 2$ levels, making Hα the most prominent atomic hydrogen emission line of the non-Lyman lines. At the same tine hydrogen is by far the most abundant element in the Universe, and in the ISM of galaxies. This makes Hα($\lambda = 6563$ Å) the strongest hydrogen emission line in the optical range, a fact that made it one of the most widely used SFR tracers.

Because the production of the Hα emission line requires the presence of photons above the ionization energy of hydrogen (13.6 eV), it probes stellar populations that are young enough to have massive stars (spectral type O) capable to produce significant amounts of far-UV radiation. As a result, Hα is the SFR indicator capable of tracing the youngest stellar populations with ages $\lesssim 15$ Myr (e.g. Figure 1.2; e.g. Kennicutt & Evans 2012; Boquien *et al.* 2014; Cerviño *et al.* 2016; Haydon *et al.* 2020). Being able to probe these young stellar populations is important for measuring the so-called *instantaneous* (i.e. current) SFR, and also for studying processes related with these very short-lived stars, like the X-ray emission related with HMXBs (e.g. Kouroumpatzakis *et al.* 2020).

A common way to measure the SFR of local Universe galaxies based on their Hα

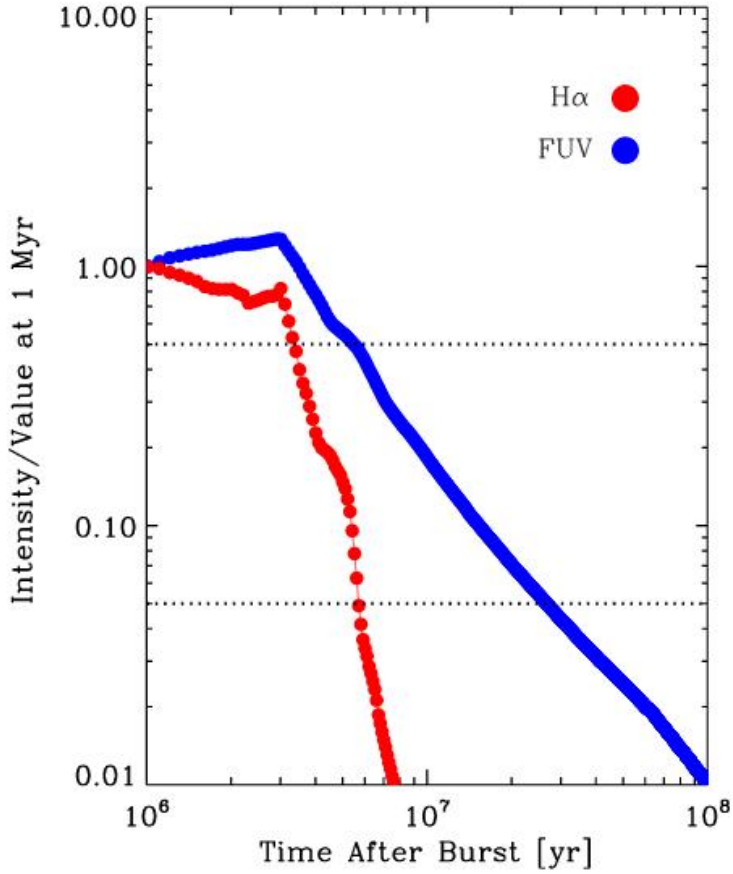

Figure 1.2: Characteristic timescales traced by Hα and FUV emission as a function of time after the star-formation burst. Adopted from Leroy *et al.* (2012)

emission is imaging observations using narrow-band filters centered on the Hα line (e.g. Moustakas & Kennicutt 2006), or spectroscopic observations (e.g. Kennicutt 1998; Kewley *et al.* 2002). While spectroscopic observations allow us to correct for the effect of extinction and also obtain additional information on the ISM (e.g. metallicity), the imaging observations allow us to map the star-forming activity across the galaxy. Another complication is the contamination of the narrow-band imaging data by the [N II]$\lambda\lambda = 6548, 6583$ Å emission lines, which are adjacent to the Hα line. This contribution varies within the galaxy, depending on the local ISM and stellar population conditions (e.g. Figure 1.3; e.g. James *et al.* 2005).

Murphy *et al.* (2011) used the stellar population-synthesis code (`Starburst99`; Leitherer *et al.* 1999) to model the relation between SFR and the production rate of ionizing photons, $Q(H^0)$, at a timescale of ~ 100 Myr assuming solar metallicity and continuous star formation.

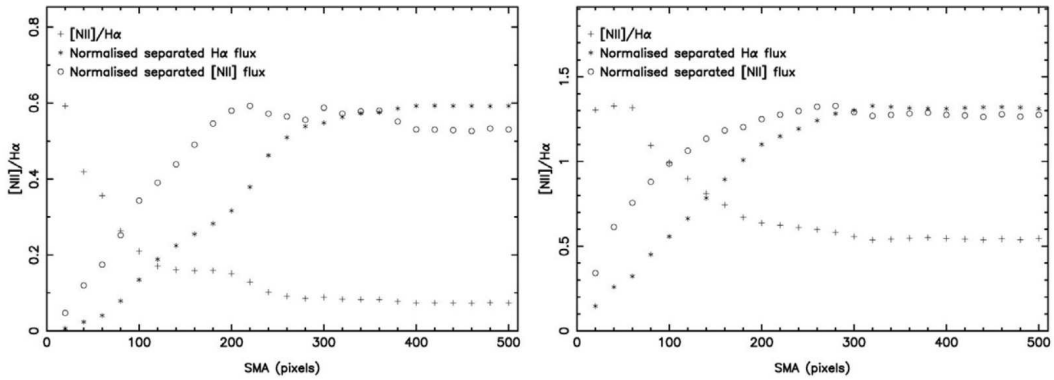

Figure 1.3: The curves of growth of the [N II]/Hα ratio, the normalized [N II], and Hα emission, for galaxies UGC 8403 (left) and UGC 11872 (right) as a function of their galactocentric radius. Adopted from James *et al.* (2005)

$$\frac{\mathrm{SFR}}{\mathrm{M}_\odot\ \mathrm{yr}^{-1}} = 7.29 \times 10^{-54} \left[\frac{\mathrm{Q(H^0)}}{\mathrm{s}^{-1}}\right] \tag{1.1}$$

The ionizing photons can be converted to extinction-corrected hydrogen recombination line flux for Case B recombination. Assuming a typical H II-region electron temperature ($T_\mathrm{e} = 10^4$ K), the Hα recombination line emission can be converted to SFR by:

$$\frac{\mathrm{SFR}_{\mathrm{H}\alpha}}{(\mathrm{M}_\odot\ \mathrm{yr}^{-1})} = 5.37 \times 10^{-42} \frac{L_{\mathrm{H}\alpha}}{(\mathrm{erg\,s}^{-1})} \tag{1.2}$$

However, the Hα emission suffers from systematic biases with most important the attenuation caused by the dust along the line of sight (e.g. Kewley *et al.* 2002; Buat *et al.* 2002). Also, because many young stars that ionize the H II regions still reside in their nursery/birth clouds, Balmer-line emission is subject to attenuation from those clouds, additional to the dust of the ISM (e.g. Calzetti *et al.* 1994; Charlot & Fall 2000; Qin *et al.* 2019). This results to extinction in the Hα emission that if not accounted can lead to systematic underestimation of the SFR. In order to overcome this limitation, there have been developed different methods that try to measure and correct the effect of extinction (e.g. Buat 1992; Buat *et al.* 2002; Bell & Kennicutt 2001, see Section 2.5.1).

1.1.2 Star-formation rates based on ultra-violet emission

The bulk of the UV emission in galaxies is dominated by the photospheric emission of massive O and B stars (e.g. Kennicutt 1998; Coe 2005; Schawinski *et al.* 2007). Therefore, observations in the UV part of the spectrum are a good tracer of these stars, and consequently the SFR.

Murphy *et al.* (2011), using the `Starburts99` code in a similar manner to the calibration of Hα emission with SFR (Equation 1.2), derived the following relation between the FUV band luminosity and SFR:

$$\frac{\mathrm{SFR_{FUV}}}{(\mathrm{M_\odot\,yr^{-1}})} = 4.42 \times 10^{-44} \frac{L_{\mathrm{FUV}}}{(\mathrm{erg\,s^{-1}})} \tag{1.3}$$

However, the UV emission is subject to strong extinction by the dust in the ISM. Figure 1.4 shows a typical extinction law demonstrating the sensitivity of the UV emission on extinction. Thus, the lack of extinction correction can lead to systematic underestimation of the SFR (e.g. Mahajan *et al.* 2019). A difference that is increasing for galaxies with higher SFR and extinction (e.g. Buat *et al.* 2002).

The *Galaxy Evolution Explorer* (*GALEX*; Martin *et al.* 2005) was a breakthrough in the UV imaging of galaxies covering about 1000 deg^2 of the sky with limiting $m_{AB} \simeq 23$, and 100 deg^2 with deeper imaging with limiting $m_{AB} \simeq 25$. GALEX observed the sky in two bands: the far-UV (FUV), and near-UV (NUV) at 1350–1750, and 1750–2750 Å respectively.

It is also noted that the UV bands trace longer timescales in comparison to the Hα. Hα traces the most massive stars producing significant luminosity above the Lyman limit, while the longer-wavelength UV emission has significant contribution from lower-mass, and hence, longer-lived stars (such as B-type stars). The reference timescale for UV emission is in the range 17.1–33.3 Myr, which also nearly monotonically increases with wavelength (Haydon *et al.* 2020). For example, the characteristic timescale for the GALEX FUV is $17.1^{+0.4}_{-0.2}$ Myr, and $19.6^{+0.2}_{-0.2}$ Myr for the NUV. Despite these limitations, UV emission remains a good proxy of recent star-forming activity.

1.1.3 Star-formation rates based on infrared emission

The UV emission emitted by massive stars can be partially or completely absorbed by dust in the ISM. Then the heated dust thermally emits radiation in the IR. Thus, the IR emission probes the dust heated by the UV emission of massive stars, and in that

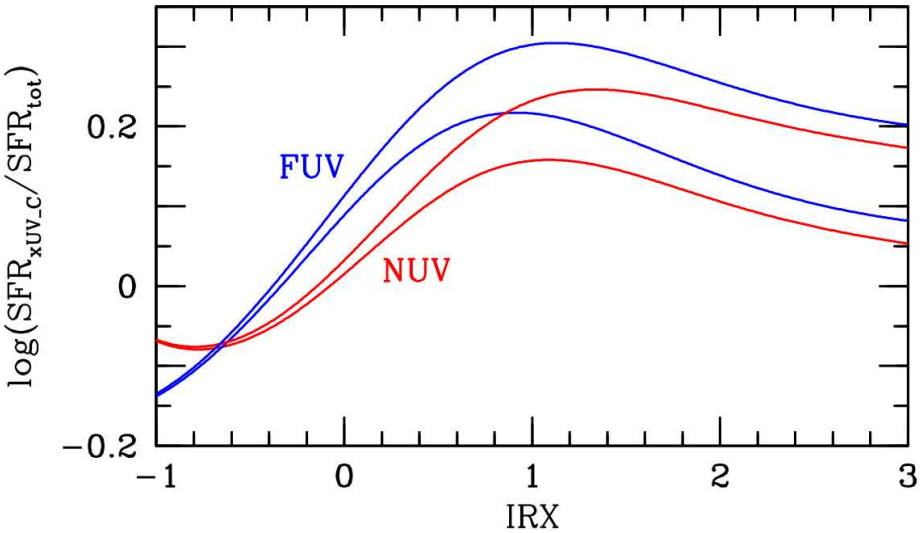

Figure 1.4: Ratio of FUV (blue) and NUV (red) SFR to SFR derived as a combination of FIR + FUV as a function of the extinction derived through the IRX. The higher and lower lines represent the 16th and 84th percentiles of $F(60)/F(100)$ of sample galaxies. Adopted from Mahajan *et al.* (2019)

sense, traces the SFR. Various IR bands have been used as SFR indicators, including the far-IR (FIR; 60 μm, 100 μm and their combinations; e.g. Helou *et al.* 1988) total-IR (TIR; 8–1000 μm; e.g. Gordon *et al.* 2000), or the 24 μm emission (e.g. Papovich & Bell 2002).

An additional commonly used indicator in the IR band is the emission from polycyclic aromatic hydrocarbons (PAHs). These are large organic molecules that are found in the photo-dissociation regions. Stellar UV radiation excites these molecules producing radiation in characteristic bands ($\sim$ 6, 8, and 12 μm). The best studied and most commonly used band is the 8 μm, which coincides with Band-3 of the IRAC instrument on the *Spitzer* Space Infrared Observatory (Zhu *et al.* 2008).

The basic assumption behind the use of IR emission as a SFR indicator is energy balance: the stellar UV emission is fully absorbed by the interstellar dust and it is re-emitted in the IR bands. Then, through calibrations making different assumptions for the IR spectral-energy distribution (SED), we can infer the re-radiated emission by the dust based on the monochromatic, or multi-band IR luminosity (e.g. Soifer *et al.* 1989). Various calibrations have been proposed for calibrations of the various IR bands used as SFR indicators (e.g. Wu *et al.* 2005; Alonso-Herrero *et al.* 2006; Calzetti *et al.*

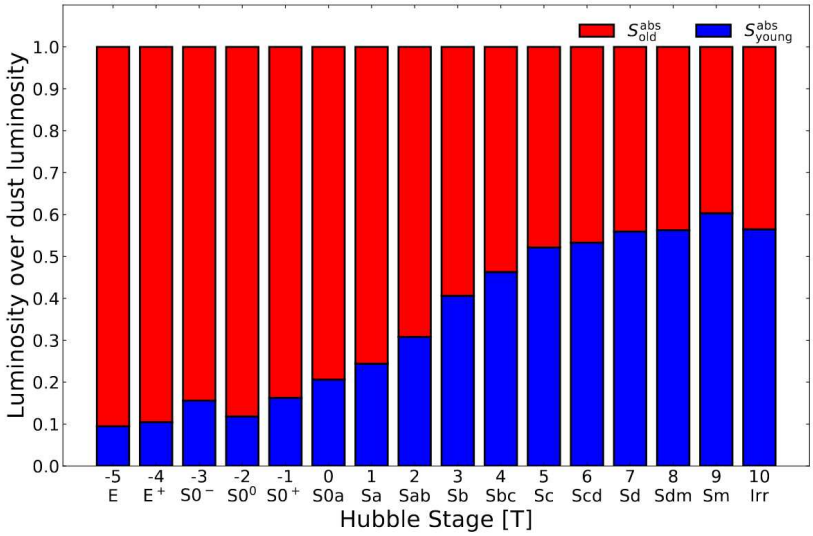

Figure 1.5: Mean values of the ratios of the luminosity absorbed by dust, for a specific stellar component to the dust luminosity. Red and blue bars refer to the old and the young stellar components respectively. Adopted from Nersesian *et al.* (2019)

2007; Relaño *et al.* 2007; Zhu *et al.* 2008; Rieke *et al.* 2009).

Obviously, the IR-based SFR indicators overcome the extinction problem that complicate the use of UV and Hα emission. However, it has been shown that a non-negligible fraction of the IR continuum can be heated by older stellar populations (e.g. Sauvage & Thuan 1992; Walterbos & Greenawalt 1996; Bendo *et al.* 2010), although warmer dust emission is more closely related to the current SFR (e.g. Helou *et al.* 2004). The ratio of the relative contribution of older stars varies, depending on the SFH, which in turn correlates with the morphological type of the galaxies, while the morphological type of a galaxy is correlated with its SFH. For example, in the extreme case of early-type galaxies (ETGs), the dust heating is mainly attributed to old stars since there are no young stellar populations (e.g. Figure 1.5; e.g. Nersesian *et al.* 2019).

Another complication arises from the fact that the production of dust requires the presence of metals. Therefore, metal-poor galaxies may be dust-deficient. In fact, it has been shown that dwarf star-forming galaxies with low-metallicity show a deficit in their IR emission (e.g. Madden *et al.* 2006; Hunt *et al.* 2010; Santos-Santos *et al.* 2017). Similarly, the IR emission will underestimate the SFR in galaxies with "porous" ISM where a fraction of the stellar UV emission can escape without being absorbed by the dust. Despite of these limitations, the IR emission is considered as one of the most accessible and reliable SFR indicators, particularly in late-type galaxies with high sSFR.

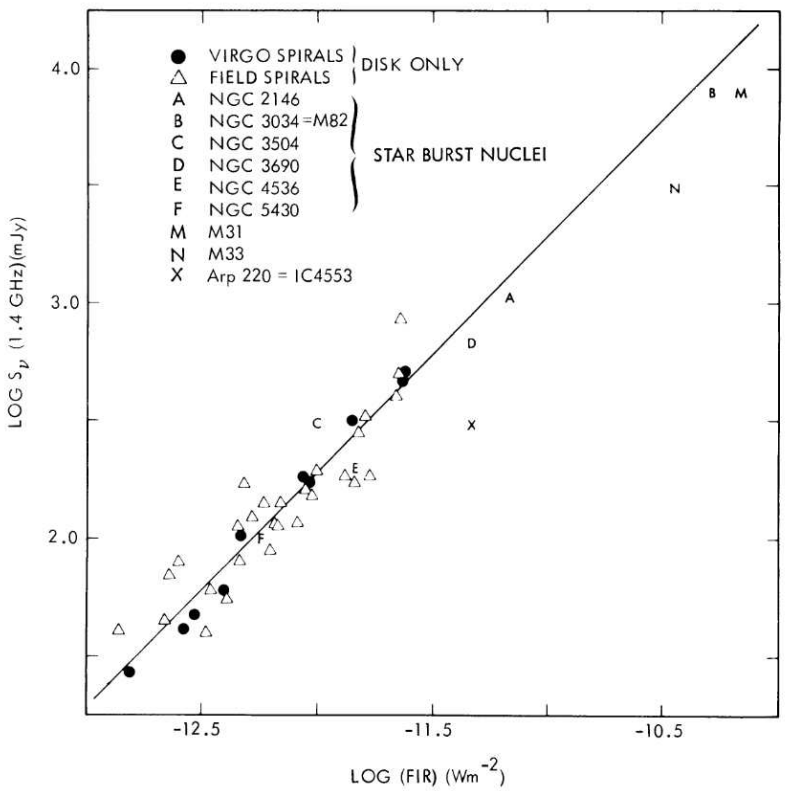

Figure 1.6: Comparison of the observed FIR and 1.4 GHz emission for non-AGN galaxies. Adopted from Helou *et al.* (1985)

1.1.4 Star-formation rates based on radio emission

The radio emission is also a widely used SFR indicator. The non-thermal synchrotron emission is produced from relativistic electrons and cosmic rays that are results of Fermi acceleration of particles at the shock front of supernova remnants. Studies of the optically thin synchrotron emission at 1.4 GHz and FIR radiation have shown a surprisingly tight empirical correlation (e.g. Figure 1.6; e.g. de Jong *et al.* 1985; Helou *et al.* 1985).

The synchrotron cooling lifetime for cosmic-ray electrons is $\sim$ 50 Myr depending on the intensity of the magnetic field. However, their inverse-Compton lifetime (through scattering of the stellar radiation) is much shorter ($\sim$ 10 Kyr) for the intense radiation fields in starburst galaxies (e.g. Condon *et al.* 1991; Lang *et al.* 2010; Lacki *et al.* 2010). Thus, the radio emission, although it can be sensitive to the intensity of the stellar radiation fields (through the inverse-Compton losses), it probes processes related to star-formation in very short timescales.

Since the calibration of the 1.4 GHz emission as a SFR indicator is very complex

and it relies on several assumptions about the galactic magnetic field, the structure of the ISM, and the poorly known escape losses (e.g. Lacki *et al.* 2010), it is usually calibrated empirically by comparisons with other SFR indicators (most commonly the FIR luminosity). A recent calibration is that of Davies *et al.* (2017):

$$\frac{\mathrm{SFR}_{1.4\ \mathrm{GHz}}}{(\mathrm{M}_\odot\ \mathrm{yr}^{-1})} = 5.25 \left(\frac{L_{1.4\ \mathrm{GHz}}}{10^{22}\ \mathrm{W\ Hz}^{-1}} \right)^{\gamma} \tag{1.4}$$

The non-linear power calibrates the reduced radio luminosity in lower SFR galaxies, a fact attributed to either cosmic ray escape losses at low SFRs (e.g. Chi & Wolfendale 1990; Bell 2003; Lacki *et al.* 2010), and/or stronger magnetic fields for starburst galaxies (e.g. Tabatabaei *et al.* 2017). Because the radio emission has the benefit that is not affected by extinction, it is an excellent probe of the total recent star-forming activity even in heavily obscured systems.

1.1.5 Hybrid star-formation rate indicators

As mentioned in the previous sections, massive stars can be traced through their UV emission, or the result of their ionizing radiation on their surrounding medium (e.g. traced by the Hα emission). These indicators probe the emission after it has been attenuated by the intervening ISM. Therefore, to infer the true star-forming activity one has to correct for this effect. On the other hand, the IR emission traces the energy that is absorbed by the dust located in and around the star-forming regions, by the dust that is been heated by the absorbed UV. Under energy balance, the energy of the absorbed UV radiation equals the energy re-emitted in the IR.

In order to account for the emerging UV or Hα emission, as well as the absorbed UV emission, various *hybrid* SFR indicators based on the aforementioned energy balance have been proposed. These indicators include combinations of IR + UV (e.g. Hirashita *et al.* 2003), 24μm + Hα (e.g. Calzetti *et al.* 2007; Kennicutt *et al.* 2009), and 8μm + Hα (e.g. Kennicutt *et al.* 2009) emission. The fact that these indicators account for absorbed and un-absorbed emission overcomes the limitation of IR SFR indicators in dust-poor galaxies (e.g. dwarf galaxies). These hybrid SFR indicators show excellent agreement with attenuation corrected SFRs (e.g. inferred from the Balmer decrement extinction indicator; e.g. Figure 1.7).

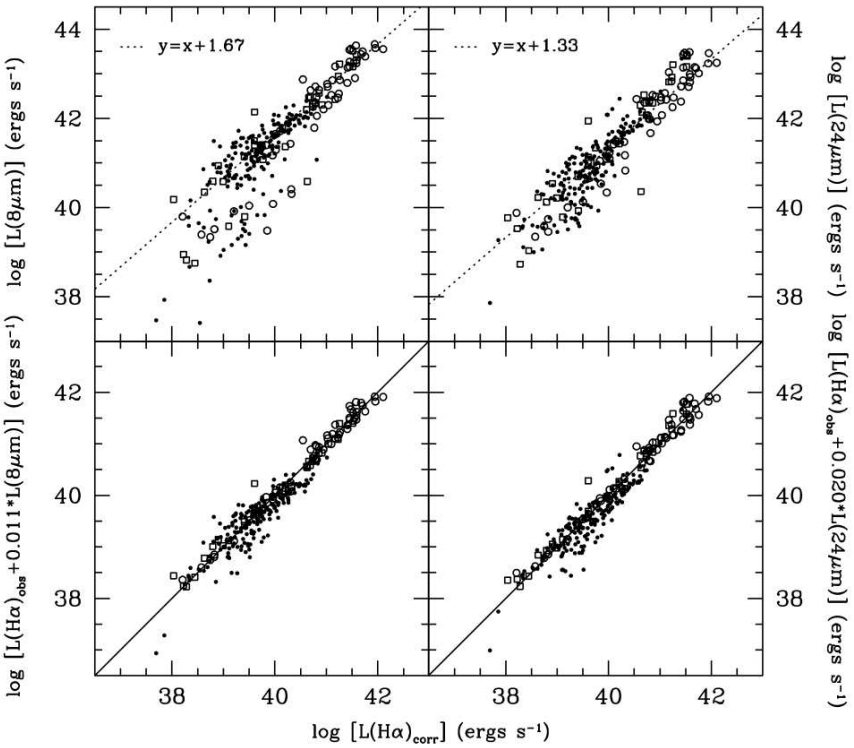

Figure 1.7: Top: 8 μm (left) and 24 μm luminosities (right) of SINGS galaxies and sub-regions, as a function of extinction-corrected Hα luminosities. Open circles denote integrated measurements of SINGS galaxies, open squares denote measurements of the central $20'' \times 20''$ regions, while small solid points denote individual H II regions from Calzetti *et al.* (2007). Bottom: best-fit combinations of uncorrected Hα and 8 μm (left) or 24 μm (right) luminosities, as a function of extinction-corrected Hα luminosities. Adopted from Kennicutt *et al.* (2009)

1.1.6 Star-formation rates based on X-ray emission

The X-ray emission of galaxies originates from hot optically thin thermal plasma (heated by the effect of supernovae and stellar winds), and X-ray binaries (XRBs). XRBs are binary systems composed from a compact object and high-mass (O, B spectral type) donor star (HMXBs), or a low-mass (< 1 M$_\odot$) donor star (Low-mass X-ray binaries; LMXBs). The material escapes from the donor star through Roche lobe overflow or strong stellar winds. A fraction of this material is captured by the compact objects often forming an accretion disk, which is responsible for the X-ray emission in these systems. The radiation consists of thermal emission from the accretion disk, and harder X-ray photons produced by inverse Compton scattering of the thermal photons (e.g. Remillard & McClintock 2006).

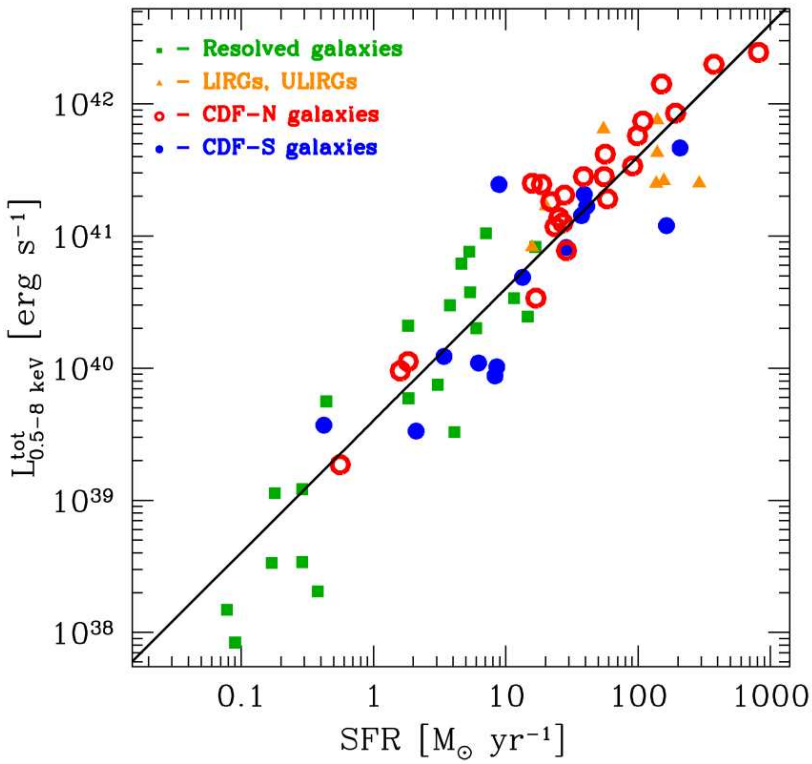

Figure 1.8: X-ray luminosity (0.5–8 keV) as a function of SFR. The solid line represents the scaling relation. Adopted from Mineo *et al.* (2014)

The X-ray emission has been recently proposed as an alternative SFR indicator. It has been shown that there is strong linear correlation between the X-ray, and Hα, FIR, or radio emission of star-forming galaxies (e.g. Grimm *et al.* 2003; Ranalli *et al.* 2003). Studies following this work have shown that the X-ray emission from HMXBs shows strong correlation with the SFR (e.g. Figure 1.8; e.g. Mineo *et al.* 2012a,b, 2014; Lehmer *et al.* 2019). Likewise, the X-ray emission from low-mass XRBs (LMXBs) correlates with galaxies' stellar mass (e.g., Gilfanov 2004; Lehmer *et al.* 2010; Boroson *et al.* 2011; Zhang *et al.* 2012).

However, more detailed studies have shown that the XRB populations in a galaxy (and its integrated X-ray emission) do depend on the age of its stellar populations (e.g. Lehmer *et al.* 2017; Antoniou *et al.* 2019b), and their metallicity, with lower metallicities resulting in higher X-ray luminosity (e.g. Mapelli *et al.* 2009, 2010; Fragos *et al.* 2016; Brorby *et al.* 2016; Madau & Fragos 2017; Fornasini *et al.* 2020). These results are in agreement with X-ray binary population synthesis models that predict that X-ray emission in stellar populations up to ~ 100 Myr originates in HMXBs, while older stellar

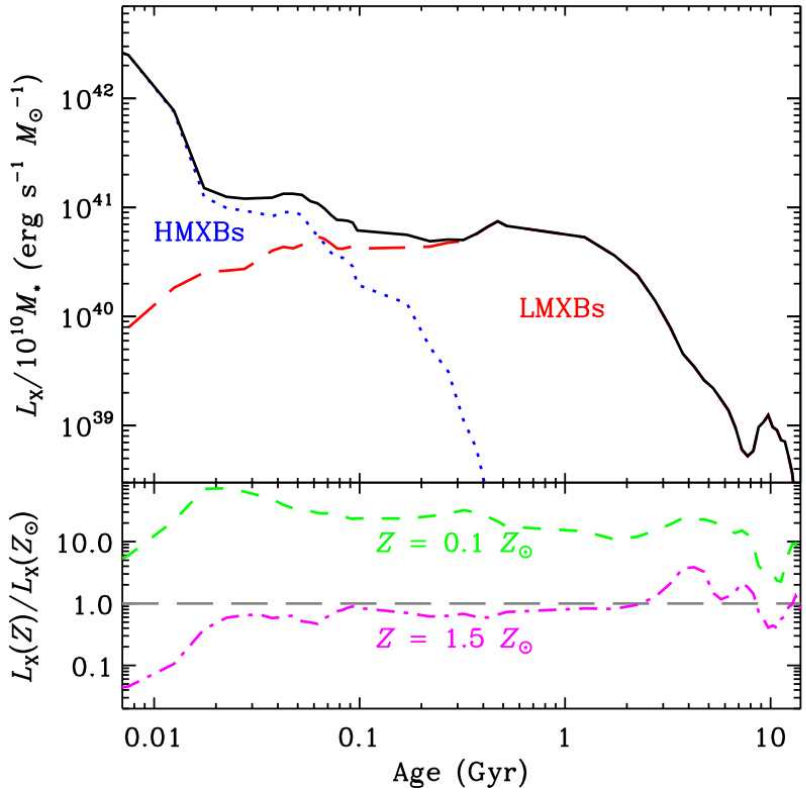

Figure 1.9: Top panel: Evolution of an XRB population formed in a single star-burst. The solid black line represents the total X-ray emission as a function of time. The dashed red, and blue dotted line represent the separate contribution of HMXBs, and LMXBs. Bottom panel: XRB evolution in respect with metallicity. Adopted from Fragos *et al.* (2013a)

populations are dominated by a declining population of LMXBs (e.g. Figure 1.9; e.g Fragos *et al.* 2013a).

Observations of the X-ray emission of galaxies at cosmological distances ($z \sim 1$–2) showed that these systems have higher X-ray luminosities per SFR than local-Universe galaxies (e.g. Lehmer *et al.* 2016). This effect is attributed to the lower metallicity of high-z galaxies (e.g. Fornasini *et al.* 2019, 2020).

This dependence has important implications for the role of HMXBs in the very early-universe where they may have been an important contributor to the heating of the intergalactic medium just before the era of reionization (e.g. Madau & Fragos 2017).

1.1.7 Comparison of SFR indicators: state of the art

Through the studies of the past $\sim$ 30 plus years, we have obtained a good framework for measuring star-forming activity. As discussed in the previous sub-sections, the

Band	Age range (Myr)	References
FUV	0–10–100	1, 2
NUV	0–10–200	1, 2
Hα	0–3–10	1, 2
TIR	0–5–100	1, 2
24 μm	0–5–100	3
70 μm	0–5–100	4
1.4 GHz	0–100	1
2–10 keV	0–100	5

Table 1.1: The timescales of the stellar populations probed by the different SFR indicators. References: (1) Murphy *et al.* (2011); (2) Hao *et al.* (2011); (3) Rieke *et al.* (2009); (4) Calzetti *et al.* (2010); (5) Ranalli *et al.* (2003). Adopted from Kennicutt & Evans (2012).

different indicators can be used to give us information on the star-formation rate in different timescales (e.g. Table 1.1). However, each indicator has limitations. Therefore, quantifying and addressing the impact of this limitations is an important subject for measuring accurately the star-forming activity and understanding the evolution of galaxies.

The IR SFR indicators are good for obscured and high SFR galaxies, but (depending on the wave-band) they can biased by emission from older stellar populations. On the other hand, UV emission is a good SFR tracer for transparent (dust deficient) dwarf galaxies (where the IR indicators fail) but for the rest of star-forming galaxies they face the problem of strong attenuation. Hα emission is the best indicator for probing the young stellar populations, but like the UV, needs to be corrected for extinction. Radio has the benefit of tracing young stellar populations, while not being affected by extinction, but it has been shown that its correlation with SFR varies depending on the local galactic conditions (e.g. magnetic and radiation field, escape losses).

Driven by the limitations of the individual SFR indicators, hybrid indicators combining UV-sensitive and IR emission tracers have been developed. In addition, analysis of broad-band spectral energy distributions (SEDs; e.g. Walcher *et al.* 2011; Boquien *et al.* 2019) of galaxies is an emerging method for measuring SFR. This method has the benefit of combining data from multiple bands, and in addition to SFR, it provides information on the stellar populations (e.g. star-formation history, stellar mass) and the properties of the ISM (e.g. extinction, dust temperature, mass).

1.2 The Star Formation Reference Survey

The Star Formation Reference Survey (SFRS; Ashby *et al.* 2011) is a project aiming to understand the behaviour of different SFR indicators in the different types of galaxies in which star-forming activity takes place in the Local Universe. The SFRS sample is the basis for the work presented in this thesis. It was selected from the PSCz catalog (Saunders *et al.* 2000) in order to fully represent the variety of conditions star formation takes place in galaxies of the local Universe. In this respect it is selected to cover the 3D space of three fundamental characteristics of galaxies: the SFR indicated by the $L_{60\,\mu\mathrm{m}}$, the $K_S - F_{60\,\mu\mathrm{m}}$ colour as a proxy of the sSFR, and the dust temperature as traced by the $F_{100\,\mu\mathrm{m}}/F_{60\,\mu\mathrm{m}}$ flux ratio (Figure 1.10). In detail, from each bin in this 3D space, 10 randomly selected objects were chosen (unless the bin contained less than 10 objects in which case all objects were selected). From this sample AGN were not excluded in order not to bias the final sample.

The SFRS sample comprises 369 local Universe galaxies with redshift up to $z = 0.30641$ (D $<$ 1259 Mpc). It has the advantage of a wide electromagnetic spectrum coverage from radio to X-rays (Table 1.2; Mahajan *et al.* 2019; Kouroumpatzakis *et al.* 2020). It also includes optical spectra of the galaxies' nuclei for the full sample, and for the host galaxies for almost half of the sample (Maragkoudakis *et al.* 2018). These optical spectra provide a classification of the nuclear activity in the SFRS galaxies through BPT diagrams (Baldwin *et al.* 1981; Veilleux & Osterbrock 1987; Kewley *et al.* 2001; Kauffmann *et al.* 2003; Schawinski *et al.* 2007) and measurements of the gas phase metallicity. Likewise, the panchromatic coverage and the optical spectra of the SFRS provide extinction estimations based on different methods through the Balmer lines ratio and the infrared excess.

The SFRS sample has been used to:

1. Investigate aperture effects in nuclear activity diagnostics of Seyfert, LINER, Composite, and star-forming galaxies (Maragkoudakis *et al.* 2014)
2. Perform one the first studies of the galaxy main sequence (SFR–stellar mass correlation) in sub-galactic scales (Maragkoudakis *et al.* 2017)
3. Study the AGN demographics in local Universe star-forming galaxies (Maragkoudakis *et al.* 2018).
4. Compare different SFR indicators and extinction determinations (Mahajan *et al.* 2019)
5. Derive scaling relations between X-ray luminosity, SFR, and stellar mass in sub-galactic scales, and explore the effect of different stellar populations in these relations (Chapter 3; Kouroumpatzakis *et al.* 2020)

Table 1.2: Summary of the multi-wavelength photometric and spectroscopic sample coverage of the SFRS sample.

Bandpass	Observatory	Coverage
1.4 GHz	VLA/NVSS	100%
12, 25, 60, 100 μm	IRAS	100%
65, 90, 140, 160 μm	AKARI	95%
3.4, 4.7, 12.1 and 22.2 μm	WISE	100%
24 μm	Spitzer/MIPS	100%
3.6, 4.5, 5.8, 8.0 μm	Spitzer/IRAC	100%
$J,\ H,\ K_S$	2MASS	100%
$J,\ H,\ K$	PAIRITEL/Skinakas	100%
PS1.y	Pan-STARRS	100%
$u,\ g,\ ,r\ ,i\ ,z$	SDSS	100%
Optical spectra	SDSS	57% (210/369)
Optical spectra	FAST (long slit)	43% (159/369)
Hα imaging	Skinakas/FLWO	83% (305/369)
0.13–0.28 μm	GALEX	90%
0.5–8.0 keV (X-rays)	Chandra/XMM	100%

6. Measure the stellar mass and stellar mass density functions of the bulge and disk sub-components in local Universe galaxies (Bonfini et al. submitted)

These works have provided a picture of the cross-calibration of different SFR indicators in a representative sample of galaxies, as well as a picture of the nuclear activity and stellar mass functions of different structural sub-components in local galaxies.

In the following section we present a systematic Hα imaging campaign for the SFRS galaxies. The addition of the Hα emission in our repository of SFR indicators allows to perform a complete study of the correlations and biases of SFR indicators probing different stellar populations and emission processes. The benefits of Hα emission in estimating the most recent SFR, in combination with the wide E/M coverage of the SFRS, are exploited in order to investigate the widely used correlations (e.g. The main sequence of galaxies, the X-ray luminosity–SFR) of galactic properties. Overall the SFRS is an excellent base to examine star-formation and related properties of galaxies as it is a sample representing the great variety of conditions from e.g. dwarf dust-deficient galaxies up to massive dusty highly star-forming galaxies.

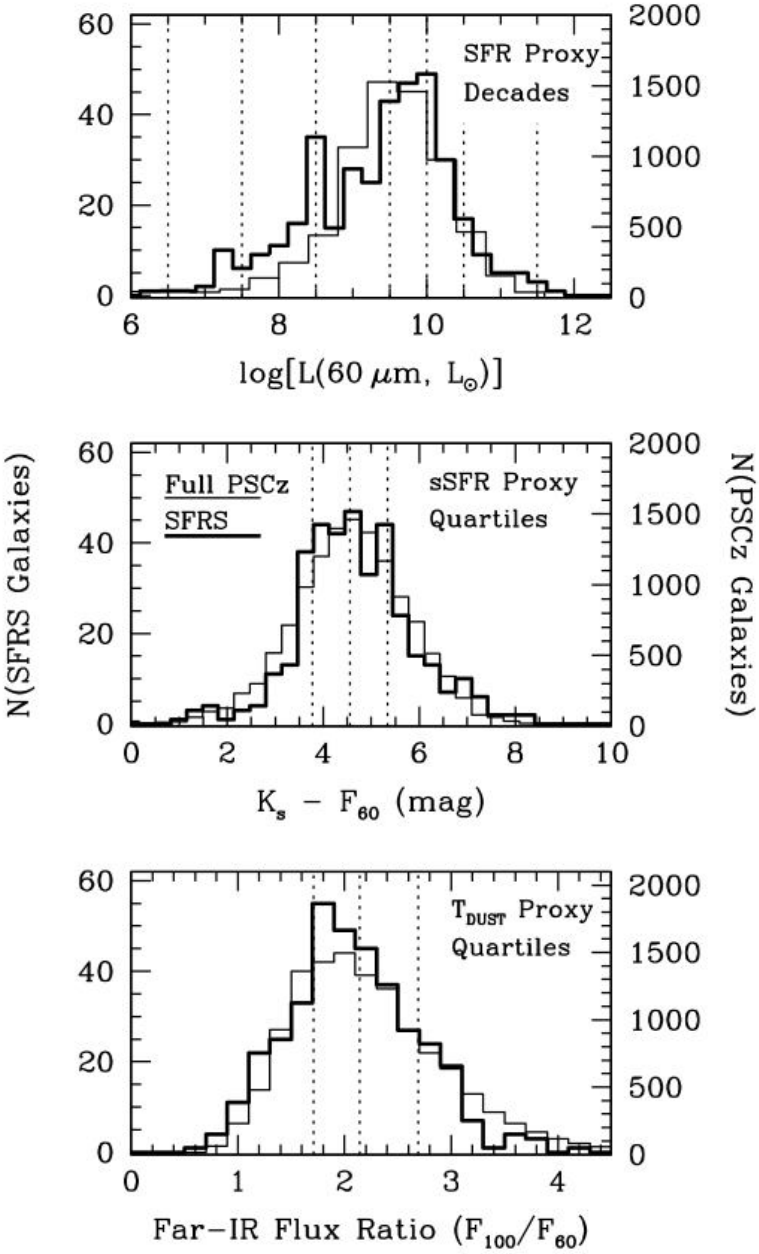

Figure 1.10: Distributions of the SFRS galaxies in the parameters used to select the sample. Thick lines represent the SFRS galaxies (left-hand axes), and thin lines represent the PSCz sample (right-hand axes). Vertical dotted lines in each panel represent the bin boundaries. Adopted from Ashby *et al.* (2011)

1.3 Motivation for this study

In order to understand the systematic effects and the limitations of Hα emission as a SFR indicator we embarked in a systematic study of the SFRS. For this sample we obtained deep Hα imaging observations with the 1.3m telescope of the Skinakas* observatory, and the 1.2m telescope of the Fred Lawrence Whipple observatory† (FLWO). Based on these observations we construct maps of their very recent star-forming activity and we measure their integrated SFR. Via comparisons with other SFR indicators and spectroscopic observations (Mahajan *et al.* 2019) we compare the Hα-based SFRs with UV, IR, and radio SFRs, and we discuss the systematic effects that affect them (Sections 2.5.1, 3.5.1).

In order to study the connection between stellar endpoints and recent star-forming activity we perform a study of the X-ray emission and SFR, in a subset of galaxies of the SFRS sample with good quality *Chandra* data. We explore the correlation between X-ray emission and SFR in sub-galactic scales, and we address the effect of stellar population ages on this correlation (Sections 3.5.1, 3.5.2, 3.5.3, 3.5.4)

Finally, in order to investigate the effect of metallicity on the X-ray luminosity-SFR scaling relation, we perform a multi-wavelength study of the ring galaxy NGC 922. Galaxies like NGC 922 form a ring through a very specific interaction, when a dwarf galaxy passes through the host like a bullet. The caustic of this interaction creates a star-forming ring with young stellar populations (of about the same age). In this study we measure metallicity differences between the ring and the central part of the ring galaxy. In Sections 4.5.1, 4.5.2, 4.5.3, 4.5.4 we also investigate the correlation between X-ray luminosity and SFR with respect to metallicity and stellar populations age.

* http://skinakas.physics.uoc.gr/en/
† http://www.sao.arizona.edu/

This page intentionally left blank

2

The Star Formation Reference Survey - V: Comparison of Hα star-formation rates with other indicators; the effect of extinction and metallicity

2.1 Introduction

Star formation is one of the defining properties of galaxies. Since the recombination epoch, star formation has been transforming the primordial gas into stars, building what is now seen as the stellar mass ($M_\star$) of the galaxies while enriching the gas with metals. The recent or current star-formation is estimated through the star-formation rate (SFR) of galaxies or large stellar populations (SPs). There are various indicators tracing SFR across the electromagnetic spectrum, based on emission produced by different physical mechanisms associated with star-formation. These mechanisms involve e.g. the direct UV emission from the photospheres of hot stars, or the indirect emission by dust that has absorbed UV, re-emitted in the IR. However, the target of all SFR indicators is to measure the amount of massive/young stars residing in the SPs. The assumption of an initial mass function (IMF; e.g. Salpeter 1955; Miller & Scalo 1979; Kroupa 2001;

Chabrier 2003) can extrapolate this measurements and give an estimation of the total amount of all the recently born stars.

Many studies of SFR indicators so far (e.g. Moustakas & Kennicutt 2006; Calzetti *et al.* 2007; Kennicutt *et al.* 2008, 2009; Rieke *et al.* 2009; Hao *et al.* 2011; Boquien *et al.* 2010; Calzetti *et al.* 2010; Murphy *et al.* 2011; Davies *et al.* 2017; Mahajan *et al.* 2019) have established a framework for measuring SFR. However, these studies also showed that measuring star-formation is a complex task subject to systematic effects and often limited by available data. For local Universe galaxies, the Hα emission is the most widely used among the various SFR indicators.

Hα emission is produced when massive/bright young stars ionize atomic hydrogen gas. The electrons cascading the atomic hydrogen (H II) energy levels emit radiation, producing the well studied *Lyman*, *Balmer*, *Paschen* lines. The great abundance of hydrogen gas in all star-forming galaxies makes Hα a strong emission line, easily detected when the galaxies host recent star formation and O stars that can ionise the interstellar medium (ISM) with their UV emission. The fact that the Hα ($\lambda = 6563$ Å) emission line is the strongest hydrogen recombination line in the visible range for the local Universe galaxies has made it one of the most commonly used tracers of star formation.

Hα is the ideal SFR indicator for probing stellar populations with ages $\lesssim 10$ Myr (e.g. Kennicutt 1998; Boquien *et al.* 2014; Cerviño *et al.* 2016; Haydon *et al.* 2020). Tracing the youngest stellar populations, unbiased by emission arising from older stars is important for studies related with these very short-lived stars, like the correlations with the X-ray emission from high-mass X-ray binaries (HMXBs; e.g. Kouroumpatzakis *et al.* 2020). This is also relevant for deriving scaling relations between stellar populations and their endpoints (neutron stars and stellar black holes) since the progenitors of these stellar remnants are very massive stars.

Despite its advantages, the Hα emission is subject to effects than can bias the SFR measurements. These effects include: absorption by dust in the vicinity of the star-forming regions (birth clouds; e.g. Calzetti *et al.* 1994; Charlot & Fall 2000) or the general ISM of a galaxy, and the contribution of the adjacent in wavelength [N II] ($\lambda\lambda 6548, 6583$) emission lines (e.g. Kennicutt *et al.* 2008). Failing to correct for these effects or lack of relevant information (e.g. extinction measurements from independent methods) can lead to systematic differences from the actual SFR.

This work presents a systematic study of Hα-based SFRs in comparison with other SFR indicators in a representative sample of nearby star-forming galaxies. Through complete photometric coverage of the sample from the UV to radio wavelegths, which also includes optical spectral information, we provide calibrations for the Hα-based SFRs

with respect to various extinction indicators, and the [N II] contribution. Furthermore, we examine the SFRs derived by spectral energy distribution (SED) fits, radio 1.4 GHz emission, and the hybrid indicator which combines 24 μm and Hα emission (Calzetti *et al.* 2007). Finally, we investigate the connection between extinction and the metallicity of the sample galaxies.

The main goal of this work was to obtain the Hα emission based SFR for the SFRS galaxies, in order to study the correlations with other fundamental galactic characteristics and other widely used in the literature SFR and extinction indicators in a representative in star-formation sample. The Hα sample presented in this work consists of 305 galaxies due to observational limitations that are explained in the following sections.

Section 2.2 describes the sample and basic data and Section 2.3 the Hα photometry. Section 2.4 presents the basic results of the analysis. Sections 2.5 and 2.6 discuss and summarize the results of this work. In the following analysis we assume a cosmology with $\Omega_m = 0.3$, $\Omega_\Lambda = 0.7$, $h = 0.7$. We adopt as solar abundances $Z_\odot = 0.0142$, $X_\odot = 0.7154$, and $[12 + \log(O/H)_\odot] = 8.69$ (Asplund *et al.* 2009)

2.2 Sample and Observations

2.2.1 Sample

The basis of our sample is the Star Formation Reference Survey (SFRS; Ashby *et al.* 2011). SFRS comprise 369 local Universe galaxies (maximum redshift $z = 0.30641$) selected to represent star formation under various conditions. More specifically, SFRS was selected out of the parent PSCz catalog (Saunders *et al.* 2000) to cover the 3D space of the fundamental galactic properties of SFR, the specific SFR (sSFR), and dust temperature. In this selection, SFR was indicated by the $L_{60\,\mu\mathrm{m}}$, sSFR by the $K_S - F_{60\,\mu\mathrm{m}}$ colour, and dust temperature by the $F_{100\,\mu\mathrm{m}}/F_{60\,\mu\mathrm{m}}$ flux ratio. SFRS galaxies have wide coverage of the electromagnetic spectrum, from radio to X-rays (Mahajan *et al.* 2019; Kouroumpatzakis *et al.* 2020), including optical spectra of the galaxy nuclei (Maragkoudakis *et al.* 2018), and thus an ionization classification through BPT diagrams (Baldwin *et al.* 1981; Veilleux & Osterbrock 1987; Kewley *et al.* 2001; Kauffmann *et al.* 2003; Schawinski *et al.* 2007).

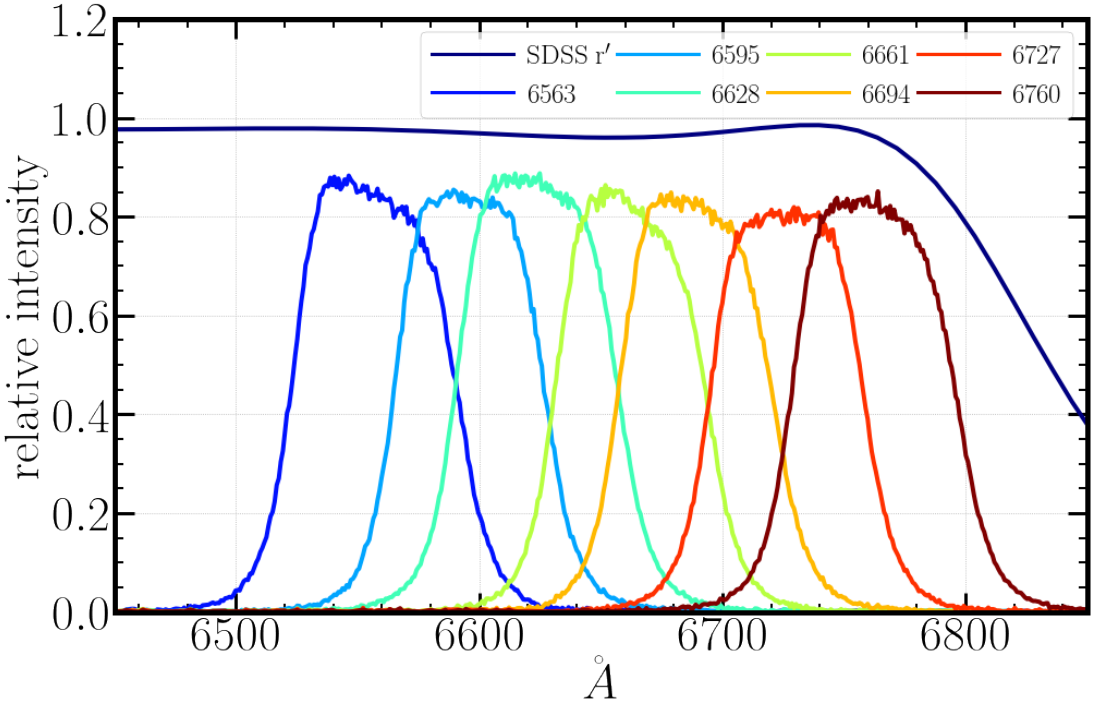

Figure 2.1: Transmission curves of the filters used in the Hα imaging campaign. The central wavelength of each filters is indicated in the legend with the same color as in the graph. These curves were measured in collimated light.

2.2.2 Hα observations

We obtained Hα + [N II] and nearby continuum imaging observations for 305 SFRS galaxies with the 1.3 m telescope of the Skinakas* observatory, and the 1.2 m telescope of the Fred Lawrence Whipple observatory† (FLWO) for a total of 180 nights at Skinakas and 31 nights at FLWO. We used a custom set of narrow-band filters to account for the redshift range of the SFRS galaxies, centered at $\lambda = 6563$, 6595, 6628, 6661, 6694, 6727, 6760 Å with average FWHM = 45 Å (Figure 2.1). SFRS galaxies with redshift $z > 0.03$ could not be covered by the available filters. Therefore, these higher-redshift SFRS galaxies were not observed, resulting to a total of 305 out of 369 galaxies with Hα observations. Due to the selection function of the SFRS, this limitation did not affected the following analysis except from limiting the high end of SFR values (Figure 2.2). We used a filter equivalent to SDSS r' for the continuum observations.

Hα and r′ observations had 1 hour and ∼10 minutes exposure times respectively. The observations took place under photometric conditions and typical seeing FWHM ∼1.2″

* http://skinakas.physics.uoc.gr/en/
† http://www.sao.arizona.edu/

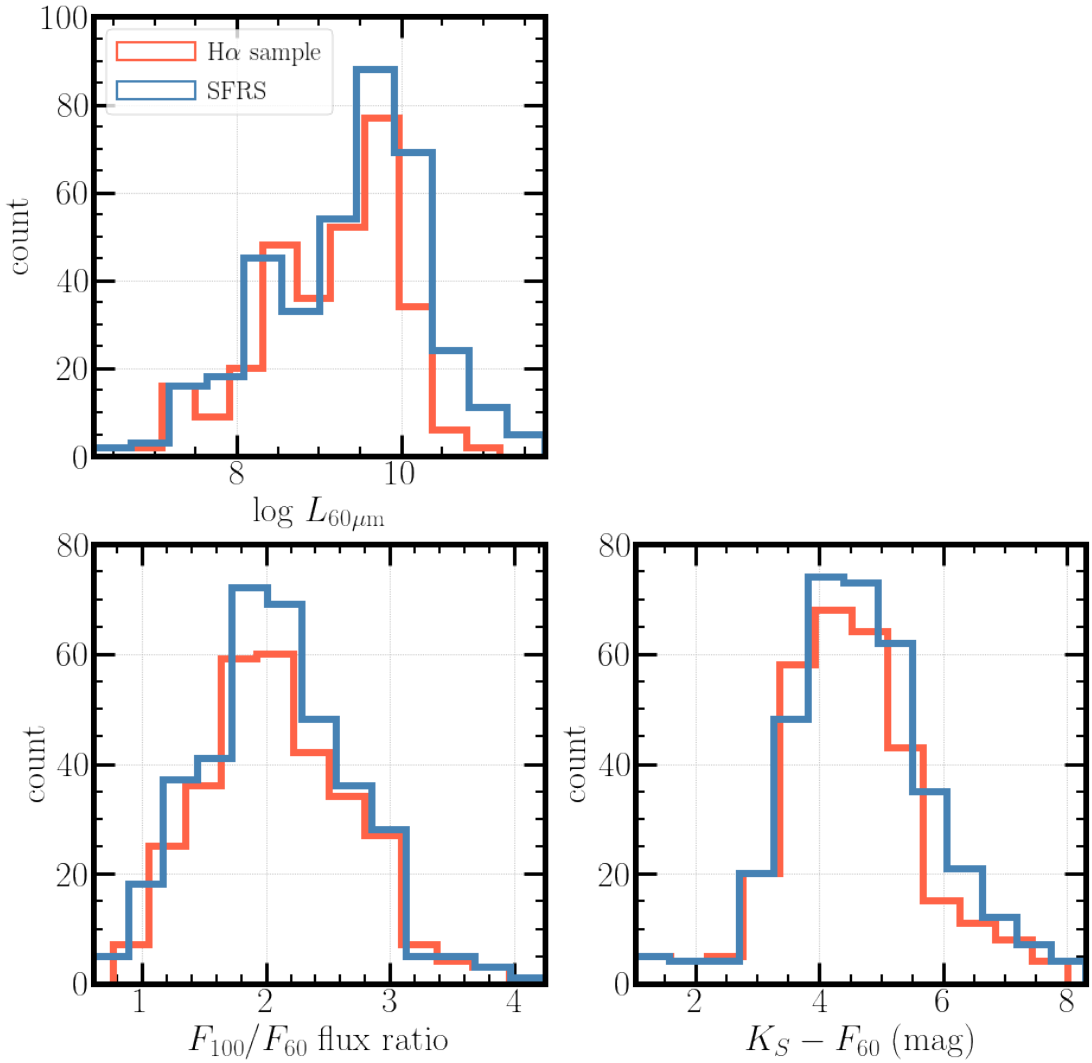

Figure 2.2: Comparison of the SFRS selection properties: $L_{60\mu m}$ (top left; a proxy of SFR), $F_{100\mu m}/F_{60\mu m}$ (bottom left; a proxy of dust temperature), and $K_S - F_{60\mu m}$ (bottom right; a proxy of sSFR), between the entire SFRS (blue), and the sample with Hα observations (red).

and $\sim$1.7$''$ for Skinakas and FLWO respectively. Some galaxies were observed in multiple occasions and different nights for phototmetric calibrations when in doubt about the photometric conditions of the original observations. The total exposure of each galaxy observed in Hα was split in either 6 observations of 600 seconds or 12 observations of 300 seconds. Thus the subtraction of cosmic rays was more efficient, and photometric conditions variations were monitored during the observations.

2.3 Hα photometry and star-formation rates

2.3.1 Basic reduction and continuum subtraction

The basic reduction was performed with `IRAF` (Tody 1986, 1993). The task `ccdproc` was used for the bias subtraction and flat fielding. The separate frames were aligned and combined with `imalign` and `imcombine` tasks respectively. Astrometry was applied to the final combined frames with *Astrometry.net* (Lang *et al.* 2010).

In order to perform continuum subtraction to the Hα images, we followed the standard procedures for narrow-band imaging (e.g. Kennicutt *et al.* 2008). We first measured the flux of the foreground stars in both the Hα and continuum-red images using the `IRAF` task `daophot`. The mode and the standard deviation of the Hα to r$'$ continuum flux ratio distribution was used as the continuum-subtraction ratio F and its uncertainty respectively. From the Hα image, we subtracted the continuum image scaled by F in order to produce the final continuum-free Hα image (e.g. Figure 2.3):

$$\mathrm{Image}_{\mathrm{H}\alpha\,\mathrm{cont.\,sub.}} = \mathrm{Image}_{\mathrm{H}\alpha} - \mathrm{Image}_{\mathrm{cont.\,r'}} \times F \tag{2.1}$$

As described by Kouroumpatzakis *et al.* (2020), the curve of growth (CoG) technique was used on the continuum subtracted images to measure the flux of the galaxies. The CoG technique has the benefit of determining the optimal aperture that contains the total flux of the object while also measuring and subtracting the background contribution. The shape of the apertures was based on elliptical-aperture fits to WISE 4.6 μm data of the SFRS galaxies following a procedure similar to Jarrett *et al.* (2019). The CoG was calculated by increasing the aperture radius while keeping the position angle of the ellipse and the major-to-minor axis ratios fixed. The maximum -running- radius of the CoG was beyond the D25 isophote in order to encompass the total galaxy emission. This was confirmed by visually inspecting the results of the process. The resolution of the CoG was varying from 1 to 5 pixels for small to large (in aperture size) galaxies,

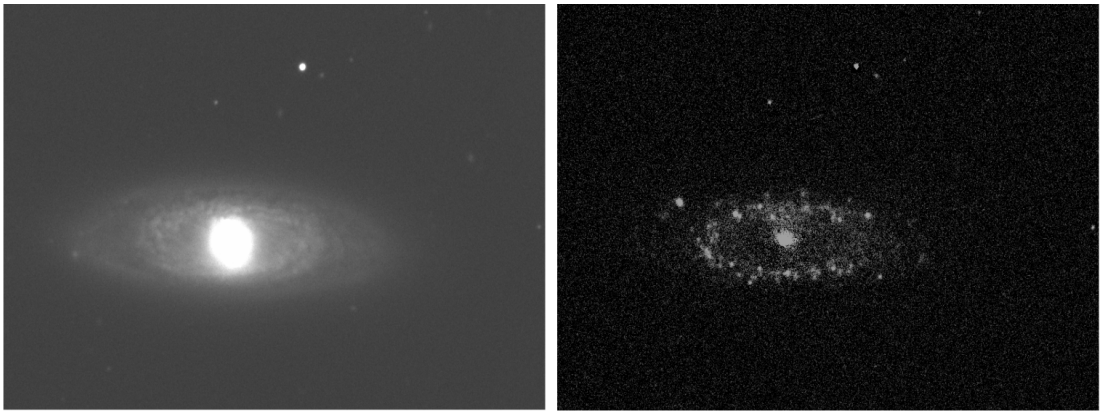

Figure 2.3: Example of continuum subtraction in galaxy NGC 4448. In the left plot is the observed Hα image, and in the right is the Hα after having subtracted the continuum.

respectively. In order to measure the asymptotic line of the CoG, a linear regression fit was performed to the last 5% of the CoG points. The CoG was iteratively repeated, while adjusting the background, until the regression-fit slope (of the last 5% of the CoG) was zero. Then, the size of the aperture was defined by the smallest radius of the CoG that reached the asymptotic line (Figure 2.4).

2.3.2 Photometry

In order to account for differences in the filter transmission curves between those measured with a parallel beam (usually reported by filter manufacturers) and the telescope's conical beam, we measured the filters' transmission curves with the Skinakas 1.3m telescope. We measured the actual transmission curve for the focal ratio of the telescope by placing the filters in the optical path of the spectrograph and observing spectra of standard stars with and without the filters (Figure 2.1).

In order to account for the photometric variations of each observation during the exposure time, we added the standard deviation of the distribution of fluxes of all the observing frames as an uncertainty in our photometry.

For the photometry absolute calibrations we observed spectrophotometric standard stars (Massey *et al.* 1988) at various airmasses during each observing run. We followed the standard procedure of fitting the instrumental magnitude as function of the airmass x in order to measure the zero-point (ZP) and the atmospheric attenuation κ for each night. The reference magnitude of standard stars at the top of the atmosphere was calculated by integrating the reference spectrum S with the filter response R:

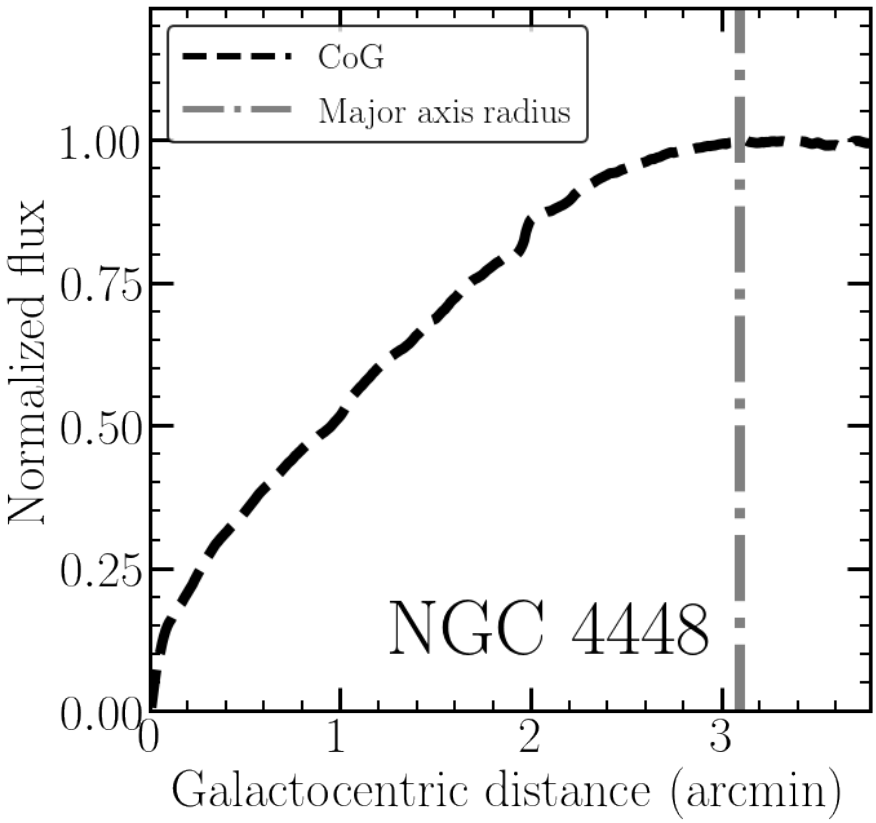

Figure 2.4: Curve of growth (dashed black line) for the Hα+[N II] flux of galaxy NGC 4448. The normalized integrated flux is shown on the vertical axis, as a function of the aperture radius. The semimajor axis of the adopted aperture is shown by a dashed-dotted grey line.

$$\mathrm{m_{ref}} = -2.5 \log \left(\frac{\int R \times S}{\int S} \right) \quad . \tag{2.2}$$

The ZP is then easily calculated as:

$$\mathrm{ZP} = m_{\mathrm{ref}} + 2.5 \log(\mathrm{CR}) \tag{2.3}$$

where CR is the count rate of the observed standard star.

The CRs were converted to flux with the scheme presented by Kennicutt *et al.* (2008). We have also included in our calculation the transmission correction (see Appendix A in Kennicutt *et al.* 2008) that corrects for the differential transmission of the narrow and

broad band filters. This correction takes into account the position of the Hα and [N II] emission lines with respect to the galaxies' redshift and the transmission curve of the filter. Therefore, we calculated the flux f_λ using the following equation:

$$f_\lambda = \lambda^2 \, 10^{-0.4\,[\mathrm{ZP}+2.397-\kappa \sec(x)]} \, T_\mathrm{c} \tag{2.4}$$

$$T_\mathrm{c} = \mathrm{FWHM_{NB}}\,\mathrm{CR}\left[T_\mathrm{NB}(\lambda) - T_\mathrm{R}(\lambda)\frac{t_\mathrm{R}}{t_\mathrm{NB}}\frac{1}{F}\right]^{-1} \tag{2.5}$$

where $\mathrm{FWHM_{NB}}$ is the full-width-half-maximum of the narrow-band filter, CR is the count-rate [counts s^{-1}], T_R and T_NB are the normalized filter transmissions, t_R and t_NB are the exposure times, of the continuum and the narrow-band filter respectively, and F the continuum subtraction ratio.

The normalized transmission of the filters (T_NB and T_R) accounts for the different transmission at the wavelengths of the Hα and [N II] emission lines by summing their respective transmissions weighted by the average Hα to [N II] ratio (0.54; following Kennicutt *et al.* (2008)). We ignore the contribution of the [N II]λ6548 line in the calculation of the filter transmission because of its significantly smaller intensity in comparison to the Hα and the [N II]λ6584 lines.

The contribution of the [N II] flux is subtracted in the next step of the analysis (see Section 2.5.1). It is in the goals of this work to give calibrations for Hα imaging including all possibilities, as in the case of not having any spectral information, thus measurements of [N II]/Hα(or e.g. M_b that can help derive an estimation of [N II/Hα]), that are required for the proper subtraction.

In the following analysis we only consider star-forming galaxies as characterized in Maragkoudakis *et al.* (2018).

2.3.3 Hα photometry comparison

Figure 2.5 compares our Hα photometry with that of the Hα survey of nearby galaxies within 11 Mpc by Kennicutt *et al.* (2008). The comparison for the 11 galaxies in common shows excellent agreement between the flux measurements of the two surveys. The standard deviation of the ratio between the two surveys is $\delta(\log f^{\mathrm{K20}}_{\mathrm{H}\alpha}/f^{\mathrm{K08}}_{\mathrm{H}\alpha}) = 0.08$ dex.

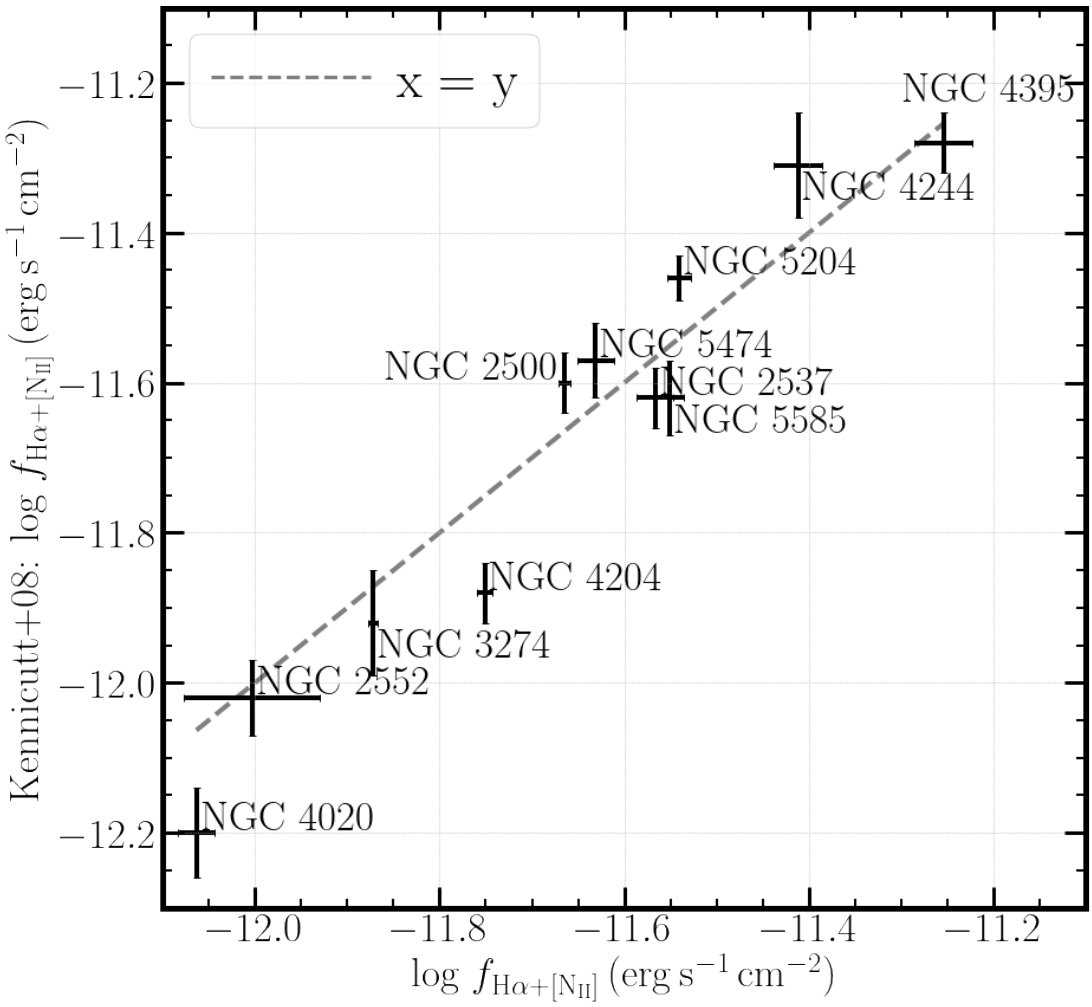

Figure 2.5: Comparison of the logarithm of the Hα + [N II] flux measurements between Kennicutt *et al.* (2008) and this work. Dashed line shows equality.

2.3.4 Extinction indicators

Visible and UV emission can be partially or completely absorbed by dust. Therefore, in order to correctly estimate SFRs from the Hα emission, we require estimation of the extinction. There are multiple ways to estimate extinction depending on the available data. This work compares extinction measurements from the Balmer decrement (the $f_{\mathrm{H}\alpha}/f_{\mathrm{H}\beta}$ ratio), the IR excess (IRX; $f_{\mathrm{FIR}}/f_{\mathrm{FUV}}$ ratio; e.g. Buat & Xu 1996; Meurer *et al.* 1999; Gordon *et al.* 2000), and SED fits. Maragkoudakis *et al.* (2018) presented the flux of the Hα and Hβ lines, extracted from the nuclear regions of the sample galaxies. The same work also gave, for a subset of the SFRS sample with long-slit spectra, Balmer

line measurements from larger apertures extending over the major axis of the galaxies. The Balmer extinction was estimated through the conversion of Domínguez *et al.* (2013):

$$\mathrm{E(B-V)} = 1.97 \log \left[\frac{(f_{\mathrm{H}\alpha}/f_{\mathrm{H}\beta})}{2.86} \right] \tag{2.6}$$

using the reddening law of Calzetti *et al.* (2000). In the following analysis we adopted $\mathrm{E(B-V)} = 0$, for 18 galaxies which were found to have $f_{\mathrm{H}\alpha}/f_{\mathrm{H}\beta} < 2.86$.

We adopted the IRX-based extinctions from Mahajan *et al.* (2019), which were calculated based on the GALEX FUV and FIR fluxes, and the $\mathrm{E(B-V)}_{\mathrm{IRX}}$ calibration of (Buat *et al.* 2005):

$$A_{\mathrm{FUV}}(\mathrm{IRX}) = -0.0333p^3 + 0.3522p^2 + 1.1960p + 0.4967 \tag{2.7}$$

where $p = \log(L_{\mathrm{FIR}}/L_{\mathrm{FUV}})$, and

$$\mathrm{E(B-V)}_{\mathrm{IRX}} = A_{\mathrm{FUV}}/k_{\mathrm{FUV}} \tag{2.8}$$

where $k_{\mathrm{FUV}} = 10.22$ from the Calzetti *et al.* (2000) attenuation law.

The extinction determined from the SED fits is modeled after the `dustatt_modified_starburst` module implemented in the `CIGALE` code. This module adopts the attenuation curve of Calzetti *et al.* (2000) extended in the UV by the Leitherer *et al.* (2002) curve. It also allows flexibility in the power-law function of the extinction-law slope, and the position and shape of the UV bump (the latter is kept fixed in our analysis).

2.4 Data and results

2.4.1 Hα based star-formation rates

The Hα, and Hα + [N II] luminosities were converted to SFR through the theoretical Murphy *et al.* (2011) relation:

$$\frac{\mathrm{SFR}_{\mathrm{H}\alpha}}{(\mathrm{M}_\odot\,\mathrm{yr}^{-1})} = 5.37 \times 10^{-42} \frac{L_{\mathrm{H}\alpha}}{(\mathrm{erg\,s}^{-1})} \tag{2.9}$$

In Table 2.4.1 we present the Hα+[N II] fluxes and luminosities for the SFRS galaxies.

Table 2.1: Hα flux for all SFRS galaxies.

SFRS ID #	Name	R.A.	DEC.	$f_{\mathrm{H}\alpha+\mathrm{N[II]}}$ log erg s^{-1} cm^{-2}	E(B−V)$_{\mathrm{SED}}$ mag	E(B−V)$_{\mathrm{Balmer}}$ mag	E(B−V)$_{\mathrm{IRX}}$ mag
1	IC 486	08:00:20.98	+26:36:48.7	-12.46 ± 0.03		0.64 ± 0.06	0.80 ± 0.08
2	IC 2217	08:00:49.73	+27:30:01.7	-11.86 ± 0.01	0.3 ± 0.01	0.55 ± 0.06	0.67 ± 0.07
3	NGC 2500	08:01:53.18	+50:44:13.7	-11.66 ± 0.01		0.08 ± 0.01	0.21 ± 0.02
4	NGC 2512	08:03:07.85	+23:23:30.6	-12.19 ± 0.14		0.5 ± 0.05	
5	MCG 6-18-009	08:03:28.94	+33:27:44.5		0.3 ± 0.01	0.61 ± 0.06	0.89 ± 0.09
6	MK 1212	08:07:05.52	+27:07:33.7			0.78 ± 0.08	
7	IRAS 08072+1847	08:10:07.01	+18:38:18.1	-13.25 ± 0.02		0.98 ± 0.10	
8	NGC 2532	08:10:15.17	+33:57:23.9	-11.69 ± 0.01	0.2 ± 0.01	1.0 ± 0.1	0.61 ± 0.06
9	UGC 4261	08:10:56.21	+36:49:41.3	-12.34 ± 0.07	0.2 ± 0.01	0.39 ± 0.04	0.42 ± 0.04
10	NGC 2535	08:11:13.49	+25:12:24.5	-11.83 ± 0.09	0.2 ± 0.01	0.37 ± 0.04	0.56 ± 0.06

The complete table can be found in Appendix Table 6.1.

2.4.2 Other star-formation rate indicators

In addition to the Hα emission, we have also used in this work SFRs based on several different continuum bands, as well as composite indicators resulting from combinations of these bands. These were presented by Mahajan *et al.* (2019). The SFRs reported there include the radio 1.4 GHz emission, tracing synchrotron radiation from relativistic electrons produced in supernovae; FIR emission from dust heated by young stars UV emission; 8μm emission from polycyclic aromatic hydrocarbons (PAHs), tracing the photo-dissociation regions around young stellar populations; UV emission from the photospheres of OB stars. We also use the combination of the $\mathrm{SFR_{FUV}}$ and $\mathrm{SFR_{FIR}}$:

$$\mathrm{SFR_{tot}} = \mathrm{SFR_{FUV}} + (1-\eta)\,\mathrm{SFR_{FIR}} \tag{2.10}$$

where η refers to the fraction of FIR emission that is associated with old stars rather than the dust heated by the massive/young stars. Mahajan *et al.* (2019) adopted $\eta = 0.0$ as the nominal value, based on comparisons of the FIR and TIR emission, showing that the FIR is a SFR indicator, less biased by the thermal stellar emission, with respect to the TIR. This was supported by the fact that the correlation with $\mathrm{SFR_{1.4\ GHz}}$ shows a preference to $\eta = 0.0$ (See also Section 2.5.5).

We have also calculated SFRs based on the 24 μm emission, which is produced by the UV-heated dust, using the 24 μm fluxes reported in Ashby *et al.* (2011). We converted the 24 μm luminosities to SFR using the calibration of Rieke *et al.* (2009):.

$$\frac{\mathrm{SFR_{24\mu m}}}{(\mathrm{M_\odot\,yr^{-1}})} = 10^{-42.69}\,\frac{\nu L_{24\mu m}}{(\mathrm{erg\ s^{-1}})} \quad . \tag{2.11}$$

where ν is the frequency of 24 μm.

The 8 μm emission is produced in the photo-dissociation regions of star-forming bubbles from PAH molecules excited by UV radiation. In order to account for the 8 μm emission attributed to PAHs, the stellar continuum was estimated and subtracted using the formula from Helou *et al.* (2004):

$$f_{8\mu m,\mathrm{PAH}} = f_{8\mu m} - 0.26\, f_{3.6\mu m} \quad . \tag{2.12}$$

Then PAH 8 μm luminosity was converted to SFR with the calibration of Pancoast *et al.*

(2010):

$$\frac{\mathrm{SFR}_{8\mu m,\mathrm{PAH}}}{(\mathrm{M}_\odot\,\mathrm{yr}^{-1})} = 6.3 \times 10^{-10} \frac{L_{8\mu\mathrm{m},\mathrm{PAH}}}{(\mathrm{L}_\odot)} \quad . \tag{2.13}$$

A widely used and robust method for estimating galaxy properties when multi-band photometry is available, comes from the analysis of their SED. SFRS galaxies benefits from such a multi-wavelength coverage. We present the SFR estimation from SED fits for the SFRS galaxies with the use of the `CIGALE` (Burgarella *et al.* 2005; Noll *et al.* 2009; Boquien *et al.* 2019) SED fitting code. The basis of the `CIGALE` code is the energy balance between the dust-absorbed energy with the energy that is re-emitted in the MIR and FIR. We assume a double-exponential star-formation history and we adopt the `DL2007` dust model. More details about the SED fits of the SFRS galaxies are presented by Maragoudakis et al.(2021; in prep.). In the following analysis we discarded galaxies that had fits with reduced $\chi^2 > 3$. The SFRs are reported in Table 2.4.2.

Table 2.2: Star-formation rates by the Hα and 24μm emission, and combinations. [N II]/Hα ratios, and metallicities of the host and nuclei of the SFRS galaxies.

SFRS ID	log SFR Hα + [N$_{\rm II}$] (M$_\odot$ yr^{-1})	log SFR Hα (M$_\odot$ yr^{-1})	log SFR SED (M$_\odot$ yr^{-1})	log SFR 24μm (M$_\odot$ yr^{-1})	log SFR 24μm + (Hα + [N$_{\rm II}$]) (M$_\odot$ yr^{-1})	log SFR 24μm + Hα (M$_\odot$ yr^{-1})	log $\frac{f_{[N_{II}]}}{f_{H\alpha}}$	Metallicity nucleus [12 + log($\frac{O}{H}$)]	Metallicity host [12 + log($\frac{O}{H}$)]
1	0.46		0.86	1.24	1.25	1.11	0.07		
2	0.71	0.5	1.07	0.75	1.08	0.96	−0.42	8.77	8.72
3	−0.5	−0.7	−0.82	−0.82	−0.24	−0.38	−0.45		
4	0.3	0.01		0.99	1.02	0.95	−0.31	8.85	8.74
5			1.35	1.35			−0.29	8.8	
6				1.48			−0.28	8.74	
7	−0.74	−1.18		1.05	0.96	0.95	−0.2	8.74	
8	0.9	0.69	1.12	1.06	1.32	1.21	−0.42	8.76	8.72
9	0.4	0.28	0.66	0.97	1.04	1.0	−0.6	8.53	
10	0.56	0.36	0.79	0.51	0.9	0.77	−0.43	8.87	8.66

The complete table can be found in Appendix Table 6.1.

2.4.3 Comparison between extinction indicators

Figure 2.6 compares the extinctions derived from SED fitting, the Balmer decrement, and the IRX (Section 2.3.4, Table 2.4.1). This comparison involves 247 star-forming galaxies with available photometries for the SED fits. SED extinctions are found to be in average 5% larger than IRX extinctions. The agreement is excellent for low extinction, but is slightly increasing for higher values. The $\mathrm{E(B{-}V)_{Balmer}}$ is found to be 95% and 96% on average higher compared to the $\mathrm{E(B{-}V)_{SED}}$ and $\mathrm{E(B{-}V)_{IRX}}$, respectively, while the difference is increasing for higher extinction. A linear regression fit of the form $\mathrm{E(B{-}V)_{Balmer}/E(B-V)_{IRX}} = \alpha + \beta\,\mathrm{E(B-V)_{Balmer}}$ shows an intercept $\alpha = 0.76 \pm 0.07$, and slope $\beta = 1.91 \pm 0.11$. Likewise, the $\mathrm{E(B{-}V)_{Balmer}/E(B-V)_{SED}} = \alpha + \beta\,\mathrm{E(B-V)_{Balmer}}$ shows an intercept $\alpha = 0.74 \pm 0.08$, and slope $\beta = 1.79 \pm 0.12$. These fits, as well all the linear regression fit in the following analysis, are robust linear regression fits performed with the `Python statsmodel RLM` (Seabold & Perktold 2010) package if not stated otherwise.

2.4.4 Hα star-formation rates corrected for the [N II] contribution

Figure 2.7 presents the Hα-derived SFRs corrected for the contribution of the adjacent [N II] emission lines, compared to un-corrected ones. Each point is colour-coded according to the extinction of each galaxy based on the Balmer decrement. The circle and star points represent measurements based on the nuclear *SDSS* and the nuclear-aperture extractions from the *FAST* long-slit spectra respectively. The fact that the two sets of data are evenly mixed indicates that the [N II]/Hα ratios are not significantly biased by the different sets of observations.

The median of the logarithm of the ratio of the corrected and un-corrected Hα emission is $<\log \mathrm{SFR_{H\alpha}/SFR_{H\alpha+[N\,II]}}> = -0.24$. The correction introduces scatter with standard deviation $\delta(\log \mathrm{SFR_{H\alpha}/SFR_{H\alpha+[N\,II]}}) = 0.25$. A linear regression fit reveals that this correlation is a function of the measured SFR, with the difference being larger for larger SFRs. The negative slope is in agreement with the known correlation between the [N II]/Hα ratio and the SFR (e.g. Kennicutt *et al.* 2008). Another point indicated in Figure 2.7 is that the galaxies with the largest deviations from the general relation (i.e. those with larger [N II]/Hα ratios) tend to have higher extinction.

2.4.5 Extinction corrected Hα star-formation rates

In this section we discuss the effect of extinction on the Hα-based SFR. We consider both the Hα and (Hα + [N II]) luminosities; the latter in order to assess the effect of

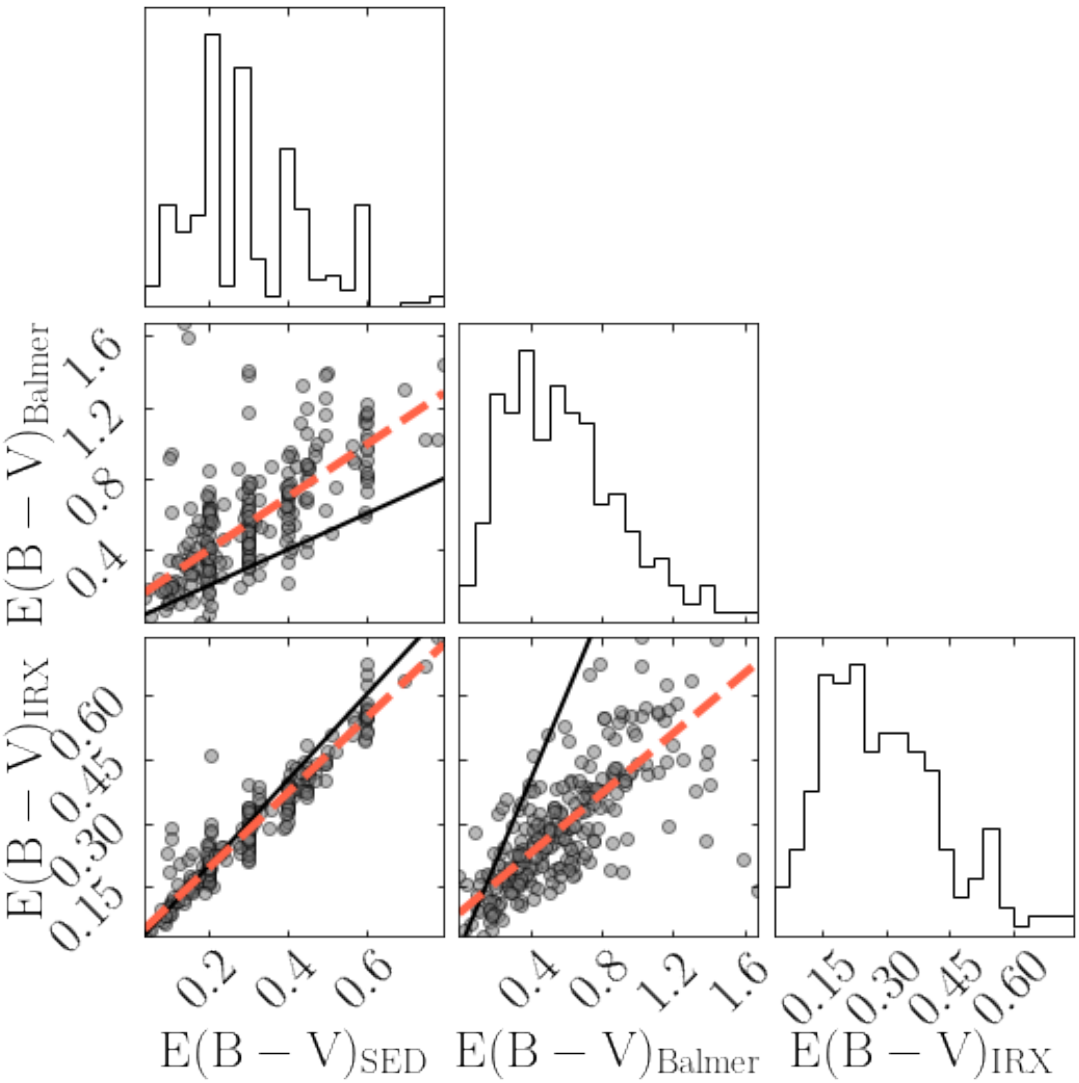

Figure 2.6: Comparisons between the extinctions derived through the Balmer decrement, the IRX, and SED fitting. The black line represents the one-to-one relation. The red dashed line represents a linear regression fit.

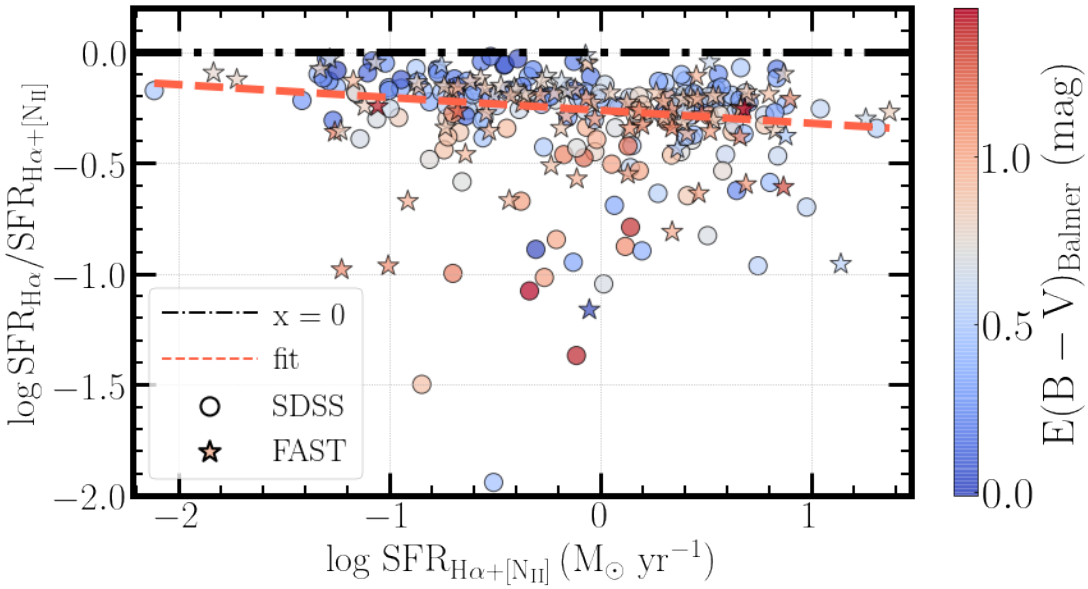

Figure 2.7: The ratio of the SFRs derived by Hα corrected for the [N II] contribution, over the not-corrected, as a function of the not-corrected. Each point represents an SFRS galaxy where circles, and stars are measurements with the FAST and Skinakas spectrographs respectively. The points are colour-coded based on their Balmer E(B-V). The red dashed line represents a robust linear regression fit.

the systematic bias introduced by the [N II] contamination in the Hα photometry when reliable subtraction of this contribution is not possible. The SFR are calculated as discussed in Section 2.4. The extinction is calculated based on the Balmer decrement, the IRX, and the SED fits as discussed in Section 2.3.4 (Table 2.4.1).

In Figure 2.8 we compare the un-corrected and extinction-corrected Hα-based SFRs against the SFR$_{tot}$. In order to highlight the differences we plot the ratio SFR$_{H\alpha}$/SFR$_{tot}$ against SFR$_{tot}$. This comparison involves 228 SFRS galaxies. In order to quantify systematic effects we also report the median values and standard deviation of the SFR$_{H\alpha}$/SFR$_{tot}$ ratio, and we calculate the slopes and intercept of the SFR$_{H\alpha}$/SFR$_{tot}$ - SFR$_{tot}$ relations. These results are shown in Table 2.3. The linear regression fits are of the form:

$$\log\frac{\mathrm{SFR_x}}{\mathrm{SFR_{tot}}} = \alpha + \beta\,\log\mathrm{SFR_{tot}} \tag{2.14}$$

where x corresponds to the extinction indicators used to correct the Hα flux.

These plots (and quantitative analysis) show that, as expected, Hα and (Hα + [N II]),

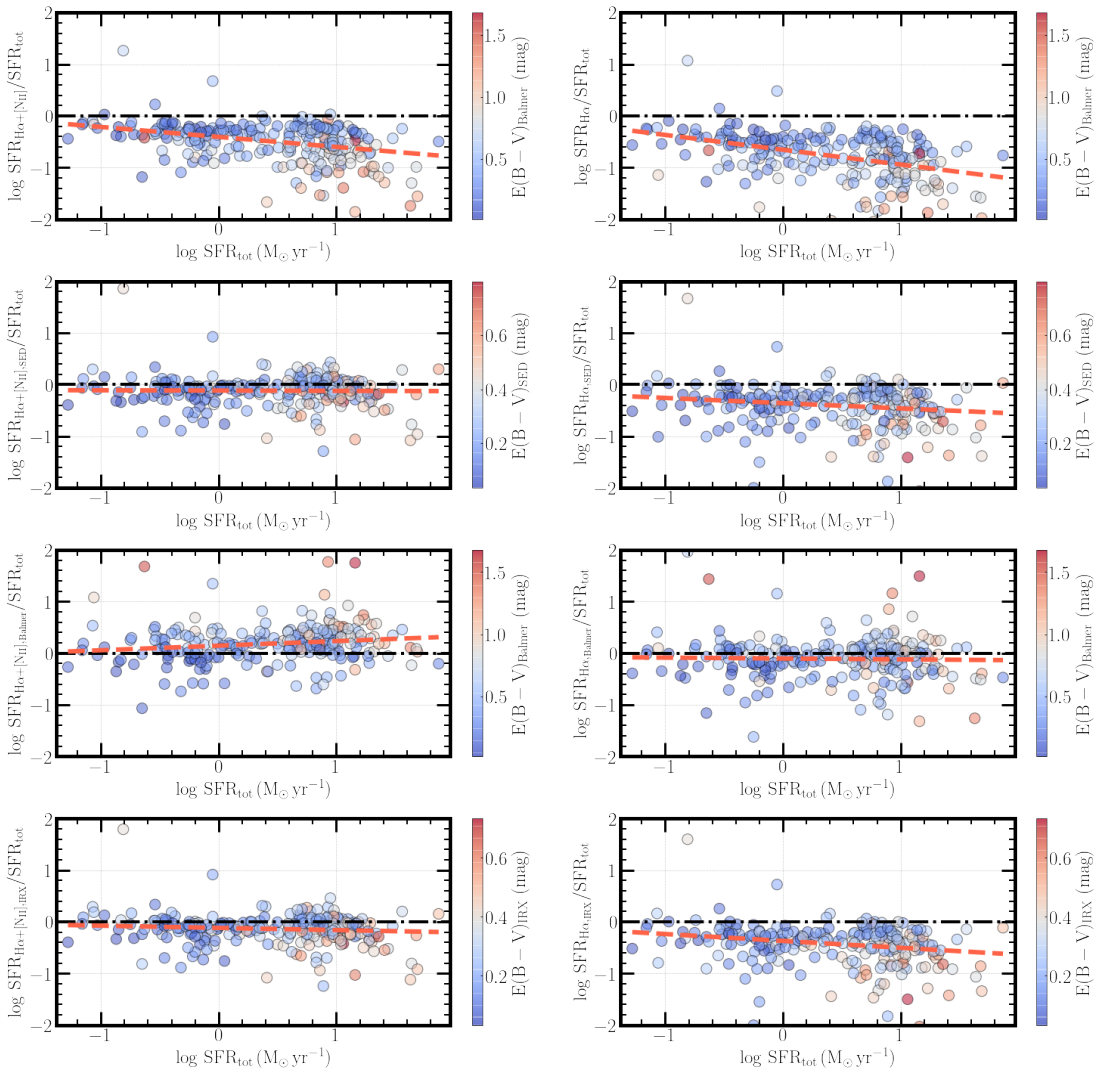

Figure 2.8: Comparisons between SFRs derived by Hα + [N II] (left column) and Hα (right column) as a function of SFR$_{\rm tot}$. From top to bottom rows show: *i*) not corrected for extinction, *ii*) corrected by the E(B−V)$_{\rm SED}$, *iii*) corrected by the E(B−V)$_{\rm Balmer}$, *iv*) corrected by the E(B−V)$_{\rm IRX}$. The black dashed-dotted line represents equality and the red-dashed line the linear regression fit (Table 2.3). Each point represents a SFRS galaxy and the points are colour-coded based on the extinction used in each case respectively (except the first row where there is no extinction correction).

Table 2.3: Results of the comparisons of the SFR derived by Hα not corrected, and corrected by different extinction indicators to SFR_{tot}.

Ext. corr.	[N II] corr.	median $< \log\frac{SFR_x}{SFR_{tot}} >$	68% std. $\delta(\log\frac{SFR_x}{SFR_{tot}})$	intercept α	slope β
		−0.42	0.39	-0.41 ± 0.03	-0.20 ± 0.03
SED		−0.10	0.32	-0.12 ± 0.02	-0.01 ± 0.02
Balmer		0.19	0.39	0.15 ± 0.02	0.09 ± 0.03
IRX		−0.12	0.31	-0.12 ± 0.02	-0.04 ± 0.02
	Yes	−0.72	0.53	-0.66 ± 0.03	-0.29 ± 0.04
SED	Yes	−0.33	0.44	-0.36 ± 0.03	-0.10 ± 0.03
Balmer	Yes	−0.07	0.42	-0.10 ± 0.03	-0.02 ± 0.03
IRX	Yes	−0.38	0.43	-0.37 ± 0.03	-0.13 ± 0.03

when not corrected for extinction, underestimate SFR in all cases, except for a few outliers. When corrected for the [N II] contribution the Hα based SFRs show ~ -0.7 dex median difference with respect to SFR_{tot} This difference is increasing for galaxies with high SFR while galaxies with higher extinction tend to show even larger underestimation of the SFR. We note that in all comparisons, the [N II] correction results in increased scatter in the comparisons with SFR_{tot}.

Due to the fact that the E(B-V) derived through the SED fits, and the IRX, are in excellent agreement (Section 2.4.3), correcting the Hα emission with one or the other has the same effect. The only difference is a slightly steeper (negative) slope for the IRX. The Balmer decrement based correction gives the best agreement for the pure Hα emission SFRs. The comparison with the SFR_{tot} results to a flat slope, considering the uncertainties, indicating that the correction is independent of the SFR. However, on average it slightly underestimates the total SFR by ~ 0.1 dex.

The (Hα+ [N II]) SFRs show very good agreement with the SFR_{tot} when it is corrected by the extinctions derived through the SED fits or the IRX. In the case of the $E(B-V)_{SED}$ the comparison is independent of the SFR (slope $\beta = 0$), while the average SFR is underestimated for ~ 0.12 dex. In the case of the IRX there is a very slight anti-correlation with the SFR_{tot}.

Based on the linear regression fits with SFR_{tot} (Table 2.3), one can correct the Hα or the (Hα + [N II]) SFRs for different extinction correction methods (or lack of) rewriting Equation 2.14 as:

$$SFR_{tot} = (SFR_x \, 10^{-\alpha})^{1/(\beta+1)} \tag{2.15}$$

2.4.6 Combinations of Hα, 24 μm, and 8 μm as hybrid star-formation indicators

Hα traces indirectly the Lyman-continuum UV photons produced by stellar populations younger than those traced by the typical UV bands that can be probed directly, and which lie in longer wavelengths (e.g. Leroy *et al.* 2012; Kennicutt & Evans 2012; Boquien *et al.* 2014; Kouroumpatzakis *et al.* 2020; Haydon *et al.* 2020). The latter include emission of B stars. However, Hα (and in general all optical and UV) emission main limitation is that it is affected by extinction, which often is hard to estimate reliably.

Hybrid indicators like the combination of 24 μm and 8 μm, with Hα or [O II] emission (e.g. Calzetti *et al.* 2007; Kennicutt *et al.* 2009) account for both the dust-absorbed and unabsorbed stellar radiation. The 24 μm emission is unaffected by extinction and traces the reprocessed emission of young stellar populations (ages $\lesssim$100 Myr; e.g. Kennicutt & Evans 2012; Kouroumpatzakis *et al.* 2020). In order to estimate the SFR from the above combinations we adopt the conversions of Kennicutt *et al.* (2009):

$$\mathrm{SFR} = 7.9 \times 10^{-42}\,(L_{\mathrm{H}\alpha} + 0.02\,L_{24\mu\mathrm{m}}) \tag{2.16}$$

where $L_{24\mu m}$ refers to νL_ν at 24 μm, and

$$\mathrm{SFR} = 7.9 \times 10^{-42}\,(L_{\mathrm{H}\alpha} + 0.011\,L_{8\mu\mathrm{m}}) \tag{2.17}$$

where $L_{8\mu m}$ refers to νL_ν at 8 μm (Eq. 3.2).

Figure 2.9 compares the 24 μm + Hα, and the 8 μm + Hα SFR indicators to $\mathrm{SFR_{tot}}$, while investigating the effect of the [N II] contribution. This comparison involves 247 SFRS star-forming galaxies which have 24 μm, Hα, and spectral information. The linear regression fit results are given in Table 2.4.

The 24 μm + Hα SFRs show in both cases (with or without the [N II] correction) only small offset compared to $\mathrm{SFR_{tot}}$ and no evidence for correlation with SFR (slope of the linear regression fit $\beta \approxeq 0$). The absolute difference is the same in both cases, with the 24 μm + (Hα + [N II]) overestimating (0.07 dex) and the 24 μm + Hα slightly underestimating (0.06 dex) the $\mathrm{SFR_{tot}}$. The scatter is slightly higher in the case of the corrected for the [N II] contribution $\mathrm{SFR}_{24\mu\mathrm{m}\,+\,\mathrm{H}\alpha}$.

The 8 μm + Hα SFRs show worse agreement in comparison to the 24 μm as in both cases the slopes of the linear regression fits are negative. This underestimation of the

Table 2.4: Results of the comparisons of the SFRs derived by Hα corrected, and not-corrected for the [N II] contribution plus the 24 μm, and by the SED fits, compared to SFR_{tot}.

	median $<\log\frac{SFR_x}{SFR_{tot}}>$	68% std. $\delta(\log\frac{SFR_x}{SFR_{tot}})$	intercept α	slope β
24 μm + (Hα + [N II])	0.06	0.28	0.07 ± 0.01	-0.02 ± 0.02
24 μm + Hα	−0.06	0.30	-0.05 ± 0.02	-0.01 ± 0.02
8 μm + (Hα + [N II])	−0.07	0.24	-0.06 ± 0.01	-0.06 ± 0.02
8 μm + Hα	0.05	0.26	0.06 ± 0.01	-0.07 ± 0.02
SED	0.03	0.52	-0.05 ± 0.01	0.08 ± 0.02

SFR is driven by a cluster of points around $\log SFR \sim 10$–$50\ M_\odot\,yr^{-1}$with significant extinction (Figure 2.9).

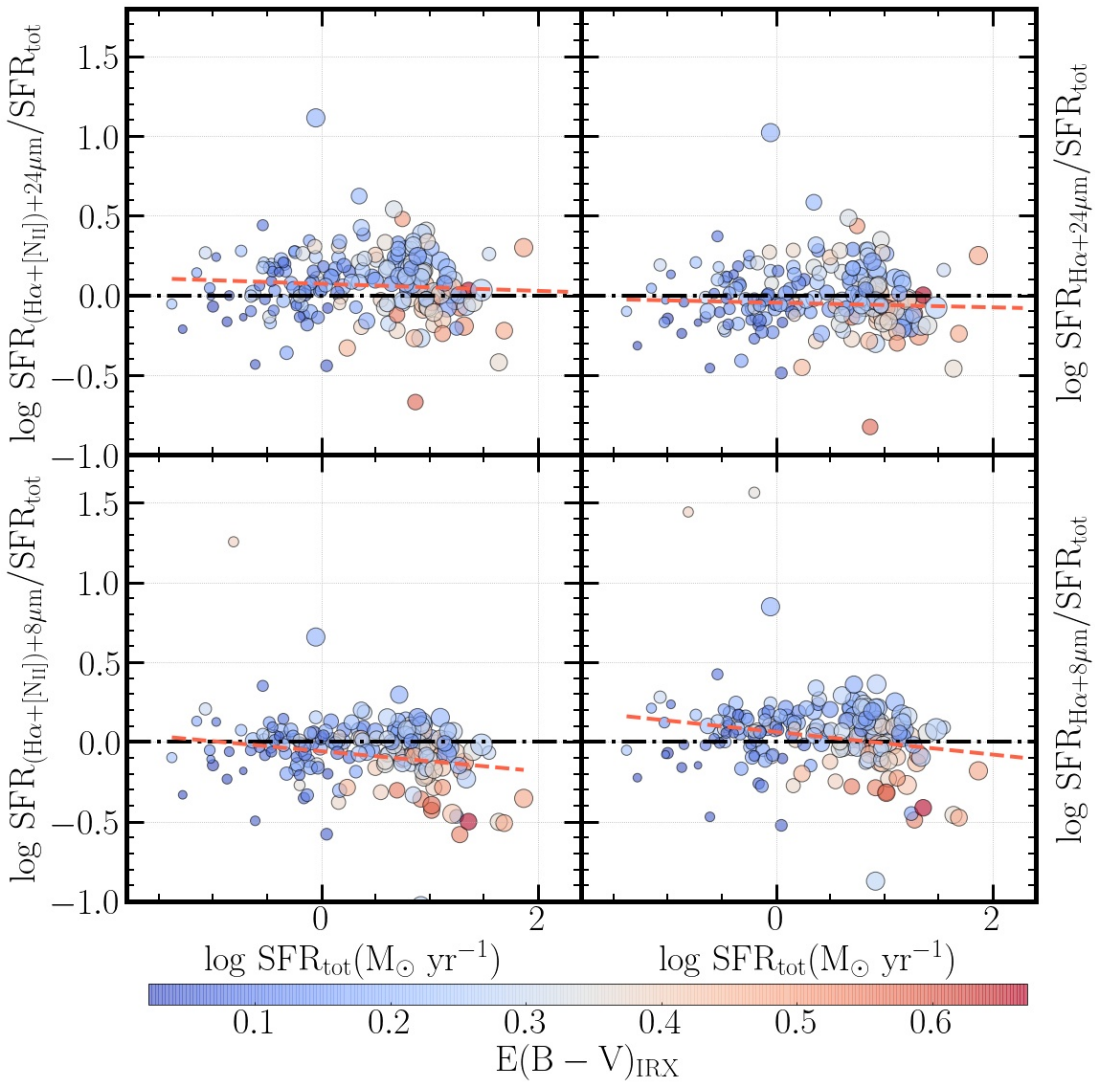

Figure 2.9: Comparison of the hybrid Hα + 24 μm (top panels), and Hα + 8 μm (bottom panels) with the FIR + FUV (adopted as SFR$_{tot}$) hybrid SFR indicators with (right panels) and without (left panels) correction for contribution of the [N II] emission. The points are colour-coded with respect to the galaxies extinction [E(B−V)$_{IRX}$], and size-coded based on the stellar mass of the galaxies. The dashed black line represent the equality and the red dashed-doted a linear regression fit.

2.5 Discussion

2.5.1 Extinction corrected Hα and the contribution of the [N II] emission.

Through the evolution of the stellar populations, the interstellar medium (ISM) is enriched with metals which can form complex molecules and dust under appropriate conditions. The attenuation laws, describing the effect of extinction as a function of wavelength, are a complex function that depends on the properties of the dust grains, as well as, the geometric/spatial distribution of dust in the ISM with respect to the stars (e.g. Calzetti *et al.* 1994, 2000). The attenuation laws can vary significantly in different galaxies (e.g. Buat *et al.* 2018; Salim *et al.* 2018).

Because star formation requires the presence of gas (and dust), the recently born stars are often embedded in regions with large dust and gas column density. Thus, their emission can be partially or completely absorbed. The total absorption is a combination of the absorption at the sites of star formation, and the intervening dust in the ISM along the line-of-sight (e.g. Charlot & Fall 2000; Wild *et al.* 2011; Price *et al.* 2014; Reddy *et al.* 2015). SFR is, directly or indirectly, measured through these young stars' emission. Therefore, in order to infer the correct SFR, one must account for the extinction. The Balmer decrement results on average to ~ 0.23 mag higher extinction compared to the IRX and SED extinction estimations while the difference is increasing for higher E(B-V) values. The ratio $R_{\rm EBV} = {\rm E(B-V)_{IRX}/E(B-V)_{Balmer}}$ is in agreement with the study of Qin *et al.* (2019) ($R_{\rm EBV} = 0.51$). However we find large scatter in our data ($\delta R_{\rm EBV} = 0.73$) probably driven by the fact that IRX includes emission from the entire galaxy while the Balmer lines were retrieved from spectra extracted from the nuclear regions of the SFRS galaxies.

The comparison of the Hα-derived SFRs with SFR$_{\rm tot}$ (Figure 2.8) offer insights on the extinction indicators in regard with the Hα, FUV, and FIR emission. The [N II]-corrected Hα luminosity is best corrected with the use of the Balmer decrement extinction, with the correction being independent of the SFR. The average difference with respect to SFR$_{\rm tot}$ is minimal considering the scatter (Table 2.3). The IRX or SED fit based (with the `dustatt_modified_starburst` attenuation mode) extinction corrections result in a significant underestimation of the total SFR.

The Balmer emission lines originate from the gas in the immediate neighborhood of massive, mainly O stars, a fact that correlates the Balmer-line emission with the shortest timescales of star-formation ($\lesssim 10$ Myr; Leroy *et al.* 2012; Boquien *et al.* 2014; Cerviño *et al.* 2016; Haydon *et al.* 2020; Kouroumpatzakis *et al.* 2020). Therefore, the Balmer

emission is closely related to the young stars that in general are still within or close to their birth clouds. Thus, the Balmer decrement can probe the attenuation caused by these birth clouds. On the other hand, the IRX, as the ratio between the FUV and FIR emission, traces stellar populations with ages of even up to $\sim 100\,\mathrm{Myr}$. FUV emission is produced in the photospheres of massive O, and B stars. Likewise, the FIR emission is produced by the UV-heated dust, thus it probes star-formation of similar timescales to the UV (e.g. Kennicutt & Evans 2012). Therefore, the FUV and the FIR emission is related with stars that had enough time to escape (or disperse) their birth clouds.

Hα + [N II] extinction corrected SFR shows excellent agreement with $\mathrm{SFR_{tot}}$, when is corrected with SED fits, or IRX-based extinctions (Table 2.3). In contrast when correcting for extinction based on the Balmer decrement, which works best for the net Hα emission, tends to overestimate the SFR with respect to the $\mathrm{SFR_{tot}}$. We attribute this to the combined effects of the [N II] emission and the Balmer decrement, both of which correlate with SFR. The [N II]/Hα ratio is a measure of the excitation of the ISM, which correlates positively with the SFR (Figure 2.10). These two effects almost cancel out, resulting to the aforementioned agreement.

The positive correlation of the [N II]/Hα ratio with SFR is because galaxies with higher SFRs tend to have higher metallicity and larger very young stellar populations. Both factors result in increased excitation of the gas (e.g. Kewley & Ellison 2008). Galaxies deviating from the general relation (with lower than average [N II]/Hα ratios; Figure 2.7) are mainly dwarf galaxies with low metallicities (see Section 2.5.6).

The $\mathrm{SFR_{H\alpha+[N\,II]}/SFR_{tot}}$ ratio shows less scatter compared to $\mathrm{SFR_{H\alpha}/SFR_{tot}}$, regardless of the extinction correction. We attribute the increased scatter to the additional error introduced by the subtraction of the [N II] emission. The [N II] emission lines can be relatively dim or partially blended with the Hα line depending on the spectrum resolution and the velocity field of the galaxy (e.g. Maragkoudakis *et al.* 2018; Kouroumpatzakis *et al.* 2021), which introduces additional uncertainty on the measurement of the [N II] flux. However, this is not a major factor, as is evident from the errors on the [N II]/Hα ratios reported in Maragkoudakis *et al.* (2018).

The ionization degree of the gas depends on the local star-formation conditions (see BPT diagrams). The [N II]/Hα ratio can vary up to 0.5 dex for ionization parameter q* varying from 10^7–$10^8\,\mathrm{cm\ s^{-1}}$ and constant metallicity (although metallicity also plays a role; see Figure 9 of Kewley & Ellison 2008). Figure 2.10 shows a positive correlation. A fit in logarithmic scale gives a slope of $\beta = 0.12 \pm 0.01$ and intercept

* The ionization parameter represents the intensity of the ionizing field with respect to the gas density.

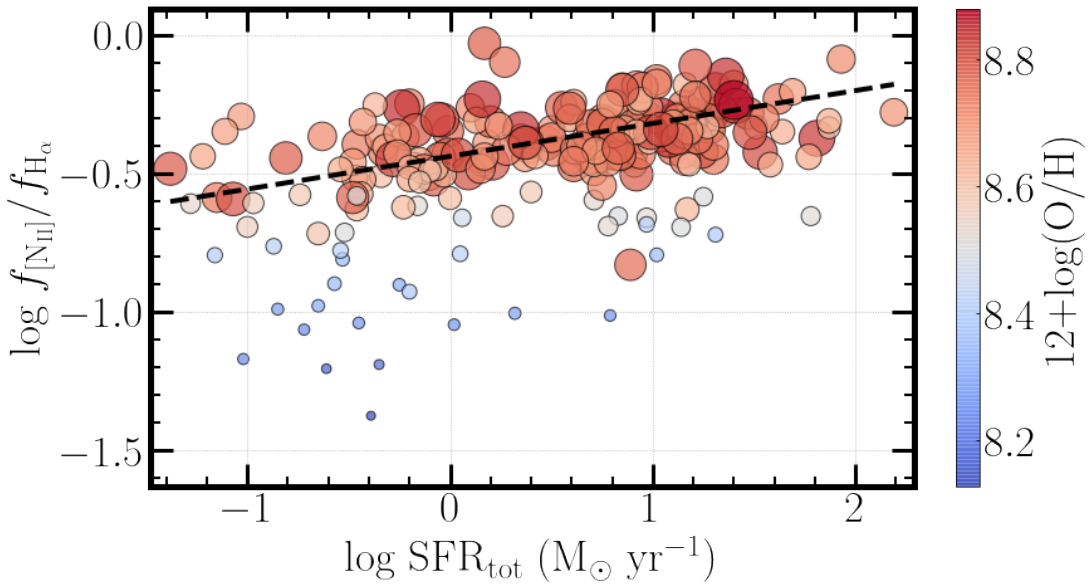

Figure 2.10: The logarithm of the [N II]/Hα ratio as a function of the logarithm of the $\mathrm{SFR_{tot}}$. The points are colour-coded based on the metallicity, and size-coded based on the stellar mass of the galaxies. The black dashed line represents the linear regression fit to the SFRS star-forming galaxies.

$\alpha = -0.44 \pm 0.01$. However, the main reason for the increased scatter is the fact that the [N II]/Hα ratio is measured from the nucleus of the galaxies or from a rectangular aperture along the galaxy's major axis (Maragkoudakis *et al.* 2018) and applied to the integrated Hα emission of the galaxy. This can introduce scatter because star formation usually appears to be patchy, and not smoothly distributed in the galaxy volume (e.g. Figure 2.3). Therefore, the regions used to measure the [N II]/Hα ratio may not fully represent the conditions in the rest of the galaxy, especially if there are large star-forming regions not encompassed by the spectral extraction regions.

As the cost of spectral observations is usually higher compared to imaging, it is common to lack measurements of the Balmer decrement or the [N II]/Hα ratio. At the same time, Hβ imaging observations require around nine times longer exposure time compared to Hα, in order to obtain observations of similar signal-to-noise ratio. Also, there is not always available photometric coverage in FIR and FUV bands which are required for the IRX extinction and for SED fits. However, Hα imaging is one of the easiest ways to retrieve the SFR of a local Universe galaxy and certainly the closest to the instantaneous SFR. Therefore, it is useful to calibrate the SFR inferred from the Hα luminosity uncorrected for extinction or the [N II]-lines contribution. Table 2.3 gives the correlations of the Hα-based SFR with $\mathrm{SFR_{tot}}$ for all combinations of the above-

mentioned corrections. These calibrations can be used with Equation 2.15 to estimate the total SFR, depending on the availability of extinction, and [N II] measurements.

2.5.2 8 μm emission as SFR indicator

In Figure 2.11 we explore the calibrations of SFRs derived through PAH emission (Section 2.4.2), $\mathrm{SFR_{tot}}$, and $\mathrm{SFR_{H\alpha}}$. The comparison with $\mathrm{SFR_{tot}}$ shows on average excellent agreement (linear regression fit intercept $a = -0.02 \pm 0.02$, and slope $b = 0.01 \pm 0.02$). However, the colour-coding of the points in Figure 2.11 reveals that high sSFR galaxies deviate from this agreement. This phenomenon occurs in both ends of high or low SFRs, and stellar masses. In the regime of low SFRs, the difference with $\mathrm{SFR_{tot}}$ is due to the fact that these galaxies are dust-deficient, and thus PAH-deficient, while $\mathrm{SFR_{tot}}$ is also traced by the UV emission. On the other hand, the large optical depth in the most luminous IR galaxies (LIRGs) with high SFR, causes extinction to the 8 μm emission.

The comparison with Hα-based SFRs shows a good agreement on average. However, the 8 μm PAHs emission tends to underestimate the SFR in low-SFR galaxies (linear regression fit intercept $a = -0.01 \pm 0.03$, and slope $b = -0.15 \pm 0.04$). As revealed from colour-coding in the bottom panel of Figure 2.11 based on their metallicity, this deviation is mainly driven from low SFR galaxies that have lower than average abundance of metals.

2.5.3 SFRs through SEDs

The SED derived SFRs are considered to be very close to the true SFRs because they model the galaxies' emission using photometric information in a wide range of wavelengths, and explicitly accounting for the effects of extinction. The comparison with $\mathrm{SFR_{tot}}$ (Figure 2.12) shows an overall quite good agreement, which is excellent for $\mathrm{SFR} > 1\ \mathrm{M_{\odot}\,yr^{-1}}$. In this range of SFRs the scatter is minimized. However, in the regime of low SFRs the comparison shows significantly increased dispersion. We attribute this to spatial variations in the age of the stellar populations within the galaxy. As a result, different regions may dominate the emission in different wavelengths, an effect that cannot be taken into account effectively in an SED analysis framework (although some efforts in this direction have been made; da Cunha *et al.* 2008). This effect becomes more important for low-SFR and small-sized galaxies, the IR luminosity of which may be dominated by a few individual star-forming regions, while their optical, NIR, and UV emission may arise from other regions regions hosting older (and less obscured) populations.

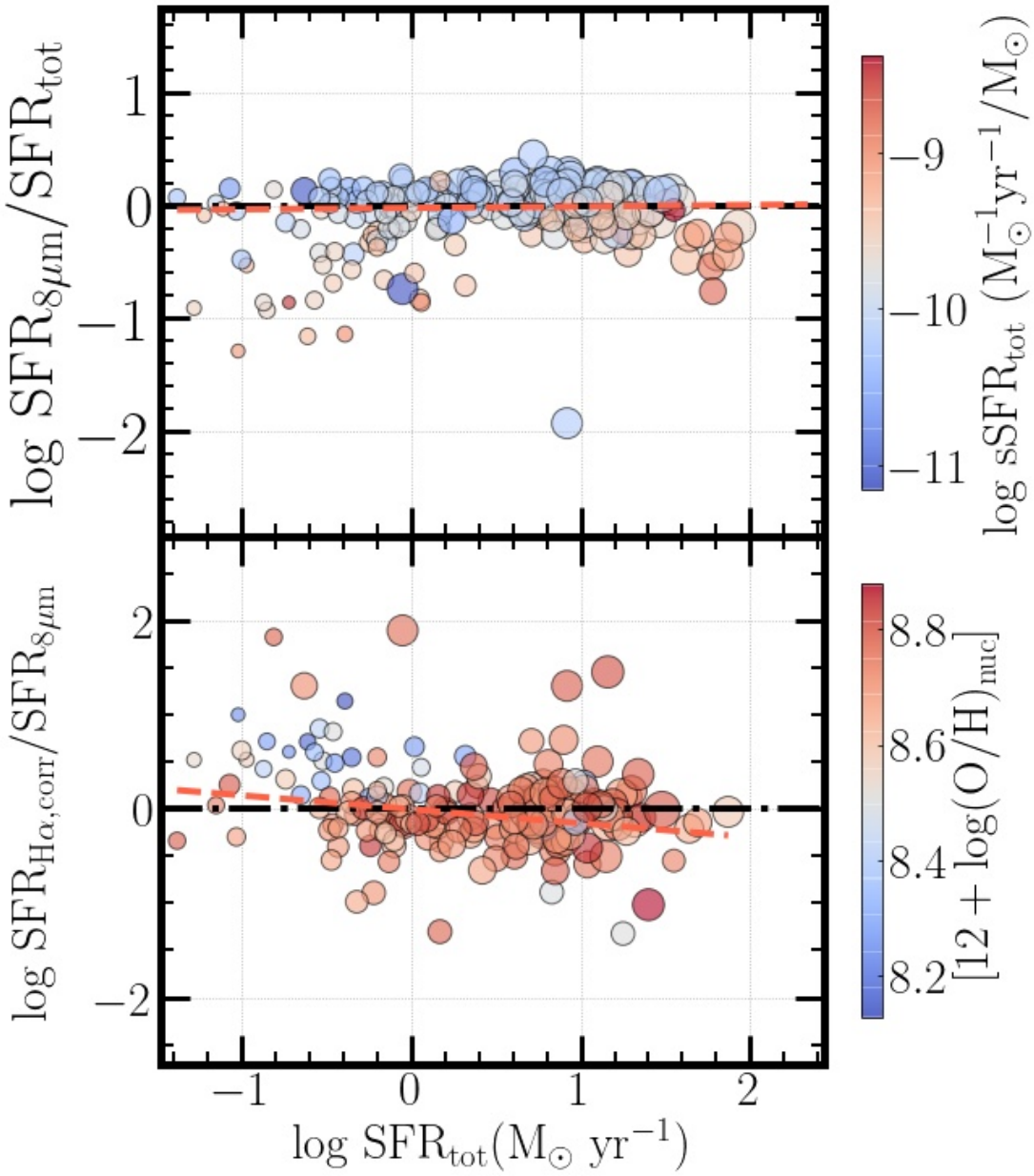

Figure 2.11: Top: $SFR_{8\ \mu m}$ to SFR_{tot} as a function of SFR_{tot}. Galaxies are colour-coded based on the logarithm of sSFR. Bottom: $SFR_{H\alpha}$ to $SFR_{8\ \mu m}$ as a function of SFR_{tot}. Galaxies are colour-coded based on their metallicity. In both panels the black dashed line represents equality, and the red line a linear regression fit. The size of points is a function of their stellar mass.

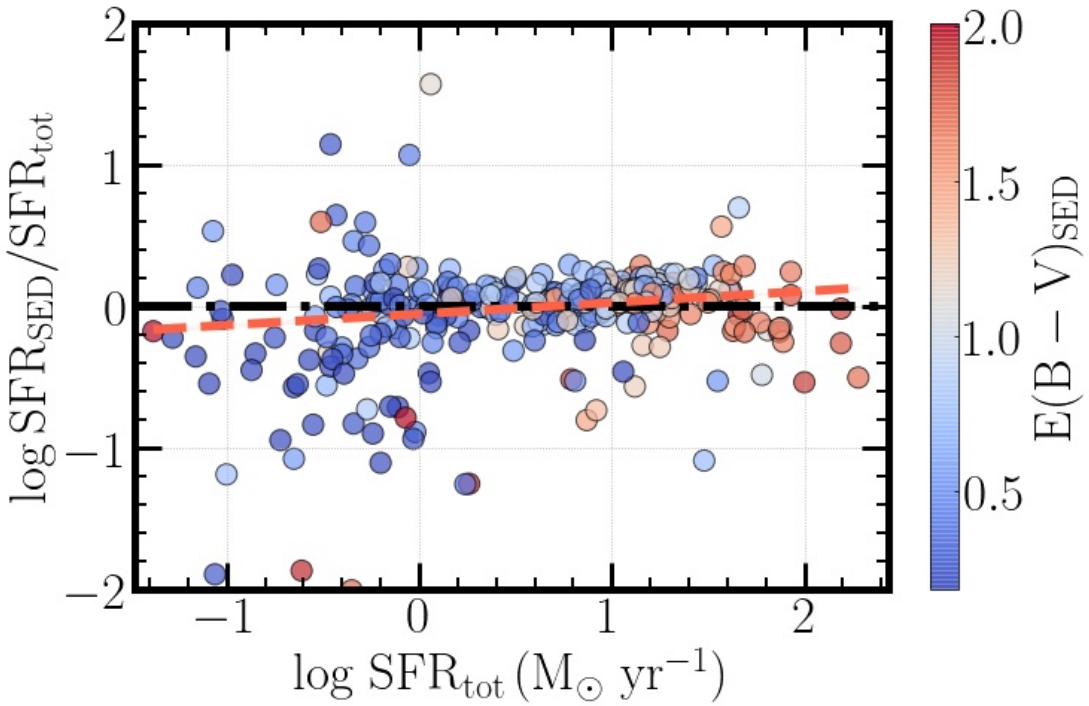

Figure 2.12: The logarithm of the SFR_{SED} to SFR_{tot} as a function of SFR_{tot}. The points are colour-coded based on the Balmer decrement extinction. The red dashed lines represent their linear regression fit. The black dashed-dotted line represent the equality.

2.5.4 SFRs through hybrid indicators

The hybrid 24 μm + Hα SFRs show an excellent agreement with the FIR + FUV emission based SFR (Figure 2.9). This agreement is not significantly affected by the [N II] contribution, due to a combination of two effects: a) the [N II]/Hα ratio is correlated with SFR (Figure 2.10) with the [N II] contribution being relatively lower in low SFRs, and b) the Hα / 24 μm flux ratio is decreasing for increasing SFRs. These effects cancel out resulting to a flat slope in both the linear fits. However, the average [N II] contribution increases the SFR measurements by $\sim$ 0.1 dex (Table 2.4). Overall, the hybrid 24 μm + Hα SFR is an excellent alternative to the FIR + FUV, even when it is not possible to correct for the contribution of the [N II] emission.

The hybrid 8 μm + Hα SFRs show a good agreement with SFR_{tot} (Figure 2.9), but this indicator tends to underestimate the SFR in the high SFR regime. As discussed in Section 2.5.2, this is caused by the fact that the 8 μm emission can be attenuated in extremely optically thick galaxies. Indeed, as shown in Figure 2.9, the objects that show the strongest deficit in 8 μm emission are also characterized by large values of extinction. Similarly to the 24 μm + Hα SFR indicator, the lack of [N II] correction is causing an

on average increase of ~ 0.1 dex in the SFR measurements.

2.5.5 Radio emission as SFR indicator

The 1.4 GHz radio continuum emission traces synchrotron emission produced by the interaction of relativistic electrons and cosmic rays produced in supernovae remnants (SNR) with the galactic magnetic field. The synchrotron cooling timescale for cosmic-ray electrons is of the order of $\sim$50 Myr depending on the underlying magnetic field, while the inverse Compton timescale is much shorter ($\sim 10^5$ yr) for the intense fields in highly star-forming galaxies (e.g. Lacki *et al.* 2010). Therefore, although the radio emission can be sensitive to the intensity of the stellar radiation fields (through the inverse-Compton losses), it traces timescales similar, or shorter, to the lifetimes of massive stars, hence, it probes similar stellar populations as the Hα emission. In addition, it has the benefit that it is not affected by extinction, and it gives a complementary view of star-formation, because it probes different processes than those producing the IR and 24 μm (heated dust), or the Hα emission (gas ionized by UV).

In Figure 2.13 we compare the $L_{1.4\,\mathrm{GHz}}$ for the SFRS sample (Mahajan *et al.* 2019) with the extinction corrected (by the Balmer indicator) $L_{\mathrm{H}\alpha}$ also corrected for the [N II] contribution (left panel), and the L_{FIR} (right panel). Many studies have shown a tight correlation between radio and infrared luminosities (e.g. Condon 1992; Blain *et al.* 1999; Flores *et al.* 1999; Bell 2003). Similarly a tight correlation is found for the SFRS sample where a linear regression fit between $L_{1.4\,\mathrm{GHz}}$ and L_{FIR} shows excellent agreement: $\log L_{1.4\,\mathrm{GHz}}$ (W Hz^{-1}) $= (-17.37 \pm 0.49) + (0.96 \pm 0.01) \log L_{\mathrm{FIR}}$ (erg s^{-1}), with scatter [$\delta(\log \frac{L_{1.4\,\mathrm{GHz}}}{L_{\mathrm{FIR}}}) = 0.34$]. The comparison between $L_{1.4\,\mathrm{GHz}}$ and $L_{\mathrm{H}\alpha}$ shows a slightly non-linear relation [linear regression fit: $\log L_{1.4\,\mathrm{GHz}}$ (W Hz^{-1}) $= (-15.63 \pm 1.41) + (0.9 \pm 0.03) \log L_{\mathrm{H}\alpha}$ (erg s^{-1})] and larger scatter [$\delta(\log \frac{L_{1.4\,\mathrm{GHz}}}{L_{\mathrm{H}\alpha}}) = 0.5$].

As it has been discussed in Bell (2003) the linearity and tightness in the FIR-radio correlation can be considered as a conspiracy. The FIR emission fails to trace star formation in low-luminosity dust-deficient galaxies, while in the more massive (and generally higher metallicity) galaxies it can be partially biased by contribution from older stellar populations. The radio emission also underestimates star formation in faint galaxies due to decreased non-thermal radio emission efficiency in these objects.

In fact, a non-linear relation between $L_{1.4\,\mathrm{GHz}}$ and SFR has been proposed to account for the reduced 1.4 GHz luminosity in lower SFR galaxies. This has been attributed to either cosmic ray escape losses at low SFRs (e.g. Chi & Wolfendale 1990; Bell 2003; Lacki *et al.* 2010), or possibly stronger magnetic fields in higher SFR galaxies (e.g. Tabatabaei *et al.* 2017). Davies *et al.* (2017) report a relation of the form SFR $\propto L^{\gamma}_{1.4\ \mathrm{GHz}}$ with

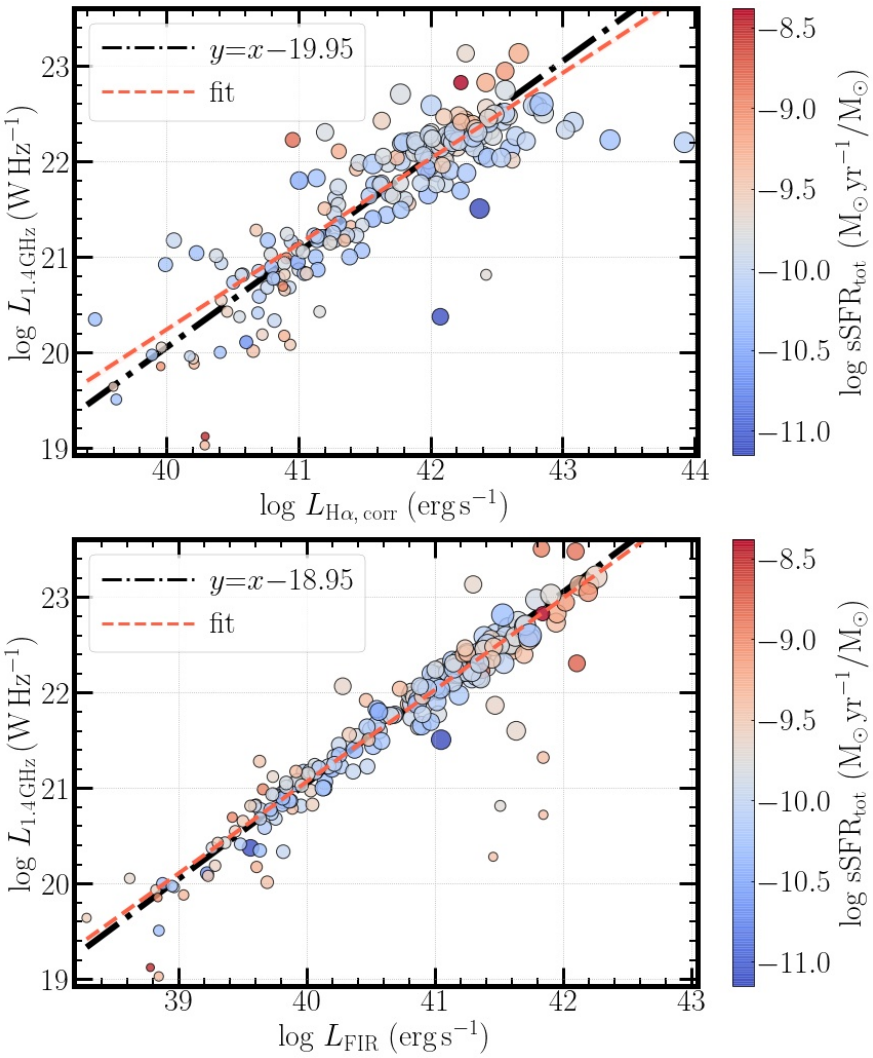

Figure 2.13: The logarithm of the $L_{1.4\ \mathrm{GHz}}$ (W Hz^{-1}) as a function of the free from [N II] contribution, corrected by the Balmer extinction $L_{\mathrm{H}\alpha}$ (erg s^{-1}) (top panel), and as a function of the L_{FIR} (erg s^{-1}) (bottom panel). Points are colour-coded based on their sSFR calculated with SFR$_{\mathrm{tot}}$, and size-coded based on their stellar mass. The red dashed line represent a linear regression fit, and the black dashed-dotted line shows a linear correlation for reference.

$\gamma = 0.75$. However, other studies have found a plethora of values for γ, ranging e.g. between 0.77 to 1.06 (Price & Duric 1992) depending on the sample, and on the reference SFR indicator (e.g. Davies *et al.* 2017). Combining Eq. 2.9 and the results of the linear regression fit between $L_{1.4\,\mathrm{GHz}}$ and $L_{\mathrm{H}\alpha}$ we find a conversion to SFR:

$$\frac{\mathrm{SFR}_{1.4\ \mathrm{GHz}}}{\mathrm{M}_\odot\,\mathrm{yr}^{-1}} = 1.2\times\ 10^{-24}\left(\frac{L_{1.4\ \mathrm{GHz}}}{\mathrm{W\ Hz}^{-1}}\right)^{1.11\pm0.03} \tag{2.18}$$

The power index of this relation is higher compared to other studies. Following Kennicutt *et al.* (2009), we calibrate the composite SFR indicator combining the radio 1.4 GHz, and the raw Hα luminosities. In Figure 2.14 we show the best fit for the combined Hα and 1.4 GHz luminosities, compared to $L_{\mathrm{H}\alpha}$ corrected for extinction. Combining with Eq. 2.9 we find:

$$\frac{\mathrm{SFR}}{\mathrm{M}_\odot\,\mathrm{yr}^{-1}} = 10^{-41.27}\left[\frac{L_{\mathrm{H}\alpha,\mathrm{obs}}}{\mathrm{erg\ s}^{-1}} + 3.35\ 10^{-17}\left(\frac{L_{1.4\ \mathrm{GHz}}}{\mathrm{W\ Hz}^{-1}}\right)^{1.11}\right] \tag{2.19}$$

The scatter in both correlations (Figures 2.13, 2.14) is probably driven by the large dispersion of points in the Hα-based SFRs (Section 2.5.1). The flatter slope in the SFR–$L_{1.4\ \mathrm{GHz}}$ relation could be due to increased inverse Compton losses at the most intense starburst galaxies, or more likely, to the underestimation of the true SFR at the most actively star-forming galaxies (Section 2.4.4) in combination with differences in the considered samples.

In Figure 2.15 we further investigate the increased dispersion in the radio-Hα relation. We have separated galaxies in bins of stellar mass, and we plot linear regression fits of the radio-Hα luminosity ratio as a function of sSFR. We find that lower-mass galaxies ($\log M_\star/\mathrm{M}_\odot < 9.5$) have on average a deficit of radio emission compared to the average of star-forming galaxies. This indicates that these galaxies show a deficit in their radio emission with respect to their SFR. Also, the flat slope found for these low-stellar-mass galaxies indicates that this deficit is independent of the sSFR. This can be attributed to two mechanisms: a) weak gravitation field in these galaxies results in higher escape fraction of relativistic electrons that contribute to the radio emission. The fact that the $L_{\mathrm{H}\alpha}/L_{1.4\ \mathrm{GHz}}$ ratio is independent of the sSFR indicates that the effect of losses dominates over the energetic particle production of the star-forming activity. b) dwarf galaxies do not have well formed spiral arms and disk, thus the integrated magnetic field density is weaker (e.g. Graur *et al.* 2017).

However, for larger galaxies ($\log M_\star/\mathrm{M}_\odot > 9.5$) the radio-Hα luminosity ratio is

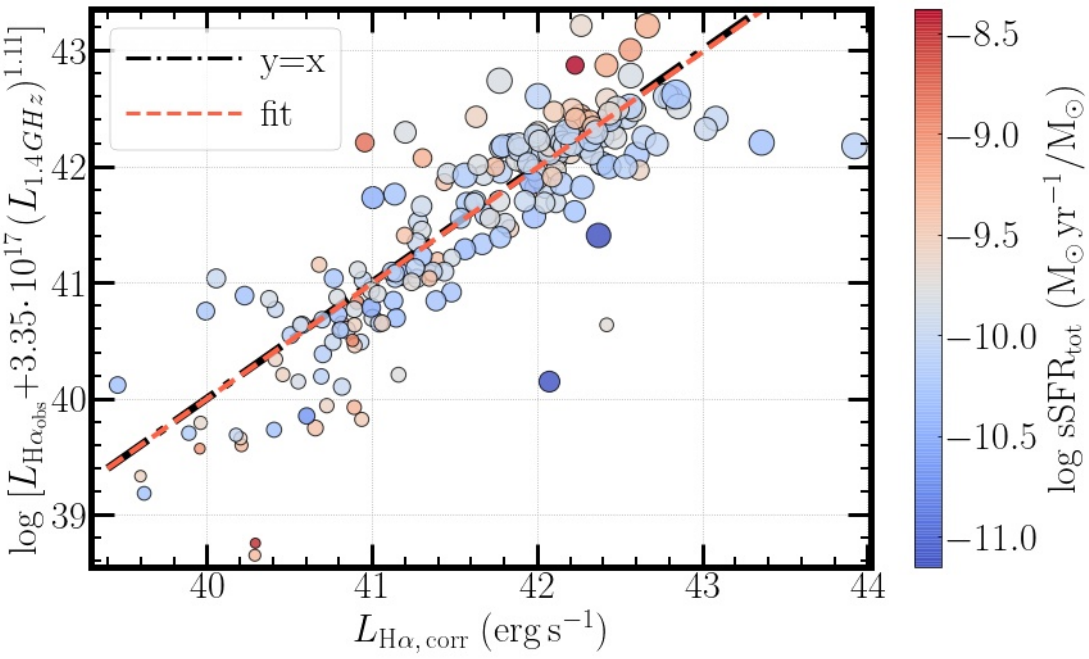

Figure 2.14: Combined observed Hα luminosity (corrected for the [N II] contribution) with the radio 1.GHz luminosity as a function of the corrected for extinction and the [N II] contribution Hα luminosity. Points are colour-coded based on their sSFR, and size-coded based on their stellar-mass. The black dashed-doted line, and the red dashed line represent the equality and a linear regression fit respectively.

found to depend on the sSFR (which can be considered as a proxy of their average stellar population age). The slope is increasing for increasing stellar mass bin. In these galaxies the gravitational field is strong enough to retain a higher percentage of the radiating relativistic electrons resulting in higher radio luminosity.

2.5.6 Metallicity and extinction

Given that the dust is composed by metals, one would expect a relation between metallicity and extinction. In fact such a positive correlation has been reported in previous studies (e.g. Boquien *et al.* 2009; Theios *et al.* 2019), although they show significant scatter.

Maragkoudakis *et al.* (2018) measured the nuclear metallicities for all star-forming galaxies in the SFRS sample. For the galaxies with available long-slit spectra, Maragkoudakis *et al.* (2018) also provided metallicities for the host galaxy from large aperture extractions encompassing the major axis of the galaxy. We adopted these metallicities

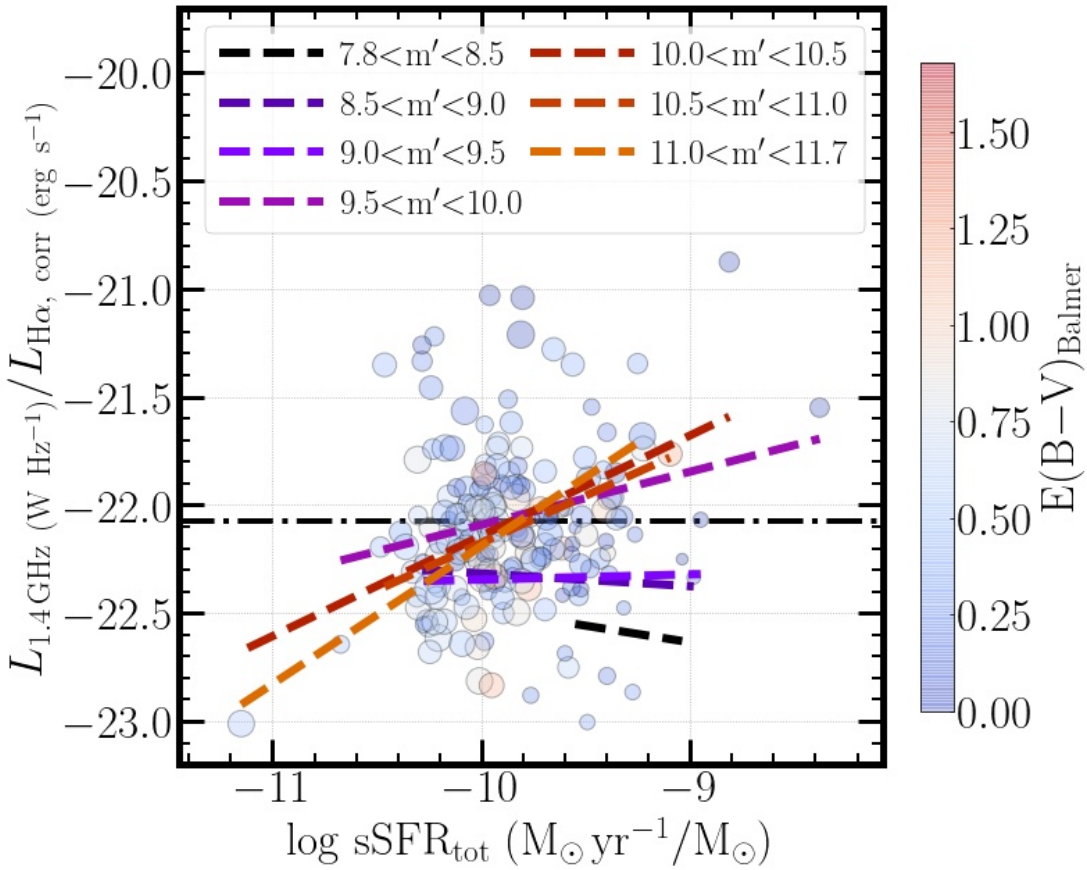

Figure 2.15: The ratio of the radio to Hα luminosity as a function of sSFR based on $\mathrm{SFR_{tot}}$. Points are colour-coded based on their extinction, and size-coded based on their stellar mass. Dashed lines represent linear regression fits of galaxies separated in different bins of stellar mass, as indicated in legend, where $\mathrm{m}' = \log(M_\star/\mathrm{M}_\odot)$. The black dashed dotted line represents the median luminosity ratio of the SFRS galaxies.

calculated through the O3N2 calibration provided by Pettini & Pagel (2004):

$$[12 + \log(\mathrm{O/H})] = 8.73 - 0.32 \times \mathrm{O3N2} \tag{2.20}$$

where

$$\mathrm{O3N2} = \log \frac{f_{[\mathrm{O\,III}]\lambda\,5007}/f_{\mathrm{H}\beta\lambda\,4863}}{f_{[\mathrm{N\,II}]\lambda\,6583}/f_{\mathrm{H}\alpha\lambda\,6563}} \tag{2.21}$$

and f corresponds to each emission-line flux.

The metallicities of the SFRS galaxies range from sub-solar to slightly hyper-solar

values ($8.1 \lesssim [12 + \log(\mathrm{O/H})_{\mathrm{nuc}}] \lesssim 9$) having continuous coverage in between (Figure 2.17). The selection of the SFRS galaxies was blind to metallicity, thus the SFRS was not designed to fully represent the distribution of nearby galaxies metallicity. However, it does give a good representation of the metallicity distribution of the star-forming galaxies in the local Universe.

In Figure 2.16 we present the SFRS galaxies metallicities as a function of their extinction, the latter as calculated from the Balmer decrement and IRX. We only consider metallicities derived from the nuclear region, because the sample with metallicities from a larger region is much smaller and biased to higher metallicity galaxies (Figure 2.17). Nonetheless, these are indicative of the average metallicities and can be used to derive general correlations. Furthermore, this is a fair comparison with the Balmer decrement based extinctions which are derived from the same spectra. The points are colour-coded based on their log $\mathrm{sSFR_{tot}}$, and size-coded based on the logarithm of their stellar mass. This comparison involves a sample of 256 SFRS galaxies with nuclear metallicities (see Maragkoudakis *et al.* 2018, for more details).

The nuclear-region metallicities of the SFRS galaxies show a non-linear behavior with respect to extinction. Galaxies with low extinction are strongly correlated with low metallicities predominantly low-mass dwarf galaxies, while galaxies with extinction higher than $\mathrm{E(B-V)_{Balmer}} \gtrsim 0.5$ have converged to the peak average metallicity of our epoch $[12+\log(\mathrm{O/H})_{\mathrm{nuc}}] \simeq 8.75$. This behavior is the same for both the Balmer and IRX extinction indicators, although the range of E(B-V) is different. The latter, indicates that this correlation is an effect related to the general dust component in the ISM, rather than the dust in the birth clouds (Section 2.5.1).

This correlation can be described by a functional form similar to that presented for the mass-metallicity relation by Curti *et al.* (2020):

$$[12 + \log(\mathrm{O/H})] = Z_0 + \log(1 - 10^{-\frac{E}{E_0}^{\gamma}}) \tag{2.22}$$

where: E is the extinction, Z_0 is the asymptotic value of the metallicity after converging to the linear part of the correlation, and E_0 is the extinction at the turn-over of the relation. This model was fitted with a MCMC using the `Python emcee` package (Foreman-Mackey *et al.* 2013a). The best-fit results for the different extinction indicators are given in Table 2.5.

This correlation describes the co-evolution of extinction and metallicity in galaxies. Unsurprisingly, we also see a trend for low-mass galaxies to have lower metallicity and extinction. This is the result of the well-studied mass-metallicity relation (e.g. Lequeux

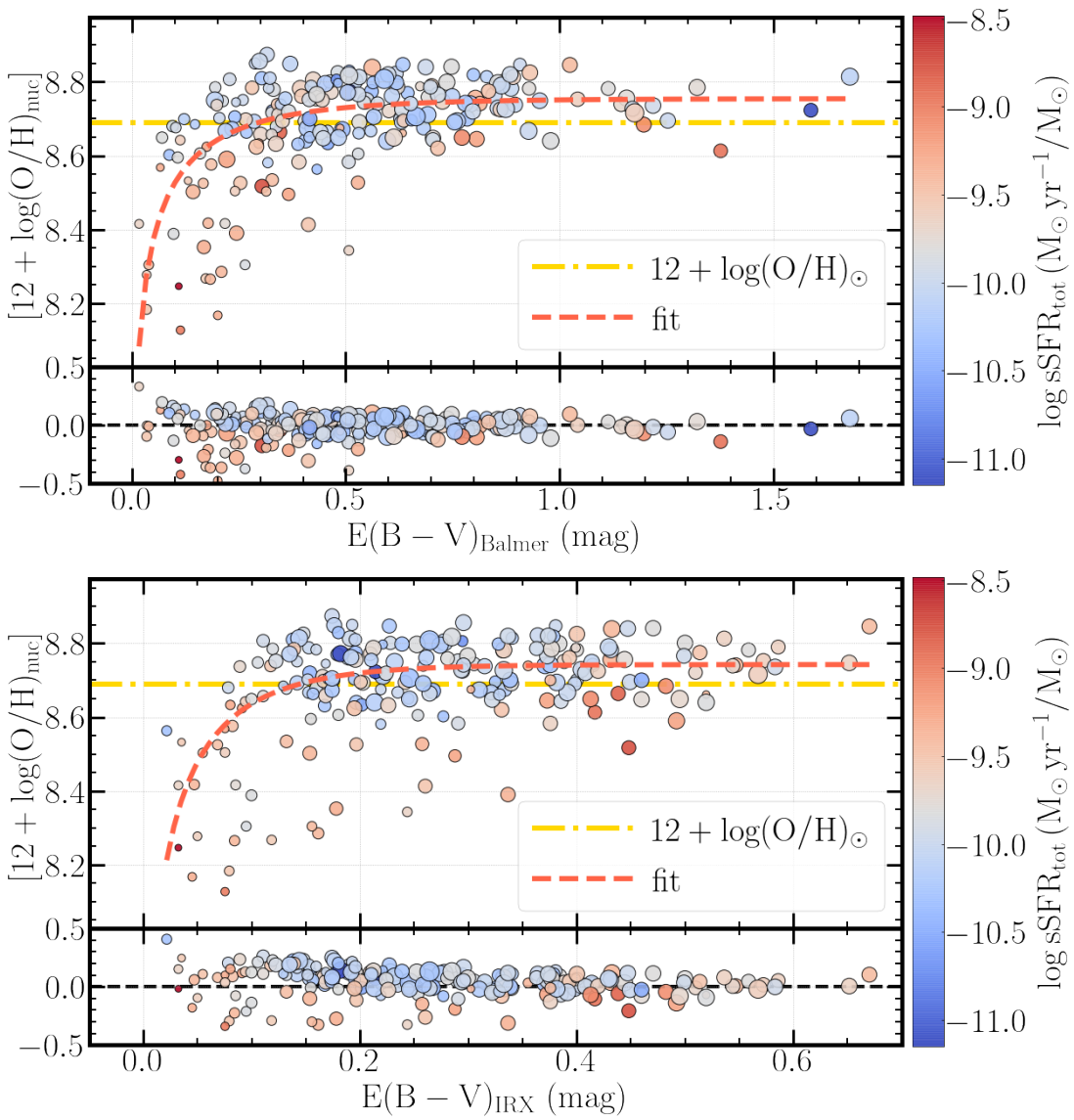

Figure 2.16: Metallicity of the SFRS galaxies as a function of their extinction. The top panel uses the Balmer decrement for the calculation of the extinction, while the bottom panel uses the IRX. The points are color-coded depending on their sSFR, while their size reflects the logarithm of the stellar mass of the galaxies (larger points indicate larger mass). The yellow dashed-dotted line indicates the solar metallicity. The best-fit relation is shown by a red dashed curve. The subplot at the bottom of each plot represent the fit residuals.

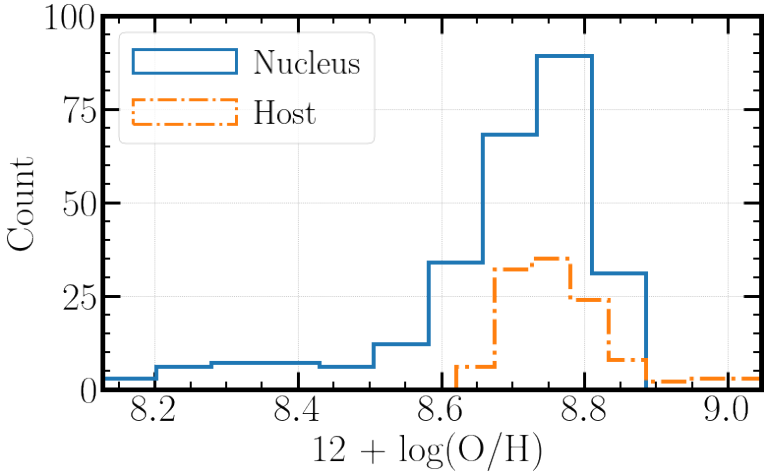

Figure 2.17: The distribution of metallicities [12 + log(O/H)] for the host and nucleus of SFRS galaxies (Maragkoudakis *et al.* 2018) with blue continuous and orange dashed-dotted lines respectively.

et al. 1979; Tremonti *et al.* 2004; Somerville & Davé 2015; Curti *et al.* 2020), which reflects the fact that low-mass galaxies have yet to build their stellar component and hence the metal content of their ISM. Therefore, the power component in Equation 2.22 describes the correlation between extinction and metallicity for the young galaxies that are still in the process of building up their stellar mass as well as their dust component. However, intermediate and larger galaxies, have already reached the average peak metallicity of our epoch, and as a result they have increased dust mass, resulting in higher extinction.

Equation 2.22 describes quite well the correlation as seen from the residuals plot. However, there is a group of points between $0 < \mathrm{E(B-V)} < 0.5$ that tends to deviate from this relation. This group of points (best seen in the residuals plot at the bottom panels of Figure 2.16) share the common characteristic of being dwarf highly star-forming galaxies (sSFR $\gtrsim 10^{-9.5}\,\mathrm{M_{\odot}yr^{-1}/M_{\odot}}$). In dwarf galaxies experiencing intense star-formation, the bulk of the Hα emission is expected to originate from individual star-formation sites rather than their main body. Therefore, the measured extinction reflects attenuation by dust in the birth clouds rather than the general ISM. Although these galaxies have lower overall dust content, the larger optical depth towards these sites of star-formation results in higher measured extinction. This deviation can be attributed to two reasons: (a) attenuation by dust in the birth clouds rather than in the general ISM; (b) these galaxies are relatively small in size, resulting in larger coverage of the star-forming regions by the general ISM (Section 2.5.1). The latter is also supported by the fact that, with the use of the IRX extinction indicator (that reflect emission from

Table 2.5: Parameters for Eq. 2.22 describing the correlation between extinction and metallicity.

Extinction indicator	Z_0	E_0	γ
Balmer	$8.803^{+0.022}_{-0.028}$	$0.993^{+0.342}_{-0.324}$	$0.506^{+0.060}_{-0.043}$
IRX	$8.766^{+0.029}_{-0.025}$	$0.312^{+0.144}_{-0.085}$	$0.683^{+0.114}_{-0.096}$
SED	$8.714^{+0.013}_{-0.012}$	$0.164^{+0.030}_{-0.023}$	$1.043^{+0.173}_{-0.156}$

the full body of the galaxy, and not only the nuclear region) these galaxies show even larger differences with respect to the overall relation.

2.6 Summary

Through the use of a representative sample of local Universe star-forming galaxies we:

1. provide Hα photometry for the SFRS galaxies
2. provide calibrations of Hα-based SFRs with the $\mathrm{SFR_{tot}}$ using extinction corrections based on the Balmer decrement, IRX, and SED fits, as well as corrections for the contribution of the [N II] emission.
3. compare the hybrid indicators of the 24 μm + Hα, 8 μm + Hα and FIR + FUV, where we find good agreement.
4. compare SFRs derived through SED fits which show excellent agreement with the SFRs based on FIR + FUV emission for SFR $\gtrsim 1\mathrm{M_\odot\,yr^{-1}}$ and increased scatter for lower SFR.
5. find that the extinction based on the Balmer decrement is about two times larger than those derived from the IRX or the SED fits (`dustatt_modified_starburst` attenuation module), while the IRX is very close with the extinction estimated by the SED fits.
6. find that the power in the calibration of the radio 1.4 GHz emission and SFR is different using as a reference the Hα-based SFRs. We find that the scatter in the comparison between $\mathrm{SFR_{1.4\ GHz}}$ and $\mathrm{SFR_{tot}}$ is minimal, while there is large scatter with the $\mathrm{SFR_{H\alpha}}$.
7. suggest that the difference between the Balmer decrement and IRX extinction is based on the fact that the former traces emission of younger stellar populations, and that it is more sensitive to the attenuation caused by the dust in the birth clouds.

8. provide a function that describes the correlation between the nuclear-region metallicity with the IRX and Balmer extinction for a wide range of metallicity and extinction.
9. we show that galaxies deviating from the latter relation are mainly dwarf, highly star-forming galaxies, where a large part of the overall attenuation is attributed to the dust at the birth clouds rather than that in the general ISM.

Acknowledgements

K. K. would like to thank Ioanna Leonidaki, Maria Kopsacheili, Jeff Andrews, John Kypriotakis, Elias Kyritis, Grigoris Maravelias, Tasos Kougentakis, Anna Steiakaki, and Vaggelis Pantoulas for assisting with the Hα observations. K. K., and A. Z. acknowledge funding from the European Research Council under the European Union's Seventh Framework Programme (FP/2007-2013)/ERC Grant Agreement n. 617001 (A-BINGOS). This project has received funding from the European Union's Horizon 2020 research and innovation programme under the Marie Sklodowska-Curie RISE action, grant agreement No 691164 (ASTROSTAT). A. Z. also acknowledges support from *Chandra* grant G02-3111X.

DATA AVAILABILITY

The data underlying this article are available in the article and in its online supplementary material.

This page intentionally left blank

3

X-ray luminosity sub-galactic scaling relations

3.1 Introduction

Star formation throughout cosmic time has transformed the Universe. Among other things, it has illuminated it and has created the foundations for more complex forms to exist. When considered on kpc scales, star formation has shaped the phenomenology of galaxies. Two of the most fundamental characteristics of galaxies are the stellar mass ($M_\star$; past star formation) and the current/recent star formation, measured by the star-formation rate (SFR). There is a strong correlation between galaxies' stellar masses and SFRs, i.e., the galactic main sequence (e.g., Noeske *et al.* 2007; Elbaz *et al.* 2007; Daddi *et al.* 2007).

Studies on sub-galactic scales can show to what extent local conditions are responsible for global scaling relations (e.g., Maragkoudakis *et al.* 2017; Enia *et al.* 2020). Comparisons on sub-galactic scales among galaxies of different types, star-formation histories (SFH), and metallicities show great differences (e.g., Boquien *et al.* 2014) because star formation is not homogeneously dispersed in the galactic volume (e.g., Larson *et al.* 2020).

X-rays probe recent and past star-formation activity and are particularly useful for characterizing star formation in obscured environments. X-ray binaries (XRBs) in

particular provide a means to quantify the numbers of stellar remnants (neutron stars and black holes) otherwise hidden from view. XRBs are formed when a donor star provides mass to a compact object to which it is gravitationally bound. The mass transfer can be via Roche lobe overflow or stellar wind, and either way, the accreting mass radiates at X-ray wavelengths. Donor stars can be high-mass OB stars or low-mass stars. Based on their donor stars, systems are described as either high-mass X-ray binaries (HMXBs) or low-mass X-ray binaries (LMXBs). Collectively, the X-ray emission from all the XRBs hosted in a galaxy shows strong correlations with galaxy-wide characteristics such as SFR and stellar mass. Specifically, LMXB X-ray emission correlates strongly with stellar mass (e.g., Gilfanov 2004; Lehmer *et al.* 2010; Boroson *et al.* 2011; Zhang *et al.* 2012), and HMXB X-ray emission correlates with SFR (e.g., Grimm *et al.* 2003; Ranalli *et al.* 2003; Mineo *et al.* 2012a,b, 2014).

Recently there have been efforts to examine the L_X–SFR–$M_\star$ correlations down to sub-galactic scales in the nearby Universe. The ratio of XRBs' X-ray output to visible luminosity varies significantly when examined on small physical scales. This is witnessed by explorations of the X-ray luminosity of individual regions of a few nearby galaxies (e.g., Anastasopoulou *et al.* 2019) and by investigations of the X-ray luminosity functions of XRBs associated with stellar populations of different ages or metallicities (e.g., Lehmer *et al.* 2019).

A complication in understanding the correlation between XRBs and SFR is that there are multiple SFR indicators based on different physical mechanisms. Indicators include 1.4 GHz emission from sychrotron radiation of relativistic electrons accelerated in supernovae remnants, absorbed ultraviolet (UV) radiation heating galactic dust and being re-emitted at 24 μm and in the far infrared, UV from high mass stars' photospheres, emission lines from atomic gases ionized by OB stars, polycyclic aromatic hydrocarbons (PAHs) emitting from the surrounding photo-dissociation regions, etc. This results in differences between the different SFR indicators that multiple galaxy-wide studies have tried to calibrate (e.g., SFRS; Mahajan *et al.* 2019). The different SFR indicators probe stellar populations of different ages (e.g., Kennicutt & Evans 2012) with the ones from ionized atomic gases probing the most recent (e.g., Boquien *et al.* 2014; Cerviño *et al.* 2016).

X-ray emission is considered an emerging SFR indicator, but the correlations still suffer from stochastic and calibration effects. These effects, which are detected in galaxy-wide correlations, are increased when examined on sub-galactic scales because star formation is a local event and hence is diluted on the surface of a galaxy. Theoretical models predict X-ray luminosity variations from different stellar populations (e.g., Fabbiano

et al. 2001; Mapelli *et al.* 2009, 2010). XRB population synthesis models show that the bulk of the X-ray output originating from XRBs is short lived ($\leq$20 Myr) because that the emission from HMXBs is orders of magnitude higher than that of LMXBs (e.g., Fragos *et al.* 2013a). Therefore, in order to understand how biases arise in the X-ray luminosity, SFR, and stellar-mass correlations, it is important to examine the correlations on sub-galactic scales and with different SFR indicators.

Sample selection can bias our interpretation and measurement of the aforementioned correlations. For example, Mineo *et al.* (2014, hereafter M14) studied the L_X–SFR scaling relation for a small sample of star-forming galaxies. Gilfanov (2004) and Boroson *et al.* (2011) studied the L_X–$M_\star$ relation for samples of early type galaxies. Lehmer *et al.* (2010) introduced an L_X–SFR–$M_\star$ scaling relation that accounts for the contribution of HMXBs (scaling with SFR) and LMXBs (scaling with stellar mass) based on samples of local as well as higher-redshift galaxies. This analysis used a sample of nearby galaxies with a large range and mix of stellar masses and SFRs.

This paper's goal is to estimate the effect different star-forming conditions and SFHs (along with the fact that different SFR indicators probe different time-scales) may induce in the correlation and to measure the scatter in each case. The paper is organized as follows: Section 3.2 describes the sample of galaxies, the data/observations, and the data reduction. Section 3.3 describes how sub-galactic analysis was performed. The maximum likelihood fits and the results of the analysis are described in Section 3.4. The results of the analysis are discussed in Section 3.5, and the summary is in Section 3.6.

3.2 Sample selection and observations

3.2.1 Sample

Our galaxy sample is based on the Star Formation Reference Survey (SFRS; Ashby *et al.* 2011). The SFRS is comprised of 369 galaxies that represent all modes of star formation in the local Universe. They fully cover the 3D space of three fundamental galaxy properties: the SFR, indicated by the 60 μm luminosity; the specific SFR (sSFR), indicated by the $K_S - F_{60}$ colour; and the dust temperature, indicated by the FIR (F_{100}/F_{60}) flux density ratio. The SFRS benefits from panchromatic coverage of the electromagnetic spectrum from radio to X-rays, including optical spectra of the galaxy nuclei (Maragkoudakis *et al.* 2017) and Hα imaging (Kouroumpatzakis et al. in prep.). The objective SFRS selection criteria let us put the sample galaxies in context of the local star-forming galaxy population.

The sample used for this work consists of 13 star-forming (non-AGN) SFRS galaxies

(Table 3.2.1) for which there are *Chandra* data of adequate quality to study the X-ray emission down to 1 kpc^2 scales (Table 3.2) available in the archive. The sample galaxies span ∼4 dex in the total SFR and ∼3 dex in sSFR. On sub-galactic scales these ranges become ∼7 dex and ∼8 dex in SFR and sSFR respectively (Fig. 3.1).

Table 3.1: Summary of sample galaxies

SFRS ID	Galaxy	Position (J2000)	D25 ($''$)	Distance (Mpc)	$\log L_{60}$ ($L_\odot$)	$K_S - F_{60}$ (AB mag)	$\frac{F_{100}}{F_{60}}$	Metallicity^a	Axis ratio
86	NGC 3245	10:27:18.41 +28:30:26.6	167	17.8	8.49	1.62	1.60	-	0.52
93	UGC 5720	10:32:31.87 +54:24:03.7	57	24.9	8.94	5.35	1.15	8.89±0.01*	0.74
99	NGC 3353	10:45:22.06 +55:57:39.9	68	18.9	8.67	5.55	1.28	8.30±0.01*	0.75
124	NGC 3656	11:23:38.64 +53:50:31.7	97	42.8	9.12	3.27	2.28	-	0.90
182	NGC 4194	12:14:09.65 +54:31:35.9	92	39.1	10.00	6.04	1.14	8.88±0.01*	0.65
266	NGC 5204	13:29:36.58 +58:25:13.3	159	5.1	7.29	4.20	1.76	8.70±0.03	0.95
300	NGC 5474	14:05:01.42 +53:39:44.4	54	7.2	7.32	3.70	2.45	8.80±0.01	0.97
312	NGC 5585	14:19:48.19 +56:43:45.6	179	8.0	7.33	3.63	2.59	8.41±0.01*	0.87
314	NGC 5584	14:22:23.76 −00:23:15.6	112	26.7	8.67	3.93	2.39	8.74±0.01*	0.79
321	MCG 6-32-070	14:35:18.38 +35:07:07.2	45	126.6	10.07	4.88	2.03	8.71±0.02	0.95
324	NGC 5691	14:37:53.33 −00:23:55.9	89	30.2	8.90	4.37	1.92	8.79±0.01	0.61
334	NGC 5879	15:09:46.78 +57:00:00.8	152	12.4	8.37	3.11	2.76	-	0.93
356	NGC 6090	16:11:40.32 +52:27:23.1	79	132.4	10.47	6.16	1.54	8.72±0.01	0.89

(a) Metallicities measured using the O3N2 diagnostic $\left(\text{based on } \log\frac{[\text{O III}]/\text{H}\beta}{[\text{N II}]/\text{H}\alpha}\right)$ from Maragkoudakis *et al.* (2018).
(*) Metallicities measured from the galaxy's nucleus.

Table 3.2: X-ray data and best-fit model parameters.

SFRS ID	Galaxy	Exp. time (ks)	Detector	Spectral Model	Γ	kT (keV)	$N_{\rm H}$ (10^{22}cm^{-2})
086	NGC 3245	9.6	ACIS-S	power-law + APEC	$2.14^{+0.08}_{-0.00}$*	$0.52^{+0.22}_{-0.22}$	$0.02^{+0.08}_{-0.00}$*
093	UGC 5720	19.2	ACIS-S	power-law + APEC	$2.25^{+0.23}_{-0.23}$	$0.83^{+0.01}_{-0.01}$	$0.01^{+0.01}_{-0.00}$*
099	NGC 3353	17.8	ACIS-S	power-law	$1.42^{+0.18}_{-0.18}$		$0.04^{+0.11}_{-0.00}$*
124	NGC 3656	53.8	ACIS-S	power-law	$3.60^{+1.00}_{-1.00}$		$0.26^{+0.15}_{-0.15}$
182	NGC 4194	35.5	ACIS-S	power-law + APEC	$2.06^{+0.21}_{-0.21}$	$0.36^{+0.07}_{-0.07}$	$0.06^{+0.04}_{-0.04}$
266	NGC 5204	9.8	ACIS-I	power-law	$1.68^{+0.10}_{-0.10}$		$0.05^{+0.04}_{-0.04}$
300	NGC 5474	1.7	ACIS-S	power-law	$1.02^{+0.05}_{-0.05}$		$0.01^{+0.02}_{-0.00}$*
312	NGC 5585	5.3	ACIS-S	power-law	$1.46^{+0.43}_{-0.43}$		$0.15^{+0.17}_{-0.00}$*
314	NGC 5584	7.0	ACIS-S	power-law	$2.41^{+0.40}_{-0.40}$		$0.30^{+0.10}_{-0.00}$*
321	MCG 6-32-070	44.6	ACIS-S	power-law	$2.42^{+0.91}_{-0.55}$		$0.01^{+0.12}_{-0.00}$*
324	NGC 5691	14.9	ACIS-S	power-law	$1.62^{+0.30}_{-0.30}$		$0.06^{+0.08}_{-0.00}$*
334	NGC 5879	89.0	ACIS-I	power-law	$1.53^{+0.15}_{-0.15}$		$0.03^{-0.05}_{-0.00}$*
356	NGC 6090	14.8	ACIS-S	power-law	$3.38^{+0.33}_{-0.33}$		$0.30^{+0.06}_{-0.06}$

(*) Parameter pegged at the low bound.

3.2.2 Hα data

The primary SFR indicator used in this work is Hα emission, which traces gas ionized by stellar populations of ages $\leq$20 Myr (e.g., Murphy *et al.* 2011). Because the formation timescale of HMXBs is typically 10–30 Myr (e.g., Fragos *et al.* 2013a), it is in principle well-matched to SFR probed by Hα emission.

We have obtained Hα observations with the 1.3 m telescope of the Skinakas* observatory. To account for the redshift range of the SFRS sample galaxies, we used a custom-built set of filters centered at $\lambda = 6563, 6595, 6628, 6661, 6694, 6727, 6760$ Å with average FWHM = 45 Å. The exposure time for Hα observations was 1 hour. We also obtained $\sim$10 minute continuum-band exposures with a filter equivalent to SDSS r'. The Hα observations were taken between 2016 and 2019 under photometric conditions and typical seeing $\sim 1''$. Details of the observations and data will be presented by Kouroumpatzakis et al. (in prep).

After the initial reductions (bias subtraction, flat fielding, flux calibration, etc.) the standard continuum subtraction technique was performed, based on the relative flux density of the foreground stars in the continuum and Hα images (e.g., Kennicutt *et al.* 2008). This comparison results in a distribution of Hα/SDSS r' band flux density ratios for the various stars included in each frame. We used the mode of this distribution as the *continuum scaling factor* and its standard deviation as a measure of the uncertainty

* http://skinakas.physics.uoc.gr/

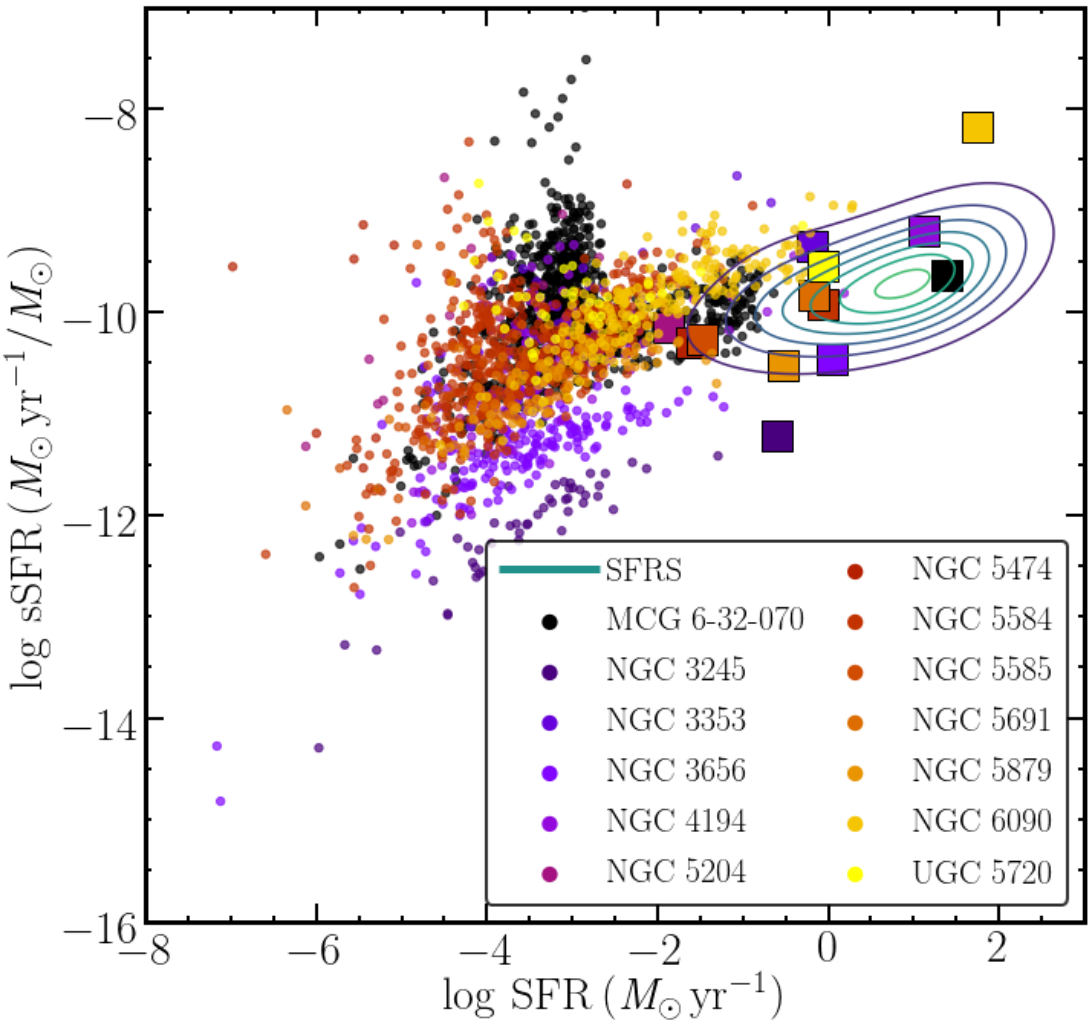

Figure 3.1: The ranges of SFR and sSFR spanned by the sample analysed in this work. Small symbols indicate our Hα-based SFR and 3.6 μm-based stellar mass estimates within $1 \times 1\,\mathrm{kpc}^2$ sub-galactic regions. Squares indicate the integrated emission of the sample galaxies. The data are colour-coded by the galaxy they refer to. The contours indicate the distribution of the complete SFRS.

of this procedure. The rescaled continuum image was subtracted from the Hα image to generate the continuum-subtracted Hα image. In order to minimize the effect of poorly subtracted stars, their residuals were masked. These residuals were usually a result of PSF differences between the narrow band and continuum observations or colour variations arising from the variety of the foreground stars in the observed frames.

A curve of growth (CoG) technique was used to measure the net Hα flux of each galaxy while simultaneously estimating and subtracting the sky background (Fig. 3.2). The background was estimated by performing a linear fit to the last 5% of the CoG. This procedure was repeated iteratively while regulating the background until this part of the CoG was flat. The galaxy aperture size was defined from the point of the CoG that reaches the asymptotic line. The aperture shapes used in our analysis were based on elliptical aperture fits to the *WISE* 4.6 μm data of the SFRS galaxies (following a procedure similar to Jarrett *et al.* 2019), keeping the position angle and ellipticity constant. The photometric calibrations were based on observations of spectrophotometric standard stars (Massey *et al.* 1988). We included a calibration uncertainty in our analysis, estimated from the standard deviation of the standard star's instrumental magnitudes during the observations. The Hα luminosity was converted to SFR with the Murphy *et al.* (2011) conversion:

$$\frac{\mathrm{SFR}_{\mathrm{H}\alpha}}{(\mathrm{M}_\odot\,\mathrm{yr}^{-1})} = 10^{-41.27}\frac{L_{H\alpha}}{(\mathrm{erg\,s}^{-1})} \tag{3.1}$$

3.2.3 Infrared data

In addition to the Hα SFR measure, we used *Spitzer* IRAC non-stellar 8 μm and MIPS 24 μm observations (Ashby *et al.* 2011). 8 μm probes PAH emission, including dust-enshrouded star formation. 24 μm observations probe warm dust heated by UV emission from young stars. These two indicators trace star formation at longer timescales than Hα emission (e.g., Peeters *et al.* 2004; Rieke *et al.* 2009; Kennicutt & Evans 2012). The annuli used for the 8 μm and MIPS 24 μm analysis were the same as the Hα ones. The background was subtracted as measured by an annulus outside the galaxy aperture, accounting for any contribution from foreground stars or background AGN. In the case of the IRAC 8 μm, the stellar continuum was subtracted by rescaling the 3.6 μm images, using the formula from Helou *et al.* (2004):

$$f_{8\mu m,\mathrm{PAH}} = f_{8\mu m} - 0.26\, f_{3.6\mu m} \quad . \tag{3.2}$$

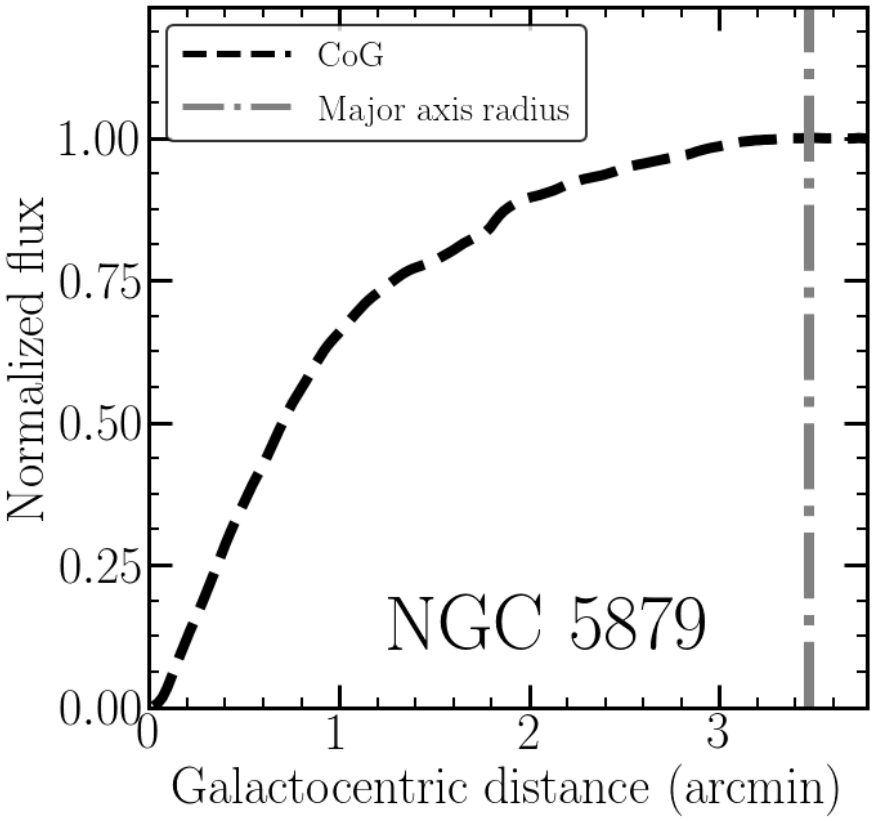

Figure 3.2: Curve of growth (dashed black line) for the Hα flux of galaxy NGC 5879. The normalized integrated flux is shown on the vertical axis, and the galactocentric distance on the horizontal. The semimajor-axis of the aperture, computed following the iterative procedure described in the text, is presented by a dashed-dotted grey line.

Then the non-stellar 8 μm luminosity was converted to SFR using the calibration of Pancoast *et al.* (2010):

$$\frac{\mathrm{SFR}_{8\mu m,\mathrm{PAH}}}{(\mathrm{M}_\odot\,\mathrm{yr}^{-1})} = 6.3 \times 10^{-10} \frac{L_{8\mu m}}{\mathrm{L}_\odot} \quad . \tag{3.3}$$

The MIPS 24 μm luminosity was converted to SFR using the calibration of Rieke *et al.* (2009):.

$$\frac{\mathrm{SFR}_{24\mu\mathrm{m}}}{(\mathrm{M}_\odot\,\mathrm{yr}^{-1})} = 10^{-42.69} \frac{L_{24\mu m}}{(\mathrm{erg\ s}^{-1})} \quad . \tag{3.4}$$

The IRAC 3.6 μm observations were used to estimate total stellar masses. The observed flux density was converted to stellar mass using the Zhu *et al.* (2010) mass-to-

light ratio calibration.

$$\frac{M_\star}{\mathrm{M}_\odot} = 10^{0.23+1.14(g-r)} \frac{\nu L_{\nu 3.6\mu m}}{\mathrm{L}_\odot} \quad . \tag{3.5}$$

where g and r are total galaxy Petrosian AB magnitudes from SDSS DR12 (Alam *et al.* 2015). We used each galaxy's integrated emission $g - r$ colour for all of its sub-galactic regions.

3.2.4 X-ray Data

The *Chandra* data were reduced with `CIAO v.4.9` and *CALDB v.4.7.3*. The raw data were reprocessed in order to apply the latest calibrations and screened for background flares. Then from the clean event files, we extracted images in the full (F: 0.5–8 keV), soft (S: 0.5–2 keV), and hard (H: 2–8 keV) bands and calculated the corresponding monochromatic exposure maps (at energies of 3.8, 1.5, and 3.8 keV respectively).

For each galaxy we also extracted its integrated spectrum using the `CIAO dmextract` command. The extraction aperture was the same as the Hα apertures. Corresponding response and ancillary response files were also calculated with the `CIAO specextract` tool. Background spectra were extracted from source-free regions within each field. The X-ray spectra were fitted with spectral models including power-law, thermal plasma (APEC; Smith *et al.* 2001), and when needed, Gaussian emission-line components. The spectral analysis was performed using `Sherpa v.4.9`. The spectra were binned to have at least 20 counts per bin in order to use the χ^2 statistic. The best-fit model parameters for the integrated spectra of each galaxy are presented in Table 3.2. The details of the spectral analysis will be presented by Sell et al. (in prep.).

The integrated flux of each galaxy was measured by integrating the best-fit spectral models. In order to account for uncertainties in the spectral parameters, the `sample_flux Sherpa` task was used. This task samples model parameters from the covariance matrix of the best-fit model, and for each sample it calculates the corresponding model integrated flux. This yielded the probability density distribution of the model flux and the corresponding uncertainties on the spectral parameters. In addition, for each sample of spectral parameters, the expected number of counts was calculated by folding the model through the ancillary response function (Davis 2001) of the corresponding spectrum. The ratio of the model integrated flux to the estimated source counts yielded the count-rate to flux conversion factor, while the distribution of this ratio gave the uncertainty of the conversion factor as a result of the uncertainty in

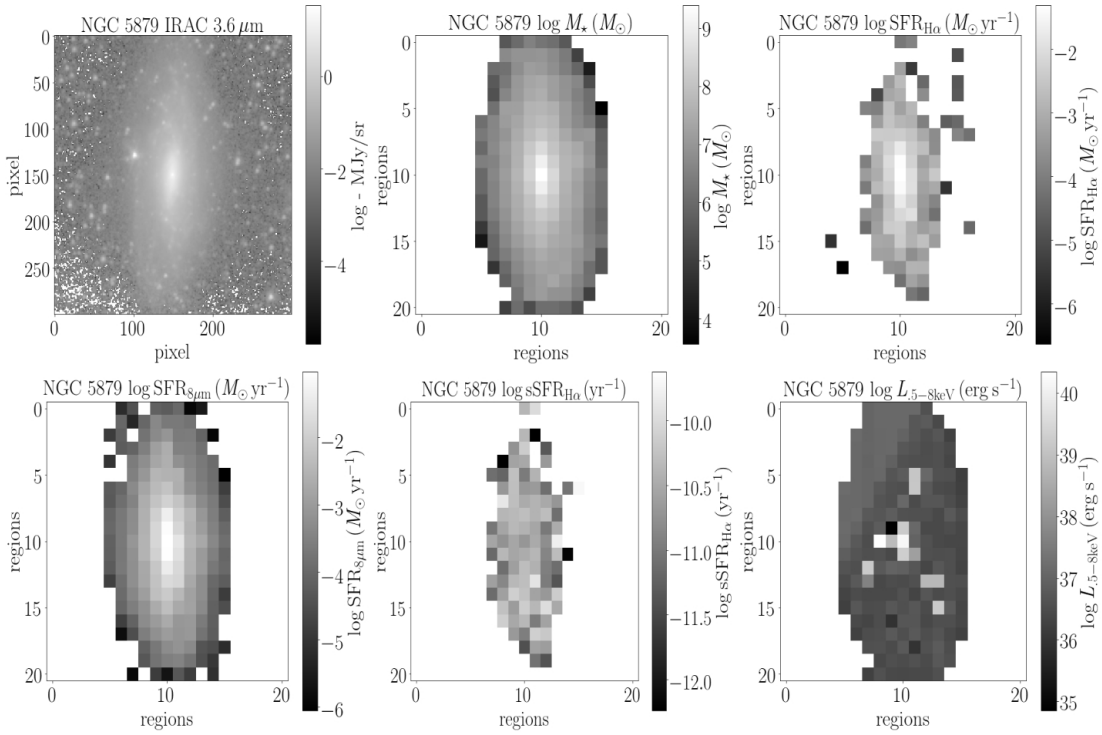

Figure 3.3: Sub-galactic maps at 1 kpc^2 scale for NGC 5879, illustrating the character of the data. Top left: the IRAC 3.6 μm image used to measure the stellar mass. Top center: the stellar mass map derived from the IRAC 3.6 μm observations. Top right: The SFR map based on the Hα observations. Bottom left: The SFR map derived from the IRAC 8 μm observations. Bottom center: The sSFR map that results from combining the Hα and the IRAC 3.6 μm observations. Bottom right: The full (0.5–8 keV) X-ray luminosity map based on the *Chandra* imaging. Bars to the right of each image show the mapping from grey scale to physical quantity.

the model parameters.

3.3 Sub-galactic analysis

In order to explore the correlations between SFR, stellar mass, and X-ray luminosity on sub-galactic scales, we defined grids of different physical scales following the same approach as Maragkoudakis *et al.* (2017). Physical scales of 1×1, 2×2, 3×3, and 4×4 kpc^2 were considered. The minimum physical scale was dictated by the MIPS 24 μm PSF (FWHM of centered point spread function =2″6), which corresponds to a scale of ∼1 kpc for the most distant galaxy (NGC 6090) in our sample (3″14 for 1 kpc regions). One additional reason for not considering smaller scales is that the SFR indicators suffer from severe stochasticity at scales $\lesssim$1 kpc (e.g., Kennicutt & Evans 2012). Another

Table 3.3: Number of sub-galactic regions per galaxy at each physical scale.

Galaxy/Surface (kpc^2)	1×1	2×2	3×3	4×4
NGC 3245	71	25	15	9
UGC 5720	54	20	9	9
NGC 3353	26	10	8	7
NGC 3656	256	74	40	24
NGC 4194	169	51	29	25
NGC 5204	24	9	8	5
NGC 5474	73	22	11	9
NGC 5585	91	23	17	9
NGC 5584	593	159	80	50
MCG 6-32-070	1292	337	164	100
NGC 5691	54	19	10	8
NGC 5879	202	62	30	15
NGC 6090	199	57	31	19
Total	3104	868	452	289

reason is to ensure that the natal kicks neutron stars (and possibly black holes) receive will not add significant scatter to the relations we find. These kicks can result in a considerable velocity for the surviving binary systems (e.g., Podsiadlowski *et al.* 2004), displacing XRBs from their formation sites. This could increase the scatter in the sub-galactic correlations between SFR and X-ray luminosity. Typical center-of-mass velocities measured for HMXBs are in the 15–30 $km\,s^{-1}$ range (e.g., van den Heuvel *et al.* 2000; Coe 2005; Antoniou & Zezas 2016). However, for a travel time of ∼20 Myr (i.e., the time between formation of the compact object and the onset of the X-ray emitting phase, e.g., Politakis *et al.* 2020), even the upper end of the velocity range gives a distance no more than ∼600 pc from the formation site of an HMXB. In the case of LMXBs, their long formation timescales ($\gtrsim$1 Gyr) mean that they trace the old stellar populations of a galaxy, which are more evenly distributed. Therefore, the natal kicks will not affect the statistical association of LMXBs with the older stellar populations.

We applied the same sub-region grids to all the observables: IRAC 3.6 μm (used to measure the stellar mass), Hα, IRAC 8 μm, MIPS 24 μm, (used to measure the SFR), and the *Chandra* data in the soft, hard, and full bands. At this stage, regions with signal-to-noise (S/N)$\leq$3 in the IRAC 3.6 μm data were discarded. This is why the number of sub-galactic regions does not increase geometrically for smaller physical scales. The resulting maps of stellar mass, SFR, sSFR, and X-ray luminosity were used to correlate these parameters in sub-galactic regions. Figure 3.3 shows an example. Table 3.3 lists the number of regions in each of the galaxies.

In order to calculate the X-ray emission in each sub-galactic region, the observed number of counts was measured using the `CIAO dmextract` tool on the *Chandra* images in each of the three bands. Because most regions had $\leq$5 counts above the background, the background could not simply be subtracted as estimated from a source-free region outside the galaxy. Instead, the `BEHR`*code (Park *et al.* 2006) was used, which gives the posterior probability distribution of the source intensity based on the formulation of van Dyk *et al.* (2001), accounting for the Poissonian nature of the source and background counts. `BEHR` also takes into account differences in the effective area between the source and background regions. A non-informative Jeffreys' prior on the source intensities was adopted. This approach allowed a reliable estimate of the intensity of the X-ray emission even in regions with weaker signals than formal detections. It also accounted for effective area variations across the galaxy's surface based on the exposure maps of each galaxy.

In order to calculate the X-ray luminosity for each sub-galactic region, the posterior distribution of the source counts (calculated as described in Section 3.2.4) was folded with the distribution of count-rate to flux conversion factors. This conversion depends on the X-ray spectrum (e.g., Zezas *et al.* 2006). Because each sub-galactic region has typically $\leq$20 total counts, no independent spectral analysis could be performed. Instead the spectrum of each sub-galactic region was assumed to be the same as the galaxy integrated spectrum. This is a reasonable assumption for the 10 galaxies fitted with an absorbed power-law spectrum and not requiring any additional thermal component. The X-ray emission of these galaxies typically has $\Gamma \geq 1.6$ (Section 3.2.4, Table 3.2). Therefore their spectra are dominated by XRBs, which on average have X-ray spectra with photon indices $1 \leq \Gamma \leq 3$. The three galaxies that require a thermal component may have spatial variations in the relative intensity of the thermal and the power-law components. Assuming that the spectral parameters of each of the two components are on average the same in the different sub-galactic regions, the X-ray colour $C \equiv \log(S) - \log(H)$ of each region can be used to infer their relative contribution in the full band. C was calculated with the `BEHR` method. Figure 3.4 shows the relation between C and the relative contribution of the power-law to total (power-law + thermal) components. Based on C, the corresponding total flux for each region and the flux arising only from the power-law component (which is relevant for the XRBs) were calculated. The mean thermal contribution for these galaxies is shown in Table 3.4.

The calculation of the X-ray luminosity for each region was performed by sampling the posterior distribution of the net counts and the corresponding distribution of count-rate

* *Bayesian Estimation of Hardness Ratios*; http://hea-www.harvard.edu/astrostat/BEHR/index.html

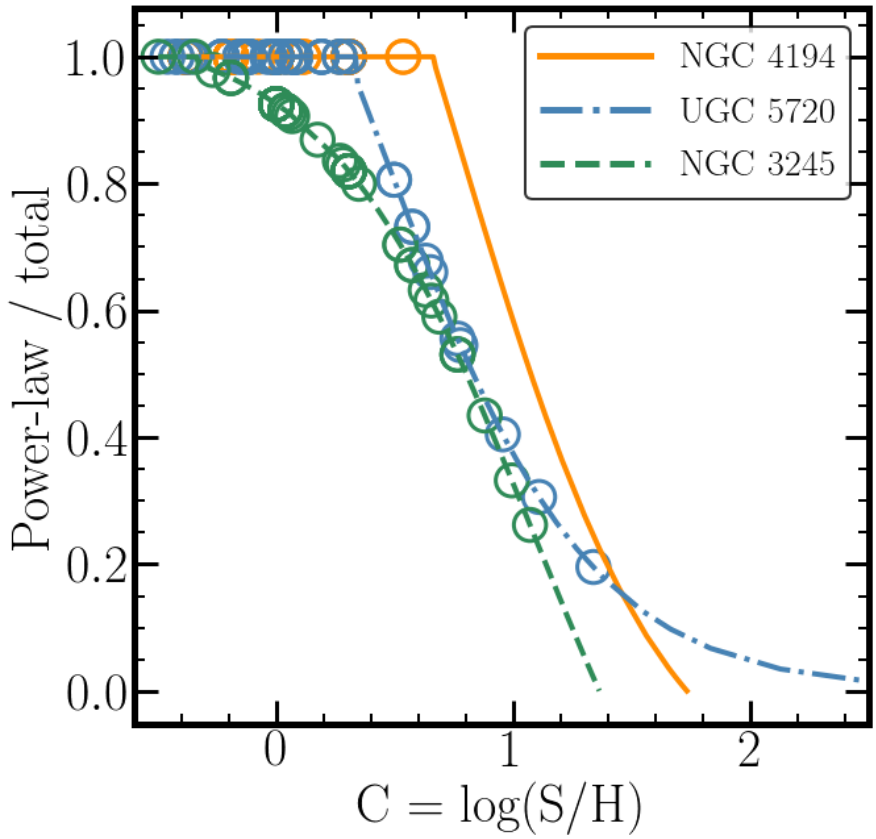

Figure 3.4: The power-law to total ratio as a function of the hardness-ratio colour defined as $C \equiv \log(S/H)$. These relations were calculated for each galaxy independently given the best-fit spectral parameters of their integrated spectra and the ACIS calibration. Then, based on each region's C, we calculated the relative normalization of the thermal and power-law component and its uncertainty. Individual $1{\times}1\,\mathrm{kpc}^2$ sub-galactic region measurements are represented with circles on top of the calculated conversion curves. Colours identify the three galaxies. The cutoff for NGC 4194 and NGC 3245 shows that X-ray luminosity for regions with C below that value is effectively emitted by a power-law spectrum.

Table 3.4: Mean (of the distribution of all the sub-galactic regions) thermal contribution of the thermal-plasma component in the full band $L_{0.5-8\,\mathrm{keV}}$ luminosity for each galaxy.

Galaxy/Surface (kpc^2)	1×1	2×2	3×3	4×4
NGC 4194	0%	0%	0%	0%
NGC 3245	18.5%	19.6%	23.1%	33.5%
UGC 5720	8.5%	6.9%	16.1%	5.8%

to flux conversions. The resulting X-ray luminosity distributions are non-Gaussian, usually positively skewed for low-emission regions.

In order to compare our results with the scaling relations of M14 and with results from the *Chandra* deep surveys, we also calculated the luminosities in each sub-galactic region in the soft and the hard bands. Because the thermal emission included in the soft band can also be correlated with recent star formation, we opted not to subtract the thermal component. Therefore the count-rate to flux conversion factors in the soft band were calculated as described above, i.e. without correcting for the thermal component. In the case of the X-ray emission above 2 keV, which is dominated by the power-law component, we simply used the best-fit photon index for each galaxy and its corresponding uncertainty to calculate the distribution of the count-rate to flux conversion factors.

3.4 Results

3.4.1 Maximum likelihood fits

In order to measure the correlation between X-ray luminosity, SFR, and stellar mass, we performed maximum likelihood fits using all the sub-galactic regions of all the galaxies of the sample combined. In order to assess the fit parameters and their uncertainties, we used the posterior probability distribution for the X-ray luminosity, calculated as described in Section 3.3, and the Gaussian uncertainty distribution on SFR and stellar mass of each region. In all cases, we simultaneously fitted the probability distributions of all points included in the fits for all the parameters considered in the model. The model is of the form

$$\log L_X = a \log \mathrm{SFR} + b + \epsilon(\mathrm{SFR}) \quad , \tag{3.6}$$

where a is the power-law slope and b the proportionality constant in linear space. We included an intrinsic scatter term ϵ to account for any additional scatter above the measurement random errors. ϵ is a Gaussian random variable with mean $\mu = 0$ and standard deviation $\sigma = \sigma_1 \log \mathrm{SFR} + \sigma_2$. The intrinsic scatter was allowed to vary linearly (parameterized by σ_1) with SFR to account for stochasticity. This approach was driven by previous studies (e.g., M14; Grimm *et al.* 2003; Lehmer *et al.* 2019) which indicated increased scatter in the L_X–SFR scaling relation at lower SFR. The results from these fits are presented in Table 3.4.3. In general, slopes are significantly sub-linear, and $\sigma_1 \simeq 0$ in all fits for all the SFR indicators and scales used in this work. Thus, even

though we are probing SFRs that extend ∼5 dex lower than previous studies, we do not find significant evidence for increased scatter at lower SFR. Therefore in the rest of our analysis we consider a model with fixed scatter that does not depend on SFR:

$$\log L_X = a \log \mathrm{SFR} + b + \sigma \quad , \tag{3.7}$$

where σ indicates a Gaussian random variable with $\mu = 0$ and standard deviation σ. The results are reported in Table 3.4.3 and described in Section 3.4.2.

In order to disentangle the contribution of HMXBs and LMXBs in the X-ray luminosity of the sub-galactic regions, we performed a joint X-ray luminosity, SFR, and stellar mass maximum likelihood fit. The model was parameterized as

$$\log L_X = \log(10^{\alpha + \log \mathrm{SFR}} + 10^{\beta + \log M_\star}) + \sigma \quad , \tag{3.8}$$

where α and β are the scaling factors of the X-ray luminosity resulting from the young and the old stellar populations (associated with HMXBs and LMXBs respectively), and σ is again a Gaussian random variable accounting for intrinsic scatter in the data. The fit results are given in Table 3.4.3 and described in Section 3.4.3. The implementation of the maximum likelihood method is described in more detail in Appendix 3.7.

3.4.2 Correlations between X-ray luminosity and SFR

Figure 3.5 presents the correlations between X-ray luminosity and SFR using the Hα, 8 μm, and 24 μm SFR indicators. Our analysis used the observed Hα and X-ray luminosities, i.e., not corrected for absorption. This is because we are interested in deriving empirical relations between observable quantities. The sample galaxies show small inclinations (minimum minor-to-major axis ratio = 0.52, median = 0.87 ± 0.14—Table 3.2.1), suggesting low intrinsic absorption. The median extinction for these thirteen galaxies (Maragkoudakis *et al.* 2018) is 0.36 mag based on their integrated or nuclear spectra. Translating the typical A_V-to-hydrogen column density conversion $N_\mathrm{H}/A_V = 1.9 \times 10^{21}\,\mathrm{atoms\,cm^{-2}\,mag^{-1}}$ (Gorenstein 1975 with cross sections from Morrison & McCammon 1983) to Hα with a Cardelli *et al.* (1989) extinction curve (with $R_V = 3.1$) gives $N_\mathrm{H}/A_{\mathrm{H}\alpha} = 1.55 \times 10^{21}\,\mathrm{atoms\,cm^{-2}\,mag^{-1}}$. This makes the absorption in Hα and at 1 keV similar within ∼30%.

The best-fit L_x–SFR results are presented in Table 3.4.3. Overall correlations between these two quantities are flatter than the reference correlation of M14. There are also

differences in the slopes depending on the star-formation indicator considered: Hα-based SFR shows systematically steeper slopes, while correlations on the 8 μm-based and the 24 μm-based emission show shallower slopes. There are also systematic trends depending on the spatial scales considered. While the correlations are shallower than linear in all cases, larger spatial scales tend towards linearity. The shallower slopes are mainly driven by regions in the extremely low SFR regime, which show an X-ray luminosity excess in comparison to the linear relation of M14 and the best maximum likelihood fits from this work.

The fits discussed above are based on the full band X-ray data, which provide the maximum S/N ratio for each sub-region. However, full band fluxes can be subject to differential absorption and residual thermal emission. In order to address the importance of these we also calculated the L_X–SFR scaling relations in the soft and hard bands, the latter being a cleaner probe of the X-ray emission produced by XRBs. The results are presented in Table 3.4.3 and illustrated in Figure 3.6. The soft band shows weaker correlation with SFR in all cases. The hard-band fits have similar slopes to the full band, a fact that reinforces the usefulness of the full band L_X–SFR correlation on sub-galactic scales despite the potential complication of differential absorption. The hard band shows significantly lower scatter than the full and the soft band in all cases. The hard band–Hα correlation shows the tightest correlation and slopes closest to one. Especially in the case of the Hα-based relation, we find remarkably similar results between the hard and the full bands. In the case of 2×2 and $3\times3\,\mathrm{kpc}^2$ 24 μm fits, the hard band shows a shallower fit than the full and soft band. This is due to the rejection of the low-S/N regions in the 24 μm MIPS data. These regions have very low SFR, reducing the range of SFR and causing the low-SFR locus to be less populated, thereby driving the flatter fits.

In order to explore galaxy-to-galaxy variations of the scaling relations, the model described by Eq. 3.7 was fitted to each individual galaxy of our sample. The best-fit slopes and intercepts for the fits for each sub-galactic scale and SFR indicator are plotted in Figure 3.7. We see a broad range of intercepts and slopes, with some galaxies showing no correlation (slope$\simeq$0) and others having slope steeper than 1. As expected, there is significant correlation between the best-fit slopes and intercepts. The best-fit parameters for most cases show large uncertainties ($\simeq$1 dex) as result of the small number of regions (Table 3.3) used to derive each correlation. This is particularly evident as we consider increasing spatial scales. However, we do see significant differences between the best-fit slopes and intercepts for the different galaxies, particularly in the case of the smaller physical scales, where differences are not masked by large uncertainties. These variations illustrate the stochasticity in the L_X–SFR correlation, arising from the differences in

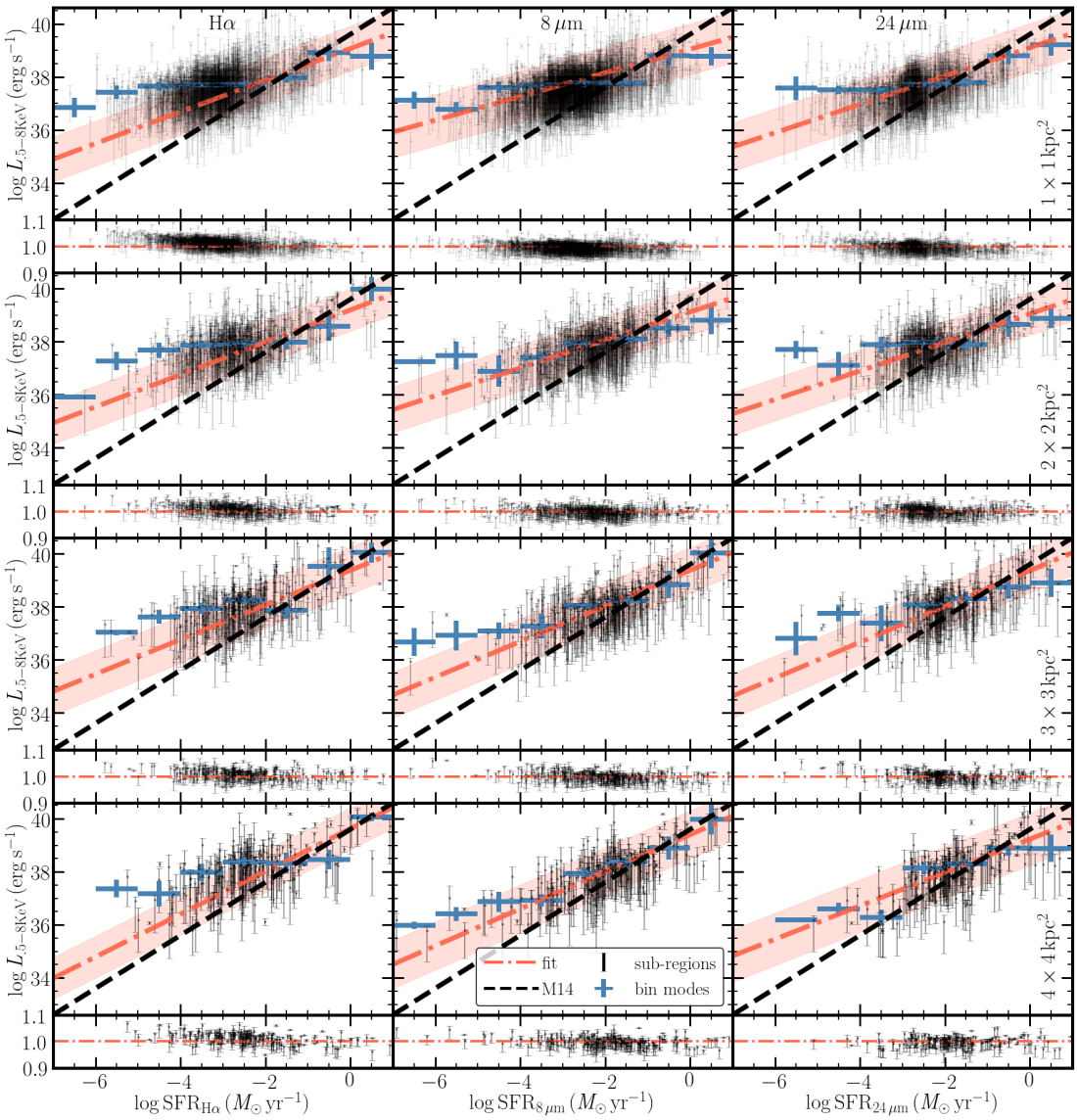

Figure 3.5: $L_{X,0.5-8\mathrm{keV}}$ as a function of SFR for three different SFR indicators (Hα, 8 μm, and 24 μm from left to right) and for four different sub-galactic scales (1×1, 2×2, 3×3, and 4×4 kpc^2 from top to bottom). All regions within all the sample galaxies are included in the fits and are represented by black error bars (including uncertainties only in the X-ray luminosity for clarity). The red dashed-dotted line represents the maximum likelihood best fit for $\log L_X = a \log \mathrm{SFR} + b + \sigma$ (Eq. 3.7) for all sub-galactic region in the sample. Parameters a, b, and σ are given in Table 3.4.3. The shaded area represents the estimates for the intrinsic scatter σ. The blue error bars represent mode values of the distributions of points included in bins of 1 dex of SFR. The M14 correlation is drawn with a dashed black line. Underneath each panel, the black error bars represent for each sub-galactic region the ratio of the measured L_X to the value expected based on the best-fit model (red dashed-dotted line).

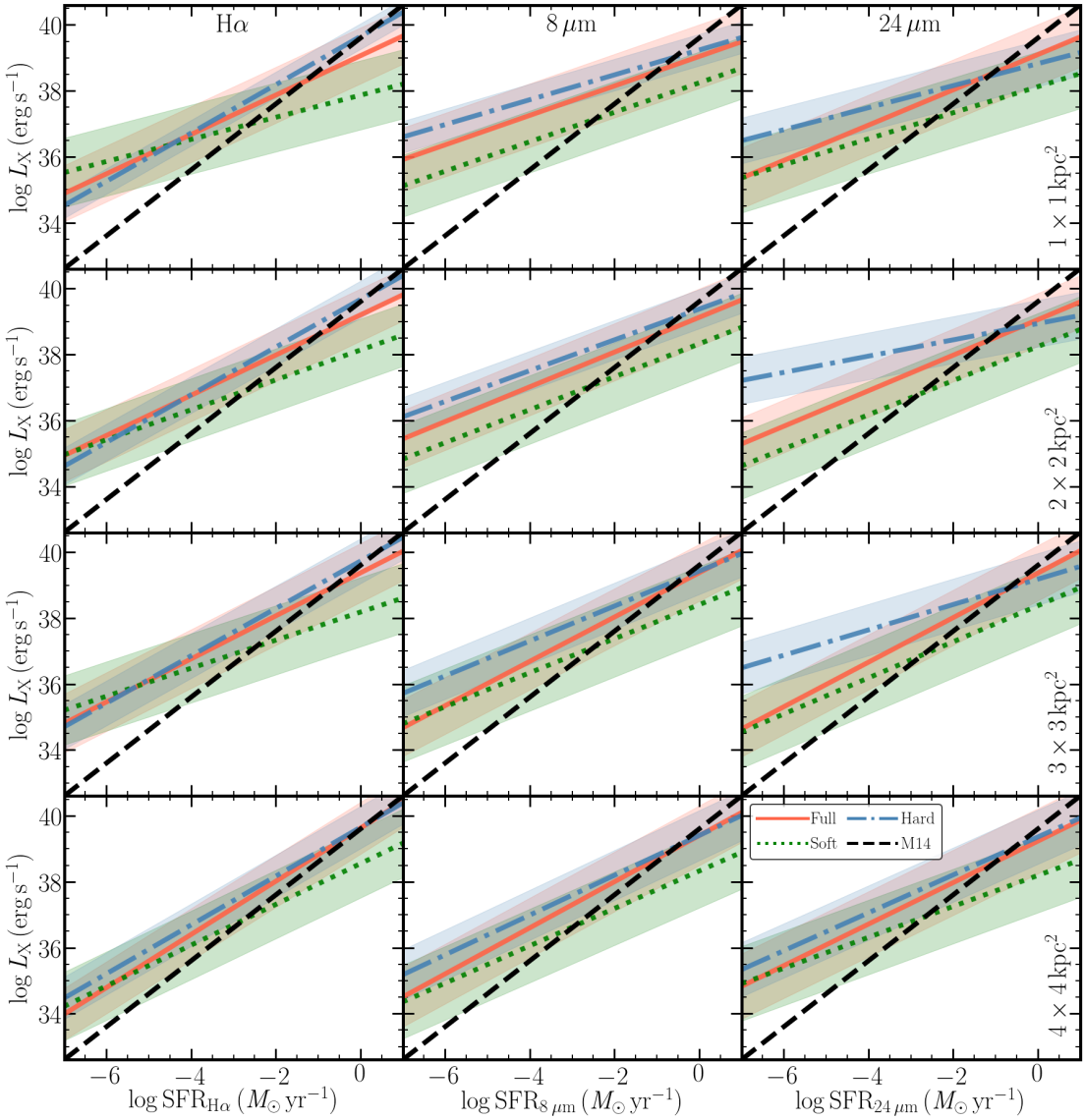

Figure 3.6: Best maximum-likelihood fits to the L_X–SFR relations (see Table 3.4.3). The different lines correspond to fits for the soft (S; 0.5–2 keV; green dotted), hard (H; 2–8 keV; blue dashed-dotted), and full (F; 0.5–8 keV; red) bands. Fits for the different SFR indicators (Hα, 8 μm, and 24 μm) are shown in the columns from left to right at four sub-galactic scales (1×1, 2×2, 3×3, and 4×4 kpc^2) from top to bottom. The shaded areas of similar colours represent the intrinsic scatter σ for each band. For comparison the M14 correlation is drawn with a black dashed line in all panels.

the SFHs and stellar populations of the galaxies.

3.4.3 Joint correlations between X-ray luminosity, SFR and stellar mass

The sSFR is a metric of the relative contribution of the young and old stellar populations in the mass assembly of the galaxy. Because HMXBs are associated with young, and LMXBs with old stellar populations, the sSFR is a proxy for the relative contribution of these two XRB populations in the overall X-ray emission of a galaxy. Figure 3.8 illustrates these correlations projected on the L_X–SFR–$M_\star$ plane. For almost all cases, we find excellent agreement with the z<0.5 (Lehmer *et al.* 2016; hereafter L16) relation for the integrated properties of galaxies, even though the results presented here consider sub-galactic scales and extend these relations to ∼2 dex lower sSFR. The agreement is better for larger scales, with smaller scales tending to give larger α (Eq. 3.8). As in the case for the L_X–SFR correlations, the scatter is smallest for the Hα SFR indicator.

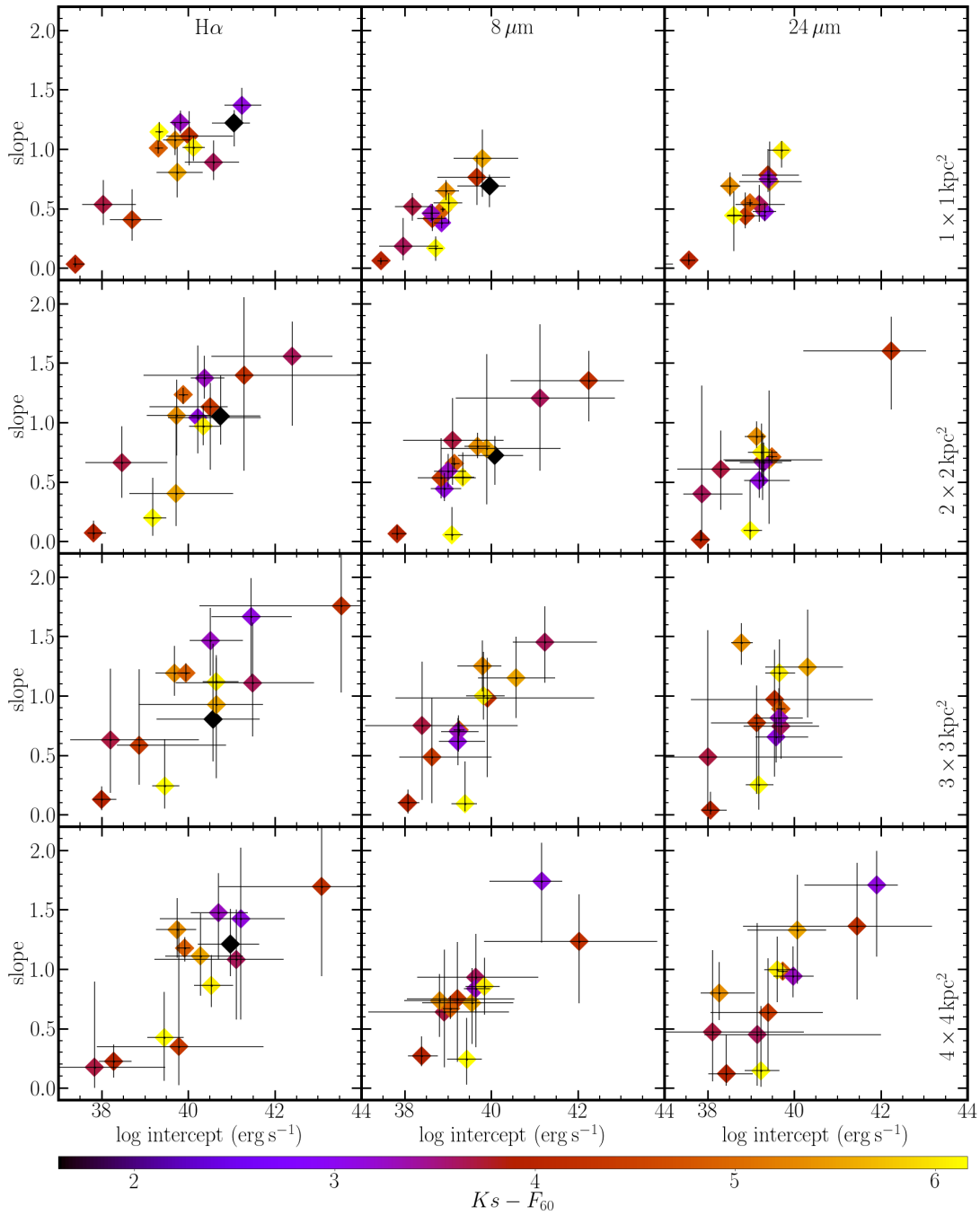

Figure 3.7: Best-fit slopes and intercepts of the sub-regions in each individual galaxy. SFR indicators (Hα, 8 μm, and 24 μm) are in columns from left to right, and four sub-galactic scales (1×1, 2×2, 3×3, and 4×4 kpc^2) are from top to bottom. The points are colour-coded based on each galaxy's integrated emission $K_S - F_{60}$ colour, a proxy for their sSFR.

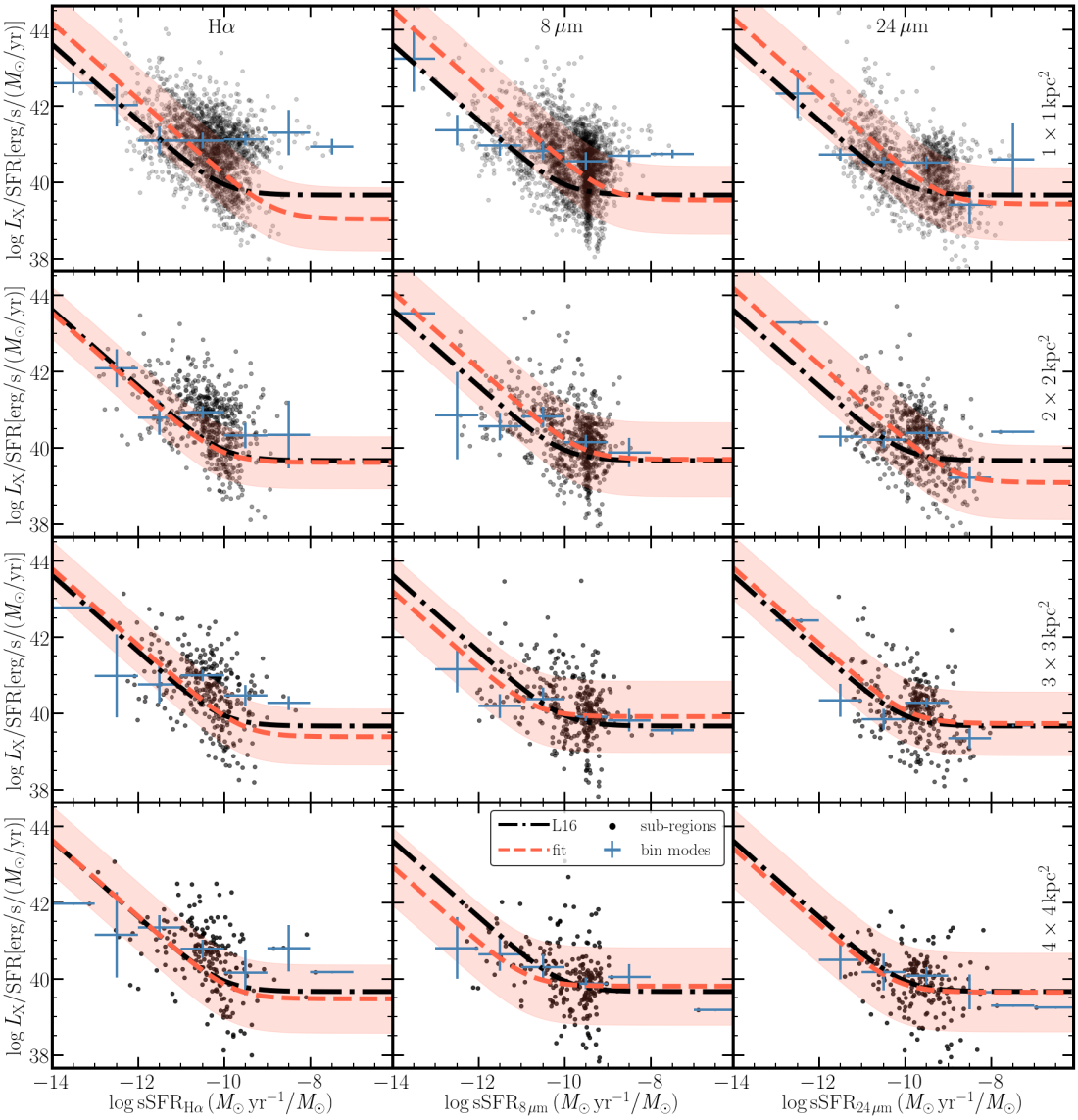

Figure 3.8: $L_{X,0.5-8\mathrm{keV}}/\mathrm{SFR}$ as a function of sSFR with the use of three different SFR indicators (Hα, 8 μm, and 24 μm from left to right) and for four different sub-galactic scales (1×1, 2×2, 3×3, and 4×4 kpc^2 from top to bottom). All regions of all the sample galaxies are represented by grey points. The red dashed curve represents the best fit for a $\log L_X = \log(10^{\alpha+\log \mathrm{SFR}} + 10^{\beta+\log M_\star}) + \sigma$ model (Eq. 3.8). The shaded area represents the calculated intrinsic scatter σ. The blue error bars represent the modes and 1σ uncertainties of the distributions of points in 1 dex bins of sSFR. The L16 relation for zero redshift is plotted with a black dashed-dotted curve.

Table 3.5: Maximum likelihood fits of the L_X–SFR relation with SFR-dependent scatter.

Scale	Hα				8 μm				24 μm			
	a	b	σ_1	σ_2	a	b	σ_1	σ_2	a	b	σ_1	σ_2
1×1 kpc^2	$0.50^{+0.02}_{-0.02}$	$38.87^{+0.03}_{-0.05}$	$0.14^{+0.01}_{-0.01}$	$1.13^{+0.04}_{-0.03}$	$0.44^{+0.01}_{-0.02}$	$38.99^{+0.05}_{-0.05}$	$0.18^{+0.02}_{-0.02}$	$1.43^{+0.05}_{-0.05}$	$0.46^{+0.03}_{-0.02}$	$38.87^{+0.09}_{-0.05}$	$0.14^{+0.02}_{-0.02}$	$1.27^{+0.04}_{-0.06}$
2×2 kpc^2	$0.60^{+0.05}_{-0.05}$	$39.15^{+0.15}_{-0.09}$	$0.04^{+0.04}_{-0.03}$	$0.87^{+0.10}_{-0.06}$	$0.51^{+0.03}_{-0.04}$	$39.11^{+0.07}_{-0.11}$	$0.01^{+0.04}_{-0.02}$	$0.91^{+0.07}_{-0.05}$	$0.46^{+0.07}_{-0.02}$	$38.93^{+0.18}_{-0.05}$	$0.11^{+0.04}_{-0.05}$	$1.10^{+0.09}_{-0.14}$
3×3 kpc^2	$0.66^{+0.09}_{-0.05}$	$39.42^{+0.15}_{-0.16}$	$-0.03^{+0.08}_{-0.04}$	$0.87^{+0.15}_{-0.12}$	$0.63^{+0.05}_{-0.05}$	$39.26^{+0.10}_{-0.14}$	$0.21^{+0.04}_{-0.04}$	$1.17^{+0.12}_{-0.06}$	$0.58^{+0.07}_{-0.04}$	$39.22^{+0.10}_{-0.13}$	$0.09^{+0.03}_{-0.04}$	$1.02^{+0.07}_{-0.09}$
4×4 kpc^2	$0.76^{+0.08}_{-0.06}$	$39.57^{+0.16}_{-0.15}$	$0.05^{+0.06}_{-0.04}$	$0.89^{+0.13}_{-0.10}$	$0.69^{+0.06}_{-0.06}$	$39.35^{+0.14}_{-0.14}$	$0.15^{+0.06}_{-0.08}$	$1.13^{+0.10}_{-0.13}$	$0.75^{+0.06}_{-0.06}$	$39.45^{+0.11}_{-0.13}$	$-0.09^{+0.04}_{-0.04}$	$0.82^{+0.09}_{-0.08}$

NOTE: Model $\log L_{\rm X} = a\,{\rm logSFR} + b + \epsilon({\rm SFR})$, where ϵ is a Gaussian random variable with mean $\mu = 0$ and standard deviation $\sigma = \sigma_1\,{\rm logSFR} + \sigma_2$ for the full (0.5-8 keV) X-ray band.

Table 3.6: Maximum-likelihood fits of the L_X–SFR relation with constant scatter.

Scale	Hα			8 μm			24 μm		
	a	b	σ	a	b	σ	a	b	σ
					Full L_X				
$1\times1\,\mathrm{kpc}^2$	$0.60^{+0.01}_{-0.01}$	$39.07^{+0.03}_{-0.03}$	$0.85^{+0.01}_{-0.01}$	$0.45^{+0.02}_{-0.01}$	$39.04^{+0.05}_{-0.04}$	$0.96^{+0.01}_{-0.01}$	$0.54^{+0.01}_{-0.02}$	$39.10^{+0.04}_{-0.05}$	$0.92^{+0.02}_{-0.01}$
$2\times2\,\mathrm{kpc}^2$	$0.61^{+0.06}_{-0.01}$	$39.20^{+0.14}_{-0.04}$	$0.79^{+0.02}_{-0.02}$	$0.53^{+0.02}_{-0.04}$	$39.13^{+0.05}_{-0.08}$	$0.87^{+0.02}_{-0.02}$	$0.54^{+0.02}_{-0.04}$	$39.05^{+0.04}_{-0.09}$	$0.80^{+0.03}_{-0.02}$
$3\times3\,\mathrm{kpc}^2$	$0.65^{+0.06}_{-0.06}$	$39.37^{+0.14}_{-0.14}$	$0.89^{+0.05}_{-0.04}$	$0.67^{+0.05}_{-0.04}$	$39.38^{+0.12}_{-0.09}$	$0.86^{+0.04}_{-0.03}$	$0.68^{+0.03}_{-0.03}$	$39.37^{+0.09}_{-0.07}$	$0.84^{+0.05}_{-0.02}$
$4\times4\,\mathrm{kpc}^2$	$0.81^{+0.07}_{-0.05}$	$39.63^{+0.15}_{-0.12}$	$0.79^{+0.04}_{-0.05}$	$0.70^{+0.06}_{-0.06}$	$39.40^{+0.11}_{-0.15}$	$0.91^{+0.05}_{-0.04}$	$0.63^{+0.05}_{-0.04}$	$39.23^{+0.11}_{-0.09}$	$0.99^{+0.05}_{-0.04}$
					Soft L_X				
$1\times1\,\mathrm{kpc}^2$	$0.34^{+0.03}_{-0.02}$	$37.87^{+0.07}_{-0.04}$	$1.05^{+0.01}_{-0.01}$	$0.45^{+0.01}_{-0.01}$	$38.24^{+0.03}_{-0.03}$	$0.94^{+0.01}_{-0.01}$	$0.40^{+0.02}_{-0.01}$	$38.13^{+0.05}_{-0.05}$	$1.06^{+0.02}_{-0.01}$
$2\times2\,\mathrm{kpc}^2$	$0.45^{+0.02}_{-0.02}$	$38.13^{+0.07}_{-0.05}$	$0.95^{+0.02}_{-0.02}$	$0.50^{+0.04}_{-0.02}$	$38.32^{+0.07}_{-0.06}$	$1.04^{+0.03}_{-0.02}$	$0.52^{+0.02}_{-0.01}$	$38.24^{+0.05}_{-0.05}$	$1.01^{+0.02}_{-0.02}$
$3\times3\,\mathrm{kpc}^2$	$0.43^{+0.03}_{-0.02}$	$38.18^{+0.12}_{-0.05}$	$1.05^{+0.03}_{-0.03}$	$0.52^{+0.06}_{-0.04}$	$38.41^{+0.08}_{-0.10}$	$1.16^{+0.05}_{-0.07}$	$0.55^{+0.04}_{-0.03}$	$38.38^{+0.09}_{-0.07}$	$1.10^{+0.04}_{-0.04}$
$4\times4\,\mathrm{kpc}^2$	$0.62^{+0.05}_{-0.07}$	$38.55^{+0.15}_{-0.10}$	$1.04^{+0.05}_{-0.05}$	$0.57^{+0.03}_{-0.11}$	$38.33^{+0.10}_{-0.11}$	$1.12^{+0.07}_{-0.04}$	$0.47^{+0.02}_{-0.07}$	$38.19^{+0.09}_{-0.11}$	$1.13^{+0.06}_{-0.04}$
					Hard L_X				
$1\times1\,\mathrm{kpc}^2$	$0.73^{+0.02}_{-0.02}$	$39.65^{+0.04}_{-0.04}$	$0.39^{+0.02}_{-0.01}$	$0.38^{+0.01}_{-0.02}$	$39.24^{+0.05}_{-0.05}$	$0.48^{+0.03}_{-0.02}$	$0.33^{+0.02}_{-0.03}$	$38.83^{+0.06}_{-0.08}$	$0.69^{+0.03}_{-0.02}$
$2\times2\,\mathrm{kpc}^2$	$0.72^{+0.03}_{-0.04}$	$39.67^{+0.07}_{-0.06}$	$0.56^{+0.04}_{-0.02}$	$0.47^{+0.03}_{-0.03}$	$39.38^{+0.07}_{-0.07}$	$0.59^{+0.04}_{-0.03}$	$0.25^{+0.05}_{-0.03}$	$38.94^{+0.09}_{-0.09}$	$0.71^{+0.05}_{-0.05}$
$3\times3\,\mathrm{kpc}^2$	$0.72^{+0.06}_{-0.04}$	$39.73^{+0.08}_{-0.11}$	$0.68^{+0.05}_{-0.06}$	$0.53^{+0.05}_{-0.04}$	$39.43^{+0.09}_{-0.11}$	$0.70^{+0.06}_{-0.06}$	$0.38^{+0.07}_{-0.04}$	$39.18^{+0.14}_{-0.10}$	$0.78^{+0.06}_{-0.06}$
$4\times4\,\mathrm{kpc}^2$	$0.74^{+0.06}_{-0.04}$	$39.65^{+0.10}_{-0.08}$	$0.64^{+0.05}_{-0.06}$	$0.60^{+0.06}_{-0.05}$	$39.40^{+0.12}_{-0.09}$	$0.76^{+0.06}_{-0.06}$	$0.58^{+0.07}_{-0.06}$	$39.36^{+0.11}_{-0.15}$	$0.82^{+0.07}_{-0.07}$

NOTE: Model $\log L_{\mathrm{X}} = a\,\mathrm{logSFR} + b + \sigma$, where σ indicates a Gaussian random variable with mean $\mu = 0$ and standard deviation σ.

Table 3.7: The maximum likelihood fit results for L_X–SFR–$M_\star$ relation.

Scale	Hα			8 μm			24 μm		
	α	β	σ	α	β	σ	α	β	σ
				Full L_X					
$1\times1\,\mathrm{kpc}^2$	$39.03^{+0.06}_{-0.06}$	$30.18^{+0.04}_{-0.03}$	$0.83^{+0.02}_{-0.02}$	$39.53^{+0.07}_{-0.07}$	$30.51^{+0.02}_{-0.02}$	$0.89^{+0.01}_{-0.01}$	$39.43^{+0.06}_{-0.10}$	$30.31^{+0.04}_{-0.04}$	$0.96^{+0.02}_{-0.01}$
$2\times2\,\mathrm{kpc}^2$	$39.61^{+0.05}_{-0.06}$	$29.54^{+0.06}_{-0.07}$	$0.68^{+0.03}_{-0.03}$	$39.69^{+0.08}_{-0.13}$	$30.08^{+0.10}_{-0.05}$	$0.97^{+0.02}_{-0.03}$	$39.09^{+0.43}_{-0.11}$	$30.19^{+0.06}_{-0.16}$	$0.97^{+0.03}_{-0.03}$
$3\times3\,\mathrm{kpc}^2$	$39.38^{+0.09}_{-0.22}$	$29.78^{+0.08}_{-0.07}$	$0.73^{+0.06}_{-0.05}$	$39.91^{+0.06}_{-0.07}$	$29.20^{+0.27}_{-0.26}$	$0.93^{+0.04}_{-0.02}$	$39.72^{+0.05}_{-0.15}$	$29.82^{+0.10}_{-0.25}$	$0.83^{+0.11}_{-0.01}$
$4\times4\,\mathrm{kpc}^2$	$39.47^{+0.21}_{-0.20}$	$29.63^{+0.13}_{-0.13}$	$0.89^{+0.07}_{-0.08}$	$39.80^{+0.16}_{-0.02}$	$28.94^{+0.35}_{-0.41}$	$1.02^{+0.04}_{-0.06}$	$39.64^{+0.13}_{-0.02}$	$29.43^{+0.17}_{-0.08}$	$1.03^{+0.02}_{-0.08}$
				Soft L_X					
$1\times1\,\mathrm{kpc}^2$	$38.04^{+0.04}_{-0.04}$	$29.60^{+0.02}_{-0.02}$	$0.91^{+0.01}_{-0.01}$	$38.15^{+0.13}_{-0.19}$	$29.85^{+0.02}_{-0.01}$	$0.94^{+0.01}_{-0.01}$	$37.64^{+0.28}_{-0.24}$	$29.80^{+0.02}_{-0.02}$	$0.96^{+0.02}_{-0.01}$
$2\times2\,\mathrm{kpc}^2$	$37.58^{+0.35}_{-0.12}$	$29.37^{+0.04}_{-0.04}$	$0.95^{+0.03}_{-0.02}$	< 37.25	$29.52^{+0.04}_{-0.03}$	$0.98^{+0.03}_{-0.02}$	< 38.79	$29.45^{+0.05}_{-0.06}$	$0.99^{+0.04}_{-0.03}$
$3\times3\,\mathrm{kpc}^2$	< 38.37	$29.34^{+0.06}_{-0.06}$	$1.01^{+0.03}_{-0.05}$	< 37.53	$29.37^{+0.05}_{-0.04}$	$0.97^{+0.04}_{-0.04}$	< 37.52	$29.33^{+0.05}_{-0.04}$	$0.99^{+0.03}_{-0.04}$
$4\times4\,\mathrm{kpc}^2$	$38.19^{+0.22}_{-0.27}$	$29.14^{+0.14}_{-0.04}$	$1.12^{+0.05}_{-0.06}$	< 37.87	$29.30^{+0.08}_{-0.06}$	$0.98^{+0.11}_{-0.04}$	< 38.55	$29.25^{+0.08}_{-0.09}$	$1.09^{+0.05}_{-0.09}$
				Hard L_X					
$1\times1\,\mathrm{kpc}^2$	$39.99^{+0.01}_{-0.01}$	$29.24^{+0.10}_{-0.10}$	$0.65^{+0.01}_{-0.01}$	$40.43^{+0.05}_{-0.04}$	$30.28^{+0.11}_{-0.07}$	$1.17^{+0.02}_{-0.02}$	$40.11^{+0.05}_{-0.04}$	$30.22^{+0.08}_{-0.06}$	$1.05^{+0.02}_{-0.02}$
$2\times2\,\mathrm{kpc}^2$	$40.00^{+0.05}_{-0.08}$	$29.10^{+0.22}_{-0.15}$	$0.76^{+0.06}_{-0.03}$	$40.05^{+0.07}_{-0.07}$	$29.80^{+0.21}_{-0.17}$	$1.13^{+0.03}_{-0.03}$	< 38.58	$30.62^{+0.06}_{-0.06}$	$1.07^{+0.04}_{-0.04}$
$3\times3\,\mathrm{kpc}^2$	$39.98^{+0.06}_{-0.09}$	$29.16^{+0.28}_{-0.37}$	$0.90^{+0.05}_{-0.03}$	$39.88^{+0.10}_{-0.09}$	$29.49^{+0.37}_{-0.31}$	$1.14^{+0.07}_{-0.05}$	< 38.98	$30.48^{+0.11}_{-0.08}$	$1.11^{+0.07}_{-0.07}$
$4\times4\,\mathrm{kpc}^2$	$39.87^{+0.07}_{-0.07}$	$28.87^{+0.41}_{-0.39}$	$0.92^{+0.04}_{-0.04}$	$39.77^{+0.09}_{-0.11}$	$29.29^{+0.41}_{-0.42}$	$1.19^{+0.05}_{-0.06}$	< 39.45	$30.25^{+0.09}_{-0.09}$	$1.04^{+0.09}_{-0.05}$

NOTE: Model $\log L_\mathrm{X} = \log(10^{\alpha+\log \mathrm{SFR}} + 10^{\beta+\log \mathrm{M}_\star}) + \sigma$, where α and β are the scaling factors of the X-ray luminosity resulting from the young and the old stellar populations and σ is a again a Gaussian random variable account for any intrinsic scatter in the data.

3.5 Discussion

3.5.1 Comparisons between different SFR indicators

There is growing evidence that the X-ray emission of XRB populations evolves as a function of time (e.g., Fragos *et al.* 2013a; Antoniou *et al.* 2019b; Lehmer *et al.* 2019). HMXBs in particular are a short-lived population, and therefore their abundance depends on SFH. Several recent studies have started to explore the sensitivity of SFR inferred from different SFHs. For example Hα traces $\sim$10 Myr stellar populations whereas 8 μm and 24 μm trace $\gtrsim$200 Myr stellar populations. However, what is not clear yet is how the X-ray scaling relations depend on the SFH of the population responsible for the X-ray emission, because previous works have used indiscriminately different SFR indicators even for different galaxies in the same scaling relations. Such variation may contribute to the observed scatter.

Our observations show a systematic difference in the L_X–SFR correlations between the different SFR indicators. The Hα SFR indicator gives a steeper, more linear slope and the lowest scatter, indicating that it is better correlated with the XRBs' X-ray emission than the 8 μm and the 24 μm indicators. The Hα emission traces the ionizing radiation from stellar populations with ages (e.g., Kennicutt & Evans 2012; Boquien *et al.* 2014; Cerviño *et al.* 2016) similar to the formation timescale of the HMXBs (e.g., Bhattacharya & van den Heuvel 1991; Tauris & van den Heuvel 2006; Fragos *et al.* 2013a). In contrast, the 8 and 24 μm bands' connection with HMXBs is diluted (Fig. 3.9) by the much larger age range those SFR indicators reflect.

The X-ray emission from LMXBs begins to dominate over that from HMXBs for stellar populations older than $\gtrsim$80 Myr (Fig. 3.9), even though the bulk of their population forms at much later times. In regions dominated by a young stellar population, the IR indicators will be dominated by the same young stellar populations traced by the Hα emission, which also host the HMXB populations. On the other hand, for regions with star-forming activity extending beyond 100 Myr, the IR indicators will include contribution from older stellar populations than those traced by the Hα emission. These older stellar populations do not include HMXBs (e.g., Fragos *et al.* 2013a), resulting in increasing scatter.

In order to obtain at least a qualitative picture of the X-ray luminosity scaling relations' dependence on SFH, we performed a simple simulation study where we calculated the X-ray luminosity, SFR, and stellar mass under different assumptions for the SFH. The top panel of Fig. 3.9 presents the X-ray output of a stellar population from the model of Fragos *et al.* (2013a) as a function of age along with the age sensitivities (response

Table 3.8: Results of the calculations based on the model of Fragos *et al.* 2013a, the Hα, 8 μm, 24 μm response functions, and the SFHs shown in Figure 3.9.

		MW	M51	$C(1)$	LMC	RB
$\log M_\star (\mathrm{M}_\odot)$	Eq. 3.9	10.74	11.02	11.00	9.03	10.44
$\mathrm{SFR}_{\mathrm{H}\alpha}$ ($\mathrm{M}_\odot \mathrm{yr}^{-1}$)	Eq. 3.10	3.17	4.30	10.00	0.40	6.09
$\mathrm{SFR}_{8\,\mu\mathrm{m}}$ ($\mathrm{M}_\odot \mathrm{yr}^{-1}$)		3.34	4.72	10.00	0.39	13.24
$\mathrm{SFR}_{24\,\mu\mathrm{m}}$ ($\mathrm{M}_\odot \mathrm{yr}^{-1}$)		3.35	4.74	10.00	0.39	13.53
$\mathrm{t_{eff}}$ (Hα; Myr)	Eq. 3.11	10	9	9	9	7
$\mathrm{t_{eff}}$ (8 μm; Myr)		709	569	594	272	194
$\mathrm{t_{eff}}$ (24 μm; Myr)		716	574	601	276	204
$\log L_{X(\mathrm{XRBs})}$ ($\mathrm{erg\,s^{-1}}$)	Eq. 3.12	42.99	43.15	43.45	42.03	43.73
$\log L_{X(\mathrm{HMXBs})}$ ($\mathrm{erg\,s^{-1}}$)		42.95	43.09	43.42	42.01	43.72
$\log L_{X(\mathrm{LMXBs})}$ ($\mathrm{erg\,s^{-1}}$)		41.97	42.27	42.35	40.85	42.43
$\log\ \alpha'/\beta'$ (Hα; $\mathrm{M}_\odot\,\mathrm{yr}^{-1}/\mathrm{M}_\odot$)	Eq. 3.13	−10.25	−10.40	−10.01	−9.44	−9.66
$\log\ \alpha'/\beta'$ (8 μm; $\mathrm{M}_\odot\,\mathrm{yr}^{-1}/\mathrm{M}_\odot$)		−10.23	−10.36	−10.01	−9.45	−9.33
$\log\ \alpha'/\beta'$ (24 μm; $\mathrm{M}_\odot\,\mathrm{yr}^{-1}/\mathrm{M}_\odot$)		−10.23	−10.36	−10.01	−9.45	−9.32

functions) of the three SFR indicators considered here.*

Based on the XRB luminosity evolution and the SFR indicator response functions, we can quantify the dependence of the L_X–SFR relations on the SFH and the SFR indicator used. To demonstrate this effect we considered five different SFHs (see Fig. 3.9). The total stellar mass is:

$$M_\star = \int_0^t \mathrm{SFH}(t')dt' \quad , \tag{3.9}$$

and the "effective" SFR for each indicator, which accounts for their sensitivity to older

* The response functions were calculated by modeling the evolution of the Hα, 8 μm, and 24 μm emission for an instantaneous burst of star formation. In order to subtract the stellar continuum from the 8 μm emission, we also calculated the ratio of the flux in the 3.6 μm and 8 μm *Spitzer*-IRAC bands for the same decaying population without including any dust contribution. These calculations were performed with *CIGALE* v.2018.0.1 (Boquien *et al.* 2019). The stellar populations were modeled after the BC03 (Bruzual & Charlot 2003) models assuming solar metallicity. We considered models with Salpeter (Salpeter 1955) or Chabrier (Chabrier 2003) IMFs, values for the absorption $E(B-V) = 0.3, 1.0$, nebular component ionization parameter $U = -1.0, -2.0, -3.0, -4.0$, and two dust emission models: those of Dale *et al.* 2014 and Draine & Li 2007. We explored different values of the α parameter in the (Dale *et al.* 2014) dust model and of the PAH mass fraction (*qpah*) and limiting ionization field (U_{min}) for the Draine *et al.* (2014) models. The response functions presented in Fig. 3.9 are the average of the results from the different models. A more detailed discussion of the response functions and the parameters they depend on will be presented in Kouroumpatzakis et al. (in prep). Similar investigations for various SFR indicators have been presented in previous works (e.g., Cerviño *et al.* 2016; Boquien *et al.* 2014) but for different SFR indicators than those used here or for more complex SFHs, which complicate the disentanglement of the contribution of different stellar populations to the measured SFR.

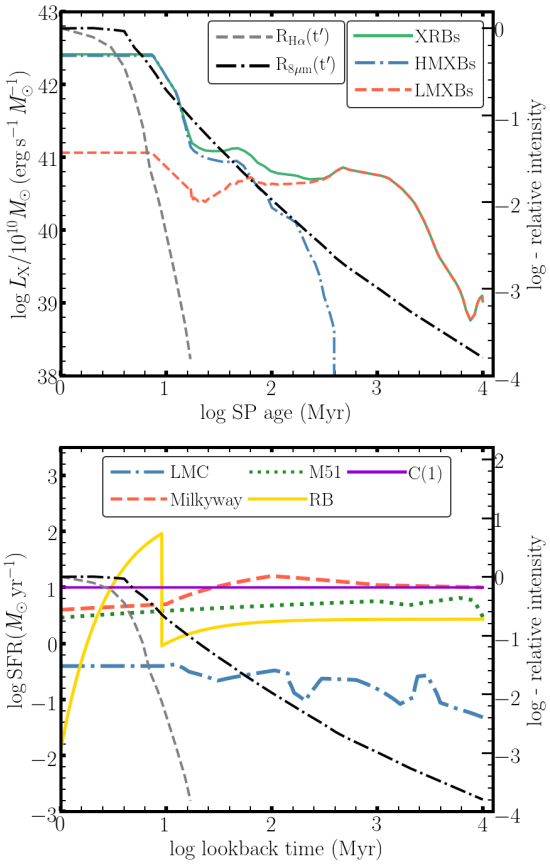

Figure 3.9: Upper panel: Bolometric X-ray luminosity per $M_\star$ (in units of $10^{10}\,M_\odot$, green line) of a stellar population as a function of the population's age from Fragos *et al.* (2013a). Contributions of HMXBs are shown by the blue dashed-dotted line and of LMXBs by the red dashed line. Response functions for Hα and 8 μm are shown with grey dashed and black dashed-dotted lines respectively, and their scales are shown on the right ordinate. The 24 μm response function is indistinguishable from the 8 μm one. Bottom panel: Measured SFR as a function of lookback time for five indicative SFHs. The SFHs comprise one representing an early-type spiral galaxy, for which we used the Milky Way's (MW) SFH (Xiang *et al.* 2018), the SFH of the Large Magellanic Cloud (LMC) as a proxy for a dwarf galaxy dominated by a recent star-formation episode (Harris & Zaritsky 2009), the SFH of M51 (Eufrasio *et al.* 2017) as a galaxy with a peak of star formation around 200 Myr ago, the SFH of a galaxy with a resent star-formation burst (RB), formulated as a double exponential model (Boquien *et al.* 2019) with $t_0 = 4000$ Myr, $t_1 = 3000$ Myr, $\tau_0 = 1000$ Myr, $\tau_1 = 1000$ Myr, and $\kappa = 10$, and a galaxy with constant SFR throughout its history with SFR $= 10^1\,M_\odot\,yr^{-1}$(labeled "C(1)") for reference. These SFHs are presented with red dashed, blue dashed-dotted, green dotted, yellow, and purple lines respectively. Gray dashed and black dash-dotted lines show the response functions from the upper panel.

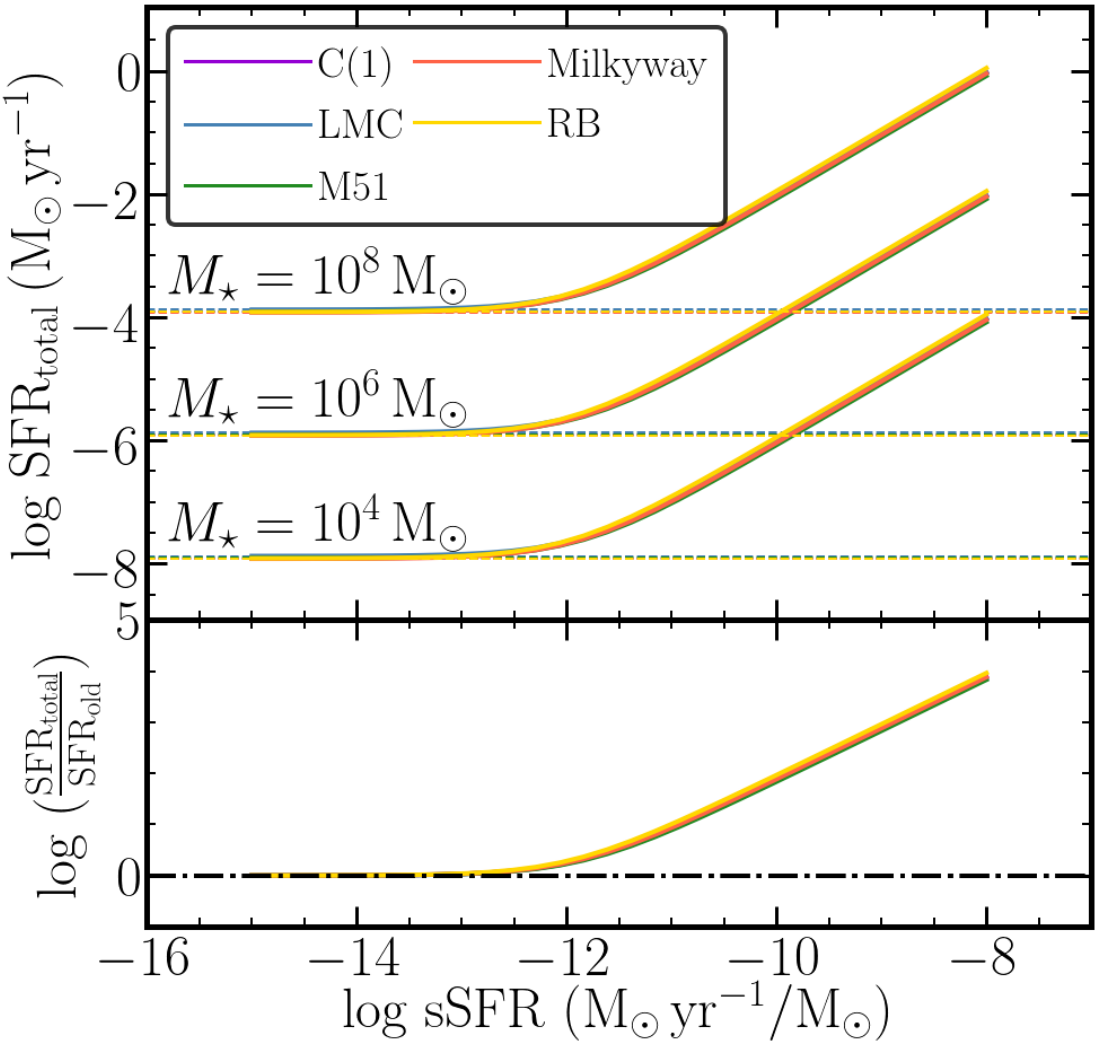

Figure 3.10: Upper panel: Inferred Hα-based SFR separating the contribution of young and old stellar populations as a function of sSFR for three stellar population masses. The lines are based on *CIGALE* simulations using the five SFHs presented in Fig. 3.9 with young and old stellar populations separated at 100 Myr. Solid lines represent total SFR, and dashed lines represent the contribution of the old stellar populations. Results are nearly identical for all SFHs. Bottom panel: ratio $\mathrm{SFR}_{total}/\mathrm{SFR}_{old}$ as a function of sSFR.

or younger stellar populations is:

$$\mathrm{SFR}_\chi = \frac{\int_0^t \mathrm{SFH}(t') R_\chi(t')\, dt'}{\int_0^t R_\chi(t')\, dt'} \quad . \tag{3.10}$$

Figure 3.9 shows five example SFHs, and results for each one are presented in Table 3.8. We expect variations in the SFR for the different SFH scenarios only if the SFR changes within the time window of each indicator (e.g., largest difference for the RB example).

Another way to show differences in the average stellar population ages traced by the different SFR indicators χ is the effective age of the stellar population for given SFH:

$$t_{\mathrm{eff},\chi} = \frac{\int_0^t t' R_\chi(t') \mathrm{SFH}(t')\, dt'}{\int_0^t R_\chi(t') \mathrm{SFH}(t')\, dt'} \quad . \tag{3.11}$$

Hα emission traces the youngest stellar populations ($t_{\mathrm{eff}} \leq 10\,\mathrm{Myr}$: Table 3.8) almost unaffected by the different SFHs. When there is a recent burst of star formation, the IR indicators trace stellar populations with younger average ages (e.g., for RB $t_{\mathrm{eff}} \simeq 200\,\mathrm{Myr}$), but when the SFH is not dominated by a recent star-formation burst, the same indicators trace much older stellar populations ($t_{\mathrm{eff}} \simeq 600\,\mathrm{Myr}$).

Although the 8 and 24 μm SFR-indicator response functions trace fairly well the HMXB X-ray luminosity as a function of time (Fig. 3.9), they can be affected by emission from stars older than those that can form HMXBs. Thus these indicators can overestimate the SFR when a stellar population is dominated by older stars and has larger t_{eff} (Table 3.8). In addition, because $\gtrsim$60 Myr populations do not contribute to the formation of HMXBs (e.g., Fragos *et al.* 2013a; Garofali *et al.* 2018; Antoniou *et al.* 2019a), the L_X–SFR scaling relations based on the 8 and 24 μm indicators will result in lower scaling factors for galaxies with SFHs not dominated by a recent burst. Therefore, Hα is the most appropriate proxy to trace the young HXMB populations as demonstrated by the tighter Hα-based scaling relations (Table 3.4.3).

All of the SFR indicators can break down in regions with extremely low SFR. In such regions, UV photons originating from A-type or post-AGB stars may give significant contributions. The UV luminosity emitted by a stellar population is the sum of the emission from *young* and *old* stars. The Hα SFR indicator is based on the *number* of Lyman continuum photons, assuming that all the Lyman photons are absorbed by the gas (case B recombination). The 8 μ m indicator is based on the number of photons at somewhat longer UV wavelengths, while the 24 μ m indicator is based on the UV *luminosity*, assuming all the energy is absorbed by dust and reradiated.

In order to quantify the contribution of older stellar populations when measuring extremely low SFRs from Hα, we calculated separately the SFRs that would be measured for the old and young populations in the aforementioned *CIGALE* simulations for the five SFH scenarios. We considered as *young* stars with ages <100 Myr and the rest as *old*. Lyman-continuum photons produced by each population were converted to the equivalent SFR via the Kennicutt (1998) factor. Dividing by stellar mass gave the equivalent sSFR. The results are shown in Figure 3.10. Older stellar populations make no significant contribution to the ionizing-photon budget in regions with sSFR $\gtrsim 10^{-12}\,\mathrm{M_\odot\,yr^{-1}/M_\odot}$. Even this upper limit assumes that all UV photons from the older stellar populations contribute to the ionization of the interstellar medium, but in real spiral galaxies, many such photons escape. Therefore, the derived limiting sSFR is a conservative limit for trustworthy SFRs from young stellar populations, but lower sSFR than this value cannot be reliably measured by Hα. This limiting sSFR is insensitive to the SFH. The corresponding limiting SFR of course depends on stellar mass. At the sSFRs of the most actively star-forming regions in our sample the ionizing photon production rate exceeds that of the old by 4dex. For the present study, as shown in Fig. 3.1, at most 3.5% of the regions (and fewer for the regions smaller than $4\times4\,\mathrm{kpc}^2$) have sSFR$<10^{-12}\,\mathrm{M_\odot\,yr^{-1}/M_\odot}$, indicating that UV photons from older stellar populations do not affect our present conclusions.

The X-ray luminosity for each SFH scenario (Fig. 3.9) is:

$$L_X^{\upsilon}(t) = \int_0^t \left(\frac{L_X(t')}{M_\star}\right)_{\upsilon} \mathrm{SFH}(t')\,dt' \quad , \tag{3.12}$$

where υ indicates the particular XRB population (HMXBs, LMXBs, XRBs), and $M_\star$ is the total stellar mass of the parent stellar population of the XRBs. The results of these calculations show $\geq$0.85 dex differences in the X-ray luminosity produced by the HMXBs and LMXBs regardless of the SFH assumed. This difference is larger for SFHs with more intense and more recent star-formation episodes.

A metric of the relative contribution of HMXB and LMXB populations in the integrated X-ray luminosity is the ratio (α/β) used in Eq. 3.8. Given that $L_{X,\mathrm{HMXB}} = \alpha\mathrm{SFR}$, and $L_{X,\mathrm{LMXB}} = \beta M_\star$, we can calculate the theoretically expected α'/β' ratio from the X-ray luminosity of the LMXB and HMXB populations given an SFH (Eq. 3.12).

$$(\alpha'/\beta')_\chi = \frac{L_{X,\mathrm{HMXB}}}{\mathrm{SFR}_\chi} \Big/ \frac{L_{X,\mathrm{LMXB}}}{M_\star} \tag{3.13}$$

for each SFR indicator (Eq. 3.10). The results for these calculations are presented in Table 3.8. The continuous SFH gives $\alpha'/\beta' = 10^{-10.01}\,\mathrm{M_\odot\,yr^{-1}/M_\odot}$. LMC-like or RB-like SFHs, with a recent star-formation episode, show $\alpha'/\beta' > 10^{-10.01}\,\mathrm{M_\odot\,yr^{-1}/M_\odot}$. On the other hand, MW and M51, which comprise far older stellar populations, show $\alpha'/\beta' < 10^{-10.01}\,\mathrm{M_\odot\,yr^{-1}/M_\odot}$, indicating a larger contribution of LMXBs to the total X-ray luminosity.

3.5.2 Distributions of X-ray luminosity for regions with different sSFR

If the X-ray emission arises from a population of HMXBs, it would be expected to scale linearly with SFR. The scaling factor depends on the formation efficiency of HMXBs and their integrated luminosity per unit SFR, which is a function of their age (Figure 3.9, Section 3.5.1). Therefore, the galaxy-wide scaling relations are expected to extend to lower SFR even on sub-galactic scales if the average properties of the stellar populations (age and metallicity) are the same. Any deviations from this linear relation or change in slope indicates a different XRB population. As discussed in Section 3.4.2, we observe an excess of X-ray emission in the low SFR regime compared to the extrapolation of the linear L_X–SFR relation from higher SFR. The excess can be quantified as the ratio of the measured luminosity to the one expected from the linear scaling relation of M14,

$$L_{X,\mathrm{excess}} = \log L_X / L_{X,\mathrm{M14(SFR)}} \quad . \tag{3.14}$$

Fig. 3.11 shows histograms of the excess in regions of different sSFR. The modes and 68.3% confidence intervals of these distributions are presented in Table 3.9. Regions with lower sSFR exhibit systematically higher excess, including the highest values seen. The bin of sSFR $\leq 10^{-12}$, in particular, isolates sub-galactic regions with very low current star formation, where no massive young stars and consequently HMXBs are expected. At these sSFRs, the dominant source of X-ray emission is expected to be LMXBs (e.g., Pancoast *et al.* 2010).

In regions encompassing large enough stellar mass, the collective emission of cataclysmic variables (CVs) and coronally active binaries (ABs) may have non-negligible contribution, particularly at the very low integrated X-ray luminosities probed ($\leq 10^{35.5}$ erg s^{-1}). The relation between the X-ray luminosity from these components ($L_{X,\mathrm{stellar}}$) and K-band luminosity (Boroson *et al.* 2011) is:

$$\frac{L_{X,\mathrm{stellar}}}{(\mathrm{erg\ s^{-1}})} = 9.5^{+2.1}_{-1.1} \times 10^{27} L_{K\odot} \tag{3.15}$$

Table 3.9: Median excess $L_{X,0.5-8\mathrm{keV}}$ over the expected by M14 in bins of different sSFR. The number of sub-galactic regions included in each bin is given in parentheses.

Size (kpc^2)	sSFR $\leq 10^{-12}$	$10^{-12} \leq$ sSFR $\leq 10^{-10}$	$10^{-10} \leq$ sSFR
1×1	2.73 ± 1.08 (34)	1.45 ± 0.77 (1263)	1.1 ± 0.83 (617)
2×2	2.24 ± 0.95 (14)	1.25 ± 0.77 (403)	0.71 ± 0.84 (157)
3×3	2.06 ± 1.1 (8)	1.23 ± 0.75 (225)	0.68 ± 0.89 (76)
4×4	1.6 ± 1.08 (9)	1.15 ± 0.78 (146)	0.56 ± 0.94 (48)

where $L_{K\odot}$ is in solar luminosities (a proxy of the total stellar mass they encompass). Because in this work we used 3.6 μm as a proxy of stellar mass, we converted 3.6 μm to K-band luminosities.* For most of the regions, CVs' and ABs' stellar contribution to the X-ray luminosity is less than observed by more than 1 dex (98%, 95%, 91%, and 90% of the 1×1, 2×2, 3×3, and 4×4 kpc^2 regions respectively), even for regions with extremely high stellar mass (Fig 3.12). However, there are a handful of regions where the calculated stellar X-ray luminosity is comparable to the observed X-ray luminosity, but they also exhibit high relative uncertainties. This minority of regions is not sufficient to explain the observed X-ray luminosity excess. Alternatives being insufficient, the bulk of the X-ray luminosity excess found in the low SFR regime must come from LMXB emission.

3.5.3 Comparison with galaxy-wide scaling relations

Sub-galactic regions show a shallower slope of L_X–SFR (Table 3.4.3, Fig. 3.5) compared to the M14 relation for all cases considered in this work. This is driven by regions with high X-ray luminosity at SFR $\leq 10^{-3}\,\mathrm{M_\odot yr^{-1}}$, particularly at the smallest physical scales. For reference, the lowest SFR used in the derivation of the galaxy-wide scaling relation was $\sim 10^{-1}\,\mathrm{M_\odot\,yr^{-1}}$, whereas our analysis extends to 5 dex lower SFR. The X-ray emission of these regions arises from an unresolved population of LMXBs (Section 3.5.2). The inclusion of the stellar mass as a parameter (Eq. 3.8) accounts for the LMXB contribution, particularly in regions with low SFR or those dominated by older stellar populations (low sSFR). As a result we obtain good fits with linear scaling of the X-ray luminosity with respect to both the SFR and stellar mass.

Even though our L_X–SFR–$M_\star$ fits follow a different approach from L16, by fitting sub-galactic regions and including an intrinsic scatter term (Eq. 3.8), our results are in

* The 3.6 μm to K-band magnitudes were calibrated and converted using the complete SFRS. The linear correlation found is:

$$m_K = 1.876 \pm 0.1 + 1.10 \pm 0.01 m_{3.6\mu m} \quad . \tag{3.16}$$

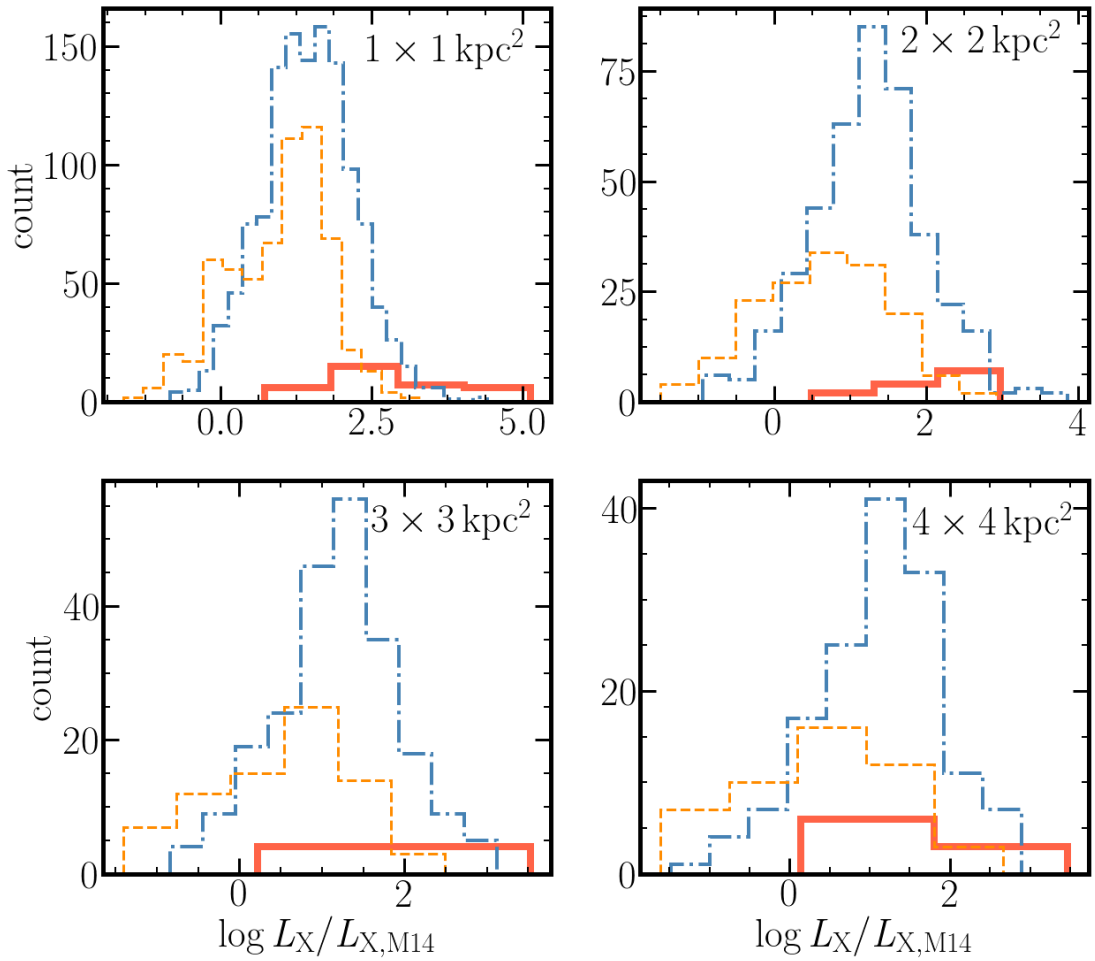

Figure 3.11: Histograms of excess X-ray luminosity relative to the M14 relation (Eq. 3.14). Panels show the distributions for sub-galactic regions as labeled. Regions with sSFR $\geq 10^{-10}$, $10^{-12} \leq$ sSFR $\leq 10^{-10}$, and sSFR $\leq 10^{-12}$ are represented by orange dashed, blue dashed-dotted, and thick red lines respectively. The Hα-based SFR was used here.

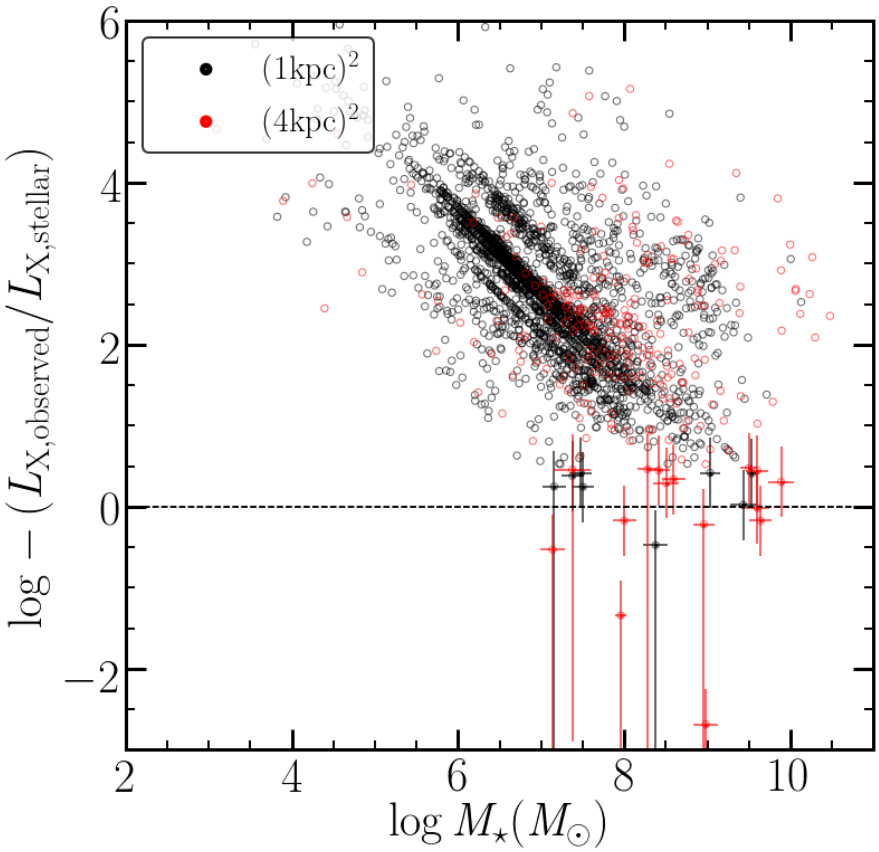

Figure 3.12: Observed X-ray luminosity over the expected stellar X-ray luminosity (Eq. 3.15) as a function of the stellar mass for sub-galactic regions of 1×1 (black) and $4 \times 4\,\mathrm{kpc}^2$ (red). Error bars are shown for regions with $\log(L_{X,\mathrm{observed}}/L_{X,\mathrm{stellar}}) \leq 0.5$. Other regions are represented only by circles to avoid clutter.

good agreement (Fig. 3.8) with only small differences in the best-fit parameters. The main difference is that we find significant intrinsic scatter. We interpret the scatter as the result of stochastic effects. In all cases, the Hα SFR indicator gives the lowest scatter and the best agreement with the relation of L16 (despite their use of UV and far-IR instead of Hα-based SFR tracers). However, we do find differences with the Lehmer *et al.* 2019 scaling relations, which are based on integration of the XRB luminosity functions (XLFs) derived for different sSFR regimes. More specifically, while for the largest physical scales ($4{\times}4\,\mathrm{kpc}^2$) and the scaling with SFR (parameter α) in the L_X–SFR–$M_\star$ fit (Eq. 3.8) we find good agreement for all SFR indicators used, in the case of smaller physical scales, we find increasing L_X–SFR scaling factors (Table 3.4.3). This can be explained by the local variations of stellar populations between the different regions, which results in localised variations of the L_X/SFR scale factor (e.g., Section

3.5.1). This effect in combination with stochastic sampling of the XLF results in a few regions with high X-ray luminosity (because of the presence of very young populations and/or luminous individual sources) and therefore small L_X and SFR uncertainties, that can drive the fits to steeper slopes. At larger scales, local variations in the X-ray emission and stellar populations are averaged out, and the scaling relations approach the galaxy-wide relations. On the other hand, the L_X–$M_\star$ scaling (parameter β in Eq. 3.8) is consistent with Lehmer *et al.* (2019) for most SFR indicators and spatial scales we consider. The smoother spatial distribution of the older stellar populations and the weak L_X–age dependence of the X-ray binaries associated with them results in more uniform sampling regardless of physical scales and therefore consistent L_X–$M_\star$ scaling factors through the different physical scales.

3.5.4 Intrinsic scatter & stochasticity

The wide range of SFRs and stellar masses probed in our study (Fig. 3.1, Table 3.2.1) is ideal for examining the intrinsic scatter under conditions found in nearby galaxies. This scatter could be the result of (a) Poisson sampling of sparsely populated luminosity functions or (b) time variability of XRBs (e.g., Gilfanov 2004). Such scatter has been previously reported in galaxy-wide scaling relations, particularly at lower SFRs (e.g., Mineo *et al.* 2014; Lehmer *et al.* 2019). However, as discussed in Section 3.5.1, an additional source of scatter could be stellar population differences through their effect on the inferred SFR and the age-dependent X-ray output of stellar populations.

There is intrinsic scatter in the sub-galactic L_X–SFR (Table 3.4.3) and L_X–SFR–$M_\star$ (Table 3.4.3) correlations. However, we do not find any evidence for anti-correlation of the intrinsic scatter with the SFR (Table 3.4.3) as would be expected from stochasticity or time variability. This could be the result of the large uncertainties in the SFR and X-ray luminosity measurements for the individual regions at low SFR, which could mask any such trend. On the other hand, the overall intrinsic scatter we measure both in the L_X–SFR and the L_X–SFR–$M_\star$ relations (typically 0.5–1.0 dex) is larger than the scatter observed in the galaxy-wide relations (e.g., $\leq$0.37 dex in L16). This additional scatter could be the result of bright X-ray sources in some of the individual regions. However, typically less than 3% of the regions in each galaxy of our sample encompass individually detected X-ray sources, making them an unlikely source for the increased scatter on sub-galactic regions.

One parameter that is particularly important on sub-galactic scales is local variations of the stellar populations, such as those resulting from the spiral structure, localized star-formation episodes, sequential star formation, and metallicity gradients. XRB

population synthesis models show that the X-ray emission for an ensemble of XRBs is a strong function of the age and metallicity of their parent stellar populations (e.g., Fragos *et al.* 2013a; Dray 2006; Linden *et al.* 2010; Lehmer *et al.* 2019). This is supported by observational studies of the XRB populations associated with different stellar generations (e.g., Antoniou & Zezas 2016; Antoniou *et al.* 2019b) or populations of different metallicity (e.g., Mapelli *et al.* 2010; Prestwich *et al.* 2013; Douna *et al.* 2015; Brorby *et al.* 2016). On galaxy-wide scales, any local variations of the stellar populations and the corresponding X-ray emission can be smeared out giving an average L_X/SFR value for the entire galaxy. On the other hand, local variations of the stellar populations within a galaxy (which can vary in age from a few Myr for very young star forming regions to several Gyr for interarm regions) can result in very different X-ray emission efficiency as discussed in Section 3.5.1.

An additional source of scatter could be local variations of absorption. In order to correct for this one would need spatially resolved extinction and $N_{\rm H}$ maps from X-ray spectral fits in each sub-galactic region, which are not available for these data (c.f. Section 3.2.4). Furthermore as discussed in Section 3.4.2, the absorption in Hα and soft X-rays is similar, which reduces the effect of differential extinction across the galaxies.

A general trend is that scaling relations based on the Hα emission show lower scatter than the relations based on the 8 μm and 24 μm SFR indicators. Hα emission traces the stellar populations with ages $\sim$10 Myr (Fig. 3.9; Table 3.8) which are most relevant to the HMXBs (which have lifetimes $\leq$30 Myr; Section 3.4.2). On the other hand, although the IR-based SFR indicators still trace young stellar populations, they are sensitive to a much wider range of ages. Therefore, they are not a clean proxy for the star-formation episodes that produced the HMXBs. This mismatch between the formation timescales of the HMXBs and the star-formation timescales probed by the different SFR indicators could be the origin of the larger scatter we measure in the sub-galactic scaling relations in comparison to the galaxy-wide relations. This is because sub-galactic regions may have significant variations in their SFHs compared to the overall galaxy averages.

3.6 Summary

We present scaling relations between L_X–SFR–$M_\star$ on sub-galactic scales using a maximum likelihood method that takes into account the posterior (not necessarily Gaussian) uncertainty distributions of all the data. In this way we obtain unbiased scaling relations by including in our analysis regions that have extremely low SFRs, stellar masses and X-ray luminosities which otherwise would be omitted. This analysis ex-

tends the L_X–SFR and the L_X–SFR–$M_\star$ relations down to SFRs $\simeq 10^{-6}\,\mathrm{M_\odot\,yr^{-1}}$, and sSFRs $\simeq 10^{-14}\,\mathrm{M_\odot\,yr^{-1}/M_\odot}$. These are 5 dex and 2 dex lower in SFR and sSFR respectively than existing galaxy-wide scaling relations. In the L_X–SFR correlation, slopes are shallower than linear on all sub-galactic scales (1×1, 2×2, 3×3, and 4×4 kpc^2) and by all SFR indicators (Hα, 8 μm, and 24 μm) used in this work. This shallower slope is driven by regions with high X-ray luminosity at low SFR ($\leq 10^{-3}\,\mathrm{M_\odot\,yr^{-1}}$), probably due to a population of LMXBs. For larger sub-galactic regions, correlations of L_X–SFR converge to the integrated galactic emission relations.

The full-band X-ray luminosity fits are very similar to those of the hard band. Although the use of the full X-ray band increases the scatter in the correlations, it integrates more flux and therefore can be very useful for low-X-ray-luminosity objects. The extended relations we present can be used to model the X-ray output of extremely low-SFR galaxies. However, one should be careful about two effects:

(a) Excess X-ray luminosity at SFRs $\leq 10^{-3}\,\mathrm{M_\odot\,yr^{-1}}$ requires accounting for LMXBs by using the L_X–SFR–$M_\star$ relation. The L_X–SFR scaling relation will be inaccurate because of this older population (Section 3.5.2).

(b) There is strong dependence of the SFR indicators on the SFHs of the galaxies (e.g., Section 3.5.1; Boquien *et al.* 2014). The same holds for the X-ray output of a stellar population as a function of its age or metallicity. This is particularly important for dwarf galaxies that might be dominated by star-formation bursts at different epochs. In order to mitigate these effects when studying the connection between X-ray luminosity and stellar populations, ideally one should use the SFH of a galaxy instead of an instantaneous SFR metric (e.g., Antoniou *et al.* 2019b).

We find no evidence for increasing intrinsic scatter in regions of lower SFR, but the overall scatter of the L_X–SFR–$M_\star$ correlations is larger than galaxy-wide relations. We attribute this to local variations of the SFH within a galaxy. The intrinsic scatter measured depends on the SFR indicator and X-ray band used. The combination of the hard band and Hα-based SFR shows the tightest correlation and the smallest intrinsic scatter in both the L_X–SFR and L_X–SFR–$M_\star$ correlations. For individual galaxies at very low SFRs, stochastic sampling of the IMF, the XLF, and source variability may result in increased scatter in their integrated X-ray luminosity. However, the scaling relations we derive should hold *on average* for the low-SFR population (subject to the caveats discussed above).

3.7 Maximum likelihood method

We fit a linear model with intrinsic scatter to the SFR and X-ray luminosity of the regions of all galaxies. Specifically, we consider the errors-in-variables regression model:

$$\begin{aligned} x_i &= x_i^t + \eta_i \\ y_i &= y_i^t + \zeta_i \\ y_i^t &= a x_i^t + b + \epsilon\left(x_i^t\right) \quad , \end{aligned} \tag{3.17}$$

where x_i and y_i are the observed $\log \mathrm{SFR}$ and $\log L_X$ of the i-th region, while x_i^t and y_i^t are the respective intrinsic values; η_i and ζ_i denote the error distributions on x_i and y_i respectively.* For the intrinsic scatter ϵ we consider two cases: (i) constant:

$$\epsilon\left(x_i^t\right) = \sigma \quad , \text{ where } \sigma \geq 0 \tag{3.18}$$

and (ii) including a term linear in the logarithm of SFR:

$$\epsilon\left(x_i^t\right) = \max\left\{0, \sigma_1 x_i^t + \sigma_2\right\} \tag{3.19}$$

where the 'max' function ensures that the intrinsic scatter is non-negative.

Assuming independent measurements, the posterior probability of the model parameters, $\vec{p} = (a, b, \sigma)$ or $(a, b, \sigma_1, \sigma_2)$:

$$\pi(\vec{p}) \prod_i P(x_i, y_i | \vec{p}) \quad , \tag{3.20}$$

where the prior is the product of the priors of each parameter

$$\pi(\vec{p}) = \pi(a)\pi(b)\pi(\sigma) \quad \text{or} \quad \pi(a)\pi(b)\pi(\sigma_1)\pi(\sigma_2) \quad , \tag{3.21}$$

and the datum likelihood is the marginalization of the likelihood considering all possible

* η_i and ζ_i are not normally distributed because they represent the logarithmic transformation of the truncated Gaussian errors on SFRs (zero-truncated) and the logarithm of the X-ray luminosity (Section 3.3)

values for the intrinsic SFR and X-ray luminosity

$$P(x_i, y_i|\vec{p}) = \iint P(x_i, y_i, x_i^t, y_i^t|\vec{p})\, dx_i^t\, dy_i^t \quad . \tag{3.22}$$

Considering that (i) the observed values depend only on the measurement errors and the intrinsic values, (ii) the intrinsic values depend only on the intrinsic model, and (iii) the errors on x_i and y_i are independent, the integrand of (3.22) becomes

$$P\left(x_i|x_i^t, \eta_i^t\right) P\left(y_i|y_i^t, \zeta_i^t\right) P(y_i^t|x_i^t, \vec{p}) P(x_i^t|\vec{p}) \quad , \tag{3.23}$$

where the probability of x_i and y_i was computed using the corresponding distributions of η_i and ζ_i, the prior on x_i^t was chosen to be uniform between two bounds $x_{\rm min}^t$ and $x_{\rm max}^t$ (ensuring that they enclose all the observed values x_i and 3σ around them), and the probability of y_i^t was given by the normal distribution density considering the intrinsic mean and scatter:

$$\left(\frac{1}{2\pi\epsilon^2\left(x_i^t\right)}\right)^{1/2} \exp\left[-\frac{\left(y_i^t - a x_i^t - b\right)^2}{2\epsilon^2\left(x_i^t\right)}\right] \quad . \tag{3.24}$$

The model parameters a, b and σ (or σ_1 and σ_2) were estimated by sampling the posterior distribution using the Markov Chain Monte Carlo technique. Specifically, we used the `emcee 3.0rc2` package for Python 3 (Foreman-Mackey *et al.* 2013b) with uniform priors for the model parameters, sufficiently wide to not be very informative but narrow enough to aid the convergence of the MCMC chains, i.e., $a \in [0, 2]\,, b \in [38, 41]\,, \sigma \in [0, 2]\,, \sigma_1 \in [-1, 1]$ and $\sigma_2 \in [0, 2]$. The priors were also used to sample the initial positions of the Markov chains.

In order to fit the scaling with both the SFR and the stellar mass, i.e.,

$$\log L_{\rm X} = \log(10^{\alpha + \log {\rm SFR}} + 10^{\beta + \log {\rm M}_\star}) + \sigma \quad , \tag{3.25}$$

we employed the intrinsic mean model

$$y_i^t = \log\left(10^{\alpha + x_i^t} + 10^{\beta + m_i^t}\right) \quad , \tag{3.26}$$

where m_i^t is the logarithm of the stellar mass of the i-th region with error distribution ξ_i

with respect to its intrinsic value:

$$m_i = m_i^t + \xi_i \quad . \tag{3.27}$$

Now, the datum likelihood is a triple integral,

$$P(x_i, m_i, y_i|\vec{p}) = \iiint P\left(x_i, m_i, y_i, x_i^t, m_i^t, y_i^t|\vec{p}\right) \quad , \tag{3.28}$$

but using the same assumptions as before (i.e., independent measurements), the integral is the same as in equation 3.23 with an additional multiplicative PDF term for the stellar mass measurement $P\left(m_i|m_i^t, \xi_i\right)$.

Results are shown in Figures 3.5, 3.6, 3.7, and 3.8 and Tables 3.4.3, 3.4.3, and 3.4.3. An example of the results of the fits is shown in Fig. 3.13.

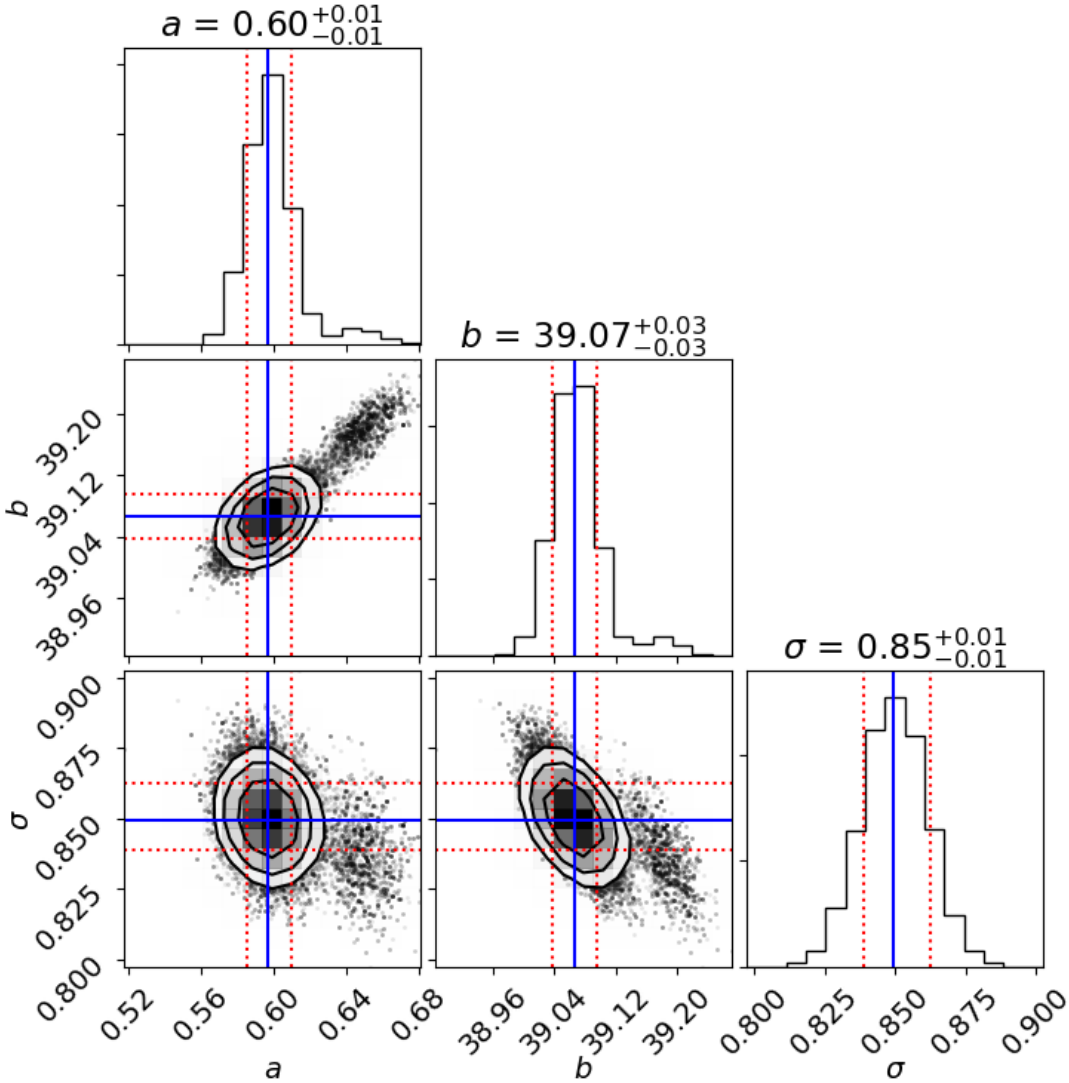

Figure 3.13: The marginal posterior distributions of the three parameters of the model: $\log L_{\rm X} = a\,\log{\rm SFR} + b + \sigma$ in the case of Hα SFR and $1\times1\,{\rm kpc}^2$ sub-galactic regions.

Acknowledgements

The authors thank the anonymous referee for comments that helped to improve the clarity of the paper. K. K., A. Z., and K. K. acknowledge funding from the European Research Council under the European Union's Seventh Framework Programme (FP/2007-2013)/ERC Grant Agreement n. 617001 (A-BINGOS). This project has received funding from the European Union's Horizon 2020 research and innovation programme under the Marie Sklodowska-Curie RISE action, grant agreement No 691164 (ASTROSTAT). AZ also acknowledges support from *Chandra* grant G02-3111X.

K. K. thanks Dan Foreman-Mackey for insightful suggestions regarding the `emcee` package and MCMC fits (private communication). This work used data obtained with the *Spitzer* Space Telescope, which is operated by the Jet Propulsion Laboratory, California Institute of Technology under a contract with NASA. This research has made use of the NASA/IPAC Extragalactic Database (NED), which is operated by the Jet Propulsion Laboratory, California Institute of Technology, under contract with the National Aeronautics and Space Administration.

This page intentionally left blank

4

Metallicity and X-ray luminosity variations in NGC 922

4.1 Introduction

Ring galaxies (RiGs) appear to form after a very special interaction where a small companion passes through a disk galaxy (e.g. Lynds & Toomre 1976; Theys & Spiegel 1976; Hernquist & Weil 1993; Mihos & Hernquist 1994). This gravitational perturbation generates symmetrical waves or caustics through the galactic disk (e.g. Struck-Marcell & Lotan 1990) leading to the creation of an enhanced star-formation ring (e.g. Appleton & Marston 1997). This relatively brief interaction gives rise to coeval star-formation in the ring, which provides an excellent environment to study the star-forming activity, neutral gas distribution, and metallic abundance in galaxy interactions.

The gas-phase metallicity is a key characteristic of any galactic environment. For example there is a well-known correlation between metallicity and stellar mass ($M_\star$) in the general galaxy population (e.g. Lequeux *et al.* 1979; Tremonti *et al.* 2004; Kewley & Ellison 2008). Studies of local star-forming galaxies have shown a negative metallicity gradient with increasing galactocentric radius (e.g. Vila-Costas & Edmunds 1992; Zaritsky *et al.* 1994; van Zee *et al.* 1998; Moustakas *et al.* 2010; Lian *et al.* 2018). RiGs provide a unique environment to explore the effect of a quasi-symmetric radial disturbance of

the galaxy disk on its metallicity gradient. Prominent RiGs (e.g. the Cartwheel galaxy, Arp 147, Lindsay-Shapley ring, Arp 284) show overall sub-solar metallicities (e.g. Fosbury & Hawarden 1977; Few *et al.* 1982; Higdon & Wallin 1997; García-Vargas *et al.* 1997; Fogarty *et al.* 2011). However, there are cases of rings in RiGs with higher oxygen and nitrogen abundance compared to their bulges (e.g. Bransford *et al.* 1998; Egorov & Moiseev 2019). This indicates that overall RiGs do not follow the metallicity gradient profile seen in disk galaxies. This could be because of the mixing of gas from different regions of the disk as a result of the interaction.

An interesting feature of RiGs, that is directly linked to the age of the stellar populations in the ring and/or their metallicity, is their association with populations of Ultra-Luminous X-ray sources (ULXs). These are generally defined as X-ray sources with luminosity in excess of 10^{39}erg s^{-1}(e.g. Kaaret *et al.* 2017, and references therein). RiGs show an excess of X-ray luminosity (L_X) and number of ULXs compared to typical star-forming galaxies (e.g. Wolter *et al.* 1999, 2015). For example, the Cartwheel galaxy, the epitome of nearby RiGs, shows the largest number of ULXs (16) for a single galaxy (Wolter & Trinchieri 2004). In addition, the X-ray luminosity function (XLF) of RiGs appears to be flatter than the typical XLF of star-forming galaxies, although with the current data this difference is not statistically significant (e.g. Wolter *et al.* 2018).

It has been proposed that the observed excess of ULXs in RiGs is driven by the low metallicity of their galactic environment (e.g. Mapelli *et al.* 2009). Indeed, more recent studies support the idea that the X-ray luminosity per unit star-formation rate (L_X/SFR) is a function of metallicity, favoring low metallicity environments (e.g. Fragos *et al.* 2016; Brorby *et al.* 2016; Madau & Fragos 2017; Fornasini *et al.* 2020).

NGC 922 is a C-shaped galaxy with an off-centre star-forming bar and a semi-complete star-forming ring that is the result of an off-axis passage of a dwarf companion through the disk of a spiral galaxy (Wong *et al.* 2006). It has a recession velocity $v_r = 3082.46 \pm 5.40$ km/s corresponding to a distance of 42.46 ± 2.48 Mpc (Koribalski *et al.* 2004). It contains a higher abundance of neutral gas for a galaxy of its size, compared to typical star-forming galaxies (Elagali *et al.* 2018b). The interaction with the dwarf companion has triggered a star-formation episode in the bulge ~ 300 Myr ago, that continues until now. The ring on the other hand is dominated by very recent star-forming activity (< 10 Myr ago), as witnessed by a population of very young star clusters (~ 7 Myr), while in the bulge there is a combination of young and older star clusters ($\gtrsim 100$ Myr; Pellerin *et al.* 2010).

NGC 922 hosts a population of many bright X-ray sources, including nine ULXs which is at odds with its near-solar metallicity (Prestwich *et al.* 2012). Prestwich

et al. (2012) find that the number of ULXs per SFR in NGC 922 is higher than that of the Cartwheel galaxy (but consistent within the uncertainties), despite the near-solar metallicity reported for NGC 922. Furthermore, this ULX rate is higher than the average ULX/SFR rate found for late-type galaxies, but consistent with that found for Sc/Sm or irregular galaxies (Kovlakas *et al.* 2020). All these characteristics make NGC 922 a perfect candidate to study the metallicity variations in RiGs, their relation to the dynamics of the interaction, and their effect on the luminous XRB populations.

In this paper we present long-slit observations of NGC 922. We extracted optical spectra and measured emission-line fluxes and gas-phase metallicities from regions spread on the disk of NGC 922 covering the bulge, the ring, and intermediate positions. We correlate these metallicity measurements with spatially resolved measurements of the stellar mass, SFR, and X-ray luminosity, based on archival multi-wavelength data. In Sections 2 and 3 we present the details of the optical spectroscopic and X-ray observations and the data analysis respectively. The results of the analysis are presented in Section 4. In Sections 5 and 6 we discuss and summarize the results.

In the following analysis we assume a cosmology with $\Omega_{\rm m} = 0.3$, $\Omega_\Lambda = 0.7$, $h = 0.7$, and distance $D = 42.46$ Mpc. We adopt as solar abundances $Z_\odot = 0.0142$, $X_\odot = 0.7154$, and $[12 + \log(O/H)_\odot] = 8.69$ from Asplund *et al.* (2009).

4.2 Observations

We acquired long slit observations targeting the NGC 922 galaxy with the European Southern Observatory (ESO) 3.58m New Technology Telescope (NTT) through the ESO Faint Object Spectrograph and Camera (EFOSC2*). We obtained spectra for three different slit positions on the galaxy. We used the 1.5"-wide slit for slit rotations 1 (P.A. = 68.7°) and 2 (P.A. = −39.7°), and the 2"-wide slit for slit rotation 3 (P.A. = −61.1°). The slit widths correspond to 309 and 412 pc respectively at the distance of the galaxy. The apertures of the spectra extractions were even wider, enough to include emission from multiple star clusters, and limit the stochasticity effects. We used two EFOSC2 grisms: (a) grism #11 which covers the wavelength range of λ 3403–7493 Å, at a dispersion of 4.1 Å/pixel and provides a resolution of 17.2–19.0 Å (FWHM) at 3727 and 7136 Å respectively (*low-resolution* grism), and (b) grism #18 which covers the wavelength range λ 4761–6754 Å, at a dispersion of 2.0 Å/pixel, and provides a resolution of 6.7–8.6 Å (FWHM)† at 5007 and 6563 Å respectively (*high-resolution grism*).

* https://www.eso.org/sci/facilities/lasilla/instruments/efosc.html

† The reported wavelength resolutions are for the 1.5"-wide slit.

Table 4.1: Long slit observations and spectral extractions summary.

Region ID #	Slit rot. ID #	slit pos. ang. degrees	Resolution grism #	frames × exp. time # × (sec)	R.A. (J2000)	Dec. (J2000)
1	1	68.7°	11	3 × 900	02:25:04.4	-24:47:19.2
1	1	68.7°	18	3 × 900	02:25:04.4	-24:47:19.2
2	1	68.7°	11	3 × 900	02:25:05.5	-24:47:54.2
2	1	68.7°	18	3 × 900	02:25:05.5	-24:47:54.2
3	2	−39.7°	11	3 × 900	02:25:04.5	-24:47:16.4
3	2	−39.7°	18	3 × 900	02:25:04.5	-24:47:16.4
4	2	−39.7°	11	3 × 900	02:25:01.5	-24:47:51.0
4	2	−39.7°	18	3 × 900	02:25:01.5	-24:47:51.0
5	3	−61.1°	11	3 × 600	02:25:03.9	-24:48:02.0
6	3	−61.1°	11	3 × 600	02:25:04.5	-24:47:48.3
7	3	−61.1°	11	3 × 600	02:25:05.2	-24:47:32.0
8	3	−61.1°	11	3 × 600	02:25:06.0	-24:47:13.6

The observations were performed under photometric conditions. Observations with slit rotation 1 and 2 received a total exposure of 5400 seconds split in 6 frames. The spectrum obtained at slit rotation 3 had a total exposure of 1800 seconds, split in three frames.

We extracted spectra for a total of eight regions that show significant emission in the two-dimensional spectra. The coordinates and the observational parameters for each extraction region are given in Table 4.1. Regions 1, 2, 3, 4 were observed with both high and low resolution (grisms #11, #18). Regions 5, 6, 7, and 8 were observed only with the low resolution grism #11. Therefore a total of 12 spectral extractions were analyzed, listed in Table 4.1. The lowest signal-to-noise ratio (S/N) spectrum extraction has a median S/N $\sim$ 4.0, at the continuum, with the emission lines having significantly higher S/N. In Figure 4.1 we present the slit placements along with the regions with spectra extractions (following the numbering convention of Table 4.1), overlaid on a composite Hα (F665N) and red continuum (F621M) image of the galaxy from archival HST-WFC3 data (P.I.: A. Prestwich; Program 11836). We also show the location of the X-ray sources obtained from the *Chandra Source Catalog*[*] (CSC; Evans *et al.* 2010). The X-ray sources in Figure 4.1 are colour-coded according to their X-ray luminosity (derived from the flux in the CSC `flux_aper_b` and the distance of the galaxy).

[*] https://cxc.harvard.edu/csc/

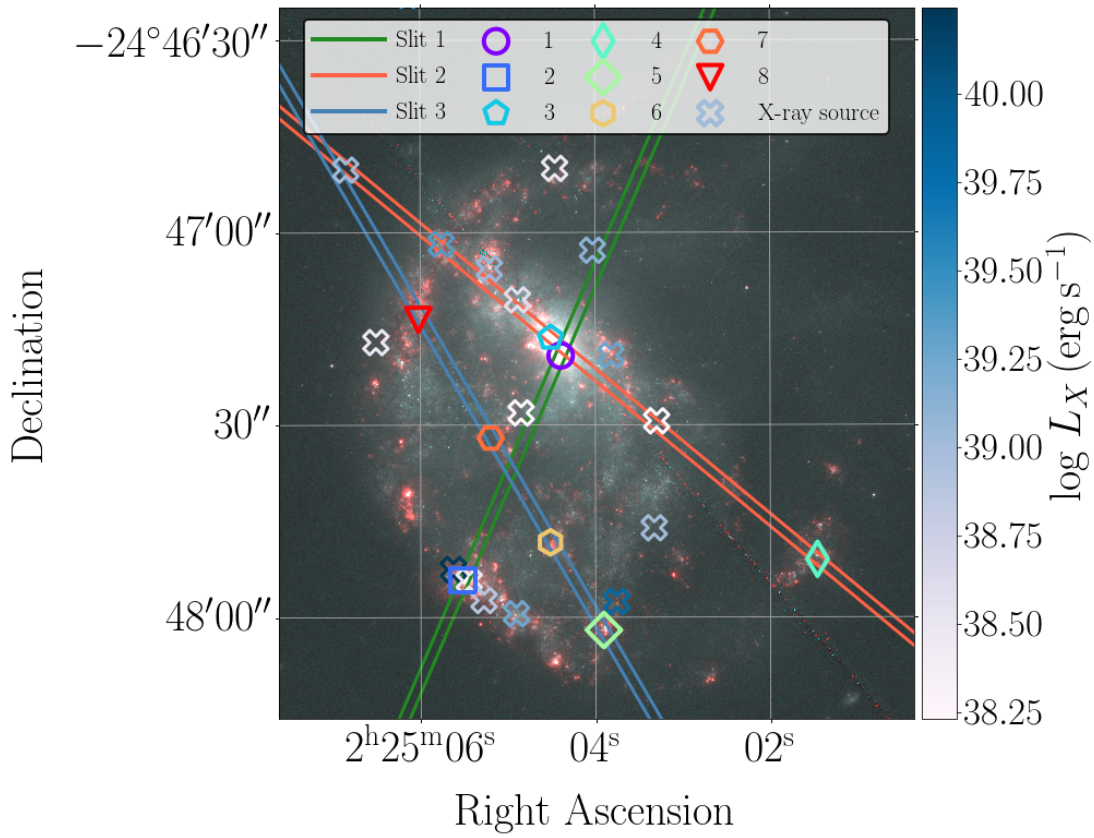

Figure 4.1: Colour composite image of NGC 922 based on HST-WFC3 Hα (F665N; red) and red continuum (F621M; blue/green). The positions of the slits used for this work, and the locations of the individual regions we extracted spectra from, are shown with unique colour and marker style, following the region IDs listed in Table 4.1. X-ray point sources are presented with an open `x` symbol. They are colour-coded according to their X-ray luminosity (calculated from col. `flux_aper_b` in the CSC).

4.3 Data analysis

4.3.1 Optical spectra

We first performed the basic reductions, such as bias subtraction and flat fielding for all the observed images. Because we are interested in spectra from different regions along the slits, the wavelength calibration was performed on the two-dimensional spectra in order to correct for slit distortions. We used spectra from HeNeAr lamps obtained before and after each observation. We used the `IRAF` (Tody 1986, 1993) tasks `identify` and `reidentify` in order to obtain wavelength calibrations for different locations along the slit, and the `transform` task in order to calculate the mapping from (x,y) pixel coordinates to (λ,y) coordinates. We extracted the spectra from the combined images

for each slit position using the `IRAF apall` task.

The spectra were photometrically calibrated with observations of several spectrophotometric standard stars from the catalogue of Massey *et al.* (1988) obtained with each different instrumental setup. The standard-star spectra were reduced the same way as the object spectra. The calibration (sensitivity function) was applied to the object spectra using the `IRAF sensfunc` task.

In general, spectra of galaxies show stellar continuum and strong stellar atmospheric absorption features, including the Balmer lines in addition to any nebular emission component (e.g. Balmer lines that would affect the determination of the stellar component). Therefore subtraction of the stellar light is necessary for the correct measurement of the ionized-gas emission-line flux. We did not attempt to model the nebular continuum component since it is much weaker than the stellar component, and it would not bias the starlight subtraction. We calculated the stellar component by fitting the spectra for each region with the `STARLIGHT` code (Cid Fernandes *et al.* 2005; Mateus *et al.* 2006). We used a base consisting of 150 single stellar populations from the `BC03` (Bruzual & Charlot 2003) models, with ages ranging between 1 Myr–18 Gyr, and metallicity ranging from Z = 0.0001–0.05. We also excluded from this analysis the range around strong nebular emission lines. The base spectra were convolved with a Gaussian function in order to account for the resolution of the instrument and the velocity dispersion of the galaxy. In our analysis, because of the low resolution of the spectra obtained with grism #11, we allowed for a velocity dispersion up to 1200 km/s. In Figure 4.2 we show examples of the resulting stellar light model compared to the observed spectrum, for the high and low resolution spectra of Regions 1 and 2 respectively. The bottom panel shows the emission-line spectrum resulting from the subtraction of the stellar component from the observed spectrum. These are the spectra used in any subsequent analysis.

We used the `Sherpa v.4.9` package (Freeman *et al.* 2001; Refsdal *et al.* 2009) in order to fit the emission lines on the starlight-subtracted spectra and measure their fluxes. `Sherpa` allows us to fit complex models and to determine their parameters and corresponding uncertainties while accounting for measurement uncertainties on the data. The emission lines of the extracted spectra suffered from non Gaussian shapes in all cases due to instrumentation and setup (e.g. Fig. 4.3). In the case of the low resolution spectra, the fact that Hα and the two [N II] emission lines are partially blended added an extra difficulty in measuring the weak [N II] λ6548 Å line. Although this line is not used in our analysis, accounting for its presence is important for accurately measuring the Hα flux in low-resolution spectra. In order to account for the complex shape of the lines, we modeled each emission line with three Gaussians. This allowed for more

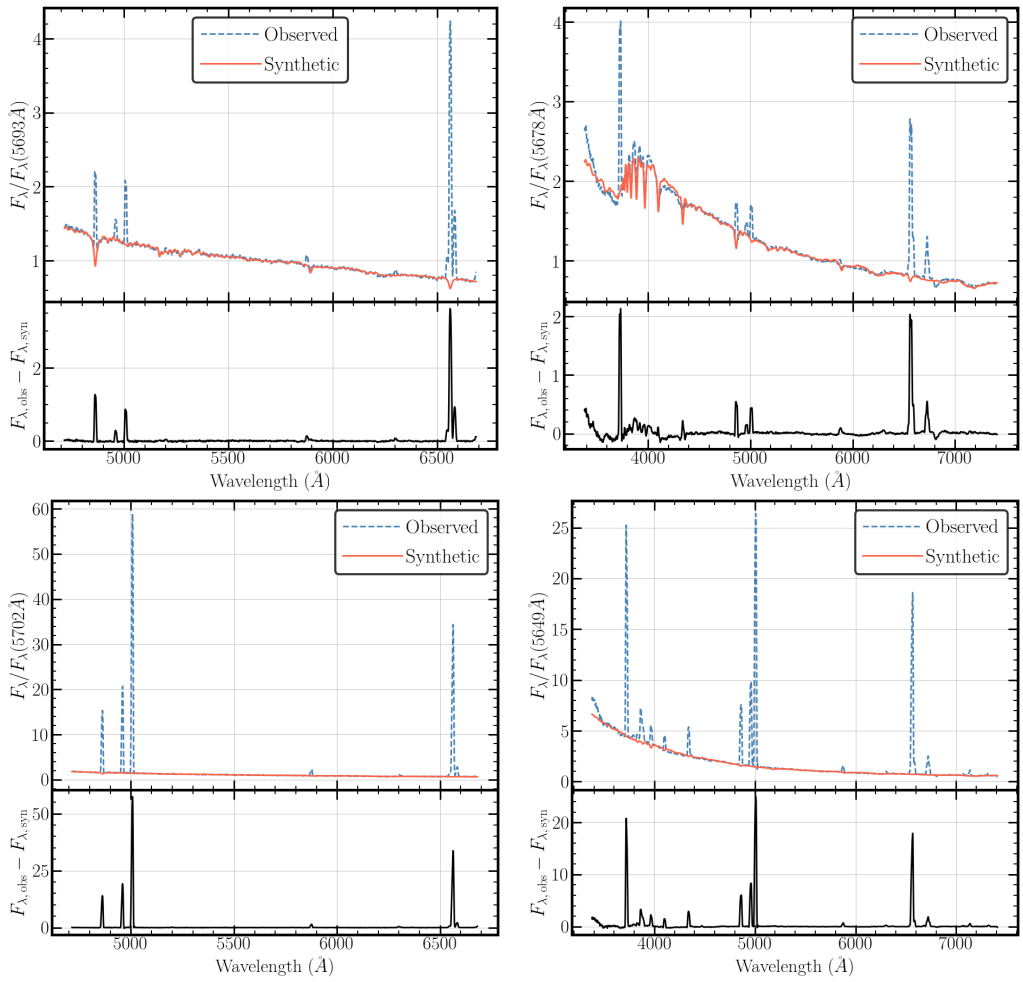

Figure 4.2: Observed (blue dashed) and model starlight spectra (red solid) for the Region 1 (top row) and Region 2 (bottom row). The high and low-resolution spectra are shown in the left-hand and the right-hand figures respectively. The bottom panel of each figure shows the starlight-subtracted (emission-line) spectrum.

flexibility, which results in better fits in comparison to single Gaussian fits. We fitted the region of the spectrum around each line of interest separately in order to account for any residual flux variations of the continuum, and variations of the spectral resolution.

4.3.2 X-ray data

Chandra has observed NGC 922 in two occasions (OBSIDs 10563, 10564; P.I.: A. Prestwich) for a total exposure of 49.7 ksec. The observations were performed with the ACIS-S camera, with the target positioned on the aim-point of the back illuminated ACIS-S3

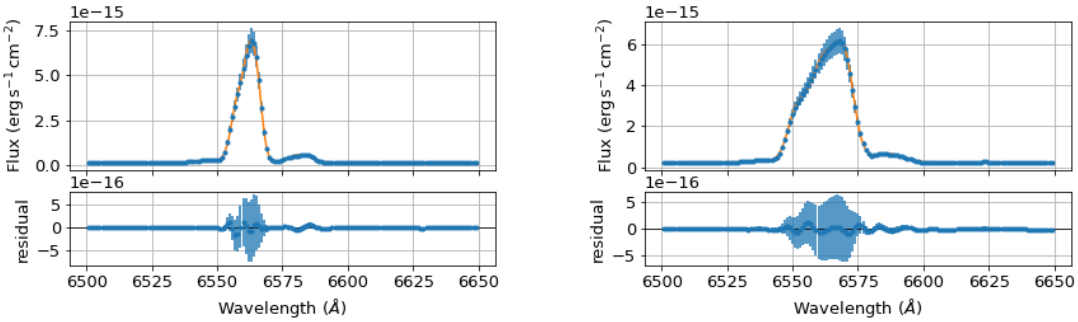

Figure 4.3: The high and low resolution data (blue) and best-fit models (orange) for the region 2, starlight-subtracted spectra, in the wavelength range around the Hα line are presented in the left and right panels respectively. The bottom panels present the fit residuals.

chip. The details of the observations and the analysis of the discrete X-ray sources and ULX populations of NGC 922 are presented in Prestwich *et al.* (2012). Because we were interested in the comparison between the X-ray emission, star-forming activity, and metallicity in the regions targeted by the optical spectroscopic observations, we obtained and reanalyzed the *Chandra* data for NGC 922.

X-ray data analysis was performed with `CIAO`* (Fruscione *et al.* 2006) version 4.12. After the initial processing with the `chandra_repro` tool, we extracted images and exposure maps in the broad (0.5–8.0 keV) band using the `merge_obs` tool. The latter combines data from different observations after re-projecting them to a common reference frame, calculating exposure maps for each observation, and combining the exposure-corrected images. To visualize the spatial distribution of the X-ray emission of NGC 922, the combined image was first adaptively smoothed with the `csmooth CIAO` tool with a minimum significance of 2σ and a maximum kernel of 25 pixels. Then, the image was exposure-corrected by dividing with the combined broad-band exposure map, which was also smoothed with the same smoothing scales. The resulting image is shown in the bottom-right panel of Figure 4.4.

The X-ray spectra were extracted from the event files using the `specextract` tool. Response and ancillary response files were calculated using `CALDB v.4.9.2.1`. Our primary regions of interest were those for which we had optical spectra and exhibited X-ray emission: regions 1 and 3 (referred to as *inner bulge* for the next part of the analysis), and region 2 (referred to as *R2*). In addition we extracted spectra from larger regions of X-ray emission associated with characteristic features of NGC 922 (the *bar*, the

* http://cxc.harvard.edu/ciao

bulge, and the *ring*; Fig. 4.1). The extraction regions (Fig. 4.4) were defined based on the Hα and WISE 12 μm maps in order to encompass the star-forming activity in the regions of interest. Special care is taken so any X-ray sources associated with each of these regions are fully included. The background spectrum was measured from source-free regions outside the optical outline of the galaxy.

The X-ray spectra were binned to include at least 15 counts in each bin, in order to allow the use of χ^2 statistics (only in the case of the *inner bulge* and the *bar* which have very few counts we fitted the unbinned spectrum using the `wstat` statistic). For all regions apart from the full galaxy, the background is negligible in the energy range of interest (0.5-8.0 keV). Instead, because of the large extent of the galaxy, the total spectrum includes significant background contamination. For this reason the total galaxy spectrum was adaptively binned, so each bin has a S/N of at least 2. The spectral analysis was performed with `Sherpa` in `CIAO v. 4.12`. We used the χ^2 statistic for all spectral fits apart from the *inner bulge* and the *bar* regions where, because of the small number of counts, we also fitted the unbinned spectrum using the w-statistic, yielding essentially identical results to the χ^2 fit (here we report results from the `wstat` analysis). The reported uncertainties correspond to the 68% confidence interval for one interesting parameter based on draws of the model parameters from a multivariate normal distribution using the `confidence` command.

All spectra were initially fitted with an absorbed power-law model (`tbabs` $\times$ `po`) using the Wilms *et al.* (2000) absorption cross-sections. This model gave an excellent fit to the spectra of the *bar*, *R2*, and the larger *ring* regions. The *bar* and *inner bulge* region gave rather steep photon indices ($\Gamma = 3.3^{+1.9}_{-1.2}$ and $\Gamma = 4.1^{+3.1}_{-1.0}$ respectively), which indicate a thermal plasma model. Indeed, an `APEC` model gave a slightly improved fit for the *inner bulge* spectrum with a best-fit temperature of kT=$0.23^{+0.02}_{-0.08}$ keV. In the case of the *bar* the thermal plasma model did not improve the quality of the fit. The *bulge* and the *total* spectrum of the galaxy showed strong residuals in the 1–2 keV range indicating an additional thermal component. Indeed, a composite model consisting of a power-law and thermal-plasma component [`tbabs` $\times$ `(apec+po)`] gave a significantly better fit. We also tried this model to the *bar* and *inner bulge* which show relatively soft spectra. While the fit of the *inner bulge* was improved, the fit of the *bar* gave effectively the same fit statistic (wstat). Therefore, we consider a power-law as the best-fit model for the *bar* spectrum, while for the *inner bulge* we adopt the composite thermal plasma - power-law model, in order to obtain a better picture of the power-law luminosity (corresponding to the XRBs component) even under the presence of a weak thermal plasma model.

We calculated the X-ray flux using the `sample_flux` command, which gives the

median and the 68% percentile of the flux distribution based on the model parameter draws from the covariance matrix of the best-fit model. In the case of the composite `apec+po` models we calculated both the total flux and the flux originating only from the power-law component. The best-fit model parameters and total flux are given in Table 4.2

Table 4.2: X-ray spectral best-fit results for the sub-galactic regions defined in Figure 4.4.

Region	net counts	$L_X^{0.5-10\,\mathrm{keV}}$	$L_X^{0.5-8\,\mathrm{keV}\star}$	$L_X^{2-10\,\mathrm{keV}}$	Model	Red. statistic	Γ	N_H	kT
		$10^{40}\,\mathrm{erg\,s^{-1}}$	$10^{40}\,\mathrm{erg\,s^{-1}}$	$10^{40}\,\mathrm{erg\,s^{-1}}$	`Sherpa`	χ^2/d.o.f		$10^{22}\,\mathrm{cm^{-2}}$	keV
total	1685.8	$6.49^{+1.68}_{-1.92}$	$5.92^{+1.48}_{-1.75}$	$3.54^{+0.97}_{-1.12}$	PO+APEC	65.8/112	$1.99^{+0.25}_{-0.21}$	$0.22^{+0.22}_{-0.12}$	$0.23^{+0.04}_{-0.04}$
bulge	306.3	$1.11^{+0.62}_{-0.52}$	$1.02^{+0.56}_{-0.47}$	$0.50^{+0.27}_{-0.25}$	PO+APEC	5.81/16	$1.90^{+0.41}_{-0.36}$	$0.31^{+0.22}_{-0.19}$	$0.23^{+0.06}_{-0.05}$
inner bulge	81.5	$0.36^{+0.65}_{-0.35}$	$0.27^{+0.35}_{-0.24}$	$0.11^{+0.64}_{-0.03}$	PO+APEC	$164.9/514^{\dagger}$	$-0.34^{+1.03}_{-0.82}$	$0.51^{+0.10}_{-0.11}$	$0.19^{+0.03}_{-0.02}$
bar	75.0	$0.24^{+0.03}_{-0.05}$	$0.23^{+0.03}_{-0.04}$	$0.09^{+0.03}_{-0.03}$	PO	$214.1/511^{\dagger}$	$2.43^{+0.37}_{-0.24}$	$0.16^{+0.06\,\P}_{-\ldots}$	-
R2	456.6	$2.12^{+0.44}_{-0.55}$	$1.89^{+0.09}_{-0.14}$	$1.45^{+1.11}_{-0.12}$	PO	16.5/27	$1.74^{+0.21}_{-0.19}$	$0.10^{+0.06}_{-0.05}$	-
ring	819.8	$3.55^{+0.63}_{-0.78}$	$3.16^{+0.50}_{-0.64}$	$2.32^{+0.52}_{-0.63}$	PO	38.6/55	$1.76^{+0.18}_{-0.17}$	$0.05^{+0.05}_{-0.05}$	-

$\star$ The 0.5–8 keV luminosities refer to the power-law component only.

† The fit was performed on the unbinned data using the `wstat` statistic.

¶ The parameter pegged at the low bound (the Galactic line-of-sight H I column density).

4.4 Results

4.4.1 SFR and stellar mass maps

In order to examine the metallicity-SFR-L_X relation at the sub-galactic level, we created spatially resolved SFR, stellar mass, and X-ray emission maps.

As a stellar mass indicator, we used the 3.4 μm WISE band-1 data retrieved from the Infrared Science Archive (IRSA*). We converted the 3.4 μm WISE band-1 luminosity to stellar mass using the conversion of Wen *et al.* (2013):

$$\log \frac{M_\star}{\mathrm{M}_\odot} = -0.040 + 1.12 \log \frac{\nu L_\nu (3.4\,\mu\mathrm{m})}{L_\odot} \quad . \tag{4.1}$$

As a SFR indicator, we used MIPS 24 μm *Spitzer* data which probe dust heated by young stellar populations. We retrieved the post-BCD (post-Basic Calibrated Data) from the IRSA archive. The MIPS 24 μm luminosity was converted to SFR using the calibration of Calzetti *et al.* (2007)

$$\frac{\mathrm{SFR}_{24\mu\mathrm{m}}}{(\mathrm{M}_\odot\,\mathrm{yr}^{-1})} = 1.27 \times 10^{-38} \left[\frac{L_{24\mu m}}{(\mathrm{erg\ s}^{-1})} \right]^{0.8850} \quad . \tag{4.2}$$

As an alternative SFR indicator we used the 12 μm WISE W3 band data (also obtained from the IRSA archive), which are dominated by emission by Polycyclic Aromatic Hydrocarbons (PAH). The WISE band-3 luminosity was converted to SFR using the Cluver *et al.* (2017) calibration.

$$\log \frac{\mathrm{SFR}_{12\mu\mathrm{m}}}{(\mathrm{M}_\odot\,\mathrm{yr}^{-1})} = 0.889 \log \frac{L_{12\mu\mathrm{m}}}{L_\odot} - 7.76 \quad . \tag{4.3}$$

The stellar mass, SFR, specific SFR (SFR/$M_\star$; sSFR) and X-ray emission maps (based on the exposure map corrected full-band images described in Section 4.3.2) of NGC 922 are presented in Figure 4.4, as well as the regions we defined and compared in the following.

* https://irsa.ipac.caltech.edu/frontpage/

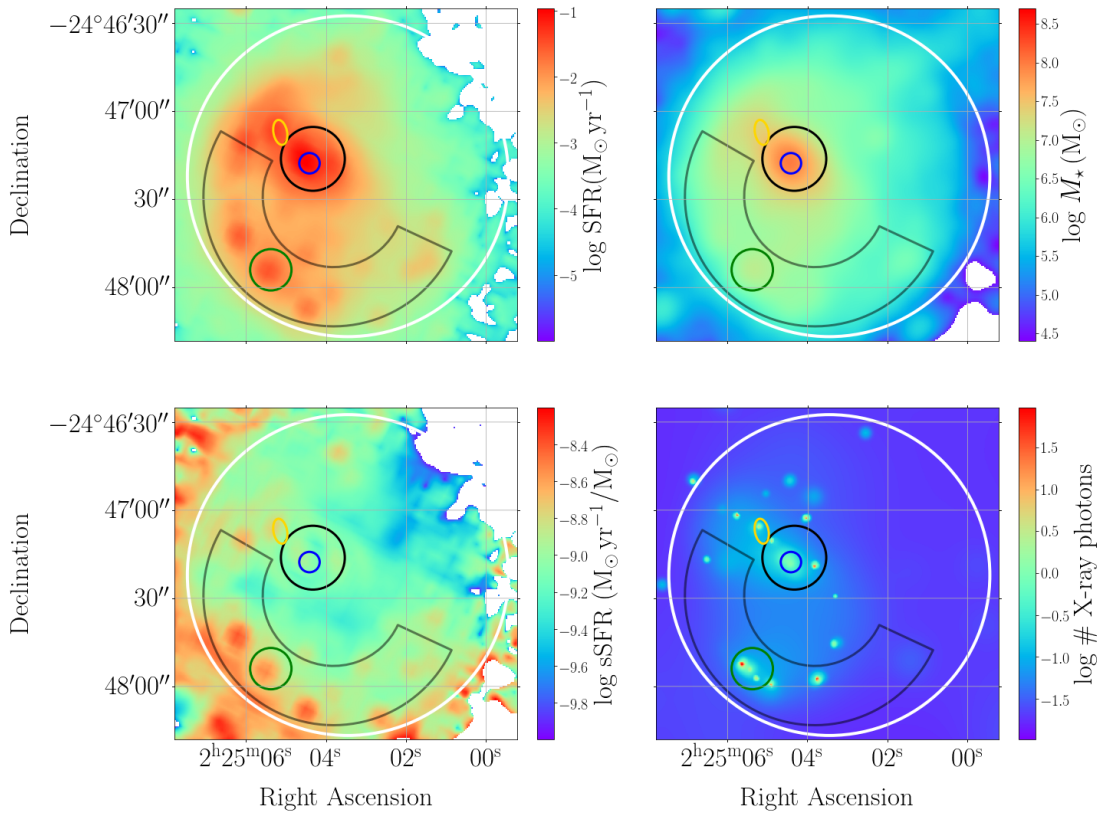

Figure 4.4: NGC 922 maps of SFR (top left) as measured from MIPS 24μm observations, stellar mass from WISE band 1 (top right), sSFR (bottom left), and X-ray intensity in the 0.5–8.0 keV band (bottom right). The *total* galaxy is defined by the white circle. The other regions define the *bulge* (black circle), *inner bulge* (blue circle), *bar* (yellow ellipse), and *R2* (green circle). The gray semi-annulus shows the *ring* region.

4.4.2 Optical spectra

The emission-line fluxes for the high and low-resolution spectra from each region of NGC 922 (as defined in Fig. 4.1 and Table 4.1) are presented in Table 4.3. As we see from the table, there is a systematic difference between the high and low resolution spectral extractions, where the former show slightly higher fluxes (0.1-0.3 dex) in the blue region ($\sim$ 4861 Å) of the spectra. Because our project required observations of NGC 922 with particular slit rotations (Section 4.2), the slit positions angle was not aligned with the parallactic angle. This difference can cause loss of flux in the blue part of the spectrum because of differential diffraction on the observed spectra, especially for observations at high airmass (e.g. Filippenko 1982). The problem cannot be fully remedied by the flux-calibration process since the standard stars were observed at not negligible average airmass ($\simeq$1.4) leading to flux loss in the blue area of the spectrum, and subsequently

higher flux in the blue part of the flux-calibrated object spectra. This effect also resulted in slightly different absolute flux calibrations between the high and low resolution spectra. Despite this systematic difference, the emission-line fluxes measured for the same regions are consistent within the measurement uncertainties. Because of the parallactic angle effects, we could not use the Balmer decrement to reliably measure the extinction in the different regions. However, this problem did not affect the accuracy of the emission-line ratios presented here, because these ratios involve emission lines that are nearby in wavelength.

Table 4.3: Logarithm of the emission-line fluxes (in units of $\mathrm{erg\,s^{-1}\,cm^{-2}}$).

Ion	Line	Region											
		1	1	2	2	3	3	4	4	5	6	7	8
	(λ Å)	low	high	low	high	low	high	low	high	low	low	low	low
[O II]	3726/9	−13.8	...	−13.8	...	−13.5	...	−14.6	...	−14.2	−14.2	−14.8	−14.1
Hγ	4340	−15.1	...	−14.6	...	−14.6	...	−15.6	...	−15.1	−15.3	−15.8	−14.9
Hβ	4861	−14.4	−14.2	−14.4	−14.2	−14.2	−13.9	−15.2	−15.0	−14.8	−14.8	−15.5	−14.6
[O III]	4959	−15.0	−14.9	−14.3	−14.0	−14.7	−14.6	−15.3	−15.1	−14.9	−15.0	−15.9	−14.8
[O III]	5007	−14.6	−14.6	−13.7	−13.5	−14.2	−14.2	−14.8	−14.7	−14.4	−14.5	−15.5	−14.2
He I	5876	−15.3	−15.4	−15.4	−15.4	−15.0	−15.0	−16.5*	−16.1*	−15.8	−15.8*	−16.6*	−15.5
[O I]	6046	−15.5	−15.8	−15.9	−15.8	−15.4	−15.3	−16.4*	−16.3*	−16.0*	−15.7*	−16.5*	−15.6
[O I]	6300	−16.1*	−16.4*	−16.3*	−16.3*	−15.6*	−15.7*	−16.9*	−16.5*	−16.4*	−16.3*	−17.3*	−16.1*
[N II]	6548	−15.4†	−15.2	−15.7†	−15.6	−15.0†	−14.9	−16.0†	−16.3	−16.3†	−16.1†	−17.3†	−15.3†
Hα	6563	−14.0	−14.0	−13.9	−14.0	−13.6	−13.6	−14.8	−14.8	−14.3	−14.5	−15.1	−14.2
[N II]	6583	−14.7	−14.6	−15.0	−15.2	−14.4	−14.3	−15.8	−15.7	−15.5	−15.5	−15.9	−15.2
[S II]	6716/31	−15.2	...	−15.5	...	−14.9	...	−16.3	...	−15.7	−15.7	−16.1	−15.6
He I	7065	−16.0*	...	−16.2*	...	−15.4*	...	−16.7*	...	−16.3*	−16.3*	−16.8*	−16.3*
[Ar III]	7136	...	...	−15.5	...	−15.3*	...	−16.3*	...	−15.9*	−16.0*	−16.6*	−15.9*
[O II]	7320/31	−17.0*	...	−16.1	...	−15.4*	...	−17.2*	...	−16.2*	−16.0*	−16.0*	−16.6*

The emission line fluxes show uncertainty $\log f \simeq \pm 0.1\,\mathrm{erg\,s^{-1}\,cm^{-2}}$ unless otherwise indicated.

* Noise dominates the spectrum in the region of the particular emission line, therefore the flux estimation is highly uncertain.

† Large uncertainty due to partial blending with Hα caused by low resolution.

One thing that is clear from the analysis of the spectra for the different star-forming region, is that they all show prominent Balmer and He I (λ 5876Å) lines regardless of their location in the galaxy (bulge, ring, or intermediate region). The presence of the He I line in particular indicates ionization by strong UV continuum that can be produced by very young stellar populations, or, in the case of the bulge regions, by a potential active galactic nucleus (AGN).

The location of the sources on line-ratio diagnostic diagrams (BPT diagrams; Baldwin *et al.* 1981; Veilleux & Osterbrock 1987) allows us to infer the source of their excitation: photoionization by stellar populations (star-forming regions), photoionization by non-stellar continuum (AGN), or shock excitation (e.g. from supernovae or strong stellar winds from massive stars). In Figure 4.5 we present the location of the different regions (Fig. 4.1) on the ([N II]/Hα–[O III]/Hβ), ([S II]/Hα–[O III]/Hβ), and ([O I]/Hα–[O III]/Hβ) BPT diagrams. All the NGC 922 sub-galactic regions examined here are encompassed by the theoretical Kewley *et al.* (2001) and the empirical Kauffmann *et al.* (2003) curves which delineate star-forming region from AGN and shock-dominated regions. We see that none of the regions in the central part of the bulge lies in the AGN locus, indicating that NGC 922 does not host an AGN. In addition none of the regions in the bulge, the ring, or the intermediate regions shows evidence for strong shock excitation indicating that the dominant source of ionization are the young stellar populations. Regions located in the ring and the bulge show distinct [N II]/Hα and [O III]/Hβ emission line ratios and reside in clearly separate loci of the [N II] BPT diagram. Regions located on the ring of NGC 922 are in the upper left of the diagram, while regions located on the bulge, or intermediate locations (like region 7), reside on the lower right part of the BPT diagram. [S II]/Hα, and [O I]/Hα emission line ratios do not distinguish the bulge and ring regions as well as the [N II]/Hα and [O III]/Hβ ratios.

4.4.3 Metallicity measurements and stellar population parameters

Metallicities were derived from the fluxes reported in Table 4.3 using calibrations provided by Pettini & Pagel (2004):

$$[12 + \log(\mathrm{O/H})] = 8.90 + 0.57 \times \mathrm{N2} \tag{4.4}$$

$$[12 + \log(\mathrm{O/H})] = 8.73 - 0.32 \times \mathrm{O3N2} \tag{4.5}$$

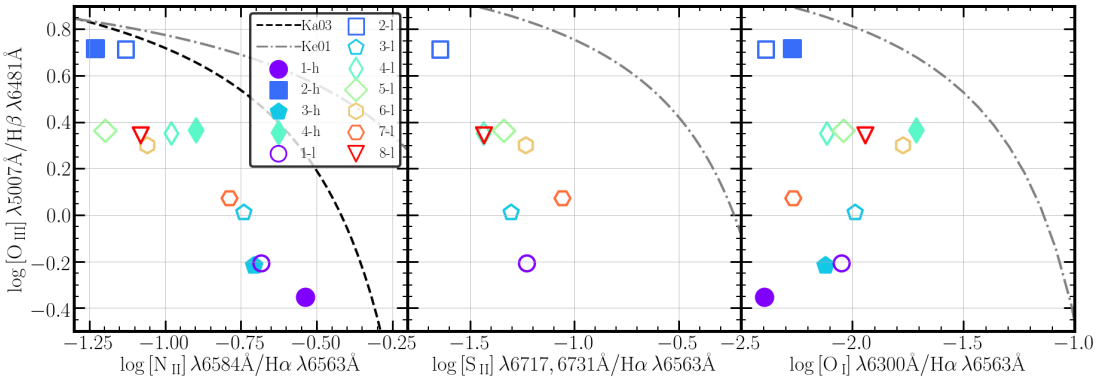

Figure 4.5: From left to right are the ([N II]/Hα–[O III]/Hβ), ([S II]/Hα–[O III]/Hβ), and ([O I]/Hα–[O III]/Hβ) BPT diagrams for all the regions (IDs in legend) and spectrum resolutions (h and l refers to high and low resolution respectively). The Kewley *et al.* (2001) and Kauffmann *et al.* (2003) curves separating regions excited by non-stellar photoinization (top right) from H II regions (lower left) are presented with gray dashed-doted and black dashed lines respectively. All regions are well within the locus of H II regions.

where

$$\mathrm{N2} = \log(f_{[\mathrm{N\,II}]_{\lambda\,6583}}/f_{\mathrm{H}\alpha_{\lambda\,6563}}) \tag{4.6}$$

$$\mathrm{O3N2} = \log \frac{f_{[\mathrm{O\,III}]_{\lambda\,5007}}/f_{\mathrm{H}\beta_{\lambda\,4863}}}{f_{[\mathrm{N\,II}]_{\lambda\,6583}}/f_{\mathrm{H}\alpha_{\lambda\,6563}}} \tag{4.7}$$

where f corresponds to each emission-line flux. These diagnostics are well calibrated for the range of metallicities we find (Kewley & Ellison 2008).

Metallicity measurements for all spectral extractions using both methods are presented in Table 4.4 and Figure 4.6. The metallicity of different regions within NGC 922 ranges from near-solar to sub-solar across the galaxy. We find that regions located on the ring (2, 4, 5, and 8) show consistently significantly lower metallicity ($8.11 < [12+\log(\mathrm{O/H})] < 8.39$) compared to regions located on the bulge (regions 1 and 3; $8.49 < [12+\log(\mathrm{O/H})] < 8.67$) regardless of the measurement method (the quoted ranges include the full range of both methods). Region 7, which is located between the ring and the bulge, shows an intermediate value ($[12 + \log(\mathrm{O/H})] = 8.45$). The metallicity of region 6, that is not placed on the ring, is $[12 + \log(\mathrm{O/H})] = 8.30$.

Metallicities derived with the O3N2 diagnostic show wider differences between the ring and the bulge compared to the N2 diagnostic (Fig. 4.6). Similarly, the high-resolution extractions tend to extend the differences in both diagnostics. This is because

Table 4.4: Metallicity measurements

Region ID	Grism #	Metallicity N2 12 + log(O/H)	Metallicity O3N2 12 + log(O/H)
1	11	8.51±0.02	8.58±0.01
1	18	8.59±0.01	8.67±0.01
2	11	8.26±0.01	8.14±0.01
2	18	8.20±0.01	8.11±0.01
3	11	8.48±0.02	8.49±0.01
3	18	8.50±0.01	8.57±0.01
4	11	8.34±0.01	8.30±0.01
4	18	8.39±0.01	8.33±0.01
5	11	8.22±0.01	8.23±0.01
6	11	8.30±0.03	8.30±0.02
7	11	8.45±0.02	8.45±0.02
8	11	8.28±0.02	8.27±0.01

of the better determination of the Balmer-line fluxes resulting from the more accurate subtraction of the stellar component and modelling of the Hα-[N II] complex.

The metallicities measured for the regions located in the bulge (regions 1 and 3; [12+log(O/H)] = 8.50–8.67) are in agreement with the one reported in Wong *et al.* (2006) for a 6.7" diameter region on the bulge, based on the N2 method ([12+log(O/H)] = 8.6). The same work also reports metallicities based on the [N II]/[S II] ratio ([12+log(O/H)] $\simeq$ 9) and the R-band luminosity-metallicity relation of Lamareille *et al.* 2004, which, however, are higher than those found from the N2O3 or the N2 methods. This overestimation could be due to the fact that the [N II]/[S II] ratio becomes insensitive to metallicity at low metallicities and the [N II]/[S II]-metallicity relation is a sensitive function of the ionization parameter (e.g. Dopita *et al.* 2013; Blanc *et al.* 2014) which is not known for the different star-forming regions in NGC 922. Our measurements of the bulge metallicity are also in agreement with the one reported in Robertson *et al.* 2013 ([12 + log(O/H)] = 8.75 ± 0.08).

In Table 4.5 we present the SFR, stellar mass, sSFR, and metallicity measurements for five sub-galactic regions and the whole NGC 922 as defined in Figure 4.4. Here we adopt the O3N2 metallicity calibration as it is considered more robust especially in star-forming galaxies (Pettini & Pagel 2004). As a metallicity for the *total* galaxy we used the median value of all our metallicity measurements (Table 4.4), and as uncertainty the standard deviation of this distribution. The extracted regions are evenly spread over the body of the galaxy thus the metallicity of the galaxy is not biased towards a particular region. Due to the lack of metallicity measurements in the *bar* we adopted the same value and uncertainty as the *total*. For the other sub-galactic regions we adopted

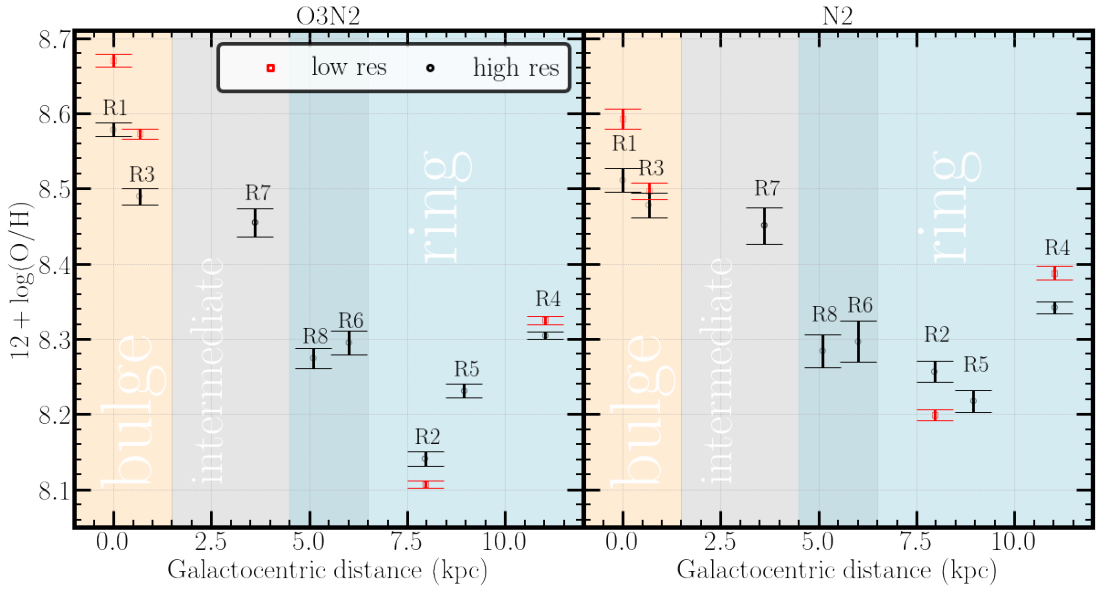

Figure 4.6: Gas phase metallicities for all the regions as a function of their galactocentric distance (adopting as center of the galaxy the center of region 1). The corresponding region IDs (Fig. 4.1) are shown on top of the points. High resolution extractions are presented with red colour and low with black. In the left and right panels are the O3N2 and N2 diagnostic results respectively. The orange, gray, and blue shaded areas represent regions encompassed in the bulge, intermediate, and ring loci of NGC 922 respectively. Due to the asymmetrical shape of NGC 922, the shading overlaps in a range of radii. This is clearly seen by comparing the position of region 8, which is located in the north-west part of the ring, that is relatively closer to bulge, with that of region 6 which does not belong to the ring.

the metallicity of the extraction regions they encompass: median of regions 1 and 3 for *bulge* and *inner bulge*, region 2 for region *R2*, and the median metallicity (and standard deviation) of extraction regions 2, 4, 5, and 8 for the *ring*.

Our estimation of the total stellar mass of NGC 922 ($2.78 \pm 0.01 \times 10^{10}\,\mathrm{M}_\odot$) is in agreement with the one reported in Pellerin *et al.* 2010 ($2.8 \times 10^{10}\,\mathrm{M}_\odot$). Our estimation of the integrated SFR of NGC 922 ($8.6 \pm 0.3\,\mathrm{M}_\odot\,\mathrm{yr}^{-1}$) is in agreement with the one reported in Elagali *et al.* 2018b ($8.5 \pm 0.6\,\mathrm{M}_\odot\,\mathrm{yr}^{-1}$) which was also calculated through $24\,\mu$m emission. This measurement is slightly higher but consistent within the uncertainties with that reported in Wong *et al.* 2006 ($\mathrm{SFR}_{\mathrm{H}\alpha} = 8.20 \pm 0.32$, $\mathrm{SFR}_{\mathrm{UV}} = 7.04 \pm 0.02\,\mathrm{M}_\odot\,\mathrm{yr}^{-1}$). WISE W3 $12\,\mu$m emission results in a slightly lower total $\mathrm{SFR}_{12\mu\mathrm{m}}$ ($6.11 \pm 0.04\,\mathrm{M}_\odot\,\mathrm{yr}^{-1}$). While the H$\alpha$-based SFR indicator is a better probe of the stellar populations associated with high-mass XRBs (HMXBs; Kouroumpatzakis *et al.* 2020), and therefore correlates better with their X-ray emission, its use at sub-galactic scales is subject to differential extinction within the galaxy. In order to correct for the varying extinction between

star-forming regions we would need extinction maps for NGC 922 which are not available. Therefore, in our sub-galactic region analysis, we adopted the IR SFR indicators to avoid biases and scatter due to the lack of spatially resolved extinction measurements.

Pellerin *et al.* (2010) reported the ages of star-clusters in different regions throughout the galaxy. Based on the ages of the individual clusters encompassed within each sub-galactic region, we find the representative age of the stellar populations in these regions. Figure 4.7 shows the distribution of the ages in the star-clusters within each sub-galactic region. We clearly see that all distributions peak at ages below ~ 10 Myr (although the *bulge* and the *total* galaxy show a secondary weaker peak at ages ~ 50 Myr). The ages of the dominant cluster populations in each region are given in Table 4.5, along with their corresponding 68% percentiles.

4.4.4 X-ray data results

The X-ray spectra for the different regions (Fig. 4.4) are very well fitted $\chi^2_\nu \leq 0.7$ with either simple power-law or composite power-law thermal-plasma models. The best-fit model parameters and total flux are given in Table 4.2 while the X-ray spectra for each region and the corresponding best-fit models are shown in Figure 4.8. All regions, except from the bulge, have H I column density slightly higher (but consistent) with the Galactic $N_{\rm H}$ along the line of sight to NGC 922 ($N_{\rm H} = 1.6 \times 10^{20}{\rm cm}^{-2}$; HI4PI Collaboration *et al.* 2016) based on the $N_{\rm H}$ tool*. In the full band the thermal component contributes less than 20% of the total emission of the composite `po+apec` spectral fits, apart from the *inner bulge* where it contributes $\sim 45\%$ of the total 0.5–10 keV emission. However, for all regions the thermal component has negligible contribution in the 2–10 keV X-ray luminosities that are used in the following discussion. Finally, we note that we do not find any point-like source above our detection limit of $\sim 10^{39}$erg s^{-1} that could indicate the presence of an AGN. This is in agreement with the non-detection of an AGN-like source in the optical spectra of the central part of the bulge.

In Figure 4.9 we compare the L_X/SFR as a function of metallicity for the considered sub-galactic regions and the total NGC 922 emission. For this comparison we adopted the MIPS 24 μm-based SFRs. The *total* galaxy X-ray emission is in agreement with the theoretical models of Fragos *et al.* (2016), and Madau & Fragos (2017), and the empirical fits of Brorby *et al.* (2016), and Fornasini *et al.* (2020). For this comparison we converted the Madau & Fragos (2017) model from the R_{23} metallicity (Kobulnicky & Kewley 2004) to O3N2 (Pettini & Pagel 2004) using the calibration of Kewley & Ellison (2008). We find that the *bulge*, *inner bulge*, and *bar* regions follow the Madau & Fragos

* https://heasarc.gsfc.nasa.gov/cgi-bin/Tools/w3nh/w3nh.pl

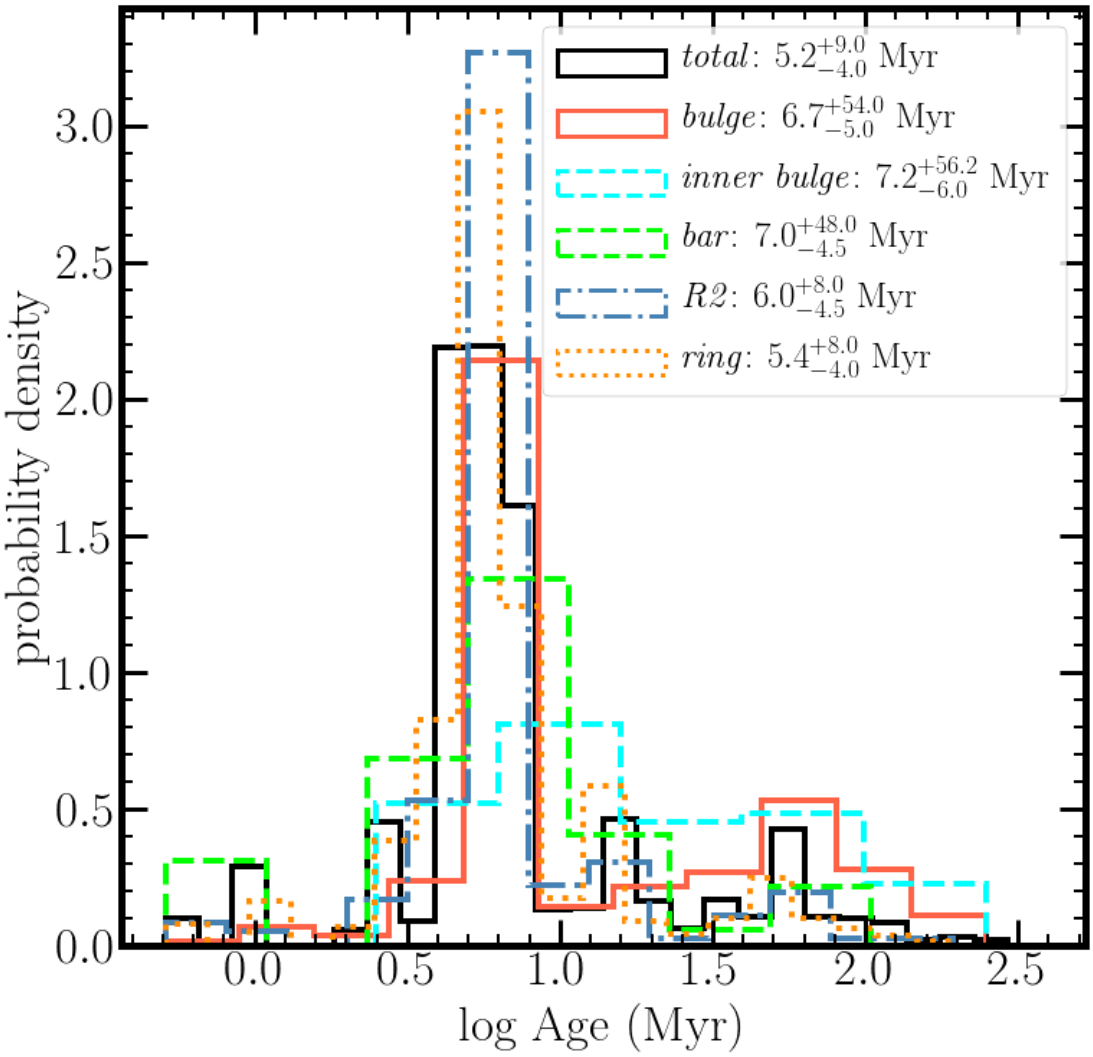

Figure 4.7: Distribution of the star clusters ages from the work of Pellerin *et al.* (2010) for the regions defined in Figure 4.4. The modes of the age distributions and the 68% confidence intervals for each sub-galactic region are shown in the legend.

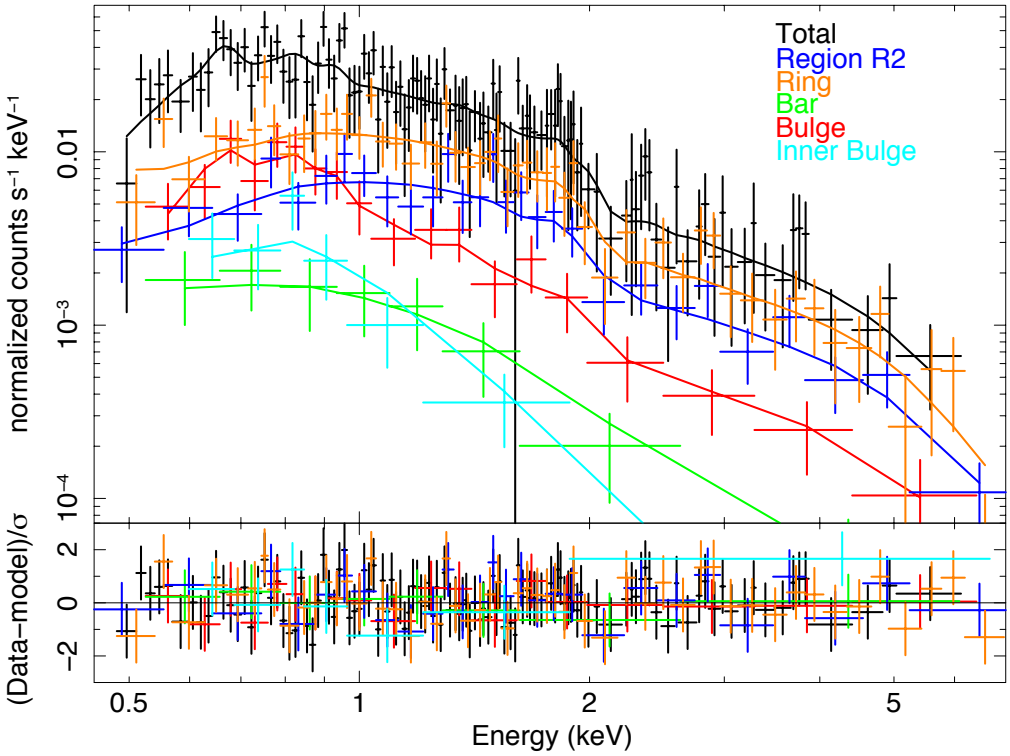

Figure 4.8: X-ray spectra and best-model fits for the *total* emission, *R2*, *ring*, *bar*, *bulge*, and *inner bulge* of NGC 922 as defined in Fig. 4.4 with black, blue, orange, green, red, and light blue colours respectively. The best-model fits for each spectrum are over-plotted with the same colours. Details of the best-model fits are given in Table 4.2. The fit for the *inner bulge* and the *bar* were performed on the unbinned spectrum, here for clarity of presentation the data have been binned to have at least 10 counts be bin. In the lower panel shows the fit residuals is units of the data uncertainties (σ).

(2017) model considering the uncertainties. All regions except *R2* and the *ring* are in the expected range by the sub-galactic $L_X{\sim}\mathrm{SFR}_{24\,\mu\mathrm{m}}$ fit of Kouroumpatzakis *et al.* (2020) considering their 1 σ uncertainty and scatter term. Kouroumpatzakis *et al.* (2020) have calculated $L_X{\sim}$SFR scaling relations for sub-galactic regions of spatial scales ranging from 1×1 kpc up to 4×4 kpc. For this comparison we used the SFR for each individual region (Table 4.5) and the scaling relation for the corresponding spatial scale. We have used the largest (4×4 kpc) fit for *total* and the *ring* that have even largest sizes. Region *R2* shows an excess of ~ 0.4 dex (erg s^{-1} M$_\odot^{-1}$ yr) with respect to all the models. The *ring* shows lower L_X/SFR compared to *R2* but still has an excess compared to the aforementioned models and empirical fits.

To assess whether this observed luminosity excess is a stochastic effect or it has a physical origin, we have followed a similar approach to Anastasopoulou *et al.* (2019),

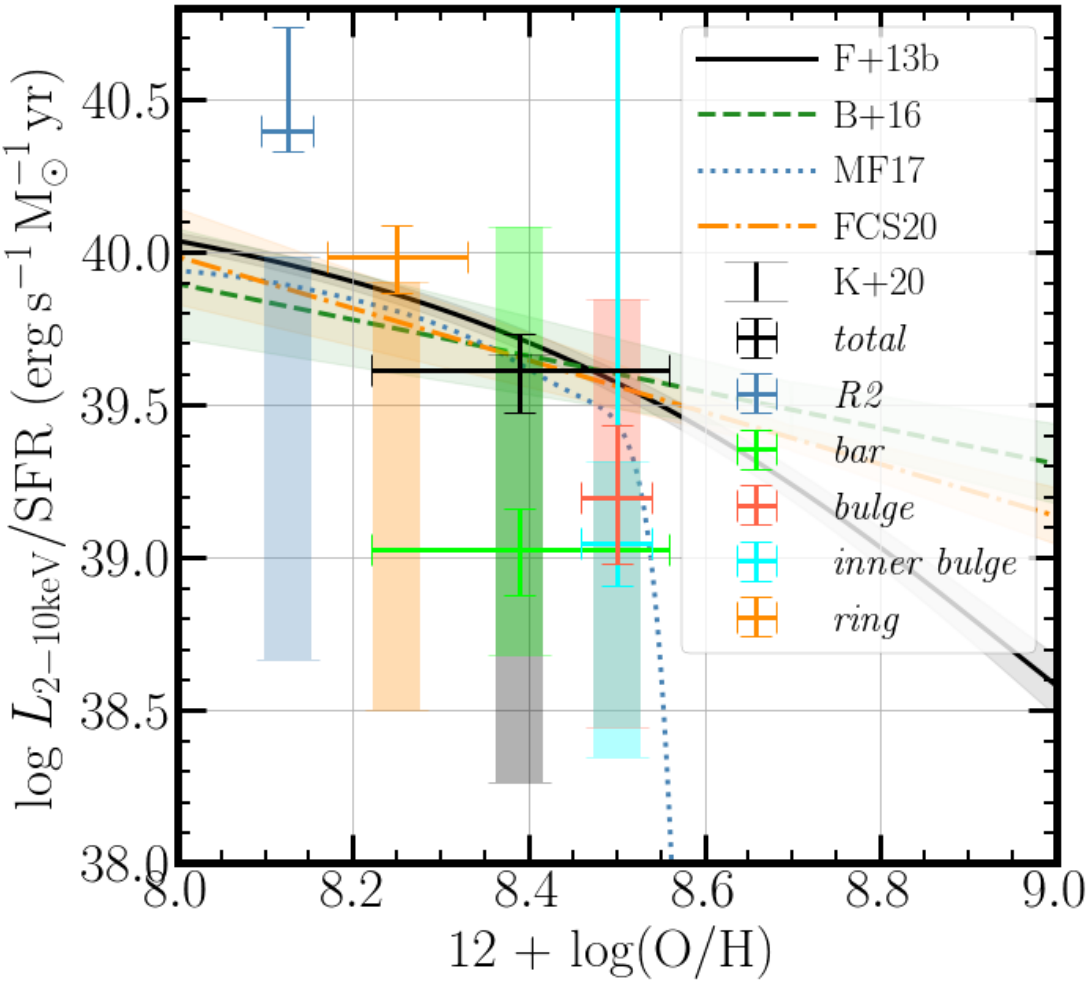

Figure 4.9: X-ray luminosity (2–10 keV) normalized by SFR as a function of metallicity for five sub-galactic regions and the integrated emission of NGC 922, as defined in Fig. 4.4. Black continuous and blue dotted lines represent the theoretical relations of Fragos *et al.* (2016) and Madau & Fragos (2017) respectively. The green dashed and orange dash-dot lines show the observational relations of Brorby *et al.* (2016) and Fornasini *et al.* (2020) respectively, while the shaded areas indicate the uncertainties of the corresponding relations. Stripes with the same colour with the datapoints represent the expected L_X/SFR (in the 2–8 keV band) ratio based on the sub-galactic L_X–SFR relation of Kouroumpatzakis *et al.* (2020) for the 24 μm SFR indicator. This is calculated for each individual sub-galactic region given their SFR and size. The wide range of the stripes indicates the 1 σ uncertainty of the scaling relation, including the term which describes the intrinsic scatter of the sub-galactic relation.

Table 4.5: Properties of the sub-galactic regions defined in Figure 4.4 derived by optical data.

Region	SFR (24μm) ($M_\odot\,yr^{-1}$)	SFR (12μm) ($M_\odot\,yr^{-1}$)	$M_\star$ ($10^{10}\,M_\odot$)	log sSFR ($M_\odot\,yr^{-1}/M_\odot$)	Metallicity [12 + log(O/H)]	Age (Myr)
total	8.60±0.30	6.11±0.04	2.78±0.01	-9.51±0.02	8.39±0.17	$5.2^{+9.0}_{-4.0}$
bulge	3.20±0.18	1.77±0.02	0.64±0.01	-9.30±0.02	8.50±0.04	$6.7^{+54.0}_{-5.0}$
inner bulge	0.99±0.10	0.34±0.01	0.11±0.01	-9.02±0.04	8.50±0.04	$7.2^{+56.2}_{-6.0}$
bar	0.88±0.10	0.54±0.01	0.11±0.01	-9.08±0.05	8.39±0.17	$7.0^{+48.0}_{-4.5}$
R2	0.58±0.08	0.22±0.01	0.04±0.01	-8.88±0.06	8.13±0.03	$6.0^{+8.0}_{-4.5}$
ring	2.39±0.16	1.38±0.02	0.41±0.01	-9.24±0.03	8.25±0.08	$5.4^{+8.0}_{-4.0}$

where we have simulated the expected X-ray luminosity distribution in each sub-galactic region as well as the entire galaxy based on galaxy-wide XRB scaling relations with stellar mass and SFR (Fig. 4.10). In more detail, we have calculated the total luminosity of the XRB populations by integrating the XLF of low-mass XRBs (LMXBs; Gilfanov 2004) and HMXBs (Mineo *et al.* 2012a) in each region above limiting luminosities of $L_{\rm min} = 10^{36}$erg s^{-1} and $L_{\rm min} = 2 \times 10^{37}$erg s^{-1} respectively. The expected number of LMXBs and HMXBs in each region (normalization of the XLF) was calculated using the scaling relations of Gilfanov (2004) and Mineo *et al.* (2012a) respectively, and the local stellar mass and SFR (Table 4.5). To account for fluctuations on the number of sources, we have drawn 500 samples from a Poisson distribution where its mean is equal to the expected number of LMXBs and HMXBs. To account also for stochastic effects on the luminosity of each region, we have obtained 500 samples of X-ray luminosity distributions from the corresponding XLF for each one of the 500 possible number of sources. This resulted in a distribution of 500,000 total XRB luminosities for each region, 250,000 originating from the LMXB and 250,000 from the HMXB population. Our results (Fig. 4.10) show that indeed the high X-ray luminosities of the *ring* and *R2* have a very small probability to be the result of stochastic sampling (4% and 2% respectively). This probability becomes 14% for the *ring* if we discard the bright X-ray source associated with the *R2* region, which contributes more than 50% of the X-ray emission of the *ring*.

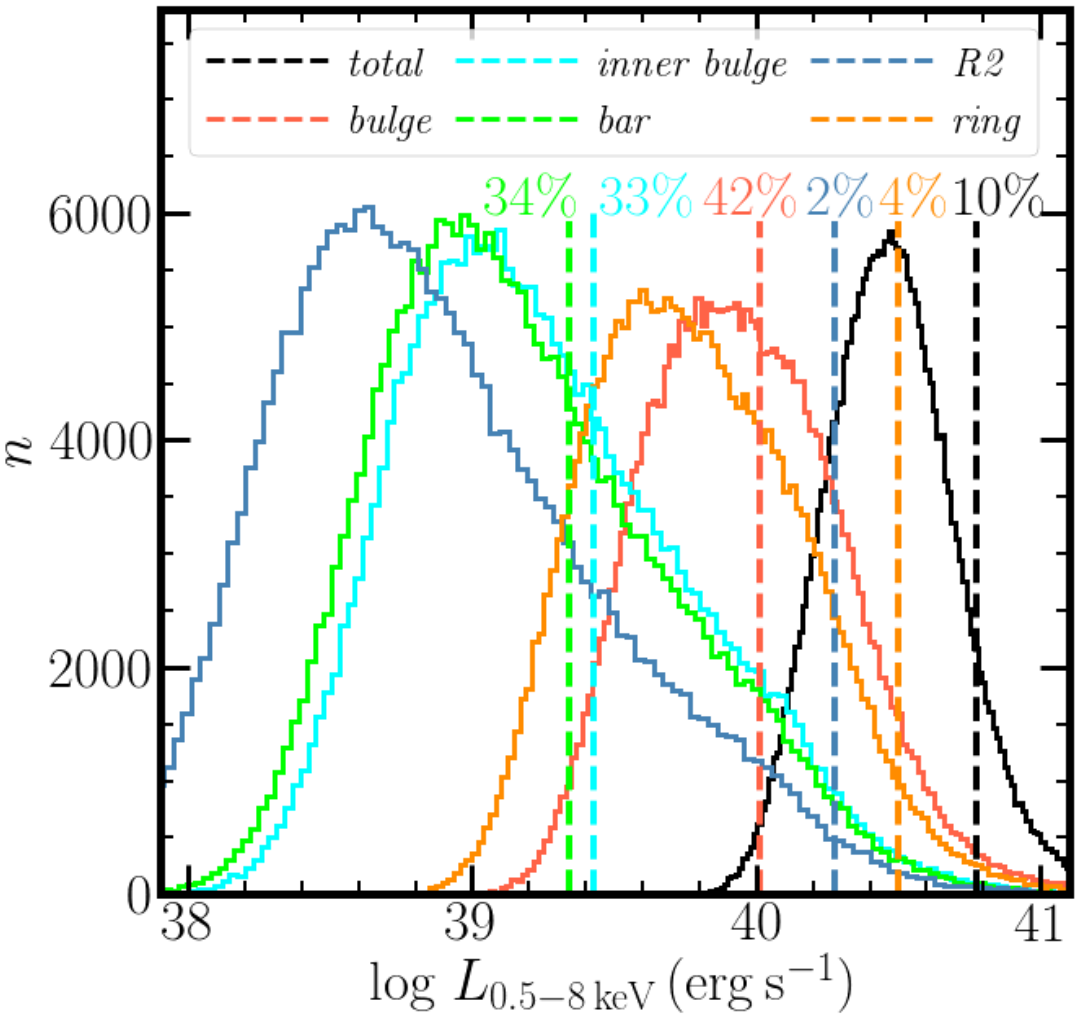

Figure 4.10: Expected X-ray luminosity (0.5–8 keV) distributions of the different regions and the integrated emission of NGC 922, drawn from the XRB XLF and the XRB scaling relations with stellar mass and SFR. The vertical dashed lines with the same colour as the distributions indicate the measured X-ray luminosity of the corresponding region. The probability to have the measured luminosity (or higher), drawn out of these distributions is 10.27%, 42.31%, 33.40%, 34.33%, 1.56%, and 3.81% for the *total* emission and the regions of the *bulge*, *inner bulge*, *bar*, *R2*, and *ring* respectively.

4.5 Discussion

4.5.1 Metallicity variations within the galaxy

NGC 922 shows overall near-solar to sub-solar metallicity ranging from $8.11 \leq [12 + \log(\mathrm{O/H})] \leq 8.67$. However, the most important finding is that regions on the ring have systematically lower metallicity than the bulge (Fig. 4.6). Elagali *et al.* (2018b) found that NGC 922 possesses a higher abundance of H I gas ($\log(M_{\mathrm{H\,I}}/M_\star) = -0.50$) compared to normal galaxies of similar stellar mass ($\log < M_{\mathrm{H\,I}}/M_\star >= -0.89$). This combined with the effect of the caustic that created the ring by displacing outwards the gas in the disc also explains the higher H I mass-to-light ratio on the ring of NGC 922 in comparison to its bulge (see Fig. 8 in Elagali *et al.* 2018b).

Several studies have suggested that the low gas phase metallicity of the RiG rings reflects the metallicity of the passing-through dwarf galaxy (e.g. Bransford *et al.* 1998; Elagali *et al.* 2018a). This scheme is supported in NGC 922, as we find that the ring shares similar metallicity ($[12 + \log(\mathrm{O/H})_{ring}] = 8.25 \pm 0.08$) with the interacting companion ($[12 + \log(\mathrm{O/H})] \simeq 8.3$; Wong *et al.* 2006) In this case the metallicity of the bulge is related with that of the host disk-like, more evolved galaxy.

The low metallicity of the ring regions with respect to the bulge region could also be the result of the negative metallicity gradients typically seen in spiral galaxies (e.g. Moustakas *et al.* 2010). If the star-forming activity is the result of the in-situ compression of gas of the original disk at the galactocentric radius of the ring, we would naturally expect that these star-forming regions will have lower metallicity than the bulge. Alternatively, if the ring consists of gas displaced from the inner parts of the galaxy, the negative metallicity gradient will result in the dilution of this gas with metal-poor material at the current location of the ring. The latter scenario, however, would result into lower metallicity differences than the former. This effect of course can be amplified by the lower metallicity of the intruder galaxy, which can also result in higher H I abundance with respect to the stellar mass or star-light in the ring.

4.5.2 Excitation of star-forming regions

An interesting feature of the spectra from all regions is that they show He I emission (Table 4.3), a strong indication that they host young stellar populations (age < 10 Myr). Furthermore, the ubiquitous presence of He I and the short lifetimes of the stars with hot photospheres capable of exciting He I suggests that their stellar populations have similar ages.

Indeed, Pellerin *et al.* (2010) found that both the ring and the bulge host very young star-clusters with ages $\simeq 7$ Myr, with the bulge also hosting a population of older clusters (30–350 Myr). More specifically, using the distribution of star-cluster ages of Pellerin *et al.* (2010), we find that all the regions of interest in our analysis are dominated by young star clusters with ages around 5–7 Myr (Fig. 4.7). The age distributions of the *bulge* and *inner bulge* show a tail to older clusters with a second, weaker, peak around 50 Myr. Clearly, the presence of extremely young star-clusters is consistent with our detection of He I emission in all regions.

The location of the different regions on the BPT diagrams (Fig.4.5) can provide additional insights into their physical conditions. All NGC 922 regions examined here are encompassed by the Kauffmann *et al.* (2003) curve, indicating purely star-formation driven ionization, without significant contribution from shock ionization (e.g. from supernovae and stellar winds in a young starburst). However, we see a clear segregation of the bulge and the ring regions in the [N II]/Hα BPT diagram: The ring regions are located at the upper left of the H II-region locus, while the bulge regions have lower [O III]/Hβ ratios, and higher [N II]/Hα ratios. Based on the detection of He I in both the ring and bulge regions, we interpret the different location of the regions on the BPT diagrams as the result of metallicity rather than age differences. Increasing metallicity (or decreasing ionization parameter) tends to move the locus of the points towards the right and lower part of the [N II]/Hα diagram, while it does not have as strong effect in the other diagrams (e.g. Kewley *et al.* 2001, 2006).

The fact that we do not find any evidence of AGN activity in NGC 922 is intriguing given the copious amounts of H I gas in the galaxy and the expected presence of a super-massive black hole (SMBH), as in most galaxies (e.g. Kormendy & Ho 2013). This can be explained through three possible scenarios: a) AGNs are known to have a duty cycle (e.g. Schmidt 1966; Best *et al.* 2005; Delvecchio *et al.* 2020) and it is possible that currently the SMBH is in a low accretion state; b) the gas has not lost its angular momentum yet and it has not reached the SMBH; c) gravitational recoil of the SMBH due to the interaction may have displaced it out of the bulge. The last scenario is the most unlikely since we do not see a strong point like source outside the bulge (c.f. Fig. 4.3). In fact, the X-ray analysis in similar galaxies shows that an active AGN is not ubiquitous in RiGs (Wolter *et al.* 2018).

4.5.3 The X-ray emission of NGC922

The X-ray spectra of the *R2* and *ring* regions can be well described solely by power-law emission with a photon index $\Gamma \sim 1.7$. This is a strong indication that their spectra

are dominated by XRBs emission. The X-ray spectrum of the *bulge* requires both a thermal (kT = 0.2 keV) and a power-law ($\Gamma \sim 1.9$) component similar to that of XRBs. The *bar* region has a considerably softer X-ray spectrum, but consistent with the typical spectrum of XRBs ($1.7 \leq \Gamma \leq 2.5$). In the case of the *inner bulge*, which is dominated by a thermal-plasma model, we can set a limit on the contribution of a power-law component. These results are consistent with those of Prestwich *et al.* (2012), who found a population of bright X-ray sources associated primarily with the ring and bar regions. The spectral parameters and total luminosity of the *R2*, which hosts the brightest ULX in the galaxy, are consistent within the uncertainties with those reported in Section 4.4.4. No bright sources were found in the bulge.

We see a very similar pattern in the X-ray emission in the Cartwheel galaxy (Wolter & Trinchieri 2004): diffuse thermal emission and a non-thermal component, described by a power-law model, due to the XRB population. The thermal plasma has a temperature of kT = 0.2 keV, like in NGC922 with $N_{\rm H} = 2.3 \times 10^{21}\,{\rm cm}^{-2}$ for an $L_X^{0.5-10\,{\rm keV}} = 3\times10^{40}\,{\rm erg\,s}^{-1}$. The non-thermal emission can been divided in three different components: the brightest (hyperluminous) X-ray source (N10), the sum of detected point sources, and the residual non-thermal component due to the unresolved XRBs. N10 is fitted by a power-law model with $\Gamma = 1.6$, $N_{\rm H} = 3.6 \times 10^{21}\,{\rm cm}^{-2}$), similar to those of *R2* in the NGC 922 ring. The other point sources, both resolved and unresolved, have a steeper spectrum of $\Gamma = 2.1 - 2.3$, $N_{\rm H} = 2 \times 10^{21}\,{\rm cm}^{-2}$. This is somewhat steeper than the spectrum of the NGC 922 *ring*, but consistent within the uncertainties. The most luminous source (N10) has a luminosity of $L_X^{0.5-10\,{\rm keV}} = 1.4 \times 10^{41}{\rm erg\ s}^{-1}$ dominating the X-ray emission of the galaxy, while the total additional contribution from all point sources is $L_X^{0.5-10\,{\rm keV}} = 1.2 \times 10^{41}{\rm erg\ s}^{-1}$. The most luminous source in NGC 922 has a factor of ~ 5 lower luminosity than the N10 source, and lower impact in its total luminosity.

4.5.4 Effect of metallicity on X-ray luminosity of X-ray binary populations

There is a growing body of observational evidence showing strong anti-correlation between the number of luminous X-ray sources and the metallicity of their host galaxies (e.g. Mapelli *et al.* 2009; Prestwich *et al.* 2012; Brorby *et al.* 2016). A similar trend holds for the integrated X-ray emission of galaxies, particularly those found at higher redshifts (e.g. Fornasini *et al.* 2019). The clear metallicity difference between the bulge and the ring of NGC 922, combined with the information on the age of the stellar populations in these regions, provides an excellent test-bed for this X-ray luminosity–metallicity

dependence.

Figure 4.9 shows an anti-correlation between the L_X/SFR ratios and the metallicity of different regions in NGC 922. Despite the large uncertainties (especially in the lower-luminosity – higher metallicity regions) we see a systematic trend for lower metallicity regions to have stronger X-ray emission for their star-forming activity (i.e. higher L_X/SFR ratios). Although younger stellar populations may also result in elevated X-ray luminosities (e.g. Fragos *et al.* 2013a), the observed relation is unlikely to be an age effect since, as discussed in the previous subsection, both the bulge and the ring regions host similarly young stellar populations (c.f. Table 4.5).

The observed relation shown in Figure 4.9 agrees very well with the theoretical models of Fragos *et al.* (2013b) and Madau & Fragos (2017), and with the observational results of Brorby *et al.* (2016) and Fornasini *et al.* (2020). Although the L_X/SFR ratios of the higher metallicity bulge regions have large uncertainties, they appear to better follow the Madau & Fragos (2017) relation.

While most regions are in good agreement with the theoretical and observational relations shown in Figure 4.9, region *R2* lies above these relations, even after accounting for the observed scatter in the sub-galactic L_X–SFR scaling relations (Kouroumpatzakis *et al.* 2020). This region has the lowest metallicity ([12 + log(O/H)] = 8.13) and highest sSFR (log sSFR = $-8.8\,\mathrm{M_\odot\,yr^{-1}/M_\odot}$) and it is ~ 0.4 dex above any of these relations. This is because this region hosts a very luminous ULX ($L_X^{2-10\,\mathrm{keV}} \simeq 1.5 \times 10^{40}\,\mathrm{erg\,s^{-1}}$) which dominates its X-ray emission. We do not expect the X-ray emission of such regions to follow the general L_X-SFR scaling relations since it is dominated by individual sources rather than the average XRB populations (in other words the central-limit theorem which is the basis for such relations does not hold). This is demonstrated in Figure 4.10, which shows that the region *R2* is highly inconsistent with these scaling relations even when we account for Poisson fluctuations of the number of XRBs and stochastic sampling of their XLF. Similarly, the slight excess of the *ring* region with respect to expected L_X/SFR ratio for its metallicity is the result of the significant contribution of the ULX located in *R2*. This source contributes 62% of the 2–10 keV X-ray luminosity of the *ring* region. In fact, when we account for the contribution of the *R2* region, the L_X/SFR ratio for the remaining ring agrees very well with that expected from the theoretical and observational relations.

4.5.5 Summary

In the previous sections we presented an analysis of the metallicity and excitation of star-forming regions in different regions of the ring galaxy NGC 922 derived from optical

data. We also analyzed the *Chandra* X-ray data for the same regions in order to study the connection between metallicity and X-ray emission. Our results can be summarized as follows:

1. We observe a significant metallicity difference between the bulge ([12 + log(O/H)] $\sim$ 8.6) and the ring ([12 + log(O/H)] $\sim$ 8.2).
2. All studied regions have systematically sub-solar metallicities with the bulge being marginally consistent with solar.
3. We do not find any evidence for AGN activity in the bulge.
4. We detect He I emission in all regions indicating excitation from very young populations, supported by the typically less than 10 Myr ages of the star-cluster in the studied regions.
5. We observe an anti-correlation between the L_X/SFR and metallicity in NGC 922. The similarity of the ages of the stellar populations in the studied regions suggests that this anti-correlation is primarily driven by the effect of metallicity.

Acknowledgements

The authors thank the anonymous referee for constructive comments that helped to improve the clarity of the paper. We also thank Anne Pellerin for sharing the NGC 922 star cluster data, and Emanuele Ripamonti for obtaining the optical data used in this paper. K. K., A. Z., and K. A. acknowledge funding from the European Research Council under the European Union's Seventh Framework Programme (FP/2007-2013)/ERC Grant Agreement n. 617001 (A-BINGOS). This project has received funding from the European Union's Horizon 2020 research and innovation programme under the Marie Sklodowska-Curie RISE action, grant agreement No 691164 (ASTROSTAT). AF acknowledges support by the Chandra X-ray Center (CXC) under National Aeronautics and Space Administration (NASA) contract NAS8-03060. AW acknowledges financial support from ASI through the ASI-INAF agreements 2017-14-H.0.

This research has made use of: (a) observations collected at the European Southern Observatory under ESO programme 088.B-0882(A); (b) data obtained from the Chandra Data Archive and software provided by the CXC in the application packages DS9, CIAO, and Sherpa. The CXC is operated for NASA by the Smithsonian Astrophysical Observatory; (c) data products from the Wide-field Infrared Survey Explorer (WISE), which is a joint project of the University of California, Los Angeles, and JPL, California Institute of Technology, funded by NASA; (d) observations made with the Spitzer Space Telescope, which was operated by JPL, California Institute of Technology under a

contract with NASA; (e) the NASA/IPAC Extragalactic Database (NED), which is operated by the Jet Propulsion Laboratory (JPL), California Institute of Technology, under contract with NASA; (f) the NASA/IPAC Infrared Science Archive (IRSA), which is funded by NASA and operated by the California Institute of Technology; (g) IRAF which was distributed by the National Optical Astronomy Observatory, which was managed by the Association of Universities for Research in Astronomy under a cooperative agreement with the National Science Foundation.

This page intentionally left blank

5

Conclusions and future perspectives

5.1 Conclusions

In this thesis we presented a systematic comparison of different SFR indicators. These include traditional indicators (e.g. Hα, UV, FIR, radio), as well as the new indicator of X-ray luminosity. The main focus of this work is the comparison of the Hα luminosity with other SFR indicators, and the exploration of systematic effects. For this purpose we use a representative sample of local Universe star-forming galaxies (the Star-formation Reference Survey; SFRS).

We obtained and reduced narrow-band imaging Hα observations for all star-forming galaxies in the SFRS sample, up to a redshift of $z = 0.30641$. Based on these data we calculate integrated Hα luminosities, and corresponding SFR, which probe stellar populations with ages of $\leq 15\,\mathrm{Myr}$. We compare the effect of different extinction indicators (Balmer decrement, SED fits, IRX index), and the contamination by the [N II]$\lambda\lambda 6548, 6583$ emission lines. Our results are summarised in the following points:

- We provide calibrations of Hα-based SFRs with the hybrid FIR + FUV SFR indicator, with extinction corrections based on the Balmer decrement, IRX, or SED fits, as well as, corrections for the contribution of the [N II] emission.
- We find excellent agreement between the hybrid indicators of the 24 μm + Hα, and FIR + FUV.

- We find that SFRs based on SED fits show excellent agreement with the SFRs based on FIR + FUV emission for SFR $\gtrsim 1$ $M_\odot\,yr^{-1}$, and increased scatter for lower SFR. This is attributed to stochastic effects (particularly in low luminosity systems) and the interplay between extinction and stellar-population age variations affecting the SED fits and the individual SFR indicators.
- We find that the Balmer-decrement based extinction is about two times larger than the extinction derived from the IRX or the SED fits, while the IRX is very close with the extinction estimated by the SED fits. This difference is attributed to the fact that Balmer lines trace emission of younger stellar populations, therefore they are more sensitive to the attenuation caused by the dust in the birth clouds, whereas the SED fits, and IRX trace emission from older, less obscured, stellar populations.
- We find that in order to match Hα-based SFRs with those derived from radio 1.4 GHz continuum, the SFR $\propto L_{1.4\mathrm{GHz}}^{-\alpha}$ calibration requires an index $\alpha \sim 1$.
- We find, as expected, a correlation between metallicity and extinction in galaxies and we provide a function that describes this correlation for extinctions based on the IRX and Balmer decrement.
- We show that galaxies deviating from this relation are mainly dwarf, highly star-forming galaxies, where a larger part of the overall attenuation is attributed to the dust at the birth clouds, rather than in the general ISM.

For the subset of galaxies in the SFRS sample with good quality *Chandra* data we performed a comparison between their X-ray luminosity (L_X) and SFR as inferred from Hα 8 μm, and 24 μm luminosity. We explore the effect of spatial variations of the X-ray luminosity-SFR calibration in sub-galactic scales of sizes ranging between 1–4 kpc, and we measure the L_X–SFR and the L_X–SFR–$M_\star$ relations down to SFRs $\simeq 10^{-6}\,M_\odot\,yr^{-1}$, and sSFRs $\simeq 10^{-14}\,M_\odot\,yr^{-1}/M_\odot$. These are ~ 5 dex and ~ 2 dex lower in SFR and sSFR respectively than existing galaxy-wide scaling relations. We also investigate the effect of stellar-population age variations in the measured correlations. In more detail:

- we find that the L_X–SFR relation at low SFR ($\leq 10^{-3}\,M_\odot\,yr^{-1}$) has a shallower slope than in higher SFR. This is attributed to the increased contribution of a population of LMXBs at those low SFR. This is supported by the fact that the L_X–SFR–$M_\star$ relation holds down to very low SFR and sSFR with parameters very similar to those derived for the integrated galaxy emission.
- we find that the full-band X-ray luminosity scaling relations are very similar in slope and normalization to those involving the hard band.

- we find that the stellar population timescales probed by Hα, best match the timescales of HMXBs.
- we calculate the effect of different star-formation histories on the X-ray luminosity - SFR scaling relations based on different SFR indicators.
- we find that the combination of the hard band and Hα-based SFR shows the tightest correlation and the smallest intrinsic scatter in both the L_X–SFR, and L_X–SFR–$M_\star$ correlations. This is the result of the very similar timescales of HMXBs and those probed by the Hα luminosity.
- we find no evidence for increasing intrinsic scatter in regions of lower SFR, but the overall scatter of the L_X–SFR–$M_\star$ correlations is larger than galaxy-wide relations. We attribute this to local variations of the SFH within a galaxy.

In order to address the effect of age, and metallicity on the X-ray luminosity–SFR scaling relations for HMXBs, we analyze long-slit optical spectra, IR, and *Chandra* data for the ring galaxy NGC 922. We find that:

- there is significant difference on the metallicity between the nucleus ([12 + log(O/H)] $\sim$ 8.6) and the ring ([12 + log(O/H)] $\sim$ 8.2).
- we do not find any evidence for AGN activity in the nucleus of NGC 922.
- there is He I emission in all observed star-forming regions indicating excitation from very young populations. This is supported by the typically less than 10 Myr ages of the star-clusters in these studied regions.
- there is an anti-correlation between the L_X/SFR and metallicity in NGC 922: the metal-poor ring regions tend to have higher L_X/SFR than the bulge regions. The similarity of the ages of the stellar populations in the studied regions suggests that this anti-correlation is primarily driven by the effect of metallicity.
- this anti-correlation is consistent with expectations from X-ray binary population synthesis models.

5.2 Future Plans

This work has the potential to be extended in several different directions. Examples of projects we have already initiated, or we plan to initiate in the near future are:

a) investigation of the L_X–SFR relation for the full SFRS sample. This work will be able to give robust calibration in this relation for the local Universe galaxies, and provide insights for the effect of the metallicity on the X-ray production of the XRBs.

b) measure the contribution of AGN in the integrated Hα luminosity of Seyfert or composite SFRS galaxies. Explore correlations with galaxy parameters (e.g. IR luminosity, colours in different bands).

c) extension of the study of metallicity variations in ring galaxies and their effect on the X-ray luminosity scaling relations.

d) investigation the L_X–SFR–metallicity relation in sub-galactic scales using integral field unit (IFU) observations. The latter will help disentangle the effects of stellar-populations age, and metallicity on the luminosity of the X-ray binary populations.

e) investigation the effect of different assumptions for the ISM in SED fitting, on the derived attenuation and SFR.

Bibliography

Alam, S., Albareti, F.D., Allende Prieto, C., Anders, F., Anderson, S.F., Anderton, T., Andrews, B.H., Armengaud, E., Aubourg, É., Bailey, S. & et al. (2015). The Eleventh and Twelfth Data Releases of the Sloan Digital Sky Survey: Final Data from SDSS-III. ApJS, **219**, 12. (in p. 70)

Alonso-Herrero, A., Rieke, G.H., Rieke, M.J., Colina, L., Pérez-González, P.G. & Ryder, S.D. (2006). Near-Infrared and Star-forming Properties of Local Luminous Infrared Galaxies. ApJ, **650**, 835–849. (in p. 8)

Anastasopoulou, K., Zezas, A., Gkiokas, V. & Kovlakas, K. (2019). Do sub-galactic regions follow the galaxy-wide X-ray scaling relations? The example of NGC 3310 and NGC 2276. MNRAS, **483**, 711–733. (in pp. 62 and 126)

Antoniou, V. & Zezas, A. (2016). Star formation history and X-ray binary populations: the case of the Large Magellanic Cloud. MNRAS, **459**, 528–553. (in pp. 72 and 97)

Antoniou, V., Zezas, A., Drake, J.J., Badenes, C., Haberl, F., Wright, N.J., Hong, J., Di Stefano, R., Gaetz, T.J., Long, K.S., Plucinsky, P.P., Sasaki, M., Williams, B.F. & Winkler, P.F. (2019a). Deep Chandra survey of the Small Magellanic Cloud. III. Formation efficiency of High-Mass X-ray binaries. *arXiv e-prints*, arXiv:1901.01237. (in p. 90)

Antoniou, V., Zezas, A., Drake, J.J., Badenes, C., Haberl, F., Wright, N.J., Hong, J., Di Stefano, R., Gaetz, T.J., Long, K.S., Plucinsky, P.P., Sasaki, M., Williams, B.F., Winkler, P.F. & SMC XVP collaboration (2019b). Deep Chandra Survey of the Small Magellanic Cloud. III. Formation Efficiency of High-mass X-Ray Binaries. ApJ, **887**, 20. (in pp. 13, 86, 97, and 98)

Appleton, P.N. & Marston, A.P. (1997). Multiwavelength Observations of Collisional Ring Galaxies.I.Broad-Band Images, Global Properties, and Radial Colors of the Sample Galaxies. AJ, **113**, 201–224. (in p. 105)

Artale, M.C., Mapelli, M., Giacobbo, N., Sabha, N.B., Spera, M., Santoliquido, F. & Bressan, A. (2019). Host galaxies of merging compact objects: mass, star formation rate, metallicity, and colours. MNRAS, **487**, 1675–1688. (in p. 2)

Ashby, M.L.N., Mahajan, S., Smith, H.A., Willner, S.P., Fazio, G.G., Raychaudhury, S., Zezas, A., Barmby, P., Bonfini, P., Cao, C., González-Alfonso, E., Ishihara, D., Kaneda, H., Lyttle, V., Madden, S., Papovich, C., Sturm, E., Surace, J., Wu, H. & Zhu, Y.N. (2011). The Star Formation Reference Survey. I. Survey Description and Basic Data. PASP, **123**, 1011. (in pp. 16, 18, 23, 33, 63, and 68)

Asplund, M., Grevesse, N., Sauval, A.J. & Scott, P. (2009). The chemical composition of the sun. *Annual Review of Astronomy and Astrophysics*, **47**, 481–522. (in pp. 23 and 107)

Baldwin, J.A., Phillips, M.M. & Terlevich, R. (1981). Classification parameters for the emission-line spectra of extragalactic objects. PASP, **93**, 5–19. (in pp. 16, 23, and 120)

Barkana, R. & Loeb, A. (2001). In the beginning: the first sources of light and the reionization of the universe. Phys. Rep., **349**, 125–238. (in p. 1)

Bell, E.F. (2003). Estimating Star Formation Rates from Infrared and Radio Luminosities: The Origin of the Radio-Infrared Correlation. ApJ, **586**, 794–813. (in pp. 11 and 50)

Bell, E.F. & Kennicutt, J., Robert C. (2001). A Comparison of Ultraviolet Imaging Telescope Far-Ultraviolet and Hα Star Formation Rates. ApJ, **548**, 681–693. (in p. 6)

Bendo, G.J., Wilson, C.D., Pohlen, M., Sauvage, M., Auld, R., Baes, M., Barlow, M.J., Bock, J.J., Boselli, A., Bradford, M., Buat, V., Castro-Rodriguez, N., Chanial, P., Charlot, S., Ciesla, L., Clements, D.L., Cooray, A., Cormier, D., Cortese, L., Davies, J.I., Dwek, E., Eales, S.A., Elbaz, D., Galametz, M., Galliano, F., Gear, W.K., Glenn, J., Gomez, H.L., Griffin, M., Hony, S., Isaak, K.G., Levenson, L.R., Lu, N., Madden, S., O'Halloran, B., Okumura, K., Oliver, S., Page, M.J., Panuzzo, P., Papageorgiou, A., Parkin, T.J., Perez-Fournon, I., Rangwala, N., Rigby, E.E., Roussel, H., Rykala, A., Sacchi, N., Schulz, B., Schirm, M.R.P., Smith, M.W.L., Spinoglio, L., Stevens, J.A., Sundar, S., Symeonidis, M., Trichas, M., Vaccari, M., Vigroux, L., Wozniak, H., Wright, G.S. & Zeilinger, W.W. (2010). The Herschel Space Observatory view of dust in M81. A&A, **518**, L65. (in p. 9)

Best, P.N., Kauffmann, G., Heckman, T.M., Brinchmann, J., Charlot, S., Ivezić, Ž. & White, S.D.M. (2005). The host galaxies of radio-loud active galactic nuclei: mass dependences, gas cooling and active galactic nuclei feedback. MNRAS, **362**, 25–40. (in p. 131)

Bhattacharya, D. & van den Heuvel, E.P.J. (1991). Formation and evolution of binary and millisecond radio pulsars. Phys. Rep., **203**, 1–124. (in p. 86)

Blain, A.W., Smail, I., Ivison, R.J. & Kneib, J.P. (1999). The history of star formation in dusty galaxies. MNRAS, **302**, 632–648. (in p. 50)

Blanc, G.A., Kewley, L., Vogt, F.P.A. & Dopita, M.A. (2014). IZI: INFERRING THE GAS PHASE METALLICITY (z) AND IONIZATION PARAMETER (q) OF IONIZED NEBULAE USING BAYESIAN STATISTICS. *The Astrophysical Journal*, **798**, 99. (in p. 122)

Boquien, M., Calzetti, D., Kennicutt, R., Dale, D., Engelbracht, C., Gordon, K.D., Hong, S., Lee, J.C. & Portouw, J. (2009). Star-Forming or Starbursting? The Ultraviolet Conundrum. ApJ, **706**, 553–570. (in p. 53)

Boquien, M., Calzetti, D., Kramer, C., Xilouris, E.M., Bertoldi, F., Braine, J., Buchbender, C., Combes, F., Israel, F., Koribalski, B., Lord, S., Quintana-Lacaci, G., Relaño, M., Röllig, M., Stacey, G., Tabatabaei, F.S., Tilanus, R.P.J., van der Tak, F., van der Werf, P. & Verley, S. (2010). 100 μm and 160 μm emission as resolved star-formation rate estimators in M 33 (HERM33ES). A&A, **518**, L70. (in pp. 4 and 22)

Boquien, M., Buat, V. & Perret, V. (2014). Impact of star formation history on the measurement of star formation rates. A&A, **571**, A72. (in pp. 4, 22, 41, 44, 61, 62, 86, 87, and 98)

Boquien, M., Burgarella, D., Roehlly, Y., Buat, V., Ciesla, L., Corre, D., Inoue, A.K. & Salas, H. (2019). CIGALE: a python Code Investigating GALaxy Emission. A&A, **622**, A103. (in pp. 15, 34, 87, and 88)

Boroson, B., Kim, D.W. & Fabbiano, G. (2011). Revisiting with Chandra the Scaling Relations of the X-ray Emission Components (Binaries, Nuclei, and Hot Gas) of Early-type Galaxies. ApJ, **729**, 12. (in pp. 13, 62, 63, and 92)

Bransford, M.A., Appleton, P.N., Marston, A.P. & Charmand aris, V. (1998). Multiwavelength Observations of Collisional Ring Galaxies. III. Oxygen/Nitrogen Abundances and Star Formation Properties of Ring Knots. AJ, **116**, 2757–2775. (in pp. 106 and 130)

Brorby, M., Kaaret, P., Prestwich, A. & Mirabel, I.F. (2016). Enhanced X-ray emission from Lyman break analogues and a possible L_X-SFR-metallicity plane. MNRAS, **457**, 4081–4088. (in pp. 13, 97, 106, 124, 127, 132, and 133)

Bruzual, G. & Charlot, S. (2003). Stellar population synthesis at the resolution of 2003. MNRAS, **344**, 1000–1028. (in pp. 87 and 110)

Buat, V. (1992). Global recent star formation in normal galaxies from a multiwavelength study. Comparison with their gas content. A&A, **264**, 444–454. (in p. 6)

Buat, V. & Xu, C. (1996). Star formation and dust extinction in disk galaxies. Comparison between the UV non-ionizing and the FIR emissions. A&A, **306**, 61. (in p. 30)

Buat, V., Boselli, A., Gavazzi, G. & Bonfanti, C. (2002). Star formation and dust extinction in nearby star-forming and starburst galaxies. A&A, **383**, 801–812. (in pp. 6 and 7)

Buat, V., Iglesias-Páramo, J., Seibert, M., Burgarella, D., Charlot, S., Martin, D.C., Xu, C.K., Heckman, T.M., Boissier, S., Boselli, A., Barlow, T., Bianchi, L., Byun, Y.I., Donas, J., Forster, K., Friedman, P.G., Jelinski, P., Lee, Y.W., Madore, B.F., Malina, R., Milliard, B., Morissey, P., Neff, S., Rich, M., Schiminovitch, D., Siegmund, O., Small, T., Szalay, A.S., Welsh, B. & Wyder, T.K. (2005). Dust Attenuation in the Nearby Universe: A Comparison between Galaxies Selected in the Ultraviolet and in the Far-Infrared. ApJ, **619**, L51–L54. (in p. 31)

Buat, V., Boquien, M., Małek, K., Corre, D., Salas, H., Roehlly, Y., Shirley, R. & Efstathiou, A. (2018). Dust attenuation and Hα emission in a sample of galaxies observed with Herschel at $0.6 < z < 1.6$. A&A, **619**, A135. (in p. 44)

Burgarella, D., Buat, V. & Iglesias-Páramo, J. (2005). Star formation and dust attenuation properties in galaxies from a statistical ultraviolet-to-far-infrared analysis. MNRAS, **360**, 1413–1425. (in p. 34)

Calzetti, D., Kinney, A.L. & Storchi-Bergmann, T. (1994). Dust Extinction of the Stellar Continua in Starburst Galaxies: The Ultraviolet and Optical Extinction Law. ApJ, **429**, 582. (in pp. 6, 22, and 44)

Calzetti, D., Armus, L., Bohlin, R.C., Kinney, A.L., Koornneef, J. & Storchi-Bergmann, T. (2000). The Dust Content and Opacity of Actively Star-forming Galaxies. ApJ, **533**, 682–695. (in pp. 31 and 44)

Calzetti, D., Kennicutt, R.C., Engelbracht, C.W., Leitherer, C., Draine, B.T., Kewley, L., Moustakas, J., Sosey, M., Dale, D.A., Gordon, K.D., Helou, G.X., Hollenbach, D.J., Armus, L., Bendo, G., Bot, C., Buckalew, B., Jarrett, T., Li, A., Meyer, M., Murphy, E.J., Prescott, M., Regan, M.W., Rieke, G.H., Roussel, H., Sheth, K., Smith, J.D.T., Thornley, M.D. & Walter, F. (2007). The Calibration of Mid-Infrared Star Formation Rate Indicators. ApJ, **666**, 870–895. (in pp. 4, 8, 11, 12, 22, 23, 41, and 116)

Calzetti, D., Wu, S.Y., Hong, S., Kennicutt, R.C., Lee, J.C., Dale, D.A., Engelbracht, C.W., van Zee, L., Draine, B.T., Hao, C.N., Gordon, K.D., Moustakas, J., Murphy, E.J., Regan, M., Begum, A., Block, M., Dalcanton, J., Funes, J., Gil de Paz, A., Johnson, B., Sakai, S., Skillman, E., Walter, F., Weisz, D., Williams, B. & Wu, Y. (2010). The Calibration of Monochromatic Far-Infrared Star Formation Rate Indicators. ApJ, **714**, 1256–1279. (in pp. 4, 15, and 22)

Cardelli, J.A., Clayton, G.C. & Mathis, J.S. (1989). The Relationship between Infrared, Optical, and Ultraviolet Extinction. ApJ, **345**, 245. (in p. 76)

Cerviño, M., Bongiovanni, A. & Hidalgo, S. (2016). Recent SFR calibrations and the constant SFR approximation. A&A, **589**, A108. (in pp. 4, 22, 44, 62, 86, and 87)

Chabrier, G. (2003). Galactic Stellar and Substellar Initial Mass Function. PASP, **115**, 763–795. (in pp. 3, 22, and 87)

Charlot, S. & Fall, S.M. (2000). A Simple Model for the Absorption of Starlight by Dust in Galaxies. ApJ, **539**, 718–731. (in pp. 6, 22, and 44)

Chi, X. & Wolfendale, A.W. (1990). Features of the local galactic magnetic field. *Journal of Physics G Nuclear Physics*, **16**, 1409–1421. (in pp. 11 and 50)

Cid Fernandes, R., Mateus, A., Sodré, L., Stasińska, G. & Gomes, J.M. (2005). Semi-empirical analysis of Sloan Digital Sky Survey galaxies - I. Spectral synthesis method. MNRAS, **358**, 363–378. (in p. 110)

Cluver, M.E., Jarrett, T.H., Dale, D.A., Smith, J.D.T., August, T. & Brown, M.J.I. (2017). Calibrating Star Formation in WISE Using Total Infrared Luminosity. ApJ, **850**, 68. (in p. 116)

Coe, M.J. (2005). An estimate of the supernova kick velocities for high-mass X-ray binaries in the Small Magellanic Cloud. MNRAS, **358**, 1379–1382. (in pp. 7 and 72)

Condon, J.J. (1992). Radio emission from normal galaxies. ARA&A, **30**, 575–611. (in p. 50)

Condon, J.J., Anderson, M.L. & Helou, G. (1991). Correlations between Far-Infrared, Radio, and Blue Luminosities of Spiral Galaxies. ApJ, **376**, 95. (in p. 10)

Curti, M., Mannucci, F., Cresci, G. & Maiolino, R. (2020). The mass-metallicity and the fundamental metallicity relation revisited on a fully T_e-based abundance scale for galaxies. MNRAS, **491**, 944–964. (in pp. 55 and 57)

da Cunha, E., Charlot, S. & Elbaz, D. (2008). A simple model to interpret the ultraviolet, optical and infrared emission from galaxies. MNRAS, **388**, 1595–1617. (in p. 47)

Daddi, E., Dickinson, M., Morrison, G., Chary, R., Cimatti, A., Elbaz, D., Frayer, D., Renzini, A., Pope, A., Alexander, D.M., Bauer, F.E., Giavalisco, M., Huynh, M., Kurk, J. & Mignoli, M. (2007). Multiwavelength Study of Massive Galaxies at z~2. I. Star Formation and Galaxy Growth. ApJ, **670**, 156–172. (in p. 61)

Dale, D.A., Helou, G., Magdis, G.E., Armus, L., Díaz-Santos, T. & Shi, Y. (2014). A Two-parameter Model for the Infrared/Submillimeter/Radio Spectral Energy Distributions of Galaxies and Active Galactic Nuclei. ApJ, **784**, 83. (in p. 87)

Davies, L.J.M., Huynh, M.T., Hopkins, A.M., Seymour, N., Driver, S.P., Robotham, A.G.R., Baldry, I.K., Bland-Hawthorn, J., Bourne, N., Bremer, M.N., Brown, M.J.I., Brough, S., Cluver, M., Grootes, M.W., Jarvis, M., Loveday, J., Moffet, A., Owers, M., Phillipps, S., Sadler, E., Wang, L., Wilkins, S. & Wright, A. (2017). Galaxy And Mass Assembly: the 1.4 GHz SFR indicator, SFR-M_* relation and predictions for ASKAP-GAMA. MNRAS, **466**, 2312–2324. (in pp. 4, 11, 22, 50, and 52)

Davis, J.E. (2001). The Formal Underpinnings of the Response Functions Used in X-Ray Spectral Analysis. ApJ, **548**, 1010–1019. (in p. 70)

de Jong, T., Klein, U., Wielebinski, R. & Wunderlich, E. (1985). Radio continuum and far-infrared emission from spiral galaxies : a close correlation. A&A, **147**, L6–L9. (in p. 10)

Delvecchio, I., Daddi, E., Aird, J., Mullaney, J.R., Bernhard, E., Grimmett, L.P., Carraro, R., Cimatti, A., Zamorani, G., Caplar, N., Vito, F., Elbaz, D. & Rodighiero, G. (2020). The Evolving AGN Duty Cycle in Galaxies Since z $\sim$ 3 as Encoded in the X-Ray Luminosity Function. ApJ, **892**, 17. (in p. 131)

Dickinson, M., Giavalisco, M. & GOODS Team (2003). The Great Observatories Origins Deep Survey. In R. Bender & A. Renzini, eds., *The Mass of Galaxies at Low and High Redshift*, 324. (in p. 3)

Domínguez, A., Siana, B., Henry, A.L., Scarlata, C., Bedregal, A.G., Malkan, M., Atek, H., Ross, N.R., Colbert, J.W., Teplitz, H.I., Rafelski, M., McCarthy, P., Bunker, A., Hathi, N.P., Dressler, A., Martin, C.L. & Masters, D. (2013). Dust Extinction from Balmer Decrements of Star-forming Galaxies at 0.75 <= z <= 1.5 with Hubble Space Telescope/Wide-Field-Camera 3 Spectroscopy from the WFC3 Infrared Spectroscopic Parallel Survey. ApJ, **763**, 145. (in p. 31)

Dopita, M.A., Sutherland, R.S., Nicholls, D.C., Kewley, L.J. & Vogt, F.P.A. (2013). New Strong-line Abundance Diagnostics for H II Regions: Effects of κ-distributed Electron Energies and New Atomic Data. ApJS, **208**, 10. (in p. 122)

Douna, V.M., Pellizza, L.J., Mirabel, I.F. & Pedrosa, S.E. (2015). Metallicity dependence of high-mass X-ray binary populations. A&A, **579**, A44. (in p. 97)

Draine, B.T. & Li, A. (2007). Infrared Emission from Interstellar Dust. IV. The Silicate-Graphite-PAH Model in the Post-Spitzer Era. ApJ, **657**, 810–837. (in pp. 2 and 87)

Draine, B.T., Aniano, G., Krause, O., Groves, B., Sandstrom, K., Braun, R., Leroy, A., Klaas, U., Linz, H., Rix, H.W., Schinnerer, E., Schmiedeke, A. & Walter, F. (2014). Andromeda's Dust. ApJ, **780**, 172. (in p. 87)

Dray, L.M. (2006). On the metallicity dependence of high-mass X-ray binaries. MNRAS, **370**, 2079–2090. (in p. 97)

Egorov, O.V. & Moiseev, A.V. (2019). Metallicity and ionization state of the gas in polar-ring galaxies. MNRAS, **486**, 4186–4197. (in p. 106)

Elagali, A., Lagos, C.D.P., Wong, O.I., Staveley-Smith, L., Trayford, J.W., Schaller, M., Yuan, T. & Abadi, M.G. (2018a). Ring galaxies in the EAGLE hydrodynamical simulations. MNRAS, **481**, 2951–2969. (in p. 130)

Elagali, A., Wong, O.I., Oh, S.H., Staveley-Smith, L., Koribalski, B.S., Bekki, K. & Zwaan, M. (2018b). An H I study of the collisional ring galaxy NGC 922. MNRAS, **476**, 5681–5691. (in pp. 106, 123, and 130)

Elbaz, D., Daddi, E., Le Borgne, D., Dickinson, M., Alexander, D.M., Chary, R.R., Starck, J.L., Brand t, W.N., Kitzbichler, M., MacDonald, E., Nonino, M., Popesso, P., Stern, D. & Vanzella, E. (2007). The reversal of the star formation-density relation in the distant universe. A&A, **468**, 33–48. (in pp. 2, 3, and 61)

Enia, A., Rodighiero, G., Morselli, L., Casasola, V., Bianchi, S., Rodriguez-Munoz, L., Mancini, C., Renzini, A., Popesso, P., Cassata, P., Negrello, M. & Franceschini, A. (2020). A panchromatic spatially-resolved analysis of nearby galaxies – I. Sub-kpc scale Main Sequence in grand-design spirals. *arXiv e-prints*, arXiv:2001.04479. (in p. 61)

Eufrasio, R.T., Lehmer, B.D., Zezas, A., Dwek, E., Arendt, R.G., Basu-Zych, A., Wiklind, T., Yukita, M., Fragos, T., Hornschemeier, A.E., Markwardt, L., Ptak, A. & Tzanavaris, P. (2017). On the Spatially Resolved Star Formation History in M51. I. Hybrid UV+IR Star Formation Laws and IR Emission from Dust Heated by Old Stars. ApJ, **851**, 10. (in p. 88)

Evans, I.N., Primini, F.A., Glotfelty, K.J., Anderson, C.S., Bonaventura, N.R., Chen, J.C., Davis, J.E., Doe, S.M., Evans, J.D., Fabbiano, G., Galle, E.C., Gibbs, I., Danny G., Grier, J.D., Hain, R.M., Hall, D.M., Harbo, P.N., He, X.H., Houck, J.C., Karovska, M., Kashyap, V.L., Lauer, J., McCollough, M.L., McDowell, J.C., Miller, J.B., Mitschang, A.W., Morgan, D.L., Mossman, A.E., Nichols, J.S., Nowak, M.A., Plummer, D.A., Refsdal, B.L., Rots, A.H., Siemiginowska, A., Sundheim, B.A., Tibbetts, M.S., Van Stone, D.W., Winkelman, S.L. & Zografou, P. (2010). The Chandra Source Catalog. ApJS, **189**, 37–82. (in p. 108)

Fabbiano, G., Zezas, A. & Murray, S.S. (2001). Chandra Observations of "The Antennae" Galaxies (NGC 4038/9). ApJ, **554**, 1035–1043. (in p. 62)

Ferrarese, L. & Merritt, D. (2000). A Fundamental Relation between Supermassive Black Holes and Their Host Galaxies. ApJ, **539**, L9–L12. (in p. 2)

Few, J.M.A., Madore, B.F. & Arp, H.C. (1982). Ring galaxies-I. Kinematics of the southern ring galaxy AM 064-741. MNRAS, **199**, 633–647. (in p. 106)

Filippenko, A.V. (1982). The importance of atmospheric differential refraction in spectrophotometry. PASP, **94**, 715–721. (in p. 117)

Flores, H., Hammer, F., Thuan, T.X., Césarsky, C., Desert, F.X., Omont, A., Lilly, S.J., Eales, S., Crampton, D. & Le Fèvre, O. (1999). 15 Micron Infrared Space Observatory Observations of the 1415+52 Canada-France Redshift Survey Field: The Cosmic Star Formation Rate as Derived from Deep Ultraviolet, Optical, Mid-Infrared, and Radio Photometry. ApJ, **517**, 148–167. (in p. 50)

Fogarty, L., Thatte, N., Tecza, M., Clarke, F., Goodsall, T., Houghton, R., Salter, G., Davies, R.L. & Kassin, S.A. (2011). SWIFT observations of the Arp 147 ring galaxy system. MNRAS, **417**, 835–844. (in p. 106)

Foreman-Mackey, D., Hogg, D.W., Lang, D. & Goodman, J. (2013a). emcee: The mcmc hammer. *PASP*, **125**, 306–312. (in p. 55)

Foreman-Mackey, D., Hogg, D.W., Lang, D. & Goodman, J. (2013b). emcee: The MCMC Hammer. PASP, **125**, 306. (in p. 100)

Fornasini, F.M., Kriek, M., Sanders, R.L., Shivaei, I., Civano, F., Reddy, N.A., Shapley, A.E., Coil, A.L., Mobasher, B., Siana, B., Aird, J., Azadi, M., Freeman, W.R., Leung, G.C.K., Price, S.H., Fetherolf, T., Zick, T. & Barro, G. (2019). The MOSDEF Survey: The Metallicity Dependence of X-Ray Binary Populations at z 2. ApJ, **885**, 65. (in pp. 14 and 132)

Fornasini, F.M., Civano, F. & Suh, H. (2020). Connecting the metallicity dependence and redshift evolution of high-mass X-ray binaries. MNRAS, **495**, 771–783. (in pp. 13, 14, 106, 124, 127, and 133)

Fosbury, R.A.E. & Hawarden, T.G. (1977). A0035 "the cartwheel" a large southern ring galaxy. MNRAS, **178**, 473–487. (in p. 106)

Fragos, T., Lehmer, B., Tremmel, M., Tzanavaris, P., Basu-Zych, A., Belczynski, K., Hornschemeier, A., Jenkins, L., Kalogera, V., Ptak, A. & Zezas, A. (2013a). X-Ray Binary Evolution Across Cosmic Time. ApJ, **764**, 41. (in pp. 14, 63, 66, 86, 87, 88, 90, 97, and 133)

Fragos, T., Lehmer, B.D., Naoz, S., Zezas, A. & Basu-Zych, A. (2013b). Energy Feedback from X-Ray Binaries in the Early Universe. ApJ, **776**, L31. (in p. 133)

Fragos, T., Lehmer, B.D., Naoz, S., Zezas, A. & Basu-Zych, A. (2016). Erratum: "Energy Feedback from X-Ray Binaries in the Early Universe" <A href="/abs/2013ApJL..776L..31F">(2013, ApJL, 776, L31)</A>. ApJ, **827**, L21. (in pp. 13, 106, 124, and 127)

Freeman, P., Doe, S. & Siemiginowska, A. (2001). Sherpa: a mission-independent data analysis application. In J.L. Starck & F.D. Murtagh, eds., *Astronomical Data Analysis*, vol. 4477 of *Society of Photo-Optical Instrumentation Engineers (SPIE) Conference Series*, 76–87. (in p. 110)

Fruscione, A., McDowell, J.C., Allen, G.E., Brickhouse, N.S., Burke, D.J., Davis, J.E., Durham, N., Elvis, M., Galle, E.C., Harris, D.E., Huenemoerder, D.P., Houck, J.C., Ishibashi, B., Karovska, M., Nicastro, F., Noble, M.S.,

Nowak, M.A., Primini, F.A., Siemiginowska, A., Smith, R.K. & Wise, M. (2006). CIAO: Chandra's data analysis system. In *Society of Photo-Optical Instrumentation Engineers (SPIE) Conference Series*, vol. 6270 of *Society of Photo-Optical Instrumentation Engineers (SPIE) Conference Series*, 62701V. (in p. 112)

García-Vargas, M.L., González-Delgado, R.M., Pérez, E., Alloin, D., Díaz, A. & Terlevich, E. (1997). The Stellar Content of Giant H II Regions in NGC 7714. ApJ, **478**, 112–123. (in p. 106)

Garofali, K., Williams, B.F., Hillis, T., Gilbert, K.M., Dolphin, A.E., Eracleous, M. & Binder, B. (2018). Formation time-scales for high-mass X-ray binaries in M33. MNRAS, **479**, 3526–3544. (in p. 90)

Gebhardt, K., Bender, R., Bower, G., Dressler, A., Faber, S.M., Filippenko, A.V., Green, R., Grillmair, C., Ho, L.C., Kormendy, J., Lauer, T.R., Magorrian, J., Pinkney, J., Richstone, D. & Tremaine, S. (2000). A Relationship between Nuclear Black Hole Mass and Galaxy Velocity Dispersion. ApJ, **539**, L13–L16. (in p. 2)

Gilfanov, M. (2004). Low-mass X-ray binaries as a stellar mass indicator for the host galaxy. MNRAS, **349**, 146–168. (in pp. 13, 62, 63, 96, and 128)

Gordon, K.D., Clayton, G.C., Witt, A.N. & Misselt, K.A. (2000). The Flux Ratio Method for Determining the Dust Attenuation of Starburst Galaxies. ApJ, **533**, 236–244. (in pp. 8 and 30)

Gorenstein, P. (1975). Empirical relation between interstellar X-ray absorption and optical extinction. ApJ, **198**, 95–101. (in p. 76)

Graur, O., Bianco, F.B., Modjaz, M., Shivvers, I., Filippenko, A.V., Li, W. & Smith, N. (2017). LOSS Revisited. II. The Relative Rates of Different Types of Supernovae Vary between Low- and High-mass Galaxies. ApJ, **837**, 121. (in p. 52)

Grimm, H.J., Gilfanov, M. & Sunyaev, R. (2003). High-mass X-ray binaries as a star formation rate indicator in distant galaxies. MNRAS, **339**, 793–809. (in pp. 13, 62, and 75)

Hao, C.N., Kennicutt, R.C., Johnson, B.D., Calzetti, D., Dale, D.A. & Moustakas, J. (2011). Dust-corrected Star Formation Rates of Galaxies. II. Combinations of Ultraviolet and Infrared Tracers. ApJ, **741**, 124. (in pp. 4, 15, and 22)

Harris, J. & Zaritsky, D. (2009). The Star Formation History of the Large Magellanic Cloud. AJ, **138**, 1243–1260. (in p. 88)

Haydon, D.T., Kruijssen, J.M.D., Chevance, M., Hygate, A.P.S., Krumholz, M.R., Schruba, A. & Longmore, S.N. (2020). An uncertainty principle for star formation - III. The characteristic emission time-scales of star formation rate tracers. MNRAS, **498**, 235–257. (in pp. 4, 7, 22, 41, and 44)

Helou, G., Soifer, B.T. & Rowan-Robinson, M. (1985). Thermal infrared and nonthermal radio : remarkable correlation in disks of galaxies. ApJ, **298**, L7–L11. (in p. 10)

Helou, G., Khan, I.R., Malek, L. & Boehmer, L. (1988). IRAS Observations of Galaxies in the Virgo Cluster Area. ApJS, **68**, 151. (in p. 8)

Helou, G., Roussel, H., Appleton, P., Frayer, D., Stolovy, S., Storrie-Lombardi, L., Hurt, R., Lowrance, P., Makovoz, D., Masci, F., Surace, J., Gordon, K.D., Alonso-Herrero, A., Engelbracht, C.W., Misselt, K., Rieke, G., Rieke, M., Willner, S.P., Pahre, M., Ashby, M.L.N., Fazio, G.G. & Smith, H.A. (2004). The Anatomy of Star Formation in NGC 300. ApJS, **154**, 253–258. (in pp. 9, 33, and 68)

Hernquist, L. & Weil, M.L. (1993). Spokes in ring galaxies. MNRAS, **261**, 804–818. (in p. 105)

HI4PI Collaboration, Ben Bekhti, N., Flöer, L., Keller, R., Kerp, J., Lenz, D., Winkel, B., Bailin, J., Calabretta, M.R., Dedes, L., Ford, H.A., Gibson, B.K., Haud, U., Janowiecki, S., Kalberla, P.M.W., Lockman, F.J., McClure-Griffiths, N.M., Murphy, T., Nakanishi, H., Pisano, D.J. & Staveley-Smith, L. (2016). HI4PI: A full-sky H I survey based on EBHIS and GASS. A&A, **594**, A116. (in p. 124)

Higdon, J.L. & Wallin, J.F. (1997). Wheels of Fire. III. Massive Star Formation in the "Double-Ringed" Ring Galaxy Am 0644-741. ApJ, **474**, 686–700. (in p. 106)

Hirashita, H., Buat, V. & Inoue, A.K. (2003). Star formation rate in galaxies from UV, IR, and Hα estimators. A&A, **410**, 83–100. (in p. 11)

Hunt, L.K., Thuan, T.X., Izotov, Y.I. & Sauvage, M. (2010). The Spitzer View of Low-Metallicity Star Formation. III. Fine-Structure Lines, Aromatic Features, and Molecules. ApJ, **712**, 164–187. (in p. 9)

James, P.A., Shane, N.S., Knapen, J.H., Etherton, J. & Percival, S.M. (2005). The Hα Galaxy Survey. II. Extinction and [NII] corrections to Hα fluxes. A&A, **429**, 851–867. (in pp. 5 and 6)

Jarrett, T.H., Cluver, M.E., Brown, M.J.I., Dale, D.A., Tsai, C.W. & Masci, F. (2019). The WISE Extended Source Catalog (WXSC). I. The 100 Largest Galaxies. ApJS, **245**, 25. (in pp. 26 and 68)

Kaaret, P., Feng, H. & Roberts, T.P. (2017). Ultraluminous X-Ray Sources. ARA&A, **55**, 303–341. (in p. 106)

Kauffmann, G., Heckman, T.M., Tremonti, C., Brinchmann, J., Charlot, S., White, S.D.M., Ridgway, S.E., Brinkmann, J., Fukugita, M., Hall, P.B., Ivezić, Ž., Richards, G.T. & Schneider, D.P. (2003). The host galaxies of active galactic nuclei. MNRAS, **346**, 1055–1077. (in pp. 16, 23, 120, 121, and 131)

Kennicutt, J., Robert C. (1998). Star Formation in Galaxies Along the Hubble Sequence. ARA&A, **36**, 189–232. (in pp. 5, 7, 22, and 91)

Kennicutt, J., Robert C., Hao, C.N., Calzetti, D., Moustakas, J., Dale, D.A., Bendo, G., Engelbracht, C.W., Johnson, B.D. & Lee, J.C. (2009). Dust-corrected Star Formation Rates of Galaxies. I. Combinations of Hα and Infrared Tracers. ApJ, **703**, 1672–1695. (in pp. 4, 11, 12, 22, 41, and 52)

Kennicutt, R.C. & Evans, N.J. (2012). Star Formation in the Milky Way and Nearby Galaxies. ARA&A, **50**, 531–608. (in pp. 1, 3, 4, 15, 41, 45, 62, 68, 71, and 86)

Kennicutt, R.C., Jr., Lee, J.C., Funes, J.G., J., S., Sakai, S. & Akiyama, S. (2008). An Hα Imaging Survey of Galaxies in the Local 11 Mpc Volume. ApJS, **178**, 247–279. (in pp. 4, 22, 26, 28, 29, 30, 36, and 66)

Kewley, L.J. & Ellison, S.L. (2008). Metallicity Calibrations and the Mass-Metallicity Relation for Star-forming Galaxies. ApJ, **681**, 1183–1204. (in pp. 45, 105, 121, and 124)

Kewley, L.J., Dopita, M.A., Sutherland, R.S., Heisler, C.A. & Trevena, J. (2001). Theoretical Modeling of Starburst Galaxies. ApJ, **556**, 121–140. (in pp. 16, 23, 120, 121, and 131)

Kewley, L.J., Geller, M.J., Jansen, R.A. & Dopita, M.A. (2002). The Hα and Infrared Star Formation Rates for the Nearby Field Galaxy Survey. AJ, **124**, 3135–3143. (in pp. 5 and 6)

Kewley, L.J., Groves, B., Kauffmann, G. & Heckman, T. (2006). The host galaxies and classification of active galactic nuclei. MNRAS, **372**, 961–976. (in p. 131)

Kiewe, M., Gal-Yam, A., Arcavi, I., Leonard, D.C., Emilio Enriquez, J., Cenko, S.B., Fox, D.B., Moon, D.S., Sand, D.J., Soderberg, A.M. & CCCP, T. (2012). Caltech Core-Collapse Project (CCCP) Observations of Type IIn Supernovae: Typical Properties and Implications for Their Progenitor Stars. ApJ, **744**, 10. (in p. 2)

Kobulnicky, H.A. & Kewley, L.J. (2004). Metallicities of 0.3<z<1.0 Galaxies in the GOODS-North Field. ApJ, **617**, 240–261. (in p. 124)

Koribalski, B.S., Staveley-Smith, L., Kilborn, V.A., Ryder, S.D., Kraan-Korteweg, R.C., Ryan-Weber, E.V., Ekers, R.D., Jerjen, H., Henning, P.A., Putman, M.E., Zwaan, M.A., de Blok, W.J.G., Calabretta, M.R., Disney, M.J., Minchin, R.F., Bhathal, R., Boyce, P.J., Drinkwater, M.J., Freeman, K.C., Gibson, B.K., Green, A.J., Haynes, R.F., Juraszek, S., Kesteven, M.J., Knezek, P.M., Mader, S., Marquarding, M., Meyer, M., Mould, J.R., Oosterloo, T., O'Brien, J., Price, R.M., Sadler, E.M., Schröder, A., Stewart, I.M., Stootman, F., Waugh, M., Warren, B.E., Webster, R.L. & Wright, A.E. (2004). The 1000 Brightest HIPASS Galaxies: H I Properties. AJ, **128**, 16–46. (in p. 106)

Kormendy, J. & Ho, L.C. (2013). Coevolution (Or Not) of Supermassive Black Holes and Host Galaxies. ARA&A, **51**, 511–653. (in pp. 2 and 131)

Kouroumpatzakis, K., Zezas, A., Sell, P., Kovlakas, K., Bonfini, P., Willner, S.P., Ashby, M.L.N., Maragkoudakis, A. & Jarrett, T.H. (2020). Sub-galactic scaling relations between X-ray luminosity, star formation rate, and stellar mass. MNRAS, **494**, 5967–5984. (in pp. 4, 16, 22, 23, 26, 41, 44, 123, 126, 127, and 133)

Kouroumpatzakis, K., Zezas, A., Wolter, A., Fruscione, A., Anastasopoulou, K. & Prestwich, A. (2021). Metallicity and X-ray luminosity variations in NGC 922. MNRAS, **500**, 962–975. (in p. 45)

Kovlakas, K., Zezas, A., Andrews, J.J., Basu-Zych, A., Fragos, T., Hornschemeier, A., Lehmer, B. & Ptak, A. (2020). A census of ultraluminous X-ray sources in the local Universe. MNRAS, **498**, 4790–4810. (in pp. 2 and 107)

Kroupa, P. (2001). On the variation of the initial mass function. MNRAS, **322**, 231–246. (in pp. 3 and 21)

Lacki, B.C., Thompson, T.A. & Quataert, E. (2010). The Physics of the Far-infrared-Radio Correlation. I. Calorimetry, Conspiracy, and Implications. ApJ, **717**, 1–28. (in pp. 10, 11, and 50)

Lamareille, F., Mouhcine, M., Contini, T., Lewis, I. & Maddox, S. (2004). The luminosity-metallicity relation in the local Universe from the 2dF Galaxy Redshift Survey. MNRAS, **350**, 396–406. (in p. 122)

Lang, D., Hogg, D.W., Mierle, K., Blanton, M. & Roweis, S. (2010). Astrometry.net: Blind Astrometric Calibration of Arbitrary Astronomical Images. AJ, **139**, 1782–1800. (in pp. 10 and 26)

Larson, K.L., Díaz-Santos, T., Armus, L., Privon, G.C., Linden, S.T., Evans, A.S., Howell, J., Charmandaris, V., U, V., Sanders, D.B., Stierwalt, S., Barcos-Muñoz, L., Rich, J., Medling, A., Cook, D., Oklopčić, A., Murphy, E.J. & Bonfini, P. (2020). Star-forming Clumps in Local Luminous Infrared Galaxies. ApJ, **888**, 92. (in p. 61)

Lehmer, B.D., Alexander, D.M., Bauer, F.E., Brandt, W.N., Goulding, A.D., Jenkins, L.P., Ptak, A. & Roberts, T.P. (2010). A Chandra Perspective on Galaxy-wide X-ray Binary Emission and its Correlation with Star Formation Rate and Stellar Mass: New Results from Luminous Infrared Galaxies. ApJ, **724**, 559–571. (in pp. 13, 62, and 63)

Lehmer, B.D., Basu-Zych, A.R., Mineo, S., Brandt, W.N., Eufrasio, R.T., Fragos, T., Hornschemeier, A.E., Luo, B., Xue, Y.Q., Bauer, F.E., Gilfanov, M., Ranalli, P., Schneider, D.P., Shemmer, O., Tozzi, P., Trump, J.R., Vignali, C., Wang, J.X., Yukita, M. & Zezas, A. (2016). The Evolution of Normal Galaxy X-Ray Emission through Cosmic History: Constraints from the 6 MS Chandra Deep Field-South. ApJ, **825**, 7. (in pp. 14 and 80)

Lehmer, B.D., Eufrasio, R.T., Markwardt, L., Zezas, A., Basu-Zych, A., Fragos, T., Hornschemeier, A.E., Ptak, A., Tzanavaris, P. & Yukita, M. (2017). On the Spatially Resolved Star Formation History in M51. II. X-Ray Binary Population Evolution. ApJ, **851**, 11. (in p. 13)

Lehmer, B.D., Eufrasio, R.T., Tzanavaris, P., Basu-Zych, A., Fragos, T., Prestwich, A., Yukita, M., Zezas, A., Hornschemeier, A.E. & Ptak, A. (2019). X-Ray Binary Luminosity Function Scaling Relations for Local Galaxies Based on Subgalactic Modeling. ApJS, **243**, 3. (in pp. 13, 62, 75, 86, 95, 96, and 97)

Leitherer, C., Schaerer, D., Goldader, J.D., Delgado, R.M.G., Robert, C., Kune, D.F., de Mello, D.F., Devost, D. & Heckman, T.M. (1999). Starburst99: Synthesis Models for Galaxies with Active Star Formation. ApJS, **123**, 3–40. (in p. 5)

Leitherer, C., Li, I.H., Calzetti, D. & Heckman, T.M. (2002). Global Far-Ultraviolet (912-1800 Å) Properties of Star-forming Galaxies. ApJS, **140**, 303–329. (in p. 31)

Lequeux, J., Peimbert, M., Rayo, J.F., Serrano, A. & Torres-Peimbert, S. (1979). Reprint of 1979A&A....80..155L. Chemical composition and evolution of irregular and blue compact galaxies. A&A, **500**, 145–156. (in pp. 55 and 105)

Leroy, A.K., Bigiel, F., de Blok, W.J.G., Boissier, S., Bolatto, A., Brinks, E., Madore, B., Munoz-Mateos, J.C., Murphy, E., Sandstrom, K., Schruba, A. & Walter, F. (2012). Estimating the Star Formation Rate at 1 kpc Scales in nearby Galaxies. AJ, **144**, 3. (in pp. 5, 41, and 44)

Lian, J., Thomas, D., Maraston, C., Goddard, D., Parikh, T., Fernández-Trincado, J.G., Roman-Lopes, A., Rong, Y., Tang, B. & Yan, R. (2018). SDSS-IV MaNGA: modelling the metallicity gradients of gas and stars - radially dependent metal outflow versus IMF. MNRAS, **476**, 3883–3901. (in p. 105)

Linden, T., Kalogera, V., Sepinsky, J.F., Prestwich, A., Zezas, A. & Gallagher, J.S. (2010). The Effect of Starburst Metallicity on Bright X-ray Binary Formation Pathways. ApJ, **725**, 1984–1994. (in p. 97)

Lynds, R. & Toomre, A. (1976). On the interpretation of ring galaxies: the binary ring system II Hz 4. ApJ, **209**, 382–388. (in p. 105)

Mac Low, M.M., Balsara, D.S., Kim, J. & de Avillez, M.A. (2005). The Distribution of Pressures in a Supernova-driven Interstellar Medium. I. Magnetized Medium. ApJ, **626**, 864–876. (in p. 2)

Madau, P. & Dickinson, M. (2014). Cosmic Star-Formation History. ARA&A, **52**, 415–486. (in p. 1)

Madau, P. & Fragos, T. (2017). Radiation Backgrounds at Cosmic Dawn: X-Rays from Compact Binaries. ApJ, **840**, 39. (in pp. 13, 14, 106, 124, 127, and 133)

Madden, S.C., Galliano, F., Jones, A.P. & Sauvage, M. (2006). ISM properties in low-metallicity environments. A&A, **446**, 877–896. (in p. 9)

Magorrian, J., Tremaine, S., Richstone, D., Bender, R., Bower, G., Dressler, A., Faber, S.M., Gebhardt, K., Green, R., Grillmair, C., Kormendy, J. & Lauer, T. (1998). The Demography of Massive Dark Objects in Galaxy Centers. AJ, **115**, 2285–2305. (in p. 2)

Mahajan, S., Ashby, M.L.N., Willner, S.P., Barmby, P., Fazio, G.G., Maragkoudakis, A., Raychaudhury, S. & Zezas, A. (2019). The Star Formation Reference Survey - III. A multiwavelength view of star formation in nearby galaxies. MNRAS, **482**, 560–577. (in pp. 4, 7, 8, 16, 19, 22, 23, 31, 33, 50, 62, and 158)

Mapelli, M., Colpi, M. & Zampieri, L. (2009). Low metallicity and ultra-luminous X-ray sources in the Cartwheel galaxy. MNRAS, **395**, L71–L75. (in pp. 13, 63, 106, and 132)

Mapelli, M., Ripamonti, E., Zampieri, L., Colpi, M. & Bressan, A. (2010). Ultra-luminous X-ray sources and remnants of massive metal-poor stars. MNRAS, **408**, 234–253. (in pp. 13, 63, and 97)

Maragkoudakis, A., Zezas, A., Ashby, M.L.N. & Willner, S.P. (2014). Aperture effects on spectroscopic galaxy activity classification. MNRAS, **441**, 2296–2308. (in p. 16)

Maragkoudakis, A., Zezas, A., Ashby, M.L.N. & Willner, S.P. (2017). The sub-galactic and nuclear main sequences for local star-forming galaxies. MNRAS, **466**, 1192–1204. (in pp. 16, 61, 63, and 71)

Maragkoudakis, A., Zezas, A., Ashby, M.L.N. & Willner, S.P. (2018). The Star Formation Reference Survey - II. Activity demographics and host-galaxy properties for infrared-selected galaxies. MNRAS, **475**, 1485–1507. (in pp. 16, 23, 29, 30, 45, 46, 53, 55, 57, 65, 76, and 158)

Martin, D.C., Fanson, J., Schiminovich, D., Morrissey, P., Friedman, P.G., Barlow, T.A., Conrow, T., Grange, R., Jelinsky, P.N., Milliard, B., Siegmund, O.H.W., Bianchi, L., Byun, Y.I., Donas, J., Forster, K., Heckman, T.M., Lee, Y.W., Madore, B.F., Malina, R.F., Neff, S.G., Rich, R.M., Small, T., Surber, F., Szalay, A.S., Welsh, B. & Wyder, T.K. (2005). The Galaxy Evolution Explorer: A Space Ultraviolet Survey Mission. ApJ, **619**, L1–L6. (in p. 7)

Massey, P., Strobel, K., Barnes, J.V. & Anderson, E. (1988). Spectrophotometric standards. ApJ, **328**, 315–333. (in pp. 27, 68, and 110)

Mateus, A., Sodré, L., Cid Fernand es, R., Stasińska, G., Schoenell, W. & Gomes, J.M. (2006). Semi-empirical analysis of Sloan Digital Sky Survey galaxies - II. The bimodality of the galaxy population revisited. MNRAS, **370**, 721–737. (in p. 110)

Meurer, G.R., Heckman, T.M. & Calzetti, D. (1999). Dust Absorption and the Ultraviolet Luminosity Density at z ~3 as Calibrated by Local Starburst Galaxies. ApJ, **521**, 64–80. (in p. 30)

Mihos, J.C. & Hernquist, L. (1994). Star-forming Galaxy Models: Blending Star Formation into TREESPH. ApJ, **437**, 611. (in p. 105)

Miller, G.E. & Scalo, J.M. (1979). The Initial Mass Function and Stellar Birthrate in the Solar Neighborhood. ApJS, **41**, 513. (in pp. 3 and 21)

Mineo, S., Gilfanov, M. & Sunyaev, R. (2012a). X-ray emission from star-forming galaxies - I. High-mass X-ray binaries. MNRAS, **419**, 2095–2115. (in pp. 13, 62, and 128)

Mineo, S., Gilfanov, M. & Sunyaev, R. (2012b). X-ray emission from star-forming galaxies - II. Hot interstellarmedium. MNRAS, **426**, 1870–1883. (in pp. 13 and 62)

Mineo, S., Gilfanov, M., Lehmer, B.D., Morrison, G.E. & Sunyaev, R. (2014). X-ray emission from star-forming galaxies - III. Calibration of the L_X-SFR relation up to redshift z $\approx$ 1.3. MNRAS, **437**, 1698–1707. (in pp. 2, 13, 62, 63, and 96)

Morrison, R. & McCammon, D. (1983). Interstellar photoelectric absorption cross sections, 0.03-10 keV. ApJ, **270**, 119–122. (in p. 76)

Moustakas, J. & Kennicutt, J., Robert C. (2006). An Integrated Spectrophotometric Survey of Nearby Star-forming Galaxies. ApJS, **164**, 81–98. (in pp. 4, 5, and 22)

Moustakas, J., Kennicutt, J., Robert C., Tremonti, C.A., Dale, D.A., Smith, J.D.T. & Calzetti, D. (2010). Optical Spectroscopy and Nebular Oxygen Abundances of the Spitzer/SINGS Galaxies. ApJS, **190**, 233–266. (in pp. 105 and 130)

Murphy, E.J., Condon, J.J., Schinnerer, E., Kennicutt, R.C., Calzetti, D., Armus, L., Helou, G., Turner, J.L., Aniano, G., Beirão, P., Bolatto, A.D., Brandl, B.R., Croxall, K.V., Dale, D.A., Donovan Meyer, J.L., Draine, B.T., Engelbracht, C., Hunt, L.K., Hao, C.N., Koda, J., Roussel, H., Skibba, R. & Smith, J.D.T. (2011). Calibrating Extinction-free Star Formation Rate Diagnostics with 33 GHz Free-free Emission in NGC 6946. ApJ, **737**, 67. (in pp. 4, 5, 7, 15, 22, 31, 66, and 68)

Nersesian, A., Xilouris, E.M., Bianchi, S., Galliano, F., Jones, A.P., Baes, M., Casasola, V., Cassarà, L.P., Clark, C.J.R., Davies, J.I., Decleir, M., Dobbels, W., De Looze, I., De Vis, P., Fritz, J., Galametz, M., Madden, S.C., Mosenkov, A.V., Trčka, A., Verstocken, S., Viaene, S. & Lianou, S. (2019). Old and young stellar populations in DustPedia galaxies and their role in dust heating. A&A, **624**, A80. (in p. 9)

Noeske, K.G., Faber, S.M., Weiner, B.J., Koo, D.C., Primack, J.R., Dekel, A., Papovich, C., Conselice, C.J., Le Floc'h, E., Rieke, G.H., Coil, A.L., Lotz, J.M., Somerville, R.S. & Bundy, K. (2007). Star Formation in AEGIS Field Galaxies since z=1.1: Staged Galaxy Formation and a Model of Mass-dependent Gas Exhaustion. ApJ, **660**, L47–L50. (in pp. 2 and 61)

Noll, S., Burgarella, D., Giovannoli, E., Buat, V., Marcillac, D. & Muñoz-Mateos, J.C. (2009). Analysis of galaxy spectral energy distributions from far-UV to far-IR with CIGALE: studying a SINGS test sample. A&A, **507**, 1793–1813. (in p. 34)

Pancoast, A., Sajina, A., Lacy, M., Noriega-Crespo, A. & Rho, J. (2010). Star Formation and Dust Obscuration in the Tidally Distorted Galaxy NGC 2442. ApJ, **723**, 530–543. (in pp. 33, 69, and 92)

Papovich, C. & Bell, E.F. (2002). On Measuring the Infrared Luminosity of Distant Galaxies with the Space Infrared Telescope Facility. ApJ, **579**, L1–L4. (in p. 8)

Park, T., Kashyap, V.L., Siemiginowska, A., van Dyk, D.A., Zezas, A., Heinke, C. & Wargelin, B.J. (2006). Bayesian Estimation of Hardness Ratios: Modeling and Computations. ApJ, **652**, 610–628. (in p. 73)

Peeters, E., Spoon, H.W.W. & Tielens, A.G.G.M. (2004). Polycyclic Aromatic Hydrocarbons as a Tracer of Star Formation? ApJ, **613**, 986–1003. (in p. 68)

Pellerin, A., Meurer, G.R., Bekki, K., Elmegreen, D.M., Wong, O.I. & Knezek, P.M. (2010). The Star Cluster Population of the Collisional Ring Galaxy NGC 922. AJ, **139**, 1369–1382. (in pp. 106, 123, 124, 125, and 131)

Pettini, M. & Pagel, B.E.J. (2004). [OIII]/[NII] as an abundance indicator at high redshift. MNRAS, **348**, L59–L63. (in pp. 54, 120, 122, and 124)

Podsiadlowski, P., Langer, N., Poelarends, A.J.T., Rappaport, S., Heger, A. & Pfahl, E. (2004). The Effects of Binary Evolution on the Dynamics of Core Collapse and Neutron Star Kicks. ApJ, **612**, 1044–1051. (in p. 72)

Politakis, B., Zezas, A., Andrews, J.J. & Williams, S.J. (2020). Vertical distribution of HMXBs in NGC 55: Constraining their centre of mass velocity. MNRAS. (in p. 72)

Prestwich, A.H., Galache, J.L., Linden, T., Kalogera, V., Zezas, A., Roberts, T.P., Kilgard, R., Wolter, A. & Trinchieri, G. (2012). Chandra Observations of the Collisional Ring Galaxy NGC 922. ApJ, **747**, 150. (in pp. 106, 112, and 132)

Prestwich, A.H., Tsantaki, M., Zezas, A., Jackson, F., Roberts, T.P., Foltz, R., Linden, T. & Kalogera, V. (2013). Ultra-luminous X-Ray Sources in the Most Metal Poor Galaxies. ApJ, **769**, 92. (in p. 97)

Price, R. & Duric, N. (1992). New Results on the Radio–Far-Infrared Relation for Galaxies. ApJ, **401**, 81. (in p. 52)

Price, S.H., Kriek, M., Brammer, G.B., Conroy, C., Förster Schreiber, N.M., Franx, M., Fumagalli, M., Lundgren, B., Momcheva, I., Nelson, E.J., Skelton, R.E., van Dokkum, P.G., Whitaker, K.E. & Wuyts, S. (2014). Direct Measurements of Dust Attenuation in z ~1.5 Star-forming Galaxies from 3D-HST: Implications for Dust Geometry and Star Formation Rates. ApJ, **788**, 86. (in p. 44)

Puls, J., Kudritzki, R.P., Herrero, A., Pauldrach, A.W.A., Haser, S.M., Lennon, D.J., Gabler, R., Voels, S.A., Vilchez, J.M., Wachter, S. & Feldmeier, A. (1996). O-star mass-loss and wind momentum rates in the Galaxy and the Magellanic Clouds Observations and theoretical predictions. A&A, **305**, 171. (in p. 2)

Qin, J., Zheng, X.Z., Wuyts, S., Pan, Z. & Ren, J. (2019). Understanding the Discrepancy between IRX and Balmer Decrement in Tracing Galaxy Dust Attenuation. ApJ, **886**, 28. (in pp. 6 and 44)

Ranalli, P., Comastri, A. & Setti, G. (2003). The 2-10 keV luminosity as a Star Formation Rate indicator. A&A, **399**, 39–50. (in pp. 13, 15, and 62)

Reddy, N.A., Kriek, M., Shapley, A.E., Freeman, W.R., Siana, B., Coil, A.L., Mobasher, B., Price, S.H., Sanders, R.L. & Shivaei, I. (2015). The MOSDEF Survey: Measurements of Balmer Decrements and the Dust Attenuation Curve at Redshifts z ~1.4-2.6. ApJ, **806**, 259. (in p. 44)

Refsdal, B.L., Doe, S.M., Nguyen, D.T., Siemiginowska, A.L., Bonaventura, N.R., Burke, D., Evans, I.N., Evans, J.D., Fruscione, A., Galle, E.C., Houck, J.C., Karovska, M., Lee, N.P. & Nowak, M.A. (2009). Sherpa: 1d/2d modeling and fitting in python. In G. Varoquaux, S. van der Walt & J. Millman, eds., *Proceedings of the 8th Python in Science Conference*, 51 – 57, Pasadena, CA USA. (in p. 110)

Relaño, M., Lisenfeld, U., Pérez-González, P.G., Vílchez, J.M. & Battaner, E. (2007). On the Metallicity Dependence of the 24 μm Luminosity as a Star Formation Tracer. ApJ, **667**, L141–L144. (in p. 9)

Remillard, R.A. & McClintock, J.E. (2006). X-Ray Properties of Black-Hole Binaries. ARA&A, **44**, 49–92. (in p. 12)

Rieke, G.H., Alonso-Herrero, A., Weiner, B.J., Pérez-González, P.G., Blaylock, M., Donley, J.L. & Marcillac, D. (2009). Determining Star Formation Rates for Infrared Galaxies. ApJ, **692**, 556–573. (in pp. 4, 9, 15, 22, 33, 68, and 69)

Robertson, P., Shields, G.A., Davé, R., Blanc, G.A. & Wright, A. (2013). Dependence of Nebular Heavy-element Abundance on H I Content for Spiral Galaxies. ApJ, **773**, 4. (in p. 122)

Salim, S., Boquien, M. & Lee, J.C. (2018). Dust Attenuation Curves in the Local Universe: Demographics and New Laws for Star-forming Galaxies and High-redshift Analogs. ApJ, **859**, 11. (in p. 44)

Salpeter, E.E. (1955). The Luminosity Function and Stellar Evolution. ApJ, **121**, 161. (in pp. 3, 21, and 87)

Santos-Santos, I.M.E., Domínguez-Tenreiro, R., Granato, G.L., Brook, C.B. & Obreja, A. (2017). Diversity of dwarf galaxy IR-submm emission patterns: CLUES from hydrodynamical simulations. A&A, **603**, A4. (in p. 9)

Saunders, W., Sutherland, W.J., Maddox, S.J., Keeble, O., Oliver, S.J., Rowan-Robinson, M., McMahon, R.G., Efstathiou, G.P., Tadros, H., White, S.D.M., Frenk, C.S., Carramiñana, A. & Hawkins, M.R.S. (2000). The PSCz catalogue. MNRAS, **317**, 55–63. (in pp. 16 and 23)

Sauvage, M. & Thuan, T.X. (1992). On the Use of Far-Infrared Luminosity as a Star Formation Indicator in Galaxies. ApJ, **396**, L69. (in p. 9)

Schawinski, K., Thomas, D., Sarzi, M., Maraston, C., Kaviraj, S., Joo, S.J., Yi, S.K. & Silk, J. (2007). Observational evidence for AGN feedback in early-type galaxies. MNRAS, **382**, 1415–1431. (in pp. 7, 16, and 23)

Schmidt, M. (1966). Lifetimes of Extragalactic Radio Sources. ApJ, **146**, 7. (in p. 131)

Seabold, S. & Perktold, J. (2010). statsmodels: Econometric and statistical modeling with python. In *9th Python in Science Conference*. (in p. 36)

Smith, R.K., Brickhouse, N.S., Liedahl, D.A. & Raymond, J.C. (2001). Collisional Plasma Models with APEC/APED: Emission-Line Diagnostics of Hydrogen-like and Helium-like Ions. ApJ, **556**, L91–L95. (in p. 70)

Soifer, B.T., Boehmer, L., Neugebauer, G. & Sanders, D.B. (1989). The IRAS Bright Galaxy Sample. IV. Complete IRAS Observations. AJ, **98**, 766. (in p. 8)

Somerville, R.S. & Davé, R. (2015). Physical Models of Galaxy Formation in a Cosmological Framework. ARA&A, **53**, 51–113. (in p. 57)

Struck-Marcell, C. & Lotan, P. (1990). The Varieties of Symmetric Stellar Rings and Radial Caustics in Galaxy Disks. ApJ, **358**, 99. (in p. 105)

Tabatabaei, F.S., Schinnerer, E., Krause, M., Dumas, G., Meidt, S., Damas-Segovia, A., Beck, R., Murphy, E.J., Mulcahy, D.D., Groves, B., Bolatto, A., Dale, D., Galametz, M., Sandstrom, K., Boquien, M., Calzetti, D., Kennicutt, R.C., Hunt, L.K., De Looze, I. & Pellegrini, E.W. (2017). The Radio Spectral Energy Distribution and Star-formation Rate Calibration in Galaxies. ApJ, **836**, 185. (in pp. 11 and 50)

Tauris, T.M. & van den Heuvel, E.P.J. (2006). Formation and evolution of compact stellar X-ray sources. *Cambridge University Press*, 623–665. (in p. 86)

Theios, R.L., Steidel, C.C., Strom, A.L., Rudie, G.C., Trainor, R.F. & Reddy, N.A. (2019). Dust Attenuation, Star Formation, and Metallicity in z $\sim$ 2-3 Galaxies from KBSS-MOSFIRE. ApJ, **871**, 128. (in p. 53)

Theys, J.C. & Spiegel, E.A. (1976). Ring galaxies. I. ApJ, **208**, 650–661. (in p. 105)

Toalá, J.A. & Arthur, S.J. (2011). Radiation-hydrodynamic Models of the Evolving Circumstellar Medium around Massive Stars. ApJ, **737**, 100. (in p. 2)

Tody, D. (1986). The IRAF Data Reduction and Analysis System. In D.L. Crawford, ed., Proc. SPIE, vol. 627 of *Society of Photo-Optical Instrumentation Engineers (SPIE) Conference Series*, 733. (in pp. 26 and 109)

Tody, D. (1993). IRAF in the Nineties. In R.J. Hanisch, R.J.V. Brissenden & J. Barnes, eds., *Astronomical Data Analysis Software and Systems II*, vol. 52 of *Astronomical Society of the Pacific Conference Series*, 173. (in pp. 26 and 109)

Tremonti, C.A., Heckman, T.M., Kauffmann, G., Brinchmann, J., Charlot, S., White, S.D.M., Seibert, M., Peng, E.W., Schlegel, D.J., Uomoto, A., Fukugita, M. & Brinkmann, J. (2004). The Origin of the Mass-Metallicity Relation: Insights from 53,000 Star-forming Galaxies in the Sloan Digital Sky Survey. ApJ, **613**, 898–913. (in pp. 57 and 105)

van den Heuvel, E.P.J., Portegies Zwart, S.F., Bhattacharya, D. & Kaper, L. (2000). On the origin of the difference between the runaway velocities of the OB-supergiant X-ray binaries and the Be/X-ray binaries. A&A, **364**, 563–572. (in p. 72)

van Dyk, D.A., Connors, A., Kashyap, V.L. & Siemiginowska, A. (2001). Analysis of Energy Spectra with Low Photon Counts via Bayesian Posterior Simulation. ApJ, **548**, 224–243. (in p. 73)

van Winckel, H. (2003). Post-AGB Stars. ARA&A, **41**, 391–427. (in p. 4)

van Zee, L., Salzer, J.J., Haynes, M.P., O'Donoghue, A.A. & Balonek, T.J. (1998). Spectroscopy of Outlying H II Regions in Spiral Galaxies: Abundances and Radial Gradients. AJ, **116**, 2805–2833. (in p. 105)

Veilleux, S. & Osterbrock, D.E. (1987). Spectral Classification of Emission-Line Galaxies. ApJS, **63**, 295. (in pp. 16, 23, and 120)

Vila-Costas, M.B. & Edmunds, M.G. (1992). The relation between abundance gradients and the physical properties of spiral galaxies. MNRAS, **259**, 121–145. (in p. 105)

Walch, S. & Naab, T. (2015). The energy and momentum input of supernova explosions in structured and ionized molecular clouds. MNRAS, **451**, 2757–2771. (in p. 2)

Walcher, J., Groves, B., Budavári, T. & Dale, D. (2011). Fitting the integrated spectral energy distributions of galaxies. Ap&SS, **331**, 1–52. (in p. 15)

Walterbos, R.A.M. & Greenawalt, B. (1996). Far-Infrared Radiation from Dust Heated by the Interstellar Radiation Field in Spiral Galaxies. ApJ, **460**, 696. (in p. 9)

Weidner, C. & Vink, J.S. (2010). The masses, and the mass discrepancy of O-type stars. A&A, **524**, A98. (in p. 3)

Wen, X.Q., Wu, H., Zhu, Y.N., Lam, M.I., Wu, C.J., Wicker, J. & Zhao, Y.H. (2013). The stellar masses of galaxies from the 3.4 μm band of the WISE All-Sky Survey. MNRAS, **433**, 2946–2957. (in p. 116)

Wild, V., Charlot, S., Brinchmann, J., Heckman, T., Vince, O., Pacifici, C. & Chevallard, J. (2011). Empirical determination of the shape of dust attenuation curves in star-forming galaxies. MNRAS, **417**, 1760–1786. (in p. 44)

Wilms, J., Allen, A. & McCray, R. (2000). On the Absorption of X-Rays in the Interstellar Medium. ApJ, **542**, 914–924. (in p. 113)

Wolter, A. & Trinchieri, G. (2004). A thorough study of the intriguing X-ray emission from the Cartwheel ring. A&A, **426**, 787–796. (in pp. 106 and 132)

Wolter, A., Trinchieri, G. & Iovino, A. (1999). High energy phenomena in the Cartwheel's ring. A&A, **342**, 41–46. (in p. 106)

Wolter, A., Esposito, P., Mapelli, M., Pizzolato, F. & Ripamonti, E. (2015). NGC 2276: a remarkable galaxy with a large number of ultraluminous X-ray sources. MNRAS, **448**, 781–791. (in p. 106)

Wolter, A., Fruscione, A. & Mapelli, M. (2018). The X-Ray Luminosity Function of Ultraluminous X-Ray Sources in Collisional Ring Galaxies. ApJ, **863**, 43. (in pp. 106 and 131)

Wong, O.I., Meurer, G.R., Bekki, K., Hanish, D.J., Kennicutt, R.C., Bland-Hawthorn, J., Ryan-Weber, E.V., Koribalski, B., Kilborn, V.A., Putman, M.E., Heiner, J.S., Webster, R.L., Allen, R.J., Dopita, M.A., Doyle, M.T., Drinkwater, M.J., Ferguson, H.C., Freeman, K.C., Heckman, T.M., Hoopes, C., Knezek, P.M., Meyer, M.J., Oey, M.S., Seibert, M., Smith, R.C., Staveley-Smith, L., Thilker, D., Werk, J. & Zwaan, M.A. (2006). NGC922 - a new drop-through ring galaxy. MNRAS, **370**, 1607–1611. (in pp. 106, 122, 123, and 130)

Wu, H., Cao, C., Hao, C.N., Liu, F.S., Wang, J.L., Xia, X.Y., Deng, Z.G. & Young, C.K.S. (2005). PAH and Mid-Infrared Luminosities as Measures of Star Formation Rate in Spitzer First Look Survey Galaxies. ApJ, **632**, L79–L82. (in p. 8)

Xiang, M., Shi, J., Liu, X., Yuan, H., Chen, B., Huang, Y., Wang, C., Wu, Y., Tian, Z., Huo, Z., Zhang, H. & Zhang, M. (2018). Stellar Mass Distribution and Star Formation History of the Galactic Disk Revealed by Mono-age Stellar Populations from LAMOST. ApJS, **237**, 33. (in p. 88)

Zaritsky, D., Kennicutt, J., Robert C. & Huchra, J.P. (1994). H II Regions and the Abundance Properties of Spiral Galaxies. ApJ, **420**, 87. (in p. 105)

Zezas, A., Fabbiano, G., Baldi, A., Schweizer, F., King, A.R., Ponman, T.J. & Rots, A.H. (2006). Chandra Monitoring Observations of The Antennae Galaxies. I. Catalog of Source Properties. ApJS, **166**, 211–248. (in p. 73)

Zhang, Z., Gilfanov, M. & Bogdán, Á. (2012). Dependence of the low-mass X-ray binary population on stellar age. A&A, **546**, A36. (in pp. 13 and 62)

Zhu, Y.N., Wu, H., Cao, C. & Li, H.N. (2008). Correlations between Mid-Infrared, Far-Infrared, Hα, and FUV Luminosities for Spitzer SWIRE Field Galaxies. ApJ, **686**, 155–171. (in pp. 8 and 9)

Zhu, Y.N., Wu, H., Li, H.N. & Cao, C. (2010). Stellar mass estimation based on IRAC photometry for Spitzer SWIRE-field galaxies. *Research in Astronomy and Astrophysics*, **10**, 329–347. (in p. 69)

6

Appendix

Table 6.1: Properties of the SFRS galaxies

In this Appendix we present the general properties of the SFRS galaxies along with the Hα photometry, extinction, metallicities, [N II]/Hα emission ratio, and star-formation rates based on Hα and 24 μm measurements derived as presented in Chapter 2.

(1): SFRS ID
(2): Common galaxy name (*2MASXJ11193404+5335181 has been shortened to 11193404+5335181, and MCG 3-35-034_NED01 to MCG 3-35-034)
(3): Right ascension (J2000)
(4): Declination (J2000)
(5): BPT classification presented in Maragkoudakis *et al.* (2018) (H II, Sy, TO, and LNR correspond to star-forming, Seyfert, transition object, and LINER galaxies respectively).
(6): Distance (Mpc)
(7): log $f_{\mathrm{H}\alpha+[\mathrm{N\,II}]}$
(8): log $f_{\mathrm{H}\alpha+[\mathrm{N\,II}]}$ 68% uncertainty
(9): $\mathrm{E(B-V)_{Balmer}}$
(10): $\mathrm{E(B-V)_{IRX}}$
(11): $[12 + \log(\mathrm{O/H})_{\mathrm{nucleus}}]$
(12): $[12 + \log(\mathrm{O/H})_{\mathrm{host}}]$
(13): log $f_{[\mathrm{N\,II}]}/f_{\mathrm{H}\alpha}$
(14): log $\mathrm{SFR_{H\alpha}}$ (Hα flux is corrected for the [N II] contribution and extinction based on Balmer decrement)
(15): log $\mathrm{SFR_{24\mu m+H\alpha}}$ (Hα flux is corrected for the [N II] contribution)
(16): log $\mathrm{SFR_{FUV+FIR}}$ presented in Mahajan *et al.* (2019).
(17): log $M_\star$ ($\mathrm{M_\odot}$)

(1)	(2)	(3)	(4)	(5)	(6)	(7)	(8)	(9)	(10)	(11)	(12)	(13)	(14)	(15)	(16)	(17)
1	IC 486	08:00:20.98	+26:36:48.7	Sy	114.4	−12.46	0.03	0.61	0.25			0.07		1.11	0.64	
2	IC 2217	08:00:49.73	+27:30:01.7	H II	76.1	−11.86	0.01	0.47	0.21	8.77	8.72	−0.42	1.12	0.96	0.78	10.48
3	NGC 2500	08:01:53.18	+50:44:13.7	LNR	15.0	−11.66	0.01	0.07	0.07			−0.45	−0.61	−0.38	−0.11	
4	NGC 2512	08:03:07.85	+23:23:30.6	H II	69.3	−12.19	0.14	0.43		8.85	8.74	−0.31	0.58	0.95		10.9
5	MCG 6-18-009	08:03:28.94	+33:27:44.5	H II	164.3			0.52	0.28	8.8		−0.29			1.2	11.24
6	MK 1212	08:07:05.52	+27:07:33.7	H II	173.3			0.66		8.74		−0.28				10.95
7	IRAS 08072+1847	08:10:07.01	+18:38:18.1	H II	70.8	−13.25	0.02	0.9		8.74		−0.2	0.01	0.95		10.01
8	NGC 2532	08:10:15.17	+33:57:23.9	H II	77.6	−11.69	0.01	0.85	0.19	8.76	8.72	−0.42	1.81	1.21	1.1	11.11
9	UGC 4261	08:10:56.21	+36:49:41.3	H II	93.2	−12.34	0.07	0.33	0.13	8.53		−0.6	0.71	1.0	0.71	10.14
10	NGC 2535	08:11:13.49	+25:12:24.5	H II	61.6	−11.83	0.09	0.32	0.17	8.87	8.66	−0.43	0.78	0.77	0.69	10.68
11	NGC 2543	08:12:57.91	+36:15:16.7	H II	26.3	−12.03	0.06	0.64	0.18	8.77		−0.35	0.21	−0.06	−0.01	10.24
12	NGC 2537	08:13:14.74	+45:59:21.9	H II	15.0	−11.57	0.02	−0.04	0.12	8.61	8.71	−0.51	−0.63	−0.27	−0.34	9.78
13	IC 2233	08:13:58.82	+45:44:43.7	H II	13.7	−12.38	0.17	0.2	0.05	8.17		−1.21	−1.06	−1.07	−0.61	8.71
14	IC 2239	08:14:06.79	+23:51:58.9	TO	88.5	−12.57	0.04	0.73	0.43			−0.14	0.54	1.05	0.86	
15	UGC 4286	08:14:16.50	+18:26:26.0	H II	73.5	−12.44	0.01	0.41	0.2	8.64		−0.37	0.4	0.93	0.35	10.55
16	UGC 4306	08:17:36.80	+35:26:44.9	H II	36.0	−12.51	0.38	0.63	0.4	8.7		−0.39	0.01	0.12	0.18	10.16
17	NGC 2552	08:19:19.58	+50:00:20.8	H II	11.4	−12.0	0.07	0.11	0.03	8.25		−1.06	−0.98	−0.89	−0.72	7.76
18	UGC 4383	08:23:34.20	+21:20:51.5	H II	79.3	−12.34	0.01	0.33	0.22	8.56		−0.46	0.53	0.6	0.6	
19	IRAS 08234+1054	08:26:07.90	+10:44:51.3	H II	272.6			0.8	0.43	8.76		−0.23			1.62	10.98
20	IRAS 08269+1514	08:29:45.19	+15:04:39.4	H II	134.5	−12.72	0.02	0.6	0.51	8.72		−0.3	0.85	1.19	0.75	10.44
21	NGC 2604	08:33:23.14	+29:32:19.7	H II	36.3	−11.97	0.09	0.19	0.08	8.58		−0.66	0.09	0.36	0.26	9.74
22	NGC 2608	08:35:17.34	+28:28:24.3	H II	36.3	−12.09	0.03	0.56	0.2	8.77	8.79	−0.31	0.29	0.11	0.2	10.53
23	MK 92	08:35:39.96	+46:29:28.1	H II	68.8	−12.05	0.02	0.24		8.65	8.73	−0.43	0.55	0.81		10.16
24	NGC 2623	08:38:24.00	+25:45:16.3	Sy	81.6	−12.74	0.04	1.4	0.47			−0.02	0.37	1.33	1.63	
25	CGCG 120-018	08:39:50.76	+23:08:36.1	H II	107.9	−12.82	0.03	1.04	0.57	8.75		−0.16	0.93	0.91	1.02	10.63

(1)	(2)	(3)	(4)	(5)	(6)	(7)	(8)	(9)	(10)	(11)	(12)	(13)	(14)	(15)	(16)	(17)
26	NGC 2644	08:41:31.85	+04:58:49.2	H II	25.0	−12.32	0.03	0.22		8.68	8.76	−0.49	−0.59	−0.19		9.75
27	UGC 4572	08:45:37.85	+36:56:04.7	TO	60.5	−12.5	0.01	0.32				−0.05	−0.65	0.39		
28	UGC 4653	08:53:54.62	+35:08:44.2	H II	234.0			0.7		8.68	8.97	−0.23				11.63
29	IRAS 08512+2727	08:54:16.78	+27:15:59.5	H II	265.3			0.55	0.29	8.75		−0.45			1.3	11.18
30	OJ287	08:54:48.86	+20:06:30.7		1258.8											
31	IRAS 08538+4256	08:57:10.32	+42:45:23.1	H II	121.2	−12.77	0.03	0.81	0.55	8.74		−0.31	0.99	1.17	1.28	10.67
32	IRAS 08550+3908	08:58:13.75	+38:56:31.9	Sy	367.8			0.06	0.41			0.12			1.66	
33	NGC 2718	08:58:50.47	+06:17:34.8	H II	57.4	−12.03	0.01	0.37	0.18	8.85		−0.33	0.51	0.78	0.77	10.84
34	NGC 2712	08:59:30.48	+44:54:50.0	H II	30.9	−11.97	0.23	0.33	0.15	8.72	8.8	−0.26	−0.09	0.05	0.1	10.49
35	NGC 2719	09:00:15.72	+35:43:39.5	H II	51.1	−12.29	0.01	0.21	0.16	8.28	8.74	−1.01	0.17	0.21	0.32	9.72
36	IRAS 08572+3915NW	09:00:25.37	+39:03:53.7	TO	244.3			0.76	0.63			−0.42			2.0	
37	IRAS 08579+3447	09:01:05.78	+34:35:28.6	H II	273.5			0.56	0.43	8.84	8.67	−0.37			1.81	11.19
38	NGC 2731	09:02:08.40	+08:18:06.0	H II	35.0	−12.11	0.02	0.33	0.22	8.72	8.98	−0.46	0.03	0.34	0.16	9.99
39	NGC 2730	09:02:15.82	+16:50:17.9	H II	58.9	−12.02	0.02	0.34	0.12	8.74		−0.41	0.56	0.67	0.39	9.92
40	IC 2431	09:04:34.39	+14:35:39.4	H II	209.0			0.35	0.44	8.66		−0.44			1.77	10.61
41	NGC 2750	09:05:47.93	+25:26:15.0	H II	37.0	−11.82	0.01	0.48	0.15	8.83	8.74	−0.39	0.54	0.49	0.47	10.36
42	IC 2434	09:07:16.06	+37:12:55.3	TO	104.5	−13.08	0.09	0.44	0.28			−0.16	−0.16	0.83	0.83	
43	NGC 2761	09:07:30.84	+18:26:05.1	H II	125.0	−12.68	0.03	1.16	0.44	8.76		−0.29	1.54	1.27	1.3	11.07
44	NGC 2773	09:09:44.16	+07:10:25.7	H II	80.4	−12.48	0.01	0.62	0.36	8.82		−0.42	0.75	0.86	0.78	10.78
45	NGC 2776	09:12:14.52	+44:57:17.4	H II	36.0	−11.62	0.01	0.29	0.14	8.69		−0.34	0.42	0.41	0.5	10.6
46	NGC 2789	09:14:59.66	+29:43:48.9	H II	93.6	−12.77	0.17	0.79	0.37	8.74		−0.19	0.57	0.86	0.85	11.16
47	IRAS 09121+3908	09:15:22.15	+38:56:35.0	LNR	37.0			0.73				−0.02				
48	NGC 2824	09:19:02.23	+26:16:11.9	H II	314.0	−12.61	0.09	0.87	0.36	8.74		−0.25	0.13	1.89	−0.2	9.2
49	IRAS 09184+4356	09:21:38.74	+43:43:34.1	H II	170.1			0.87	0.5	8.8	8.81	−0.3			1.11	10.92
50	CGCG 238-041	09:22:25.30	+47:14:39.9	H II	131.5	−13.39	0.19	0.37	0.29	8.49		−0.66	0.04	1.12	0.83	10.08

(1)	(2)	(3)	(4)	(5)	(6)	(7)	(8)	(9)	(10)	(11)	(12)	(13)	(14)	(15)	(16)	(17)
51	IRAS 09197+2210	09:22:37.39	+21:57:26.8	TO	143.4	−13.19	0.04	0.97	0.42			−0.27	0.88	1.22		
52	NGC 2854	09:24:02.83	+49:12:13.7	TO	25.0	−12.41	0.02	0.73	0.21			−0.17	−0.33	−0.43	−0.34	
53	UGC 5046	09:28:06.65	+17:11:47.4	H II	64.9	−12.5	0.01	0.33	0.33	8.78		−0.47	0.19	0.76	0.61	10.47
54	UGC 5055	09:30:11.76	+55:51:08.7	H II	110.6	−12.46	0.02	0.53	0.19	8.81		−0.32	0.85	1.06	0.94	10.9
55	NGC 2893	09:30:16.97	+29:32:23.9	H II	24.0	−12.3	0.03	0.29	0.19	8.85	8.72	−0.26	−0.69	−0.03	−0.24	9.76
56	MCG 3-24-062	09:30:22.99	+19:28:09.3	H II	66.2	−12.82	0.03	0.68	0.33	8.68	8.8	−0.39	0.3	0.53	0.35	10.51
57	CGCG 238-066	09:31:06.77	+49:04:47.1	TO	147.0	−12.87	0.13	0.54	0.38			−0.11	0.35	1.38	1.03	
58	UGC 5097	09:34:10.63	+00:14:31.9	H II	72.5	−11.97	0.01	0.25	0.2	8.53		−0.69	0.8	0.91	0.78	10.3
59	CGCG 289-012	09:36:31.87	+59:23:54.3	H II	172.4			0.42	0.26	8.81	8.69	−0.42			1.24	10.91
60	MCG 8-18-013	09:36:37.18	+48:28:28.0	H II	110.9	−12.7	0.12	0.87	0.42	8.69	8.75	−0.28	1.02	1.24	1.32	
61	CGCG 181-068	09:37:19.22	+33:49:25.8	TO	100.6	−13.45	0.06	0.5	0.51			−0.18	−0.44	0.83	0.66	
62	NGC 2936	09:37:44.14	+02:45:39.0	LNR	100.5	−12.58	0.06	0.33	0.23			0.03		0.66	0.97	
63	NGC 2955	09:41:16.61	+35:52:56.2	H II	103.5	−12.17	0.02	0.69	0.22	8.71	8.82	−0.36	1.33	1.07	0.94	11.15
64	CGCG 182-010	09:45:15.22	+34:42:44.2	H II	175.1			0.74	0.38	8.8		−0.33			1.27	11.08
65	UGC 5228	09:46:03.60	+01:40:06.1	H II	28.2	−12.4	0.03	0.56	0.15	8.67	8.73	−0.48	−0.13	−0.15	−0.12	9.96
66	IRAS 09438+1141	09:46:32.57	+11:27:19.5	H II	203.0			0.56		8.77		−0.44				10.75
67	NGC 3015	09:49:22.92	+01:08:43.5	TO	108.8	−12.29	0.01	0.61	0.29			−0.18	0.94	1.05	0.96	
68	MCG 2-25-039	09:49:36.98	+09:00:18.8	H II	77.6	−12.69	0.02	0.54	0.31	8.74		−0.42	0.41	0.7	0.51	10.38
69	NGC 3020	09:50:06.65	+12:48:49.0	H II	18.3	−12.02	0.02	0.17	0.07	8.52		−0.62	−0.59	−0.35	−0.16	9.31
70	NGC 3049	09:54:49.56	+09:16:15.9	H II	18.3	−11.98	0.01	0.26	0.14	8.75		−0.42	−0.51	−0.27	−0.33	9.63
71	NGC 3055	09:55:18.07	+04:16:12.1	H II	25.0	−11.76	0.07	0.34	0.16	8.68		−0.31	0.0	0.17	0.13	10.08
72	IC 2520	09:56:20.11	+27:13:39.3	H II	26.4	−11.94	0.01	0.53	0.25	8.6		−0.43	0.21	0.1	−0.05	9.81
73	UGC 5403	10:02:35.54	+19:10:36.9	H II	33.0	−12.8	0.09	0.83	0.34	8.81		−0.31	−0.15	0.04	−0.04	10.07
74	UGC 5459	10:08:10.08	+53:05:01.5	H II	25.8	−12.49	0.34	0.39	0.17	8.63	8.62	−0.52	−0.5	−0.25	−0.1	10.13
75	MCG 5-24-022	10:10:03.38	+32:04:12.9	H II	92.1	−13.23	0.09	0.57	0.41	8.74		−0.37	0.03	0.74	0.5	10.42

(1)	(2)	(3)	(4)	(5)	(6)	(7)	(8)	(9)	(10)	(11)	(12)	(13)	(14)	(15)	(16)	(17)
76	IC 2551	10:10:40.32	+24:24:50.9	H II	94.9	−12.12	0.01	0.53	0.34	8.69		−0.33	1.07	1.32	0.97	10.77
77	IRAS 10106+2745	10:13:29.50	+27:30:40.1	H II	215.6			0.59	0.53	8.71		−0.43			1.15	
78	NGC 3162	10:13:31.58	+22:44:15.2	H II	26.4	−11.6	0.1	0.23	0.11	8.81	8.7	−0.46	0.17	0.29	0.21	10.15
79	IRAS 10120+1653	10:14:47.90	+16:38:50.1	LNR	517.2			1.04	0.72			0.06			1.88	
80	NGC 3190	10:18:05.66	+21:49:56.1		26.4	−12.15	0.08		0.37						−0.02	
81	IC 602	10:18:19.73	+07:02:57.5	H II	57.6	−11.74	0.0	0.34	0.17	8.71		−0.43	0.84	0.79	0.68	10.4
82	NGC 3191	10:19:05.14	+46:27:14.8	H II	134.0	−12.26	0.02	0.43	0.2	8.76	8.71	−0.45	1.18	1.26	1.16	10.91
83	NGC 3206	10:21:47.59	+56:55:49.5	H II	25.8	−12.4	0.13	0.18	0.05	8.42		−0.79	−0.61	−0.44	0.05	9.45
84	UGC 5613	10:23:32.54	+52:20:31.3	TO	139.8	−12.66	0.07	0.72	0.36			−0.22	0.99	1.21	1.44	
85	UGC 5644	10:25:46.25	+13:43:00.7	LNR	137.6	−12.63	0.11	0.0	0.18			0.07		0.37	0.79	
86	NGC 3245	10:27:18.41	+28:30:26.6	TO	20.9	−12.36	0.02	0.62	0.29			−0.1	−0.77	−0.65	−0.55	
87	IRAS 10246+2042	10:27:25.87	+20:26:51.4	H II	84.2	−12.51	0.01	0.76		8.82		−0.25	0.78	0.87		10.56
88	MCG 7-22-012	10:30:11.42	+43:21:38.1	H II	66.0	−12.73	0.03	0.63	0.4	8.69	8.72	−0.45	0.36	0.08	0.37	10.41
89	IRAS 10276+1119	10:30:14.76	+11:04:15.9	H II	271.3			0.39	0.33	8.78		−0.28			1.47	11.08
90	NGC 3265	10:31:06.77	+28:47:48.0	H II	21.8	−12.29	0.02	0.35	0.26	8.74		−0.4	−0.57	−0.35	−0.46	9.61
91	UGC 5713	10:31:38.90	+25:59:02.1	Sy	95.0	−13.43	0.11	0.58	0.26			0.16		0.91	0.4	
92	NGC 3274	10:32:17.23	+27:40:07.7	H II	10.0	−11.87	0.01	0.03	0.05	8.28	8.8	−0.99	−1.07	−0.89	−0.85	8.76
93	UGC 5720	10:32:31.87	+54:24:03.7	H II	20.0	−11.61	0.01	−2.66	0.16	8.89		0.72			−0.11	9.49
94	KUG1031+351	10:34:02.40	+34:52:10.2	H II	298.2			0.5		8.77		−0.38				11.57
95	NGC 3306	10:37:10.22	+12:39:09.3	H II	46.6	−12.18	0.01	0.46	0.23	8.8	8.78	−0.39	0.35	0.46	0.38	10.31
96	NGC 3323	10:39:39.02	+25:19:21.9	H II	79.5	−12.06	0.01	0.27	0.17	8.7		−0.5	0.74	0.88	0.71	10.36
97	IC 2598	10:39:42.38	+26:43:38.6	H II	89.1	−12.36	0.01	0.44	0.39	8.75		−0.43	0.73	0.94	0.9	10.6
98	NGC 3338	10:42:07.54	+13:44:49.2	LNR	21.4	−11.77	0.01	−0.01	0.13			−0.06	−1.21	−0.31	0.14	
99	NGC 3353	10:45:22.06	+55:57:39.9	H II	16.0	−11.67	0.0	0.04	0.16	8.3		−0.9	−0.46	0.0	−0.25	9.15
100	UGC 5881	10:46:42.53	+25:55:53.6	TO	93.0	−12.59	0.03	0.54	0.33			−0.21	0.44	0.84	0.65	

(1)	(2)	(3)	(4)	(5)	(6)	(7)	(8)	(9)	(10)	(11)	(12)	(13)	(14)	(15)	(16)	(17)
101	NGC 3370	10:47:04.06	+17:16:25.0	H II	20.9	−11.8	0.07	0.42	0.15	8.79	8.62	−0.43	0.0	−0.09	−0.01	10.01
102	NGC 3381	10:48:24.82	+34:42:41.1	H II	25.7	−12.0	0.02	0.19	0.12	8.78		−0.52	−0.27	−0.08	−0.08	9.77
103	UGC 5941_NED02	10:50:21.60	+41:27:50.5	H II	107.0	−12.67	0.02	0.69	0.45	8.84		−0.3	0.81	0.98	0.96	10.93
104	NGC 3413	10:51:20.74	+32:45:59.0	H II	16.2	−12.24	0.02	0.26	0.09	8.3		−0.98	−0.72	−0.79	−0.65	9.2
105	NGC 3408	10:52:11.69	+58:26:17.3	H II	138.0	−12.46	0.01	0.51	0.18	8.77		−0.44	1.1	0.97	−0.05	11.1
106	NGC 3430	10:52:11.40	+32:57:01.5	H II	28.4	−11.78	0.03	0.7	0.59	8.79	8.66	−0.42	0.66	0.04	0.87	10.51
107	CGCG 95-055	10:52:50.74	+16:59:07.6	Sy	257.0			0.69	0.06			0.11			0.06	
108	IRAS 10565+2448W	10:59:18.12	+24:32:34.7	H II	185.2			1.13		8.75	8.76	−0.29				11.17
109	UGC 6074	10:59:58.25	+50:54:10.6	H II	38.0	−12.69	0.05	0.91	0.38	8.85		−0.23	0.1	0.44	0.16	10.15
110	NGC 3495	11:01:16.22	+03:37:40.7	H II	17.5	−12.41	0.32	0.24	0.17	8.7	8.68	−0.37	−1.04	−0.3	−0.22	10.06
111	UGC 6103	11:01:58.99	+45:13:40.9	H II	91.7	−12.29	0.01	0.41	0.2	8.69		−0.24	0.61	0.97	0.91	10.71
112	MCG 7-23-019	11:03:54.31	+40:51:00.1	H II	150.6	−12.82	0.04	0.81	0.37	8.64	8.77	−0.35	1.15	1.18	1.64	10.86
113	UGC 6135	11:04:36.96	+45:07:30.8	LNR	90.9	−12.28	0.1	0.49	0.24			0.1		0.58	0.84	
114	CGCG 241-078	11:06:37.37	+46:02:19.6	H II	110.9	−13.07	0.1	1.14	0.54	8.74		−0.18	0.88	0.93	0.92	10.64
115	IRAS 11069+2711	11:09:38.89	+26:54:56.1	H II	296.4			0.3	0.45	8.52		−0.66			1.78	10.53
116	IC 676	11:12:39.82	+09:03:21.0	H II	26.9	−12.29	0.02	0.56	0.33	8.8		−0.34	−0.14	0.03	−0.17	10.1
117	IRAS 11102+3026	11:12:57.36	+30:10:28.6	Sy	129.6	−13.37	0.02	1.44	0.73			−0.04	0.49	0.6	1.06	
118	IC 2637	11:13:49.75	+09:35:10.7	Sy	128.2	−12.27	0.0	0.55	0.27			−0.05	0.51	0.87	1.05	
119	MCG 9-19-013	11:14:49.37	+50:19:22.5	H II	201.8			0.7	0.46	8.65		−0.32			1.14	10.9
120	7ZW384	11:16:54.00	+59:31:48.0		340.4			0.34	0.35			−0.22			1.61	
121	11193404+5335181	11:19:34.01	+53:35:18.7	Sy	447.3			0.48	0.5			−0.34			1.93	
122	NGC 3633	11:20:26.21	+03:35:08.2	H II	30.0	−12.49	0.03	0.8	0.38	8.82		−0.31	0.04	0.21	−0.06	10.19
123	NGC 3652	11:22:39.02	+37:45:54.4	H II	15.5	−12.19	0.02	0.23		8.69		−0.51	−0.85	−0.68		9.28
124	NGC 3656	11:23:38.64	+53:50:31.7	LNR	37.0	−12.49	0.06	0.59	0.3			−0.31	−0.07	−0.16	0.09	
125	NGC 3659	11:23:45.53	+17:49:07.2	H II	21.0	−12.19	0.04	0.24		8.67	8.7	−0.53	−0.58	−0.49		9.62

(1)	(2)	(3)	(4)	(5)	(6)	(7)	(8)	(9)	(10)	(11)	(12)	(13)	(14)	(15)	(16)	(17)
126	NGC 3664	11:24:24.26	+03:19:31.0	H II	26.9	−11.92	0.01	−0.05	0.04	8.47	8.75	−0.66	−0.43	−0.11	0.06	9.01
127	NGC 3666	11:24:26.06	+11:20:32.0	H II	16.3	−11.96	0.02	0.56	0.19	8.7		−0.37	−0.23	−0.53	−0.35	9.87
128	IC 691	11:26:44.30	+59:09:19.5	H II	16.0	−12.09	0.02	0.51	0.24	8.34		−0.81	−0.27	−0.35	−0.53	9.14
129	NGC 3686	11:27:43.97	+17:13:27.0	H II	21.0	−11.57	0.0	0.3	0.14	8.81	8.75	−0.5	0.12	0.1	0.09	10.35
130	UGC 6469	11:28:17.71	+02:39:14.3	H II	102.6	−12.14	0.02	0.3	0.17	8.66	8.74	−0.47	0.91	0.89	0.91	10.6
131	NGC 3690	11:28:31.51	+58:33:51.4	H II	52.6	−10.88	0.0	0.22	0.49	8.59	8.82	−0.34	1.4	2.12	1.87	11.1
132	IC 698	11:29:03.84	+09:06:43.4	H II	96.8	−12.39	0.01	0.86	0.4	8.73		−0.36	1.27	0.96	1.05	11.05
133	IRAS 11267+1558	11:29:24.70	+15:41:41.3	H II	736.6			0.99	0.64	8.7	8.76	−0.28			2.19	
134	NGC 3705	11:30:07.03	+09:16:40.8	LNR	16.3	−12.24	0.06	0.92	0.17			−0.05	−0.74	−0.59	−0.2	
135	MCG 3-29-061	11:31:03.70	+20:14:08.3	H II	67.5	−12.91	0.03	0.93	0.4	8.78		−0.26	0.44	0.48	0.55	10.34
136	NGC 3720	11:32:21.60	+00:48:14.4	H II	89.8	−12.86	0.05	0.45	0.27	8.8		−0.5	0.29	0.62	0.92	11.09
137	NGC 3729	11:33:49.32	+53:07:32.0	H II	17.1	−11.8	0.18	0.46	0.2	8.63	8.78	−0.25	−0.27	−0.33	−0.37	10.11
138	MCG 10-17-019	11:35:24.79	+57:38:59.8	H II	127.5	−12.48	0.01	0.75		8.75		−0.44	1.33	0.89		10.99
139	NGC 3758	11:36:28.94	+21:35:46.5	Sy	131.6	−12.18	0.0	1.38	0.26			−0.12	2.09	1.1	0.93	11.2
140	UGC 6583	11:36:54.36	+19:58:18.1	H II	93.2	−12.21	0.03	0.35	0.24	8.69	8.69	−0.44	0.8	1.14	0.85	10.53
141	MCG 1-30-003	11:37:06.58	+02:50:44.9	H II	128.9	−12.94	0.12	0.8		8.75		−0.36	0.9	1.02		10.56
142	NGC 3769	11:37:44.11	+47:53:35.1	H II	17.1	−12.69	0.05	0.27	0.16	8.66		−0.4	−1.28	−0.73	−0.32	9.91
143	NGC 3773	11:38:13.06	+12:06:44.4	H II	16.3	−11.55	0.01	0.22	0.09	8.42	8.88	−0.78	−0.11	−0.17	−0.54	9.22
144	NGC 3781	11:39:03.77	+26:21:42.2	Sy	103.5	−12.57	0.01	1.3	0.63			0.24		1.2	1.32	
145	UGC 6625	11:39:47.54	+19:56:00.2	TO	158.2			0.38	0.18			−0.18			1.25	
146	NGC 3808_NED02	11:40:44.64	+22:26:49.0	H II	107.2	−12.79	0.04	0.4	0.39	8.76		−0.37	0.36	0.81	1.04	10.6
147	NGC 3811	11:41:16.63	+47:41:27.0	H II	54.2	−11.98	0.02	0.57		8.74	8.73	−0.4	0.83	0.5		10.75
148	NGC 3822	11:42:11.08	+10:16:40.0	Sy	94.6	−12.42	0.01	0.65	0.35			−0.07	0.39	0.81	1.01	
149	UGC 6665	11:42:12.22	+00:20:04.1	H II	85.0	−11.83	0.01	0.17	0.18	8.35		−0.8	0.98	1.28	1.02	10.35
150	MCG 3-30-051	11:42:24.50	+20:07:09.5	H II	90.4	−12.7	0.02	0.63	0.29	8.72		−0.55	0.71	0.66	0.75	10.65

(1)	(2)	(3)	(4)	(5)	(6)	(7)	(8)	(9)	(10)	(11)	(12)	(13)	(14)	(15)	(16)	(17)
151	NGC 3839	11:43:54.34	+10:47:04.9	H II	91.3	−12.33	0.07	0.65		8.74		−0.45	1.07	0.93		10.74
152	UGC 6732	11:45:33.14	+58:58:41.2	Sy	53.6	−13.1	0.02	1.4	0.39			0.14		0.24	0.07	
153	IC 730	11:45:35.26	+03:13:54.6	H II	93.1	−12.53	0.01	0.89	0.43	8.78		−0.34	1.12	0.78	0.94	10.96
154	IC 732_NED01	11:45:59.59	+20:26:49.8	H II	110.0	−12.71	0.03	1.06		8.68	8.72	−0.34	1.32	1.03		10.62
155	NGC 3912	11:50:04.46	+26:28:45.3	H II	22.5	−12.26	0.03	0.46	0.23	8.67		−0.47	−0.32	−0.32	−0.18	9.83
156	NGC 3928	11:51:47.62	+48:40:59.3	H II	16.9	−11.9	0.13	0.12	0.18	8.7		−0.32	−0.76	−0.42	−0.43	9.69
157	NGC 3934	11:52:12.65	+16:51:06.7	LNR	61.6	−13.64	0.18	0.99	0.44			−0.25	−0.3	0.01	0.41	
158	UGC 6865	11:53:39.96	+43:27:39.4	H II	91.2	−12.54	0.01	0.78	0.38	8.74		−0.44	1.02	0.74	0.82	11.03
159	UGC 6901	11:55:38.35	+43:02:45.1	H II	107.6	−12.56	0.05	0.95	0.41	8.75		−0.43	1.38	0.82	0.94	10.98
160	CGCG 013-010	11:57:05.93	+01:07:32.1	TO	172.3			0.92	0.55			−0.17			1.52	
161	NGC 3991	11:57:30.96	+32:20:13.3	H II	55.6	−11.78	0.0	−0.25	0.1	8.26	8.95	−1.01	0.14	0.79	0.79	10.15
162	NGC 4004	11:58:05.23	+27:52:43.9	H II	57.9	−11.64	0.01	0.64	0.2	8.7		−0.46	1.35	0.88	0.71	10.29
163	NGC 4014	11:58:35.83	+16:10:38.1	H II	62.6	−11.99	0.01	0.49	0.27	8.67	8.79	−0.24	0.7	0.58	0.61	10.97
164	NGC 4010	11:58:37.90	+47:15:41.4	H II	17.1	−12.52	0.02	0.42	0.22	8.68		−0.52	−0.85	−0.69	−0.47	9.51
165	NGC 4018	11:58:40.78	+25:18:58.9	H II	72.6	−12.74	0.01	0.7	0.39	8.64		−0.41	0.51	0.43	0.7	10.63
166	NGC 4020	11:58:56.69	+30:24:42.8	LNR	14.3	−12.06	0.02	0.34	0.11			−0.51	−0.66	−0.8	−0.75	
167	IRAS 11571+3003	11:59:42.60	+29:47:12.5	H II	218.6			0.89	0.54	8.81		−0.3			1.14	10.77
168	UGC 7017	12:02:22.51	+29:51:42.4	H II	55.2	−12.62	0.06	0.69	0.28	8.76		−0.41	0.37	0.4	0.62	10.43
169	UGC 7016	12:02:23.98	+14:50:37.1	Sy	110.3	−12.88	0.07	0.68	0.39			−0.04	−0.13	0.55	0.81	
170	MCG 3-31-030	12:03:35.95	+16:03:19.9	H II	13.1	−12.33	0.04	0.24	0.17	8.74	8.78	−0.59	−1.09	−1.1	−1.15	8.84
171	NGC 4062	12:04:03.84	+31:53:44.9	H II	16.3	−12.23	0.05	0.63	0.18	8.7		−0.35	−0.41	−0.52	−0.26	
172	NGC 4064	12:04:11.10	+18:26:38.1	H II	8.5	−11.84	0.03	0.48	0.29	8.81	8.86	−0.59	−0.66	−0.88	−1.07	9.6
173	CGCG 098-059	12:07:09.55	+16:59:44.2	H II	102.3	−12.38	0.02	0.75	0.47	8.84		−0.38	1.2	1.03	1.08	10.89
174	NGC 4116	12:07:36.82	+02:41:32.3	H II	16.0	−11.78	0.02	0.17	0.09	8.62	8.74	−0.62	−0.45	−0.38	−0.23	9.03
175	NGC 4136	12:09:17.71	+29:55:39.4	H II	16.3	−11.59	0.01	0.1	0.08	8.68	8.71	−0.45	−0.42	−0.31	−0.15	9.83

(1)	(2)	(3)	(4)	(5)	(6)	(7)	(8)	(9)	(10)	(11)	(12)	(13)	(14)	(15)	(16)	(17)
176	NGC 4150	12:10:33.67	+30:24:05.8	Sy	13.7	−12.31	0.08	0.94	0.27			−0.05	−0.96	−1.4	−1.06	
177	IRAS 12086+1441	12:11:14.38	+14:24:35.2	H II	194.0			0.63	0.52	8.66		−0.44			−1.22	8.19
178	NGC 4162	12:11:52.47	+24:07:25.2	H II	42.5	−12.31	0.08	0.23	0.17	8.67	8.74	−0.44	−0.13	0.18	0.42	10.66
179	NGC 4178	12:12:46.45	+10:51:57.5	H II	16.8	−11.8	0.01	0.33	0.11	8.66	8.76	−0.5	−0.28	−0.26	−0.03	9.74
180	IRAS 12112+0305	12:13:46.08	+02:48:41.5	Sy	303.6			0.78				−0.3				
181	NGC 4189	12:13:47.26	+13:25:29.3	H II	16.8	−11.86	0.02	0.51	0.18	8.83		−0.45	−0.12	−0.3	−0.28	10.03
182	NGC 4194	12:14:09.65	+54:31:35.9	H II	36.0	−11.51	0.01	−1.08		8.88		0.41		0.75		10.31
183	NGC 4204	12:15:14.45	+20:39:30.9	H II	10.0	−11.75	0.01	0.07	0.08	8.57		−0.61	−0.98	−0.84	−0.97	8.35
184	NGC 4207	12:15:30.50	+09:35:05.6	H II	16.8	−12.41	0.04	0.65	0.32	8.7		−0.46	−0.47	−0.68	−0.48	9.82
185	UGC 7286	12:15:59.26	+27:26:31.9	H II	115.4	−12.96	0.06	0.78	0.34	8.7	8.73	−0.3	0.71	0.41	0.59	10.89
186	NGC 4234	12:17:09.08	+03:40:50.2	H II	30.0	−12.04	0.01	0.15	0.14	8.61	8.86	−0.59	−0.21	−0.06	0.0	9.57
187	NGC 4237	12:17:11.42	+15:19:26.3	TO	16.8	−11.82	0.01	0.41	0.26			−0.3	−0.32	−0.41	−0.4	
188	NGC 4244	12:17:29.45	+37:48:26.5	H II	4.3	−11.41	0.03	0.43	0.02	8.56		−0.69	−0.86	−1.15	−1.0	9.28
189	NGC 4253	12:18:26.52	+29:48:46.5	H II	64.9	−11.96	0.0	0.22	0.32	8.67		−0.37	0.52	1.16	0.67	10.81
190	MCG 3-32-005	12:20:47.23	+17:00:57.9	H II	131.0	−12.59	0.03	0.67	0.4	8.79		−0.44	1.15	1.09	−0.81	8.91
191	NGC 4290	12:20:47.52	+58:05:33.0	H II	37.0	−12.01	0.02	0.63	0.23	8.85		−0.34	0.51	0.33	0.35	10.57
192	NGC 4294	12:21:17.83	+11:30:37.6	H II	16.8	−11.71	0.05	0.1	0.1	8.39	8.8	−0.93	−0.38	−0.22	−0.2	9.63
193	NGC 4314	12:22:32.02	+29:53:43.8	LNR	16.3	−11.73	0.07	0.21	0.21			0.05		−0.89	−0.4	
194	NGC 4385	12:25:42.79	+00:34:21.4	H II	29.0	−11.78	0.0	−1.75	0.19	8.79	8.9	−0.03	−3.54	0.3	0.17	10.13
195	NGC 4395	12:25:48.86	+33:32:48.7	Sy	4.7	−11.25	0.03	0.13				−0.72	−1.03	−0.92		
196	NGC 4396	12:25:59.16	+15:40:15.6	H II	16.8	−12.57	0.01	0.19	0.12	8.62		−0.63	−1.17	−0.85	−0.46	
197	NGC 4412	12:26:36.07	+03:57:52.9	Sy	30.6	−12.21	0.04	0.52	0.16			−0.1	−0.41	−0.03	0.15	
198	NGC 4418	12:26:54.62	-00:52:39.4	LNR	29.0	−12.58	0.0	0.92				−0.01	−1.12	1.28		
199	NGC 4420	12:26:58.49	+02:29:39.7	H II	17.6	−11.82	0.02	0.2	0.15	8.7		−0.43	−0.45	−0.35	−0.26	9.72
200	NGC 4424	12:27:11.62	+09:25:14.4	H II	6.0	−12.48	0.07	0.48	0.22	8.8	8.8	−0.48	−1.65	−1.48	−1.38	8.9

(1)	(2)	(3)	(4)	(5)	(6)	(7)	(8)	(9)	(10)	(11)	(12)	(13)	(14)	(15)	(16)	(17)
201	NGC 4435	12:27:40.46	+13:04:44.4	TO	16.7	−12.48	0.43	0.21	0.33			−0.25	−1.31	−0.96	−0.83	
202	NGC 4438	12:27:45.62	+13:00:31.7	LNR	16.8	−11.63	0.03	0.23	0.23			0.25			−0.3	
203	NGC 4448	12:28:15.46	+28:37:13.1	H II	16.3	−12.29	0.43	1.59	0.21	8.72	8.72	−0.37	0.8	−0.73	−0.63	10.49
204	3C273	12:29:06.70	+02:03:08.6		657.8											
205	NGC 4470	12:29:37.78	+07:49:27.1	H II	16.8	−11.94	0.01	0.1	0.13	8.68		−0.52	−0.7	−0.51	−0.43	9.47
206	IRAS 12274+0018	12:29:58.85	+00:01:38.0		38.1	−13.13	0.02	0.75		8.72		−0.47	−0.34	−0.56		9.45
207	NGC 4491	12:30:57.12	+11:29:00.7	H II	16.8	−13.09	0.1	0.09	0.28	8.6	9.0	−0.72	−1.81	−0.66	−0.65	9.63
208	NGC 4500	12:31:22.15	+57:57:52.5	TO	52.0	−11.85	0.01	0.3				−0.28	0.47	0.66		
209	NGC 4495	12:31:22.90	+29:08:11.3	H II	74.2	−11.92	0.01	0.9	0.32	8.74		−0.25	1.45	0.79	0.81	10.83
210	IC 3476	12:32:41.88	+14:03:01.6	H II	16.8	−12.13	0.17	0.11	0.09	8.64	8.77	−0.57	−0.85	−0.62	−0.44	9.16
211	NGC 4509	12:33:06.72	+32:05:34.5	H II	11.1	−12.18	0.01	−0.09	0.11	8.24	8.82	−1.17	−1.43	−1.05	−1.02	8.02
212	NGC 4519	12:33:30.26	+08:39:17.1	H II	16.8	−12.26	0.02	0.21	0.11	8.75		−0.49	−0.89	−0.36	−0.13	9.74
213	NGC 4548	12:35:26.45	+14:29:46.8	Sy	16.2	−11.78	0.18	0.91	0.18			0.31			−0.24	
214	IRAS 12337+5044	12:36:06.70	+50:28:18.7	H II	172.5			0.72	0.33	8.62		−0.47			1.18	10.68
215	IC 3581	12:36:38.06	+24:25:43.6	H II	106.1	−12.22	0.01	0.64		8.73		−0.28	1.15	1.03		10.9
216	NGC 4592	12:39:18.74	-00:31:55.0	H II	11.1	−11.67	0.01	0.24	0.08	8.5		−0.71	−0.54	−0.63	−0.52	9.08
217	NGC 4607	12:41:12.22	+11:53:11.9	LNR	16.8	−12.4	0.01	0.67	0.38			−0.23	−0.65	−0.68	−0.51	
218	NGC 4625	12:41:52.73	+41:16:26.3	H II	9.2	−12.0	0.05	0.15	0.13	8.68	8.75	−0.3	−1.38	−1.2	−1.03	9.13
219	NGC 4630	12:42:31.13	+03:57:36.9	H II	15.6	−11.82	0.02	0.32	0.16	8.78		−0.59	−0.34	−0.39	−0.48	9.49
220	IC 3690	12:42:49.20	+10:21:26.9	TO	13.1	−13.27	0.04	1.05				−0.1	0.35	−0.73		
221	UGC 7905_NED01	12:43:47.93	+54:53:45.2	H II	78.7	−12.66	0.01	0.3		8.3	8.87	−0.97	0.29	0.52		10.16
222	MCG 5-30-069	12:44:41.26	+26:25:10.5	H II	74.0	−13.24	0.03	1.11	0.56	8.78		−0.33	0.5	0.56	0.7	10.51
223	IC 3721	12:44:53.11	+18:45:18.9	H II	98.5	−12.13	0.01	0.41	0.31	8.67	8.76	−0.35	0.96	0.9	0.84	11.02
224	NGC 4670	12:45:17.26	+27:07:32.2	H II	14.3	−11.51	0.03	0.03	0.08	8.18		−1.19	−0.37	−0.17	−0.35	9.17
225	NGC 4675	12:45:31.90	+54:44:15.4	H II	76.9	−12.6	0.03	0.99		8.77		−0.22	0.9	0.56		10.71

(1)	(2)	(3)	(4)	(5)	(6)	(7)	(8)	(9)	(10)	(11)	(12)	(13)	(14)	(15)	(16)	(17)
226	MCG 7-26-051	12:46:56.83	+42:15:59.1	H II	146.9	−12.8	0.01	0.98	0.52	8.64	8.85	−0.26	1.3	1.07	1.32	11.15
227	NGC 4689	12:47:45.55	+13:45:46.1	H II	16.8	−11.81	0.06	0.47		8.68	8.8	−0.23	−0.31	−0.36		10.42
228	NGC 4688	12:47:46.51	+04:20:09.8	H II	15.6	−11.81	0.01	0.31	0.05	8.5	8.68	−0.58	−0.33	−0.48	−0.46	9.03
229	NGC 4704	12:48:46.44	+41:55:16.5	Sy	122.8	−12.49	0.14	0.35	0.21			0.57			0.95	
230	NGC 4701	12:49:11.59	+03:23:19.4	H II	15.6	−11.63	0.02	0.28		8.82		−0.49	−0.23	−0.31		9.58
231	IRAS 12468+3436	12:49:17.16	+34:19:43.0	Sy	498.3			1.18	0.92			−0.24			1.89	
232	IRAS 12470+1404	12:49:34.80	+13:48:09.8	H II	191.1			0.17		8.76		−0.28				7.97
233	MCG 8-23-097	12:50:39.84	+47:56:00.3	TO	131.2	−12.92	0.13	1.12	0.56			−0.06	0.72	1.08	1.41	
234	NGC 4747	12:51:45.60	+25:46:30.1	H II	14.3	−11.98	0.01	0.32	0.22	8.58	8.77	−0.58	−0.58	−0.53	−0.74	9.35
235	UGC 8017	12:52:53.59	+28:22:16.6	TO	107.1	−11.89	0.01	0.57	0.32			−0.1	1.03	0.87	0.95	
236	NGC 4765	12:53:14.57	+04:27:47.7	H II	15.6	−11.76	0.01	0.17	0.12	8.27		−1.04	−0.38	−0.33	−0.45	9.12
237	VCC2096	12:53:24.79	+11:42:36.4	H II	281.3			0.49	0.3	8.68		−0.35			−1.11	8.29
238	UGC 8041	12:55:12.65	+00:06:59.9	H II	23.0	−12.13	0.21	0.3	0.08	8.63		−0.48	−0.38	−0.47	−0.2	9.08
239	UGC 8058	12:56:14.23	+56:52:25.3		179.6											
240	NGC 4837_NED01	12:56:48.31	+48:17:48.9	H II	132.5	−12.22	0.02	0.19	0.23	8.75	8.85	−0.26	0.74	1.04	1.15	11.23
241	UM530	12:58:08.35	+01:51:44.4	H II	282.7			0.24	0.34	8.39		−0.72			1.31	10.65
242	NGC 4861	12:59:00.370	+34:50:44.310	Sy	18.5	−11.41	0.0	−0.24	0.08			−1.53	−0.41	0.17	−0.27	
243	NGC 4868	12:59:08.90	+37:18:37.4	H II	74.0	−12.15	0.01	0.32		8.86	8.66	−0.42	0.6	0.81		11.09
244	NGC 4922_NED02	13:01:25.27	+29:18:49.5	Sy	107.2	−12.29	0.0	0.75	0.52			−0.15	1.04	1.52	1.29	
245	UGC 8179	13:05:14.16	+31:59:59.0	H II	222.1			0.66	0.25	8.71		−0.34			1.29	11.58
246	NGC 5001	13:09:33.12	+53:29:39.4	H II	134.8	−12.4	0.02	0.93	0.39	8.67	8.83	−0.23	1.51	1.09	1.24	11.23
247	IC 856	13:10:41.33	+20:32:10.6	H II	64.3	−12.11	0.02	0.51	0.29	8.58		−0.57	0.84	0.54	0.4	10.3
248	UGC 8269	13:11:15.12	+46:42:02.3	TO	124.1	−13.69	0.4	1.16	0.63			−0.05	−0.16	0.47	1.16	
249	NGC 5014	13:11:31.22	+36:16:55.7	H II	18.5	−12.18	0.02	0.42	0.24	8.65	8.82	−0.49	−0.46	−0.44	−0.54	9.66
250	NGC 5012	13:11:37.03	+22:54:55.8	LNR	40.2	−12.05	0.01	0.34	0.17			0.07		−0.05	0.46	

(1)	(2)	(3)	(4)	(5)	(6)	(7)	(8)	(9)	(10)	(11)	(12)	(13)	(14)	(15)	(16)	(17)
251	IRAS 13116+4508	13:13:47.88	+44:52:58.6	H II	258.3			0.73	0.65	8.75		−0.4			1.3	10.95
252	IC 860	13:15:03.50	+24:37:07.8	LNR	54.5	−13.19	0.08	0.85	0.71			0.22		0.79	1.12	
253	IRAS 13144+4508	13:16:39.74	+44:52:35.0	Sy	381.8			0.37	0.32			−0.36			1.57	
254	NGC 5060	13:17:16.22	+06:02:14.8	H II	97.4	−12.25	0.01	0.3	0.3	8.86	8.77	−0.3	0.63	0.95	1.04	11.02
255	UGC 8357_NED01	13:17:58.80	-00:18:42.0	TO	146.9	−12.6	0.13	0.41	0.28			−0.41	0.87	1.17	1.28	
256	UGC 8361	13:18:18.58	+06:20:07.4	H II	106.3	−12.72	0.05	0.8	0.41	8.72	8.77	−0.26	0.85	0.85	0.98	10.92
257	IC 883	13:20:35.40	+34:08:21.6	H II	104.7	−12.72	0.03	1.2	0.48	8.68		−0.21	1.29	1.45	1.69	10.79
258	NGC 5100_NED02	13:20:59.59	+08:58:41.9	TO	142.2	−12.65	0.19	0.76	0.35			−0.11	0.83	0.96	1.18	
259	NGC 5104	13:21:23.09	+00:20:32.7	Sy	87.8	−12.55	0.04	1.38	0.44			−0.08	1.18	1.02	1.23	
260	NGC 5107	13:21:24.70	+38:32:15.4	H II	18.5	−12.09	0.03	−0.4	0.09	8.34	8.77	−0.9	−1.34	−0.56	−0.57	8.99
261	NGC 5112	13:21:56.40	+38:44:05.0	TO	18.5	−11.62	0.02	0.45				−0.38	0.08	−0.24		
262	NGC 5123	13:23:10.51	+43:05:10.5	H II	123.4	−12.15	0.01	0.6	0.21	8.64	8.87	−0.18	1.17	0.98	1.16	11.31
263	IRAS 13218+0552	13:24:19.90	+05:37:04.7		850.4				0.42						2.34	
264	IRAS 13232+1731	13:25:43.87	+17:15:52.8	H II	331.8			0.51	0.28	8.82		−0.42			1.53	11.38
265	NGC 5147	13:26:19.73	+02:06:03.1	H II	18.0	−11.47	0.01	0.07	0.1	8.65	8.72	−0.48	−0.24	−0.06	−0.07	9.75
266	NGC 5204	13:29:36.58	+58:25:13.3	H II	3.2	−11.54	0.01	0.13	0.04	8.53	8.7	−0.61	−1.67	−1.6	−1.28	8.27
267	UGC 8502_NED02	13:30:39.36	+31:17:02.6	H II	149.9	−13.34	0.08	−0.2	0.15	8.51	9.05	−0.58	−0.58	1.03	1.25	10.06
268	UGC 8561	13:34:57.26	+34:02:38.7	H II	107.5	−12.09	0.06	0.62	0.21	8.79	8.72	−0.32	1.32	1.06	1.19	10.94
269	NGC 5230	13:35:31.87	+13:40:34.2	H II	105.6	−12.17	0.02	1.68	0.14	8.81	8.76	−0.35	2.65	0.95	1.16	11.25
270	IRAS 13349+2438	13:37:18.72	+24:23:03.4		453.5				0.27						1.66	
271	NGC 5256	13:38:17.11	+48:16:36.1	Sy	125.2	−11.69	0.05	0.53	0.34			−0.26	1.67	1.66	1.56	
272	UGC 8626	13:38:23.47	+06:53:15.6	H II	108.8	−12.72	0.03	0.75	0.26	8.76		−0.32	0.88	0.62	0.75	10.88
273	NGC 5263	13:39:55.66	+28:24:02.7	H II	77.5	−12.11	0.03	1.17	0.29	8.73	8.71	−0.32	1.75	0.82	0.9	10.85
274	MCG 1-35-028	13:40:27.19	+04:46:25.8	H II	105.1	−12.47	0.02	0.72	0.37	8.76		−0.19	0.88	1.02	0.95	10.88
275	IC 910	13:41:07.85	+23:16:55.4	Sy	120.3	−12.57	0.06	1.05	0.41			0.16		1.16	1.3	

(1)	(2)	(3)	(4)	(5)	(6)	(7)	(8)	(9)	(10)	(11)	(12)	(13)	(14)	(15)	(16)	(17)
276	MK 268	13:41:11.14	+30:22:41.3	Sy	173.7			0.26	0.36			0.42			1.08	
277	NGC 5278	13:41:39.24	+55:40:14.1	LNR	114.4	−12.12	0.02	0.43	0.22			−0.13	0.78	0.77	1.01	
278	NGC 5273	13:42:08.38	+35:39:15.5	Sy	16.5	−12.0	0.08	−0.14	0.2			0.08		−1.91	−1.09	
279	UGC 8685	13:43:08.83	+30:20:15.9	H II	152.6	−12.39	0.03	0.86	0.25	8.8		−0.28	1.59	1.15	1.34	11.17
280	UGC 8686	13:43:40.13	+03:53:47.3	H II	105.4	−12.17	0.02	0.44	0.26	8.66	8.69	−0.24	0.9	0.89	0.93	10.87
281	UGC 8696	13:44:42.17	+55:53:13.6	Sy	163.0			0.88	0.56			0.01			2.19	
282	NGC 5297	13:46:23.66	+43:52:20.4	LNR	30.9	−12.32	0.04	−0.05	0.15			0.08		−0.37	0.24	
283	MK 796	13:46:49.46	+14:24:01.7	H II	98.5	−12.09	0.0	0.39	0.38	8.58		−0.39	1.0	1.25	0.98	10.63
284	IRAS 13446+1121	13:47:04.37	+11:06:22.6	Sy	104.5	−12.51	0.01	0.91	0.56			−0.18	1.08	1.2	0.98	
285	NGC 5303	13:47:45.00	+38:18:16.7	H II	23.0	−11.93	0.01	0.16	0.18	8.61	8.74	−0.49	−0.36	−0.13	−0.1	9.72
286	NGC 5313	13:49:44.35	+39:59:05.2	LNR	30.9	−11.9	0.17	0.45	0.25			0.08		−0.3	0.2	
287	MCG 3-35-034	13:53:09.67	+14:39:20.9	TO	178.6			0.58	0.38			−0.14			1.14	
288	NGC 5347	13:53:17.78	+33:29:27.1	Sy	39.0	−12.26	0.13	0.5	0.17			−0.2	−0.03	0.52	0.02	
289	NGC 5350	13:53:21.62	+40:21:50.2	H II	30.9	−11.72	0.09	0.34	0.16	8.76		−0.1	−0.18	0.09	0.27	
290	NGC 5368	13:54:29.16	+54:19:50.4	H II	74.6	−12.41	0.07	0.59		8.77		−0.16	0.4	0.34		10.84
291	UGC 8827	13:54:31.18	+15:02:38.9	H II	85.4	−12.26	0.0	0.45	0.32	8.65		−0.23	0.62	1.0	0.94	10.86
292	UGC 8850	13:56:02.62	+18:22:17.8	Sy	216.5			0.36				−0.24				
293	UGC 8856_NED01	13:56:07.90	+30:04:52.9	H II	137.9	−12.78	0.02	0.86	0.42	8.72		−0.3	1.15	0.89	1.12	10.75
294	NGC 5374	13:57:29.64	+06:05:49.2	H II	68.9	−11.97	0.01	0.61	0.19	8.76	8.78	−0.44	1.12	0.8	0.84	10.91
295	UGC 8902	13:59:02.81	+15:33:56.7	TO	114.4	−13.58	0.18	0.71	0.23			−0.13	−0.3	0.54	0.89	
296	NGC 5403	13:59:50.76	+38:10:56.2	TO	37.0	−13.0	0.12	0.68	0.4			−0.3	−0.46	−0.19	0.26	
297	MCG 7-29-036	14:00:57.84	+42:51:20.4	H II	144.6	−12.61	0.06	0.99	0.51	8.74	8.69	−0.32	1.54	1.08	1.19	
298	NGC 5414	14:02:03.53	+09:55:45.6	H II	68.3	−12.2	0.01	0.32		8.56		−0.58	0.57	0.67		10.25
299	MCG 5-33-046	14:04:48.00	+30:44:37.3	H II	116.4	−13.02	0.03	1.22	0.58	8.74		−0.18	1.06	0.94	1.02	10.95
300	NGC 5474	14:05:01.42	+53:39:44.4	H II	5.6	−11.63	0.02	0.17	0.1	8.4	8.8	−0.8	−1.18	−1.16	−1.16	

(1)	(2)	(3)	(4)	(5)	(6)	(7)	(8)	(9)	(10)	(11)	(12)	(13)	(14)	(15)	(16)	(17)
301	NGC 5480	14:06:21.58	+50:43:30.4	H II	30.5	−11.86	0.01	0.49		8.82	8.72	−0.42	0.36	0.19		10.28
302	MCG 6-31-070	14:06:49.08	+33:46:18.3	H II	155.8			1.32	0.38	8.78	8.72	−0.2			1.31	11.07
303	CGCG 74-129	14:10:41.35	+13:33:28.8	Sy	76.5	−12.78	0.02	1.02	0.55			−0.07	0.3	1.06	0.71	
304	NGC 5520	14:12:22.80	+50:20:54.4	H II	30.5	−12.01	0.02	0.32	0.2	8.81	8.74	−0.44	−0.01	−0.02	0.04	10.09
305	NGC 5515	14:12:38.16	+39:18:36.6	Sy	114.1	−12.41	0.07	0.69	0.33			−0.07	0.6	0.75	0.97	
306	NGC 5526_NED02	14:13:53.76	+57:46:16.8	H II	27.9	−12.37	0.04	0.53	0.33	8.66	8.82	−0.52	−0.13	−0.28	−0.2	9.88
307	NGC 5522	14:14:50.38	+15:08:48.8	TO	72.1	−12.63	0.02	0.72	0.29			−0.2	0.41	0.35	0.59	
308	NGC 5541	14:16:31.80	+39:35:20.6	TO	115.4	−11.92	0.02	0.25	0.24			0.08		0.6	1.12	
309	IC 4395	14:17:21.07	+26:51:26.8	H II	160.4			0.87	0.33	8.73		−0.18			1.4	11.37
310	UGC 9165	14:18:47.78	+24:56:25.9	H II	81.3	−13.3	0.24	1.25	0.45	8.7	8.87	−0.34	0.72	0.58	0.86	10.85
311	MK 1490	14:19:43.22	+49:14:11.9	H II	116.2	−12.75	0.03	1.02	0.67	8.85		−0.15	1.01	1.36	1.36	10.77
312	NGC 5585	14:19:48.19	+56:43:45.6	H II	5.6	−11.55	0.02	0.02	0.03	8.41		−0.76	−1.31	−1.11	−0.87	8.8
313	IC 4408	14:21:13.10	+29:59:36.6	H II	134.9	−12.5	0.04	0.76	0.38	8.69		−0.32	1.29	1.01	1.1	11.17
314	NGC 5584	14:22:23.76	-00:23:15.6	H II	23.1	−11.65	0.03	0.2	0.09	8.74		−0.48	−0.03	0.04	0.15	9.86
315	NGC 5633	14:27:28.39	+46:08:47.5	H II	36.5	−11.93	0.02	0.36	0.21	8.76		−0.42	0.27	0.25	0.28	10.4
316	NGC 5660	14:29:49.82	+49:37:21.6	H II	38.9	−11.55	0.01	0.41	0.12	8.75	8.73	−0.4	0.77	0.57	0.65	10.55
317	NGC 5656	14:30:25.51	+35:19:15.7	LNR	53.7	−12.07	0.28	0.36	0.23			−0.06	−0.22	0.29	0.6	
318	NGC 5657	14:30:43.60	+29:10:51.0	H II	64.4	−12.06	0.02	0.62	0.24	8.8		−0.39	0.96	0.69	0.37	10.62
319	CGCG 133-083	14:31:54.10	+21:56:18.3	H II	190.6			0.93	0.4	8.82		−0.26			1.41	10.93
320	MCG 7-30-028	14:33:48.36	+40:05:38.9	H II	116.1	−12.53	0.01	0.6	0.34	8.82		−0.35	0.94	0.82	0.99	10.94
321	MCG 6-32-070	14:35:18.38	+35:07:07.2	H II	127.0	−12.14	0.02	0.43	0.3	8.77	8.71	−0.38	1.21	1.2	1.22	11.03
322	UGC 9412	14:36:22.08	+58:47:39.3	Sy	138.7	−11.95	0.01	−0.43	0.09			−0.05	−0.39	1.64	1.44	
323	NGC 5698	14:37:14.69	+38:27:15.4	H II	60.9	−12.4	0.02	0.55		8.87	8.72	−0.3	0.4	0.45		10.6
324	NGC 5691	14:37:53.33	-00:23:55.9	H II	19.8	−11.87	0.02	0.11	0.15	8.6	8.79	−0.53	−0.48	−0.21	−0.15	9.66
325	MCG 9-24-035	14:45:45.12	+51:34:50.9	H II	137.4	−12.67	0.1	0.86	0.43	8.79		−0.11	0.91	1.18	1.21	11.23

(1)	(2)	(3)	(4)	(5)	(6)	(7)	(8)	(9)	(10)	(11)	(12)	(13)	(14)	(15)	(16)	(17)
326	MCG 9-24-038	14:46:37.08	+56:13:58.7	TO	166.6			1.12	0.42			−0.32			1.12	
327	UGC 9560	14:50:56.57	+35:34:19.6	H II	23.0	−12.05	0.0	0.11	0.08	8.13	8.71	−1.38	−0.39	−0.26	−0.39	8.59
328	IC 1076	14:54:59.62	+18:02:14.4	H II	92.5	−12.3	0.02	0.37	0.22	8.72		−0.46	0.74	0.76	0.78	10.64
329	IRAS 14538+1730	14:56:08.54	+17:18:34.4	H II	432.9			1.18	0.57	8.72		−0.09			1.93	11.53
330	NGC 5795	14:56:19.34	+49:23:55.4	H II	38.2	−12.4	0.2	0.41	0.38	8.7	9.0	−0.44	−0.07	0.05	0.17	9.59
331	UGC 9618_NED02	14:57:00.79	+24:37:02.2	TO	145.8	−12.44	0.02	0.81	0.55			−0.13	1.17	1.34	1.68	
332	UGC 9639	14:58:36.00	+44:53:01.0	Sy	157.7			0.73	0.36			−0.03			1.33	
333	MCG 6-33-022	15:08:05.98	+34:23:27.2	H II	194.5			1.38	0.42	8.61		−0.33			1.51	10.44
334	NGC 5879	15:09:46.78	+57:00:00.8	LNR	15.5	−11.69	0.02	0.43	0.15			−0.0	−1.87	−0.72	−0.25	
335	MCG 9-25-036	15:12:52.33	+51:23:55.0	H II	160.1			0.53	0.5	8.77		−0.35			0.81	10.75
336	NGC 5899	15:15:03.22	+42:02:59.5	Sy	43.5	−11.87	0.01	0.57	0.28			0.25		−0.25	0.49	
337	NGC 5905	15:15:23.33	+55:31:02.3	H II	58.7	−11.88	0.02	0.57	0.17	8.7	8.83	−0.42	1.0	0.73	0.72	10.9
338	MK 848	15:18:06.14	+42:44:45.1	H II	173.9			0.77	0.41	8.65		−0.31			1.87	10.94
339	IC 4553	15:34:57.22	+23:30:13.2	Sy	83.5	−12.38	0.1	0.07	0.65			0.82		1.87	2.28	
340	UGC 9922_NED02	15:35:53.88	+38:40:31.8		86.7	−12.11	0.04	0.31	0.23			−0.52	0.83	0.87	0.83	
341	IC 4567	15:37:13.27	+43:17:53.9	H II	88.6	−12.03	0.01	0.48	0.25	8.65		−0.35	1.05	0.89	0.92	11.03
342	MCG 4-37-016	15:39:27.50	+24:56:51.4	H II	102.9	−12.47	0.09	−0.51	0.29	8.8	8.8	−0.2	−0.75	1.1	0.85	10.65
343	NGC 5975	15:39:57.96	+21:28:14.3	LNR	69.3	−12.75	0.01	1.04	0.44			−0.04	0.1	0.53	0.77	
344	NGC 5980	15:41:30.43	+15:47:15.6	H II	65.2	−11.91	0.05	0.75	0.26	8.69	8.76	−0.25	1.16	0.73	0.79	11.01
345	NGC 5992	15:44:21.50	+41:05:10.9	H II	140.2	−12.26	0.01	0.34	0.23	8.63	8.75	−0.63	1.17	1.24	1.17	10.84
346	NGC 5996	15:46:58.87	+17:53:03.0	H II	54.0	−11.61	0.0	0.28	0.14	8.78		−0.41	0.82	0.87	0.83	10.36
347	IRAS 15519+3537	15:53:48.86	+35:28:02.2	H II	354.1			0.61	0.5	8.65	8.74	−0.47			1.58	11.3
348	UGC 10099	15:56:36.41	+41:52:50.5	H II	152.2	−12.34	0.02	0.29	0.19	8.62		−0.33	0.94	1.15	1.27	10.76
349	MCG 5-38-006	15:58:43.70	+26:49:05.3	H II	69.6	−12.42	0.01	0.7	0.36	8.79	8.8	−0.26	0.66	0.87	0.59	10.55
350	UGC 10120	15:59:09.62	+35:01:47.5	H II	138.9	−12.43	0.03	0.5	0.14	8.77	8.7	−0.83	1.27	1.1	0.89	10.98

(1)	(2)	(3)	(4)	(5)	(6)	(7)	(8)	(9)	(10)	(11)	(12)	(13)	(14)	(15)	(16)	(17)
351	NGC 6027A	15:59:11.18	+20:45:16.8	H II	70.6	−13.05	0.22	0.42	0.46	8.7	8.73	−0.33	−0.26	−0.21	0.24	10.7
352	NGC 6040B	16:04:26.52	+17:44:31.2	LNR	177.0			0.14	0.16			0.25			1.06	
353	UGC 10200	16:05:45.89	+41:20:41.1	H II	31.2	−11.92	0.01	0.18	0.08	8.26	8.94	−1.05	0.08	0.17	0.02	9.41
354	IRAS 16052+5334	16:06:33.00	+53:26:32.1	TO	366.1			1.03	0.74			−0.26			1.62	
355	IRAS 16053+1836	16:07:38.52	+18:28:48.3	H II	161.4			0.96	0.55	8.77		−0.22			1.21	
356	NGC 6090_NED01	16:11:40.32	+52:27:23.1	H II	131.2	−11.78	0.0	−0.23	0.29	8.74	8.72	−0.3	0.65	1.71	1.55	9.93
357	UGC 10273_NED01	16:12:44.69	+28:17:10.0	H II	111.3	−12.44	0.02	0.53	0.26	8.53	8.76	−0.66	1.05	0.9	0.97	10.32
358	IRAS 16150+2233	16:17:08.95	+22:26:28.0	Sy	278.1			0.79	0.68			−0.05			1.5	
359	UGC 10322	16:18:07.85	+22:13:32.3	H II	69.1	−12.49	0.02	0.65	0.3	8.74	8.8	−0.46	0.68	0.49	0.61	10.6
360	NGC 6120	16:19:48.12	+37:46:27.7	H II	134.9	−12.19	0.1	−0.58	0.34	8.88	8.7	−0.24	−0.26	1.21	1.4	11.21
361	MCG 3-42-004	16:24:15.17	+20:11:00.8	H II	171.9			0.78	0.29	8.71	8.8	−0.35			1.18	
362	UGC 10407	16:28:27.89	+41:13:03.5	H II	124.7	−12.13	0.04	0.14	0.15	8.5	8.77	−0.7	0.96	1.15	1.14	10.51
363	IRAS 16320+3922	16:33:49.63	+39:15:47.5	LNR	139.4	−12.45	0.15	0.21	0.2			−0.12	0.3	0.34	0.86	
364	NGC 6186	16:34:25.49	+21:32:27.2	H II	162.8	−12.19	0.01	0.59	0.26	8.81		−0.35	1.57	1.4	1.48	11.72
365	MCG 9-27-053	16:35:15.41	+52:46:49.9		129.2	−13.14	0.08	0.59				−0.14	0.1	0.49		
366	UGC 10514	16:42:23.66	+25:05:11.5	H II	100.5	−12.43	0.01	0.41	0.26	8.41		−0.68	0.83	0.91	0.97	10.48
367	IRAS 16435+2154	16:45:40.68	+21:49:19.0	H II	142.3	−12.91	0.04	0.83	0.51	8.78		−0.38	1.07	0.82	1.12	10.62
368	IC 4623	16:51:05.33	+22:31:38.6	H II	138.5	−12.91	0.02	0.88	0.37	8.82	8.71	−0.34	1.09	0.88	1.04	10.99
369	IRAS 16516+3030	16:53:37.18	+30:26:09.7	LNR	306.1			−0.67	0.6			0.56			1.69	